Experimental characterization and modeling of the permeability of fibrous preforms using gas for direct processes application.

Yi Hou

NNT : 2012 EMSE 0667

THÈSE

présentée par

Yi HOU

pour obtenir le grade de
Docteur de l'École Nationale Supérieure des Mines de Saint-Étienne

Spécialité : Mécanique et Ingénierie

EXPERIMENTAL CHARACTERIZATION AND MODELING OF THE PERMEABILITY OF FIBROUS PREFORMS USING GAS FOR DIRECT PROCESSES APPLICATION

soutenance prévue à Saint-Etienne, le 25 Octobre 2012

Membres du jury

Rapporteurs :	Véronique MICHAUD	Prof., École Polytechnique Fédérale de Lausanne
	Simon BICKERTON	Prof., University of Auckland
Examinateur :	Fabrice SCHMIDT	Prof., École des Mines d'Albi-Carmaux
Directeurs de thèse :	Sylvain DRAPIER	Prof., École des Mines de Saint-Étienne
	Christophe BINETRUY	Prof., École Centrale de Nantes
Encadrant :	Sébastien COMAS-CARDONA	Prof., École Centrale de Nantes
Invité :	Pierre BEAUCHÊNE	Dr-Ingénieur de Recherche, ONERA, Chatillon

Spécialités doctorales :	Responsables :
SCIENCES ET GENIE DES MATERIAUX	K. Wolski Directeur de recherche
MECANIQUE ET INGENIERIE	S. Drapier, professeur
GENIE DES PROCEDES	F. Gruy, Maître de recherche
SCIENCES DE LA TERRE	B. Guy, Directeur de recherche
SCIENCES ET GENIE DE L'ENVIRONNEMENT	D. Graillot, Directeur de recherche
MATHEMATIQUES APPLIQUEES	O. Roustant, Maître-assistant
INFORMATIQUE	O. Boissier, Professeur
IMAGE, VISION, SIGNAL	JC. Pinoli, Professeur
GENIE INDUSTRIEL	A. Dolgui, Professeur
MICROELECTRONIQUE	Ph. Collot, Professeur

EMSE : Enseignants-chercheurs et chercheurs autorisés à diriger des thèses de doctorat (titulaires d'un doctorat d'État ou d'une HDR)

AVRIL	Stéphane	MA	Mécanique & Ingénierie	CIS
BATTON-HUBERT	Mireille	MA	Sciences & Génie de l'Environnement	Fayol
BENABEN	Patrick	PR 1	Sciences & Génie des Matériaux	CMP
BERNACHE-ASSOLLANT	Didier	PR 0	Génie des Procédés	CIS
BIGOT	Jean-Pierre	MR	Génie des Procédés	SPIN
BILAL	Essaïd	DR	Sciences de la Terre	SPIN
BOISSIER	Olivier	PR 1	Informatique	Fayol
BORBELY	Andras	MR	Sciences et Génie des Matériaux	SMS
BOUCHER	Xavier	MA	Génie Industriel	Fayol
BRODHAG	Christian	DR	Sciences & Génie de l'Environnement	Fayol
BURLAT	Patrick	PR 2	Génie industriel	Fayol
COLLOT	Philippe	PR 1	Microélectronique	CMP
COURNIL	Michel	PR 0	Génie des Procédés	SPIN
DARRIEULAT	Michel	IGM	Sciences & Génie des Matériaux	SMS
DAUZERE-PERES	Stéphane	PR 1	Génie industriel	CMP
DEBAYLE	Johan	CR	Image, Vision, Signal	CIS
DELAFOSSE	David	PR1	Sciences & Génie des Matériaux	SMS
DESRAYAUD	Christophe	MA	Mécanique & Ingénierie	SMS
DOLGUI	Alexandre	PR 1	Génie Industriel	Fayol
DRAPIER	Sylvain	PR 2	Sciences & Génie des Matériaux	SMS
FEILLET	Dominique	PR 2	Génie Industriel	CMP
FOREST	Bernard	PR 1	Sciences & Génie des Matériaux	CIS
FORMISYN	Pascal	PR 1	Sciences & Génie de l'Environnement	Fayol
FRACZKIEWICZ	Anna	DR	Sciences & Génie des Matériaux	SMS
GARCIA	Daniel	MR	Sciences de la terre	SPIN
GIRARDOT	Jean-Jacques	MR	Informatique	Fayol
GOEURIOT	Dominique	MR	Sciences & Génie des Matériaux	SMS
GRAILLOT	Didier	DR	Sciences & Génie de l'Environnement	Fayol
GROSSEAU	Philippe	MR	Génie des Procédés	SPIN
GRUY	Frédéric	MR	Génie des Procédés	SPIN
GUY	Bernard	MR	Sciences de la Terre	SPIN
GUYONNET	René	DR	Génie des Procédés	SPIN
HAN	Woo-Suck	CR		SMS
HERRI	Jean-Michel	PR 2	Génie des Procédés	SPIN
INAL	Karim	PR 2	Microélectronique	CMP
KLÖCKER	Helmut	DR	Sciences & Génie des Matériaux	SMS
LAFOREST	Valérie	CR	Sciences & Génie de l'Environnement	Fayol
LERICHE	Rodolphe	CR CNRS	Mécanique et Ingénierie	SMS
LI	Jean-Michel	EC (CCI MP)	Microélectronique	CMP
MALLIARAS	George Grégory	PR 1	Microélectronique	CMP
MOLIMARD	Jérôme	PR2	Mécanique et Ingénierie	SMS
MONTHEILLET	Frank	DR 1 CNRS	Sciences & Génie des Matériaux	SMS
PERIER-CAMBY	Laurent	PR 2	Génie des Procédés	SPIN
PIJOLAT	Christophe	PR 1	Génie des Procédés	SPIN
PIJOLAT	Michèle	PR 1	Génie des Procédés	SPIN
PINOLI	Jean-Charles	PR 0	Image, Vision, Signal	CIS
ROUSTANT	Olivier	MA		Fayol
STOLARZ	Jacques	CR	Sciences & Génie des Matériaux	SMS
SZAFNICKI	Konrad	MR	Sciences & Génie de l'Environnement	Fayol
TRIA	Assia		Microélectronique	CMP
VALDIVIESO	François	MA	Sciences & Génie des Matériaux	SMS
VIRICELLE	Jean-Paul	MR	Génie des procédés	SPIN
WOLSKI	Krzysztof	DR	Sciences & Génie des Matériaux	SMS
XIE	Xiaolan	PR 1	Génie industriel	CIS

ENISE : Enseignants-chercheurs et chercheurs autorisés à diriger des thèses de doctorat (titulaires d'un doctorat d'État ou d'une HDR)

FORTUNIER	Roland	PR	Sciences et Génie des matériaux	ENISE
BERGHEAU	Jean-Michel	PU	Mécanique et Ingénierie	ENISE
DUBUJET	Philippe	PU	Mécanique et Ingénierie	ENISE
LYONNET	Patrick	PU	Mécanique et Ingénierie	ENISE
SMUROV	Igor	PU	Mécanique et Ingénierie	ENISE
ZAHOUANI	Hassan	PU	Mécanique et Ingénierie	ENISE
BERTRAND	Philippe	MCF	Génie des procédés	ENISE
HAMDI	Hédi	MCF	Mécanique et Ingénierie	ENISE
KERMOUCHE	Guillaume	MCF	Mécanique et Ingénierie	ENISE
RECH	Joël	MCF	Mécanique et Ingénierie	ENISE
TOSCANO	Rosario	MCF	Mécanique et Ingénierie	ENISE
GUSSAROV Andrey	Andrey	Enseignant contractuel	Génie des procédés	ENISE

Glossaire :

PR 0	Professeur classe exceptionnelle	Ing.	Ingénieur
PR 1	Professeur 1ère classe	MCF	Maître de conférences
PR 2	Professeur 2ème classe	MR(DR2)	Maître de recherche
PU	Professeur des Universités	CR	Chargé de recherche
MA(MDC)	Maître assistant	EC	Enseignant-chercheur
DR	Directeur de recherche	IGM	Ingénieur général des mines

Centres :

SMS	Sciences des Matériaux et des Structures
SPIN	Sciences des Processus Industriels et Naturels
FAYOL	Institut Henri Fayol
CMP	Centre de Microélectronique de Provence
CIS	Centre Ingénierie et Santé

Dernière mise à jour le : 02 avril 2012

Abstract

A methodology to measure in-plane permeability of fibrous media using a transient one dimensional air flow is developed. The method, based on the measurement of gas pressure at the boundaries throughout the transient flow, is convenient, clean and fast, avoids usage of a gas flow meter and offers a way to study the gas transport within fibrous media.

The gas transport through fibrous porous media is described by several models to comply with different flow regimes. The permeability, only depending on the fibrous structure, is determined by inverse method, fitting the simulation results to the experimental data obtained using rising or dropping pressure methods. The results of viscous permeability K_v of Glass/Carbon Twill Woven fabrics (viscous permeability K_v ranging from 10^{-11} to 10^{-10} m^2) measured using gas match well the permeability measured with liquid compression and injection techniques from previous works. The deviation from Darcy's law caused by gas sliding effect on low permeability Carbon Uni-Directional fabrics (K_v from 10^{-14} to 10^{-12} m^2) is analyzed and a related parameter of fabric material shows a dependence in permeability, with a similar trend as the Klinkenberg sliding parameter in soils and rocks.

The experimental errors due to dimensions, thermal effect, pressure variation, sample handling, and trapped gas at boundaries are analyzed. It comes out that the sensitivities of pressure sensors and trapped gas volumes at the boundaries have the most important effects.

A design for 2D measurement using gas to obtain 2D permeability tensor in one single test is proposed to avoid the issues of trapped gas at boundaries. Simulated experiments show that the measurements based on pressure measured at three proposed locations could provide robust and accurate results for fabrics of anisotropic permeability ratios (K_1/K_2) ranging from 0.1 to 10, with various principal permeability direction orientations.

Résumé

Une méthodologie pour mesurer la perméabilité plane d'un milieu fibreux par un flux d'air transitoire est développée. Le procédé, basé sur la mesure de pression d'un gaz aux bornes du système, au cours d'un écoulement transitoire, est pratique, propre et rapide, et permet d'éviter l'utilisation d'un débitmètre de gaz et offre la possibilité d'étudier le transport d'un gaz à l'intérieur du milieu fibreux.

Le transport du gaz dans un milieu poreux fibreux est décrit par plusieurs modèles suivant les différents régimes d'écoulement. La perméabilité, dépendant uniquement de l'architecture fibreuse, est déterminée par une méthode inverse, en ajustant les résultats de la simulation aux données expérimentales obtenues par une hausse ou une chute de la pression. Les résultats pour la perméabilité visqueuse K_v des tissus sergés des verre/carbone (K_v allant de 10^{-11} à 10^{-10} m^2) mesurée à l'aide d'un gaz corrèlent bien à la perméabilité mesurée avec des techniques d'injection ou compression utilisant un liquide. L'écart avec la loi de Darcy causé par le glissement du gaz sur les tissus à faible perméabilité (tissus unidirectionnels de carbone: K_v de 10^{-14} à 10^{-12} m^2) est analysé et un paramètre lié au tissu montre une dépendance avec la perméabilité, avec une tendance similaire au paramètre de Klinkenberg utilisé pour les sols et les roches.

Les erreurs expérimentales dues à des dimensions, à l'effet thermique, à la variation de pression, à la manipulation des échantillons, et à du gaz emprisonné sur les bords sont analysés. Il en ressort que la sensibilité des capteurs de pression et des volumes de gaz piégés sur les bords sont les facteurs les plus importants.

La mise en place d'une méthode permettant une mesure directe de la perméabilité à l'aide d'un gaz du tenseur 2D de perméabilité est proposée pour les problèmes de gaz piégés sur les bords. Les expériences simulées montrent que les mesures basées sur la pression mesurée à trois positions pourraient fournir des résultats fiables et précis pour des tissus avec des rapports d'anisotropie perméabilité (K_1/K_2) allant de 0,1 à 10, et avec des orientations principales quelconques.

List of acronyms

RVE	Representative Volume Element
DPM	Dropping Pressure Method
RPM	Raised Pressure Method
CUD	Carbon uni-directional fabric
CBD	Carbon bidirectional fabric
CTW	Carbon twill weave fabric
GTW	Glass twill weave fabric
LCM	Liquid Composites Molding
RFI	Resin Film Infusion
SCRIMP	Seeman Composites Resin Infusion Molding Process
1D	One dimensional
2D	Two dimensional
3D	Three dimensional
BC	Boundary condition
DGM	Dust gas model

List of symbols

General Symbols

ρ	Density
$\dot{\rho}^{\Delta}$	Density variation rate due to chemical reaction or absorption
t	Time
t_0	Characteristic time
$\boldsymbol{I}$	Identity matrix
P	Pressure
P_a	Pressure of atmosphere
P_{vac}	Vacuum pressure obtained in experiments
$\boldsymbol{T}$	Deviatoric stress tensor
$\boldsymbol{E}$	Strain rate tensor
$\boldsymbol{F}$	Exterior force per volume
$\boldsymbol{f}$	Body force
$\boldsymbol{x}$	Material coordinates in Lagrangian frame
$\boldsymbol{\xi}$	Spatial coordinates in Eulerian frame
$\boldsymbol{e}_i$	A set of orthonormal vectors in a Cartesian coordinate system
$\boldsymbol{a}$	Acceleration
$\boldsymbol{f}$	Body forces per unit volume acting on the fluid
$\boldsymbol{g}$	Acceleration of gravity
$\boldsymbol{v}$	Pore (interstitial) velocity
$\boldsymbol{q}$	Filtration velocity or Darcy flux
Q	Discharge per unit time and unit penetration length of the porous bed
μ	Viscosity

μ^v	Volume viscosity coefficient, second viscosity coefficient or bulk viscosity.
μ_0	Reference viscosity in Sutherland's equation
T_0	Reference temperature in Sutherland's equation
C	Sutherland's constant
$\boldsymbol{K}_v$	Viscous permeability tensor
K	Scalar permeability of isotropic fabric
R_k	Permeability anisotropy ratio: K_1/K_2
K_r	In-plane permeability of isotropic fabric
K_z	Transverse permeability
K_g	Apparent permeability measured using gas
K_s	Saturated permeability in Comsol Earth Science Module
K_∞	Absolute permeability measured using gas under extremely large gas pressure
b	Klinkenberg parameter
C_b	Klinkenberg effect coefficient
β	Factor in Forchheimer equation to be determined experimentally
K_n	Knudsen number
K_m	Knudsen flow parameter (m)
ϖ	Dimensionless probability factor
$\bar{v}$	Mean molecular velocity
σ	Diameter of gas molecules
$\tilde{n}$	Molecular density (mol/m^3)
M	Molecular mass
λ	Mean free path of gas
κ_B	Boltzmann constant, 1.38×10^{23} J/K
n	Number of moles
T	Temperature in Kelvin
T_a	Room temperature
R	Universal gas constant
ω	Average molecular weight of the gas phase
U	Average internal energy
Q_h	Heat coming from out of the system
H	Enthalpy
$\hat{C}_v$	Dimensionless isochoric specific heat capacity
h_c	Heat transfer coefficient
κ	Heat conductivity
γ	Adiabatic index
$\hat{\gamma}$	Efficient adiabatic index
l_r	Characteristic length of RVE in porous media

l_ϕ	Characteristic length of pores
L	Sample length
L_b	Sample width
L_e	Flow-path length within porous media
V_f	Fiber volume fraction
ϕ	Porosity
$\mathscr{O}$	Sphericity of the particles in the packed bed
$\mathscr{D}$	Diameter of the related spherical particle
$\mathscr{R}$	Radius of the related fibers
$\mathscr{R}_t$	Hydraulic radius of the tube
$\mathscr{T}$	Tortuosity
$\mathscr{M}$	Specific surface area (per unit volume of solid material)
h	Preform thickness
$\hat{h}$	Dimensionless preform thickness
V	Volume of air trapped in the cavity
A	Sectional area of gas flow through preform
C_k	Parameter which shows the effect of volume area ratio
N_p	Number of plies of fabric in one sample
ε	Error between experimental and simulated pressures
W_f	Weight per unit area of the fabric
P_i	Pressure at inlet boundary
P_o	Pressure at outlet boundary
P_I	Loading pressure in measurements use gas
P_O	Pressure responses in measurements use gas
N	Data points number on one output pressure curve during a test
N'	Number of output pressure curves in one test
r_o	Sample radius in radial measurements
r_i	Inner boundary radius of the sample
C_{vr}	Coefficient of variation

Operators

$\square^*$	Dimensionless variables
$\dot{\square}, \dfrac{\partial}{\partial t}$	Local derivative
$\dfrac{D}{Dt}$	Convective derivative, or the material derivation
∇	Gradient of a scalar function:
	$\dfrac{\partial}{\partial x}\boldsymbol{e}_x + \dfrac{\partial}{\partial y}\boldsymbol{e}_y + \dfrac{\partial}{\partial z}\boldsymbol{e}_z$ in Cartesian coordinates;
	$\dfrac{\partial}{\partial r}\boldsymbol{e}_r + \dfrac{\partial}{r\partial\theta}\boldsymbol{e}_\theta + \dfrac{\partial}{\partial z}\boldsymbol{e}_z$ in Cylindrical coordinates.
$\nabla\cdot$	Divergence
$\nabla\times$	Curl
Δ	Laplace operator $\nabla\cdot\nabla$:
	$\dfrac{\partial^2\square_x}{\partial x^2} + \dfrac{\partial^2\square_y}{\partial y^2} + \dfrac{\partial^2\square_z}{\partial z^2}$ in Cartesian coordinates;
	$\dfrac{\partial}{r\partial r}\left(r\dfrac{\partial\square_r}{\partial r}\right) + \dfrac{\partial^2\square_\theta}{r^2\partial\theta^2} + \dfrac{\partial^2\square_z}{\partial z^2}$ in Cylindrical coordinates.

Contents

List of Figures

List of Tables

General introduction

Liquid composite molding (LCM) consists of a variety of composite manufacturing processes, including Resin Transfer Molding (RTM), Vacuum-Assisted RTM (VARTM), the Seemann Composite Resin Infusion Molding Process (SCRIMP), and Injection Compression Molding (ICM). These processes are capable of producing high-quality, complex-shaped fiber reinforced polymeric products and, hence, are used mainly in the aerospace, automotive, marine, and civil industries.

Permeability is a very important parameter of composite materials in resin filling simulations performed for LCM (liquid composite molding) processes to choose resin inlet/outlet locations and to predict the injection times. However, most of the permeability measurement techniques rely on liquid injection experiments and still show high discrepancies. In order to reduce the experimental discrepancies, one option is to simplify as much as possible the experimental benches to avoid errors accumulating. Experimentally, compared with liquid measurement, the use of gas has an advantage of short experimental time due to low gas viscosity, and hence gas permeability measurement has been extensively applied to materials with small permeabilities, such as rocks, soils, membranes and ceramics. Also, using gas instead of liquid provides a measurement cleaner and less consumptive in terms of materials waste.

However, what determines the permeability for gas is to be investigated. Moreover, there remains the questions whether the differences between air permeability and liquid permeability can be neglected, or how gas permeability relates with liquid permeability? The objective of this thesis is to understand the mechanics of air flow through porous media.

Models are built in various flow regimes (continuous, discontinuous, and sliding

regimes) with the corresponding assumptions. A fast permeability measurement method using air is designed and the comparison is made between permeability measurements using liquid and air. Factors leading to errors in 1D (one dimensional) permeability measurements using air are detailed and the robustness and accuracy are analyzed for 2D (two dimensional) measurements. The structure of the thesis will be shown as follow,

1. The first chapter presents a literature review on theories and experiments. The gas transport mechanisms are classified into 3 types: *Knudsen flow*, *Sliding flow* and *Viscous flow* (consisting of *Darcian flow* and *Non-Darcian flow*). The methods to determine permeability using liquid and air are reviewed with their respective advantages and drawbacks.

2. The second chapter introduces a fast permeability measurement using transient gas flow. These measurements are performed on various materials (carbon unidirectional, carbon twill weave, glass twill weave and carbon bidirectional stitched fabrics). The regimes of gas transport are analyzed for each fabrics under the experimental conditions and the results are compared with permeability values measured using liquid.

3. The third chapter introduces a 2D permeability measurement. The robustness and accuracy for cases of various anisotropy ratios of permeability and various principal permeability orientations are analyzed to demonstrate the measurement capability.

CHAPTER 1

Literature review

Abstract of Chap. 1

This chapter is a review about the fundamental theory, development of experiments and major issue on permeability measured with air of porous medium. What the previous researchers focused on could be classified into 4 kinds of problems: mechanism of flow, innovation or criticism on experimental measurements, VARTM process, property of materials (to measure the permeability with specific fluid through specific materials, or to figure out how permeability relies on their structure or humidity).

This review will contain two main parts. First, the theory of fluid flow will be detailed (the concept of air permeability, the equations of the physical process used at different scales, and the assumptions and simplification of models). Several models are built to describe the gas transport through fibrous porous media in different flow regimes: Knudsen flow, sliding flow and viscous flow (consists of Darcian flow and Non-darcian flow).

The second part will introduce issues on experimental methods such as, the determination of permeability with fluids through porous media, the main issues of air permeability measurements, and the errors or drawbacks of different techniques.

Résumé de Chap. 1

Ce chapitre est une revue de la théorie fondamentale, du développement d'expériences et des problèmes majeurs pour la détermination de la perméabilité d'un milieu poreux à l'aide d'un gaz. Les précédents chercheurs montrent que les problématiques peuvent être classées en quatre catégories. : le mécanisme de l'écoulement, la sensibilité des mesures expérimentales, le procédé VARTM, et les propriétés des matériaux (pour mesurer la perméabilité d'un matériau par l'intermédiaire d'un fluide spécifique, ou comprendre la relation entre la perméabilité et la structure ou l'humidité).

Cet revue comprendra deux principales parties. Tout d'abord, la théorie de l'écoulement du fluide sera détaillée (la notion de perméabilité à l'air, les équations du processus physique utilisé à différentes échelles, ainsi que les hypothèses et la simplification des modèles). Plusieurs modèles sont construits pour décrire le transport du gaz à travers les milieux poreux fibreux dans différents régimes d'écoulement: écoulement de Knudsen, l'écoulement glissant et l'écoulement visqueux (comprenant les écoulements de Darcy et les écoulements de non-Darciéns).

La deuxième partie présentera les questions sur les méthodes expérimentales telles que la détermination de la perméabilité d'un milieu poreux par l'intermédiaire d'un fluide, les principaux problèmes de mesure de la perméabilité par air, et les erreurs ou les inconvénients de ces différentes techniques.

1.1 Introduction

This review will contain two main parts: first, the mechanisms of gas transport through porous media are introduced, with models built in various regimes; then, permeability measurement techniques using liquid and gas will be described.

1.2 Gas transport through porous media

Permeability, diffusion and adsorption are the main mechanisms used to describe how gas or fluids are driven respectively by pressure gradient, concentration and surface tension, through porous media, like soil, cementitious composites [12] and fabric structures. Absorption is not considered here since in this study there is no chemistry interaction between glass/carbon and air/nitrogen. Hence gas transport through porous media is considered to be based on four independent mechanisms [13]:

1. Viscous flow, in which the characteristic length of pores within the medium is much larger than the mean free path (*i.e.*, the average distance between molecules) so that molecule-molecule collisions dominate molecule-wall collisions. The gas can be considered as a continuous fluid so the Navier-Stokes equation can be applied with a no-slip boundary condition at the walls.

2. Free-molecular or Knudsen flow, in which the gas density or the pore size is so low that the number of collisions between molecules can be neglected compared with the number of collisions of molecules with the walls of the porous medium.

3. Continuum diffusion, in which the different species of a mixture move relative to each other under the influence of concentration gradients, temperature gradients, or external forces.

4. Surface flow or diffusion, in which molecules move along a solid surface in an adsorbed layer.

For gas permeability measurement of fiber reinforcement, viscous and Knudsen flows dominate, thus diffusions can be neglected. The gas transport regimes are determined by the Knudsen number K_n [14],

$$K_n = \frac{\lambda}{l_\phi} \tag{1.1}$$

where λ is the mean free path and l_ϕ the characteristic length of pores within a medium. The regime of the flow is viscous for $K_n \ll 1$. For $K_n \sim 1$ there is an interaction of viscous and Knudsen flows, leading to the phenomenon of slip flow, involving the slipping of a gas over a solid surface. When $K_n > 1$ Knudsen (free-molecular) flow takes place. For an ideal gas, the mean free path λ may be calculated by [15],

$$\lambda = \frac{k_B T}{\sqrt{2}\pi\sigma^2 P} \tag{1.2}$$

where k_B is the Boltzmann constant (1.38×10^{-23}J/K), T the absolute temperature, P the absolute pressure and σ the diameter of gas molecules. Under standard temperature and pressure, *i.e.*, 25°C and 1 atm, λ is approximately 8×10^{-8} m.

This chapter will contain four parts:

1. The fundamental equations of fluid continuum (the conservation laws and constitutive assumptions), providing a view into the flow in a porous medium at the micro-scale.

2. The momentum conservative equations of continuous flow through a porous medium: Navier-Stokes equation for local flow field. The averaging method makes the porous medium to be treated as a continuum in overall flow field using Darcy's law, which gives a linear relationship between flow rate and pressure gradient; while for non-Darcian flow Forchheimer equation is valid. Brinkman Equation is used to combine Navier-Stokes equation and Darcy's law in two scale media.

3. Knudsen flow for fluids which can not be considered as continuum due to high Knudsen numbers, *i.e.*, the characteristic dimensions of the flow space are of smaller order of magnitude as the mean free path.

4. Various sliding models, used when the characteristic dimension of the flow space is of the same order of magnitude as the mean free path.

1.3 Mass conservation

1.3.1 Principle

Fundamental equations of fluids consist of the conservation equations and constitutive assumptions. Using Gauss's divergence theorem, comes the conservation

equation [16],

$$\frac{\partial g}{\partial t} + \nabla \cdot (g\boldsymbol{v}) = \dot{g}^{\Delta} \tag{1.3}$$

or, the conservation equation in Lagrangian frame,

$$\frac{Dg}{Dt} + g\nabla \cdot \boldsymbol{v} = \dot{g}^{\Delta} \tag{1.4}$$

where $\dot{g}^{\Delta}$ is the quantity of g produced or absorbed during the transport process,

For a fluid system which has one component, the general conservation equation is given by the following equation in a view of Eulerian frame [16]:

$$\frac{\partial \rho}{\partial t} + \nabla \cdot (\rho\boldsymbol{v}) = \dot{\rho}^{\Delta} \tag{1.5}$$

where $\dot{\rho}^{\Delta}$, dim: M L $^{-3}$ T^{-1}, is the rate at which mass is produced per unit volume of the system by chemical reactions or reduced by absorption, and ρ is the density. In this study, there is no chemical reaction or absorption between fibers and gas, hence mass conservation writes as,

$$\frac{\partial \rho}{\partial t} + \nabla \cdot (\rho\boldsymbol{v}) = 0 \tag{1.6}$$

1.3.2 Incompressible flow and Compressible flows

For incompressible flow, of which the density ρ is constant, mass conservation Eq. 1.6 is reduced as,

$$\nabla \cdot \boldsymbol{v} = 0 \tag{1.7}$$

For compressible flow, of which the density ρ depends on stress, temperature, *etc.*, a definite function of density should be provided for the mass conservation (Eq. 1.6).

1.4 Momentum conservation

1.4.1 Principle

Different forms of momentum conservation principle are used at different scales: the classic Newton's second law, $\boldsymbol{F} = m\boldsymbol{a}$, for particles; for fluid, by inserting $g = \rho\boldsymbol{v}$, the momentum conservative equation could be obtained [11],

$$\frac{\partial \rho\boldsymbol{v}}{\partial t} + \nabla \cdot (\rho\boldsymbol{v}\boldsymbol{v}) = (\dot{\rho\boldsymbol{v}})^{\nabla} \tag{1.8}$$

where $\boldsymbol{vv}$ are dyadic products of $\boldsymbol{v}$ and $\boldsymbol{v}$, and $(\dot{\rho\boldsymbol{v}})^{\nabla}$ is produced by the exterior source. Inserting the mass conservation equation, the equation becomes,

$$\rho\frac{\partial \boldsymbol{v}}{\partial t} + \rho\nabla\cdot(\boldsymbol{vv}) + S_m\boldsymbol{v} = \rho(\dot{\boldsymbol{v}})^{\nabla} + (\dot{\rho})^{\nabla}\boldsymbol{v} = \boldsymbol{F} + S_m\boldsymbol{v}_0 \tag{1.9}$$

where $\boldsymbol{F}$ is the exterior force per volume, the sum of body force $\boldsymbol{f}$ and stress σ, and S_m is the exterior mass source and $\boldsymbol{v}_0$ is the corresponding flow rate. In a case where S_m vanishes, the equation becomes the Navier-Stokes equation, which can describe fluid with boundary conditions, usually applied for porous medium at the micro-scale. At the macro-scale, considering the porous medium as a homogeneous continuum, Navier-Stokes equation is up-scaled to Darcy's law, a linear relationship between pressure gradient and flow rate with a linear coefficient K, called "permeability" of porous media.

1.4.2 Continuous flow through porous medium

When $K_n \ll 1$, the size of pores within a medium is large enough for molecules to collide frequently. In this case the flow is continuous, viscous and can be driven by pressure gradients within the pores. A Newtonian viscous flow can be described by the Navier-Stokes equation. Random paths of molecules after collisions with walls induce a no-slip (zero velocity) boundary condition.

Given a certain micro-structure and fluid, flow field can always be solved precisely with Navier-Stokes equation. This method is applicable for local flow, while for a overall flow field, the computational time will be too high. To allow more efficient measurements and computations, porous medium, discontinuous locally with voids in solid matrix, is very often considered continuous. Local fundamental equations are up-scaled using local volume averaging on a Representative Volume Element [17], with the conditions on the size of RVE, $l_\phi \ll l_r \ll L$. l_r and L are the characteristic lengths of respectively the REV and the structure; l_ϕ the characteristic length scale of the local heterogeneities, typically the pore size in a porous medium.

Although up-scaling can give fundamental equations at the macro-scale, the first momentum equation of porous media is revealed by experiments and referred to as Darcy's law [18]. Darcy's law is only valid for slow, viscous flow; fortunately, most groundwater flow cases fall in this category, and for air flow cases the conditions can be set cautiously to make Darcy's law valid. The Reynolds number (Re), a dimensionless parameter which identifies the ratio of momentum forces to viscous forces and expresses the level of turbulence, is used to check if it is a Darcian flow. Reynolds number for porous media flow is typically expressed as,

$$Re_\phi = \frac{\rho v l_\phi}{\mu} = \frac{\rho q l_\phi}{\phi \mu} \tag{1.10}$$

where ρ is the density of the fluid (units of mass per volume), v is the average pore flow velocity, q is the specific discharge which equals to ϕv, l_ϕ is a representative grain diameter or pore size for the porous medium (often taken as the 30% passing size from a grain size analysis using sieves; and for fibers, the square root of permeability K is a good order of magnitude, and μ is the dynamic viscosity of the fluid.

Typically any flow with Reynolds number (based on a pore size length scale) less than one is considered laminar, and it would be valid to apply Darcy's law. For Reynolds number $Re_\phi > 10$, the flow changes from purely viscous to inertial dominated and a nonlinear relationship between the pressure gradient and flow rate appears (Tab. 1.1) [11]. Bear (1972) suggested a critical Re_ϕ of 3 to 10 [16]. Hassanizadeh and Gray (1987) reported critical value $Re_\phi = 1$ - 15, and suggested $Re_\phi = 10$ as a critical value for non-Darcy flow [19]. From experiments with gas flow through packed particles Ergun gave a critical value of Re_ϕ from 3 to 10 [20]; Scheidegger (1974) noted a range of Re_ϕ from 0.1 to 75 in the review of experiments [21]. Du Plessis and Masliyah (1988) used a representative unit cell to model fluid flow in porous media and obtained a critical Re_ϕ from 3 to 17 [22].

Re_ϕ	Mechanisms	Momentum equations ($\nabla P = f(\boldsymbol{q})$)
< 1	Darcian flow	Linear (Eq. 1.15)
1 - 10	Transition region	
10 - 200	Inertial dominated flow	Quadratic (Eq. 1.20)
200 - 300	Unsteady laminar flow	
300 - 350	Formation of vortices	
> 350	Highly unsteady & chaotic (similar as turbulent flow)	Cubic

Table 1.1: Flow modes through porous media related to Re_ϕ [11].

In this section, 4 momentum conservative equations will be introduced, along with Navier-Stokes equations for micro-scale, Darcy's or non-Darcian flow for macro-scale and Brinkman's equation for meso-scale (scales of porous media shown in Fig. 1.1). The problem of flow through porous media can be solved with constitutive equations (ideal gas law), mass conservation and momentum conservation equations.

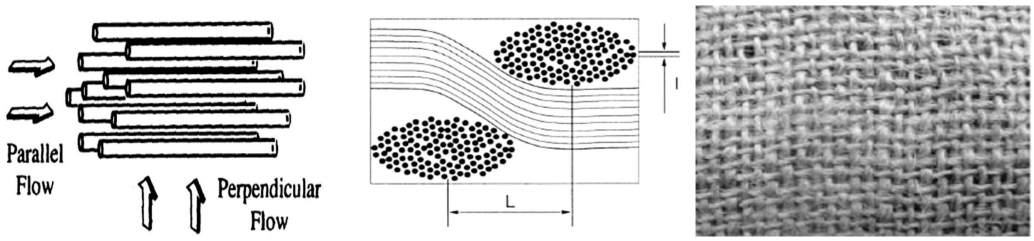

(a) micro (b) meso (c) macro

Fig. 1.1: Three different scales of fibrous media concerned with modeling.

1.4.3 Navier-Stokes equation

The Navier-Stokes equation describes the fluid flow at the micro-scale. In an inertial frame of reference, the general form of the equation of fluid motion is [23]:

$$\rho \frac{D\boldsymbol{v}}{Dt} = -\nabla P + \nabla \cdot \boldsymbol{T} + \boldsymbol{f} \tag{1.11}$$

or, with the derivative expanded out,

$$\rho \left(\frac{\partial \boldsymbol{v}}{\partial t} + \boldsymbol{v} \cdot \nabla \boldsymbol{v} \right) = -\nabla P + \nabla \cdot \boldsymbol{T} + \boldsymbol{f} \tag{1.12}$$

where $\boldsymbol{v}$ is the flow velocity, ρ the fluid density, P the pressure, $\boldsymbol{T}$ the deviatoric stress tensor.

1.4.3.1 Incompressible flow of Newtonian fluids

A simplification of the resulting flow equations is obtained when considering an incompressible flow of a Newtonian fluid. Taking the incompressible flow assumption into account and assuming constant viscosity, the Navier-Stokes equation will read, in vector form:

$$\rho \left(\frac{\partial \boldsymbol{v}}{\partial t} + \boldsymbol{v} \cdot \nabla \boldsymbol{v} \right) = -\nabla P + \mu \nabla^2 \boldsymbol{v} + \boldsymbol{f} \tag{1.13}$$

Here $\boldsymbol{f}$ represents "other" body forces (forces per unit volume), such as gravity or centrifugal force. The shear stress term $\nabla \cdot \boldsymbol{T}$ becomes the useful quantity $\mu \nabla^2 \boldsymbol{v}$ when the fluid is assumed incompressible and Newtonian, where μ is the dynamic viscosity [24].

It is worth observing the meaning of each term:

$$\overbrace{\underbrace{\rho\left(\frac{\partial \boldsymbol{v}}{\partial t}\right)}_{\substack{\text{Unsteady}\\ \text{acceleration}}} + \underbrace{\rho\boldsymbol{v}\cdot\nabla\boldsymbol{v}}_{\substack{\text{Convective}\\ \text{acceleration}}}}^{\text{Inertia per volume}} = \overbrace{\underbrace{-\nabla P}_{\substack{\text{Pressure}\\ \text{gradient}}} + \underbrace{\mu\nabla^2\boldsymbol{v}}_{\text{Viscosity}} + \underbrace{\boldsymbol{f}}_{\substack{\text{Other}\\ \text{body}\\ \text{forces}}}}^{\text{Divergence of stress}} \tag{1.14}$$

1.4.4 Darcy's flow

Besides mass conservation, additional information as constitutive assumptions of constitutive equations is necessary. Considering air as a Newtonian fluid, the momentum conservation for the air flow across a porous medium may be described using Darcy's law, which is the simplest assumption in the form of first gradient law,

$$\boldsymbol{q} = -\frac{\boldsymbol{K}_v}{\mu}\cdot(\nabla P - \rho\boldsymbol{g}) \tag{1.15}$$

where $\boldsymbol{q}$ is the filtration or Darcy's velocity and ∇P is the pressure gradient vector. The velocity $\boldsymbol{q}$ is related to the pore (interstitial) average velocity $\boldsymbol{v}$ and the porosity ϕ,

$$\boldsymbol{v} = \frac{\boldsymbol{q}}{\phi} \tag{1.16}$$

$\boldsymbol{K}_v$ is the viscous permeability of the porous medium; for isotropic material permeability $\boldsymbol{K}_v$ becomes $K_v\boldsymbol{I}$ and hence K_v is used to represent the permeability. For a gas used as a fluid, the effect of the gravity can be neglected,

$$\boldsymbol{q} = -\frac{\boldsymbol{K}_v}{\mu}\cdot\nabla P \tag{1.17}$$

The viscous flux J_{visc} (mol/(s $\cdot$m^2)) is given by [14],

$$J_{visc} = -(\tilde{n}K_v/\mu)\frac{\Delta P}{\delta} \tag{1.18}$$

where ΔP is the pressure difference across the distance δ, μ is the fluid viscosity and $\tilde{n}$ is the molecular density (mol/m^3). The value of the viscous permeability K_v for certain geometries can be calculated. For example, for a long, straight, circular tube of radius $\mathscr{R}_t$, the value of K_v is $\mathscr{R}_t^2/8$. Permeability of a porous medium could be obtained from local permeability by the local averaging method over a RVE [13],

$$K_v = \phi\mathscr{R}_t^2/8\mathscr{T} \tag{1.19}$$

where $\mathscr{T}$ is the tortuosity. The local averaging method can be used to predict the permeability of porous medium by upscaling of the Navier-Stokes equation. Bruschke and Advani [25] and Gebart [10] demonstrated that predictions of the permeability from the Stokes flow for homogeneous arrays of aligned cylinders are accurate. However, Sadiq et al [26] showed that predictive methods are not available for more complicated preform architectures consisting of fiber tows.

1.4.5 Forchheimer equation

For a sufficiently high flow velocity, since the flow is nonlinear, Dupuit and Forchheimer have proposed to generalize the flow equation to

$$-\nabla P = \frac{\mu}{K}\boldsymbol{q} + \beta\rho q\boldsymbol{q} \tag{1.20}$$

where β is a factor to be experimentally determined [27]. Assuming the vector velocity field $\boldsymbol{v}$ can be represented as a function of the pressure gradient using the formula,

$$\boldsymbol{v} = -f_\beta(|\nabla P|)\nabla P \tag{1.21}$$

where

$$f_\beta(|\nabla P|) = \frac{2}{(\mu/K) + \sqrt{(\mu/K)^2 + 4\beta|\nabla P|}} \tag{1.22}$$

Eq. 1.21, referred to as Darcy-Forchheimer equation, is convenient in simulations because Darcy's model can solve Forchheimer problem when K/μ is replaced with $f_\beta(|\nabla P|)$.

1.4.6 Brinkman's Equation

An approach to model flow through heterogeneous porous media with more than one typical pore size is to divide the porous medium into two regions: in the larger pores (the Stokes' equations),

$$\nabla P = \mu\nabla^2 v \tag{1.23}$$

and in homogeneous regions of smaller pores (the permeable medium using Darcy's law). The two boundary conditions to be satisfied at the pore/permeable medium interface are continuity of the fluid velocity and the shear stress. Darcy's law alone is not sufficient to satisfy these boundary conditions. The Brinkman equation [28] is a generalization of Darcy's law that facilitates the matching of boundary conditions at an interface between the larger pores and the bounding permeable medium.

$$-\frac{\mu}{K}\boldsymbol{v} + \mu'\nabla^2\boldsymbol{v} = \nabla P \tag{1.24}$$

where μ is the viscosity and μ' is the effective viscosity term, which is to be determined by experiments and assumptions [28] so as to secure a consistency on the interface as,

$$\mu \left.\frac{d\,v}{d\,s}\right|_{Stokes} = \mu' \left.\frac{d\,v}{d\,s}\right|_{Darcy} \tag{1.25}$$

where $d\,s$ is the distance along the interface. When the discretization size in simulation is larger than $\sqrt{K}$, Beaver-Joseph-Saffman's interface condition can be used to replace the Brinkman's interface condition [29].

1.5 Knudsen flow

When $K_n > 1$, the molecules do not collide with each other within the pores. The original studies of Knudsen flow were limited to small holes in very thin plates, and molecules were assumed to move entirely independently of each other during their passage through the holes. Hence the flux of molecules through the holes is equal to the number of molecules passing into the entrance of the hole per unit area and time, multiplied by the probability that a molecule passes through the holes without bouncing back.

Considering a gas with a molecular density $\tilde{n}$ (mol/m^3) at one end of the hole and vacuum at the other end, the Knudsen flux J_k (mol/(s $\cdot$ m^2)) is [14],

$$J_k = \varpi\tilde{n}\bar{v} \tag{1.26}$$

where ϖ is a dimensionless probability factor and $\bar{v}$ is the mean molecular velocity given by,

$$\bar{v} = \sqrt{8k_BT/\pi M} \tag{1.27}$$

where M is the molecular mass. For an infinitesimally thin orifice, $\varpi = 1/4$, and for a long straight circular tube of radius $\mathscr{R}_t$ and length δ ($\delta \gg \mathscr{R}_t$) where molecules rebound on the surface, ϖ is $(2\mathscr{R}_t/3\delta)$. The net flux is proportional to the difference in gas number densities at both sides. The Knudsen flux for a tube can be obtained by inserting ϖ into Eq. 1.26. A Knudsen flow parameter K_m (m), only related to geometry of the hole and the gas-surface scattering law, can be defined [13],

$$J_k = -\frac{2}{3}\mathscr{R}_t \bar{v} \frac{\Delta \tilde{n}}{\delta} = -K_m \bar{v} \nabla \tilde{n} \tag{1.28}$$

Also, for a porous medium with tortuous pores,

$$K_m = 2\phi \mathscr{R}_t / 3\mathscr{T} \tag{1.29}$$

where ϕ is the porosity and $\mathscr{T}$ is the tortuosity. In practice, it is usually much easier to measure K_m experimentally than calculate it from Eq. 1.29, because of the difficulty to measure or estimate the tortuosity.

According to Scheidegger [21], when $K_n \sim 1$ a slip-flow regime occurs and when $K_n > 1$ we have Knudsen flow or *free molecular flow*. While according to Cieplak's works, when $K_n \sim 5$, the flow shows a Knudsen flow when the wall of pipe is *repulsive* and a sliding flow when the wall is *attractive* [2]. The velocity profile of Knudsen flow Fig. 1.2(b) is almost flat in the tube while for slip-flow, velocity keeps a Poiseuille velocity profile in the center but shows a *slip* at the wall of the tube.

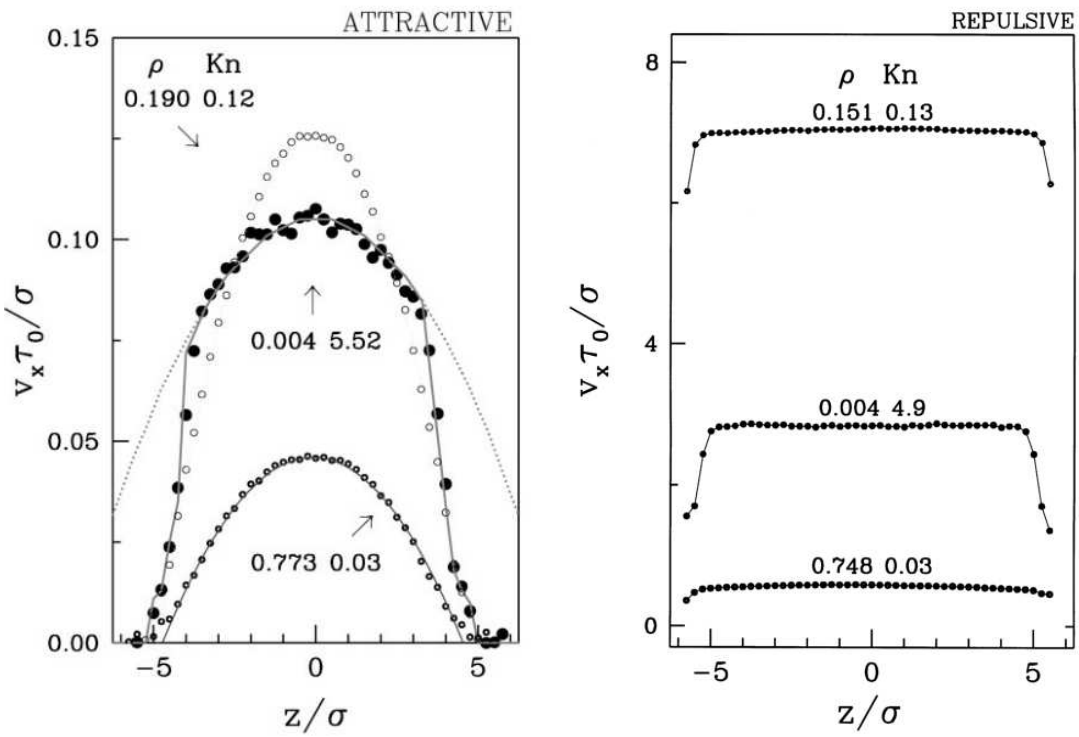

(a) Sliding regime

(b) Knudsen regime

Fig. 1.2: Velocity profiles of fluid flows through attractive and repulsive walls, by molecular dynamics simulations. When $K_n \sim 5$, transport of gas follows different regimes for various properties of walls: (a). Sliding flow for attractive walls [1]; (b). Knudsen flow for repulsive walls [2].

1.6 Sliding models

When $K_n \sim 1$, an interaction between Knudsen and viscous flows produces a flow pattern referred to as sliding flow.

1.6.1 Dust gas model (DGM)

In the dust gas model [30, 13], the porous medium is visualized as an array of dust particles held stationary in space and the presence of gas-surface interactions is taken into account by treating the dust particles as giant molecules, in terms of the classical kinetic theory of gases. Based on this model, a general flux equation for a gas that permeates through a porous medium in the Knudsen-viscous transition region could be obtained as

$$J_{slid} = -\frac{1}{RT}[K_m \bar{v} + \frac{P_{avg} K_v}{\mu}]\frac{\Delta P}{\delta} \tag{1.30}$$

where R is the ideal gas constant, ΔP is the pressure difference across the distance δ and P_{avg} is the average of pressures at both sides of the considered domain. From a mathematical point of view, Eq. 1.30 is a linear addition of Eqs. 1.28 (Knudsen flow) and 1.18 (viscous flow) substituting $\tilde{n}$ using the ideal gas law. With this formulation, the viscous permeability K_v can be extracted from the overall flow even if it combines viscous and Knudsen flows. The phenomenon of gas transport in slip regime involves convection, Knudsen diffusion, and ordinary or Stefan-Maxwell diffusion. Unlike the dusty-gas model, Adam has developed a consistent set of equations to describes gas-phase transport, in which convective and diffusive fluxes are not assumed to be linearly additive, but remain in their coupled form instead [31]. There are also other models to combine the two equations in different ways [32, 33].

1.6.2 Klinkenberg's sliding effect

The Klinkenberg's sliding effect is observed and promoted on gas transport through fine-grained low-permeability porous media, such as soils, with small pore size. Klinkenberg [34] used nitrogen and brine as fluids in a mini-permeameter device. When high rates of flow can be maintained, the results are comparable. At low rates, the effective permeability measured with N_2 gas will be higher than the viscous permeability measured with brine. Klinkenberg explains the change of gas permeability under different pressures by the slippage of gases along the pore walls, since gas does not adhere to the pore walls as liquid does. The effective gas

permeability K_g depending on gas pressure is given by

$$K_g = K_\infty \left(1 + \frac{b}{P}\right) \tag{1.31}$$

where K_∞ is the intrinsic permeability, which is considered to be the absolute gas permeability under very large gas pressure at which condition the Klinkenberg effect is negligible. The Klinkenberg factor b, as a parameter indicating the magnitude of the gas slippage effect, depends on the mean free path of the gas molecules which also depends on pressure, temperature and molecular weight of the gas.

Jones and Owens carried experiments at 0.7 and 6.9 MPa upstream pressure and atmospheric pressure downstream, and found that b decreases with increasing permeability [35]. It has been experimentally fitted to:

$$b = C_b K_\infty^{-0.36} \tag{1.32}$$

where C_b is the Klinkenberg effect coefficient, which is fitted to 0.251 based on the experimental data of 100 rock samples ranging in permeability from 10^{-17} to 10^{-12} m^2 [36]. Heid et al. suggested the relation for air at 25°C for oil-field cores with permeability values of about$10^{-12}\mathrm{m}^2$ and $10^{-17}\mathrm{m}^2$ [37],

$$b = 0.11 K_\infty^{-0.39} \tag{1.33}$$

which is the American Petroleum Institute (API) standard correction and is based on air-dry consolidated media and may not be applicable to unconsolidated media or certain soils, such as for dry Oakley sand. Stonestrom and Rubin reported Equation (1.33) systematically underestimates b for soil, and that the Oakley sand deviation is most severe [38]. Other researchers [35] and [39] also presented the similar fitted value of b from a study using approximately 100 low permeability rock samples.

DGM and Klinkenberg's model are used equivalently in this thesis.

1.7 Constitutive assumptions

1.7.1 The stress tensor for fluids

The stress tensor can be represented as the isotropic term $P\boldsymbol{I}$ and the deviatoric $\boldsymbol{T}$, which are yet unknown, so the general form of the equations of motion is not usable to solve problems. Besides the equations of motion, Newton's second law–a constitutive model is needed relating the stresses to the fluid motion. For this

reason, assumptions on the specific behavior of a fluid are made (based on natural observations) and applied in order to specify the stresses in terms of the other flow variables, such as velocity and density.

The deviatoric stress tensor could be related to the flow rate from the following assumptions [23].

i. The deviatoric stress vanishes for a fluid at rest, and – by Galilean invariation – also does not depend directly on the flow velocity itself, but only on spatial derivatives of the flow velocity, which means $\boldsymbol{T} = \boldsymbol{f}(\nabla \boldsymbol{v})$, the function $\boldsymbol{f}$ could take any form.

ii. The deviatoric stress is expressed as the product of the tensor gradient of the flow velocity with a viscosity tensor, such as $\boldsymbol{T} = \boldsymbol{A} : \nabla \boldsymbol{v}$, which means that the deviatoric stress depends only on $\nabla \boldsymbol{v}$. This assumption is referred to as the "Newtonian fluid assumption".

iii. The fluid is assumed to be isotropic, as valid for gases and simple liquids, and consequently viscosity is an isotropic tensor; furthermore, since the deviatoric stress tensor is symmetric, it turns out that it can be expressed in terms of two scalar dynamic viscosities μ and μ'': $\boldsymbol{T} = 2\mu \boldsymbol{E} + \mu'' \Delta \boldsymbol{I}$, where $\boldsymbol{E}$ is the strain rate tensor $\boldsymbol{E} = (\nabla \boldsymbol{v})/2 + (\nabla \boldsymbol{v})^T/2$ and $\Delta = \nabla \cdot \boldsymbol{v}$ is the rate of expansion of the flow.

   The deviatoric stress tensor has zero trace, so for a three-dimensional flow $2\mu + 3\mu'' = 0$.

As a result, the deviatoric stress tensor has the following form [23],

$$\boldsymbol{T} = 2\mu \left(\boldsymbol{E} - \frac{1}{3} \Delta \boldsymbol{I} \right), \tag{1.34}$$

where the terms between brackets is the deviatoric part of the strain rate tensor $\boldsymbol{E}$. The dynamic viscosity μ does not need to be constant – in general it depends on conditions like temperature and pressure, and in turbulence modeling the concept of eddy viscosity is used to approximate the average deviatoric stress. As for incompressible Newtonian fluid, the isochoric strain rate leads to,

$$\boldsymbol{T} = 2\mu \boldsymbol{E} \tag{1.35}$$

1.7.2 Equation of state for gas

Pressure P is modeled using an equation of state [23]. For the special case of an incompressible flow, the pressure constrains the flow in such a way that the volume

of fluid elements is constant: isochoric flow resulting in a solenoidal velocity field with $\nabla \cdot \boldsymbol{v} = 0$, [23]; for compressible liquid, with the assumption for gas comes the ideal gas law,

$$P = \frac{\rho RT}{\omega} = \frac{nRT}{V} = \tilde{n}RT \tag{1.36}$$

where ω is the average molecular weight of the gas phase, T the temperature in Kelvin, R the universal gas constant, 8.314 J/(mol $\cdot$ K), and $\tilde{n}$ the molecular density (mol/m^3).

The equation of state Eq. 1.36 applies only to an ideal gas, or as an approximation to a real gas that behaves sufficiently like an ideal gas. Since it neglects both molecular size and intermolecular attractions, the ideal gas law is most accurate for monatomic gases at high temperatures and low pressures. Molecular size becomes negligible at lower pressure when it is quite small compared with the average distance between adjacent molecules. The relative importance of intermolecular attractions diminishes with increasing thermal kinetic energy, *i.e.*, with increasing temperatures. There are in fact many different forms of the equation of state for different gases. More detailed equations of state, such as the Van Der Waals equation, allow deviations from ideality caused by molecular size and intermolecular forces to be taken into account.

1.7.3 Viscosity of gas

Dynamic viscosity in gas arises principally from the molecular diffusion that transports momentum between layers of flow. The kinetic theory of gases allows accurate prediction of the behavior of gaseous viscosity. For gas, viscosity is independent of pressure and viscosity increases as temperature increases[13].

James Clerk Maxwell published a famous paper in 1866 using the kinetic theory of gases to study gaseous viscosity[14]. To understand why the viscosity is independent on pressure let us consider two adjacent boundary layers (A and B) moving with respect to each other. The internal friction (the viscosity) of the gas is determined by the probability that a particle of layer A enters layer B with a corresponding transfer of momentum. Maxwell's calculations showed that the viscosity coefficient is proportional to the density, the mean free path and the mean velocity of the atoms. On the other hand, the mean free path is inversely proportional to the density. So an increase in pressure does not result in any change of viscosity.

Although the viscosity of gas is independent on pressure, increasing pressure would transform the gas phase into liquid and solid phases, in which case viscosity will increase rapidly, and become extremely high for a solid.

The viscosity of gas is determined by Sutherland's formula,

$$\mu = \mu_0 \frac{T_0 + C}{T + C} \left(\frac{T}{T_0} \right)^{3/2} \tag{1.37}$$

where μ is the viscosity at temperature T, μ_0 the reference viscosity at the reference temperature T_0, C the Sutherland's constant. Temperatures are given in degree K. Sutherland's constant and reference temperature for some gases are shown in Tab. 1.2, which are valid for temperatures between $0 < T < 555K$ with an error due to pressure change less than 10% below 3.45 MPa.

Gas	C [K]	T_0 [K]	μ_0 [$\times 10^{-6}$Pa $\cdot s$]
air	120	291.15	18.27
nitrogen	111	300.55	17.81

Table 1.2: Sutherland's constant and reference temperature for gases of interest

For hydrocarbon vapors and natural gases, the input temperature T is restricted to the range $0 < T < 810.93[K]$. For other gases, the input temperature must be at least absolute zero (0 K). The impact of pressure is minor, and the viscosity correction for pressure is less than 10% for pressures up to 500 psi (34.5 bar) [40].

Viscosity of nitrogen in all phases is shown in Fig. 1.3, in which we can see the phase change is characterized by a sharp change of viscosity. Since the critical point for nitrogen is: [126K (-146.9°C), 3.4 MPa (33.5 atm)], the state of the nitrogen at room temperature is only gas. To evaluate the variation of viscosity raised by pressure change, the viscosity of Sutherland's formula is compared with the viscosity values under various pressures and temperatures by the empirical formula in Lemmon's article [3], as shown in the Fig. 1.4. In conclusion, for standard pressure and temperature conditions, a variation of temperature by 1°C will induce a variation of 0.27% in viscosity, but this can be easily taken into account.

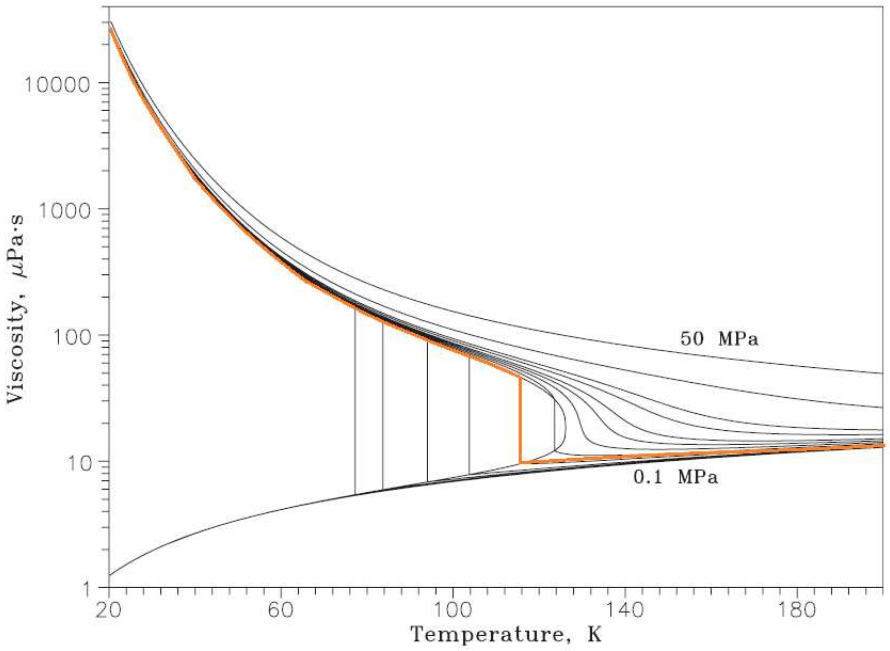

Fig. 1.3: Viscosity versus temperature diagram for nitrogen showing the isobars 0.1, 0.2, 0.5, 1, 2, 3, 4, 5, 6, 8, 10, 20, and 50 MPa [3].

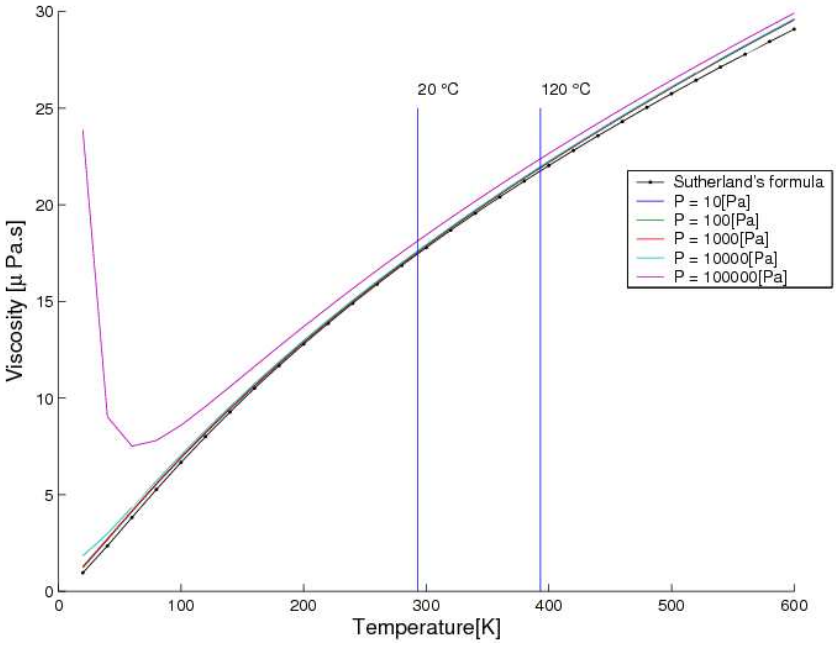

Fig. 1.4: Viscosity of air under 0.1 MPa calculated by Sutherland's formula, Equation (1.37), and Lemmon's formula [3].

1.8 Parameters which affect permeability

The measurement of permeability parameters (viscous permeability and Klinkenberg parameter) is generally dependent on the type of flow (laminar flow or turbulent flow), fluid properties (*i.e.* viscosity, generally as a function of temperature) and the matrix micro-structures, which are affected by many factors, like humidity, macro-strains under load, curing process, *etc.*

1.8.1 Micro-structure of porous medium

Darcy's law is first gradient law, analogous to Fourier's law in the field of heat conduction, Ohm's law in the field of electrical networks, or Fick's law in diffusion theory, and the similarity in mathematical forms of these various physical processes leads to something in common: they all depend on the structure, hence the porosity and tortuosity are not only used to describe the fluid flow in porous medium, but also commonly applied on the diffusion in soil [41, 42] and heat transfer [43]. Many articles reveal that the micro-structure is the key to permeability of the porous medium.

To relate pore structure to transport coefficients, there are two ways: up-scaling Navier-Stokes equation from a specific micro-structure; or prediction for a transport coefficient on easily measured single properties of the pore structure, which means to build a pore structure-transport property (PST) theory. The porosity and tortuosity are introduced to characterize the micro-structure of a medium.

1.8.1.1 Porosity

Porosity is a measure of the void spaces in a material, and is a fraction of the volume of voids over the total volume, between 0 and 1. For some kinds of porous media such as rocks, the porosity can be split into *connected* and *unconnected porosity*. *Unconnected porosity* ϕ can be estimated with the information of porous medium density ρ_p and the material density ρ_f,

$$\phi = 1 - V_f = 1 - \frac{\rho_p}{\rho_f} \tag{1.38}$$

Connected porosity, which is concerned in fluid transport, is more easily measured through the volume of gas or liquid that can flow into the rock, whereas fluids cannot access unconnected pores.

The Kozeny-Carman equation is an expression of Darcy's law with the permeability parameter substituted by a function of porosity, given as [44],

$$\boldsymbol{q} = \frac{\mathscr{O}^2\mathscr{D}^2}{150\mu}\frac{\phi^3}{(1-\phi)^2}\nabla P \tag{1.39}$$

where $\boldsymbol{q}$ is the superficial or "empty-tower" velocity, μ is the viscosity of the fluid, ϕ is the porosity of the medium, $\mathscr{O}$ is the sphericity of the particles in the packed medium, and $\mathscr{D}$ is the diameter of the related spherical particle. This equation holds for flow through packed media with particle Reynolds numbers up to approximately 1, after which point frequent shifting of flow channels in the porous media causes considerable kinetic energy losses.

Lord [45, 46] measured the airflow rates over a wide range of ten plug porosity (roughly varying from 0.77 to 0.9999) for eight samples of cotton and eleven sample of various solid fibers, and modified the Kozeny equation into the following form,

$$\boldsymbol{q} = 0.903\frac{1}{\mu}\frac{\phi^5}{(1-\phi)^c}\frac{1}{\mathscr{M}^2}\nabla P \tag{1.40}$$

where $\mathscr{M}$ is the specific surface area (per unit volume of solid material), c the constant value corresponding for specific material, approximately 1.3.

1.8.1.2 Tortuosity

Tortuosity is a property of a curve being tortuous (twisted; having many turns). Carman introduces the effect of tortuosity in two ways [44]:

Effect (1) The effect on velocity: let the direction of the straight line of length L, connecting the two ends of a tortuous tube of length L_e, be defined as the direction s, and the projection on the direction s of the average velocity in the tube be v_s. Even if $\bar{V}$ (the magnitude of the average tangential velocity) is constant, the component v_s varies, and the average v_s (referred to as $\bar{v}_s$) equals to $\bar{V}(L/L_e)$.

Effect (2) The effect on the driving force: let ∇P_s be the absolute value of the component in the direction s of the pressure gradient, which acts as the driving force in the porous medium, and $\bar{\nabla P_s}$ equal to $\Delta P/L_e(L/L_e)$.

Starting from the extension of Poiseuille's law to flow in a noncircular tube,

$$v = \frac{\mathscr{R}_t^2}{m\mu}\frac{\Delta P}{L_e} \tag{1.41}$$

where $\mathscr{R}_t$ is the hydraulic radius of the tube and m is a numerical coefficient (shape factor) accounting for the noncircular shape of the tube, Carman obtains,

$$\bar{v_s} = \frac{\mathscr{R}_t^2 \mathscr{T}}{m\mu} \nabla P_s \tag{1.42}$$

where $\mathscr{T} = (L/Le)^2 < 1$ is called the tortuosity of the porous medium, where L_e is the flow path length and L is the sample length [44]. Some other authors give a definition as L_e/L (ratio of flow-path length to sample length) [47, 48], which Jacob considers as a mistake that arises from failure to recognize Effect (1) discussed previously.

With the estimates on the numerical value of the tortuosity factor $(L/Le)^2$ given by several authors, comes the Kozeny-Carman equation for permeability,

$$K = \frac{\mathscr{T} \phi^3}{2\mathscr{M}^2 (1-\phi)^2} \tag{1.43}$$

Carman mentions the empirical value $L/L_e = 1/\sqrt{2} = 0.71$. Other values mentioned in the literature for L/L_e vary in the range 0.56 to 0.8 [16].

1.8.2 Humidity of air

For hygroscopic fibers, such as cotton, wool, hemp, flax, silk and nylon, since fibers swell at high humidity, leading to changes in structure, the measured air permeability changes [49, 4].

Wehner's experiments [49] indicated that the air permeability of textile structures decreases as relative humidity is increased and the extent of the decreasing is governed by internal constraints on fabrics ability to change in thickness.

Gibson [4] set an instrumentation to measure the humidity-dependent air permeability of fabrics as cotton, wool, silk, and nylon, woven and non-woven, to understand how fabric porosity and pore geometry are influenced by weave type and fibre/ yarn swelling. For cotton, wool and silk, fibres swell causes smaller v_f (gas phase volume fraction) and higher permeability; for nylon, permeability decreases slightly, which is attributed to the axially swelling rather than radially as most other textile fibers do (Fig. 1.5). In this study, the air humidity will not be considered since since the effects on micro-structure of glass and carbon fabrics are negligible.

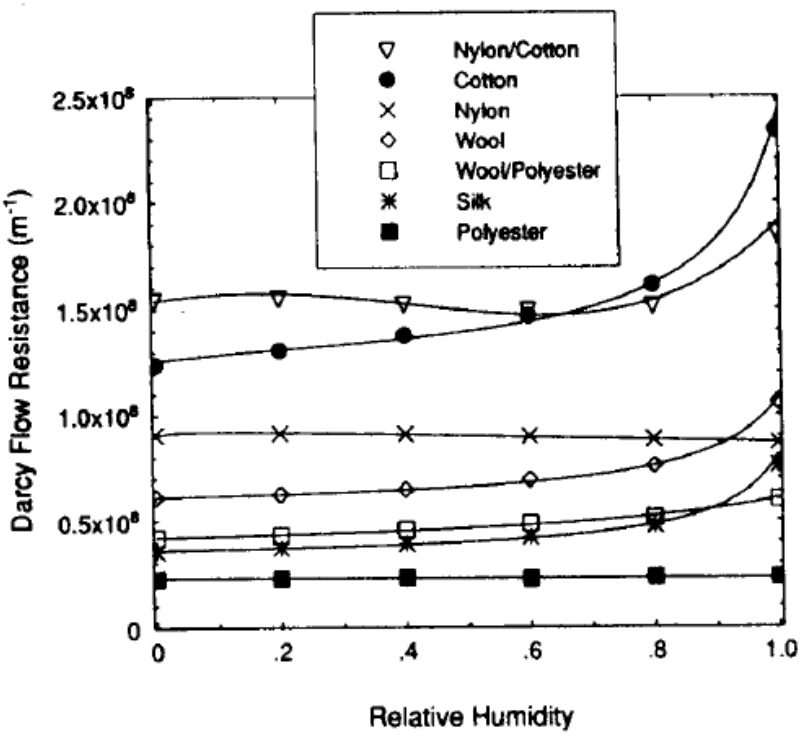

Fig. 1.5: Humidity-dependent air flow resistance of seven fabrics[4].

1.9 Permeability measurement

1.9.1 Introduction

In Darcy's law, permeability is assumed to be a tensor of second order relating velocity and pressure gradient (Eq. 1.15). The permeability of composite fiber reinforcements usually is not isotropic. For all the measurements permeability is assumed to be a symmetric tensor and can be classified as in-plane permeability (two principal permeabilities K_1 and K_2) and transverse permeability K_z, The assumption is found to be true from experiments for general cylindrical channels and layered, randomly deposited particles [50]. However, the tensor can become non-symmetric for an imperfectly layered porous medium [51].

The fibrous media used in Liquid Composite Molding are basically of two types as far as classification in terms of length scales is concerned. One is called random mat which is essentially a random array of fibers and it is considered that only one length scale exists. The others are fibrous materials which are either woven, stitched or braided using tows or bundles of fibers. Each of these tows consist of typically several thousands of fibers. The fiber diameters are usually in micrometers and the tow diameter is of the order of millimeters. Such a fibrous porous medium

consists of the pore sizes of the order of micrometers inside the fiber tows, and of the order of millimeters between the tows and such material can be characterized as a dual length scale porous medium.

In-plane permeability is isotropic for random mats and certain fabrics (the isotropic in-plane permeability is referred to as K_r) and not isotropic for most of the other woven fabrics (the two principal components of anisotropic in-plane permeability are referred to as K_1 and K_2). In-plane permeability measurements are applied on composite reinforcements.

The permeability in the transverse direction K_z is usually different from the in-plane permeabilities. In general, resin flow in the thickness direction can be neglected for thin parts, but the resin flow in the transverse direction is important for thicker parts. Some researchers have performed permeability measurements in the transverse direction of preforms [6, 52, 53].

1.9.2 Measurements using liquid flow

Preform samples can be saturated by a liquid before experiments; if samples are not saturated in advance, permeability is measured during impregnation (with a moving front). Therefore they are referred to respectively as saturated flow and a transient saturating flow experiments. In the last one, the impregnation of the sample will consist of two separate parts: inter-tow flow (also called macro-flow) and intra-tow flow (called micro-flow) [54, 55]. Both can usually be carried out in the same experimental set-up. Comparisons between the two modes of operation shows that they give essentially the same result (within the experimental accuracy) [56, 57, 5]; while some researchers investigated the variation of permeability due to partial saturation in dual scale porous media [58] or capillary action at the flow front in a random mat [59].

1.9.2.1 Fluid injection permeability measurement

Fluid injection technique can be performed unidirectionally, radially or three dimensionally.

In the One dimensional (1D) flow methods, permeability values in a specified direction are measured [60, 61, 62, 57, 63, 64]. Such measurement can also be distinguished by saturated and saturating flow methods. In the saturated 1D method, experiments are conducted by forcing a test fluid in one direction through the entire mold cavity in which the fabric is placed and compressed in advance, and measuring the steady-state relationship between the flow and the pressure drop across the whole length of the sample. Usually a linear relationship is obtained between the

steady-state flow of a Newtonian fluid and the pressure drop. In the saturating 1D test, the fluid flows through the dry fiber bed, replacing the air present in the material.

Although the 1D test is the most straightforward set-up, there are a number of errors associated with it. The most serious one is the "race tracking", or "edge effect" error, which is due to a small gap between the edge of the preform and the mold side. The sensitivity of 1D test to the edge effect is a function of the mold width [65, 66].

One method to avoid *race tracking* is to perform radial flow measurements. The flow is injected through a hole in the center of the sample. The fabric is saturated radially. The 2 principal permeabilities can be obtained simultaneously from the flow front position over time [67, 68, 69, 70]. If prepared carefully, the permeability of the woven fabric can be measured reproducibly within 15% in either radial flow or saturated 1-D flow geometries [60, 59]. The results given by Parnas indicate that the actual flow geometry (parallel or radial) does not influence the measured in-plane permeability [59], while the differences in permeability obtained in the wetting radial flow and the wetting parallel flow are observed and explained with differences in the flow front speed [71].

In order to exclude all the discrepancies during experiments, Gebart proposed a parallel flow technique which allows to determine the complete in-plane permeability tensor in a single experiment. The multi-cavity parallel flow technique [57, 5] determines the in-plane permeability tensor of anisotropic porous media by measuring the effective permeabilities in the three directions of the sample and one known permeability as a reference, simultaneously in one experiment (Fig. 1.6). The measured standard deviation in the repeatability study is about 10%.

Many composite parts produced using LCM (Liquid Composites Molding) processes have wall thicknesses much smaller than their in-plane dimensions. It is often a relevant assumption that resin velocities remain in the plane, reducing mold filling problems essentially to a two dimensional analysis. There are some exceptions for which the in-plane flow assumption is not valid, such as LRI (Liquid Resin Infusion) and RFI (Resin Film Infusion) processes. Several techniques have been presented in the literature to characterize the three-dimensional permeability tensor in a single experiment [56, 72, 73]. Some techniques utilize embedded optical fibers to detect the position of the flow front [56].

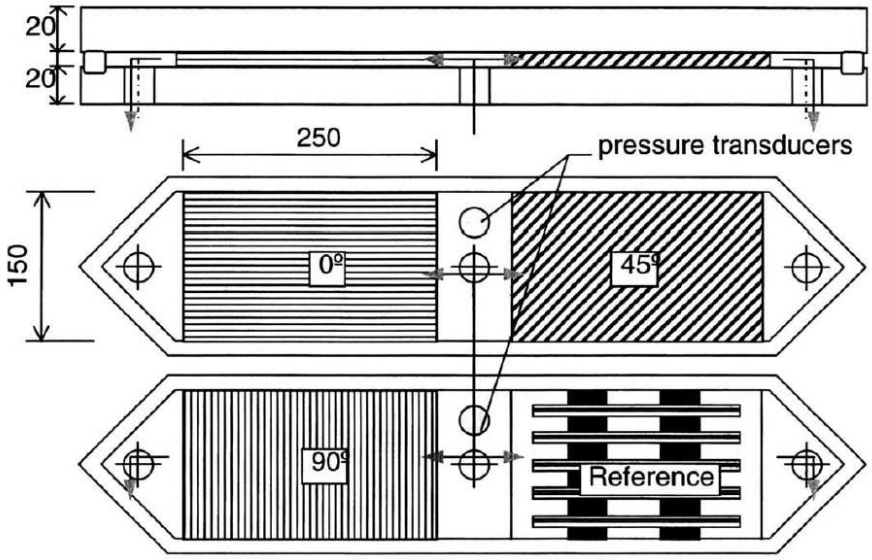

Fig. 1.6: Sketch of the mold in the multi-cavity parallel flow technique [5].

1.9.2.2 Compression flow permeability measurement

Compression flow permeability measurement is an innovative method, which allows for continuous measurement of permeability over wide fibre volume fraction ranges, in a single efficient test [74, 9].

This measurement generates an in-plane fluid flow by compressing a sample of fabrics between two flat platens. The fabrics are fully saturated prior to the test, and liquid is driven out during the compaction. The fluid pressure in the center P_o and thickness changing rate $\dot{h}$ are recorded to calculate the isotropic in-plane permeability K_r,

$$K_r = \frac{\mu \dot{h}}{4 P_o h} r_o^2 \tag{1.44}$$

where r_o is the sample radius. This relationship is deduced from the consolidation model developed in cylindric coordinates (r, z) by Gutowski [75],

$$K_r \frac{1}{r} \frac{\partial}{\partial r} \left(r \frac{\partial P}{\partial r} \right) + K_z \left(\frac{V_f}{V_0} \right)^2 \frac{\partial^2 P}{\partial z^2} = -\mu \frac{\dot{V}_f}{V_f} \tag{1.45}$$

where $\dot{V}_f$ is the rate of change of the fiber volume fraction, V_0 is the fiber volume fraction before compaction, K_r is the isotropic in-plane permeability and K_z is the transverse permeability. This method can also be used to measure K_z when a perforated compression platen is inserted between the sample and the bottom to allow a flow in the thickness direction.

1.9.3 Measurements using gas flow

Because of low permeabilities of soils, rocks, ceramics and membranes, many setups have been built using "positive" pressures (greater than atmospheric pressure) to ease the measurements [76, 77, 78]. Measurements can be stationary (e.g., constant flow rate) or transient (e.g. raised or dropping pressure). The stationary flow measurement is the simplest one to calculate permeability because the flow rate is directly measured [38, 79]. On the other hand, transient flow measurement has the advantage of requiring simple equipments and no flow rate meter [80]. The permeability obtained by a pressure-decay method and the stationary state permeability shows an agreement by Innocentini for dense ceramics [78]. Unsteady gas flow is used extensively to determine permeability of soil in field tests [81] or in laboratory tests with falling [79, 78, 82] or raised pressure methods [83].

The literature of fibrous permeability measurement using gas as fluid is rich. Because of the nature of the process, the chemical vapor infiltration (CVI) requires a good knowledge of gas permeability. Starr and Hablutzel proposed a 1D steady state gas flow technique using helium [84]. Permeability is extracted from Darcy's law integrated for an incompressible fluid and using a differential pressure gauge and a flow meter. Later, several researchers have modified and/or improved the steady gas flow technique to measure fibrous reinforcement permeability [85, 86, 8, 87]. Those authors built 1D or 2D (annular) benches and measured permeability with various gases: nitrogen, helium or air. The system of equations to model the flow included Darcy's law and mass conservation (compressible fluid). The permeability is either obtained from an analytical solution of the system of equation or minimizing a residual by an inverse method.

1.9.3.1 Stationary one dimensional flow

Set-up for one dimensional flow measurements using gas are quite the same as liquid [79]. Constant pressures are applied at the inlet and outlet boundaries, referred to respectively as P_i and P_o. Considering the compressibility, the permeability is not linearly dependent on pressure,

$$K = Q_o \frac{2\mu L}{A} \frac{P_o}{P_i^2 - P_i^2} \tag{1.46}$$

where L is the distance of the sample and A is the flow sectional area, Q_o is the flux at the outlet.

1.9.3.2 Stationary two dimensional flow

In two-dimensional experiments (also called radial flow experiments), the fluid is driven through a preform of annular shape from the center. Let r_i and r_o stand respectively for the radii of inner and outer boundaries of the preform, and the flux can be given as a function of the radii and pressures at boundaries $P(r_i)$ and $P(r_o)$. Applying Darcy's law under the assumption that in-plane permeability is homogeneous and isotropic, in radial coordinates yields [8],

$$q_r = -\frac{K_r}{\mu}\frac{dP}{dr} \tag{1.47}$$

where q_r is the in-plane average fluid velocity in r direction, K_r the in-plane permeability, μ the fluid viscosity and dP/dr is the radial pressure gradient. Mass conservation requires that in the annulus of cross sectional area A,

$$\frac{d}{dr}\left(\rho q_r A\right) = 0 \tag{1.48}$$

Equations (1.47) and (1.48) in conjunction with the ideal gas law, could be used to derive the governing equation,

$$\frac{d}{dr}\left(\frac{P}{RT}\frac{K_r}{\mu}\frac{dP}{dr}\left(2\pi r h\right)\right) = 0 \tag{1.49}$$

where h is the total thickness of the sample stack. The pressures at boundaries $P\left(r_i\right) = P_i$ and $P\left(r_o\right) = P_o$, are measured in the absolute sense. In the absence of heat transfer to the solid surface and for changes in velocity small compared with the speed of sound, conservation of energy requires constant enthalpy. Under those assumptions, the process is thus regarded as isothermal. After integration the flow rate is,

$$Q = (vA) = \frac{\pi K_r h}{\mu \ln\left(r_i/r_o\right)}\frac{\left(P_i^2 - P_o^2\right)}{P_o} \tag{1.50}$$

For porous medium or soils, measurement can be conducted with air at a field scale (*i.e.*, outdoors) instead of a sample scale (*i.e.*, in the laboratory). Field-scale air permeability is often measured by air injection or extraction tests. Air is pumped either into or out from the unsaturated zone and the resulting pressure change in the surrounding unsaturated ground zone is monitored.

Massmann [88] compared various solutions that have been used to predict gas transport parameters from pump test data [7, 89, 81, 90]. Joss developed a flow model (AIR2D) [91] to simulate air movement in the unsaturated zone and can be used to estimate unsaturated-zone air-phase permeability from pump test data.

1.9.3.3 Transient gas flow

Theoretically, all the equipments for stationary flow can be used to perform transient flows. To simplify the calculation, 1D flow is often used. One of the typical 1D measurements using transient gas flow is Falling Pressure Measurement to determine the through-thickness permeability K_z by Li [82] and Tavares and Michaud [6], implying the relationship,

$$\ln\left[\frac{(P_a + P(t))(P_a - P_i)}{(P_a - P(T))(P_a + P_i)}\right] = \frac{K_z A P_a}{\mu_a Z V} t \tag{1.51}$$

where A is the sectional area of flow through the preform, V is the volume gas in the tank, and P_a the pressure of atmosphere (Fig. 1.7), under assumptions that the change of pressure across the sample during experiments is negligible compared with the average of pressure across the sample during measurements (referred to as P_{avg}) and that,

$$\frac{\mu\phi Z^2}{K_z P_{avg}} \frac{P(t)}{P_a^2 - P^2(t)} \left|\frac{dP}{dt}\right| \ll 1 \tag{1.52}$$

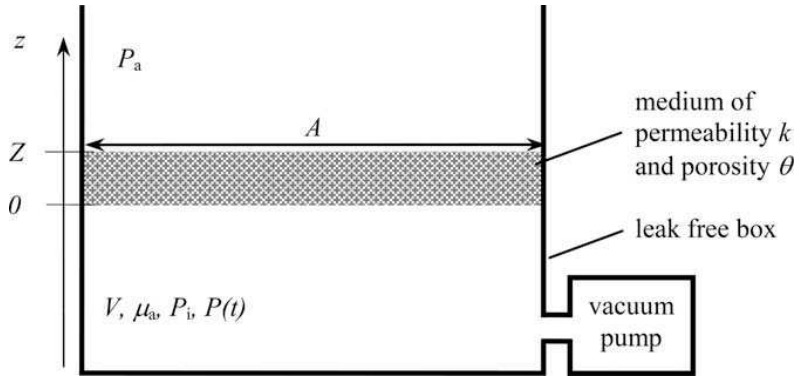

Fig. 1.7: Schematic of the set-up for the determination of the air permeability of a material by a falling pressure method [6].

Kim uses the analytic solutions deduced under several assumptions (introduced at the end of this section) in the transient gas flow technique [92], then obtains the in-plane permeability by an inverse parameter estimation technique [93], as shown in Fig. 1.8. The permeability solution is the value that minimizes the following least-squares expression of the tested pressures P_k ($k = 0, 1, ...N$, N is the total number of sensors) and analytical pressures $\hat{P}_k$ dependent on permeability K,

$$S(K) = \sum_{k=1}^{N} \int_{t=0}^{t=t_f} \left[P_k(t, K) - \hat{P}_k(t, K)\right]^2 dt \tag{1.53}$$

To solve the optimization problem numerically, the Levenberg-Marquardt method

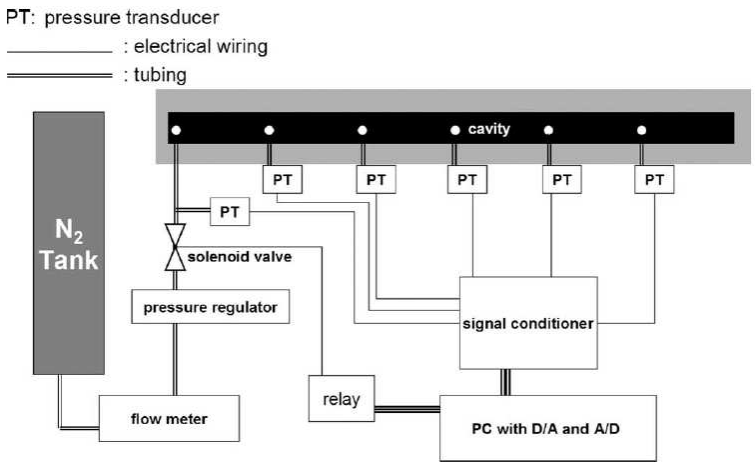

Fig. 1.8: Schematic of the set-up for the determination of the in-plane permeability by a falling pressure method [6].

is employed [94]. An existing optimization code (BCLSJ) was employed for the implementation of the inverse method [95].

The analytic solutions for one dimensional transient gas flow can be obtained following the procedure as shown below [92]. Consider the pressure $P(x,t)$ for one-dimensional gas flow, where x is the distance from the vent. Combining the Darcy's law Eq. 3.2, mass conservation Eq. 1.6 and ideal gas equation Eq. 1.36, we have,

$$\frac{\partial P}{\partial t} - \frac{K}{\phi\mu}\frac{\partial}{\partial x}\left(P\frac{\partial P}{\partial x}\right) = 0 \tag{1.54}$$

In the actual gas flow test, the pressure variation should be very small in comparison with the atmospheric pressure to maintain the validity of Darcy's law [92]. Considering the assumptions,

$$P\frac{\partial^2 P}{\partial x^2} \ll \left(\frac{\partial P}{\partial x}\right)^2 \tag{1.55a}$$

$$\frac{P}{P_0} \approx 1 \tag{1.55b}$$

where P_0 is the initial pressure, the above expression can be linearized as follows,

$$\frac{\partial P}{\partial t} - \frac{KP_0}{\phi\mu}\frac{\partial^2 P}{\partial x^2} = 0 \tag{1.56}$$

The governing equation could be non-dimensionalized as

$$\frac{\partial P^+}{\partial t^+} - \frac{\partial^2 P^+}{\partial^2 x^+} = 0 \tag{1.57}$$

where

$$P^+ = \frac{P}{P_0}, x^+ = \frac{x}{L}, t^+ = \frac{P_0 K}{\phi \mu L^2} t \tag{1.58}$$

For the transient 1-D permeability experiment [92], the initial pressure and boundary conditions are,

$$P^+\left(x^+, 0\right) = 1, \text{ for } 0 \leq x^+ \leq 1 \tag{1.59}$$

$$P^+\left(0, t^+\right) = 0 \text{ and } \left.\frac{\partial P^+}{\partial x^+}\right|_{x^+=1} = 0, \text{ for } t^+ > 0 \tag{1.60}$$

For the above problem, the exact solution is given as [96, 97]

$$P^+\left(x^+, t^+\right) = 2\sum_{n=1}^{\infty} \frac{1}{\kappa_n} \exp\left(-\kappa_n^2 t^+\right) \sin \kappa_n x^+ \tag{1.61}$$

where $\kappa_n = (2n-1)\,\pi/2$ is the wavelength. The assumptions Eq. 1.55 are used to linearize the governing equation. The pressure solution gives,

$$\frac{\partial P^+}{\partial x} = 2\sum_{n=1}^{\infty} \exp\left(-\kappa_n^2 t^+\right) \cos \kappa_n x^+ \tag{1.62}$$

and

$$\frac{\partial^2 P^+}{\partial x^2} = -2\sum_{n=1}^{\infty} \kappa_n \exp\left(-\kappa_n^2 t^+\right) \sin \kappa_n x^+ \tag{1.63}$$

Since the profile of the pressure over x is smooth, $\kappa_n \gg 1$ for $n > 1$. Hence the values of $\partial P^+ \partial x$ and $\partial^2 P^+ / \partial x^2$ are mainly determined by the first orders. The assumption is suitable when the $x^+ \to 1$, and causes a large error when $x^+ \to 0$.

1.9.4 Comparison of permeability measured using liquid & gas

When gas is used as test fluid, and K_n (the Knudsen number) approaches 1, Darcy's law is not valid. The incorporation of the Klinkenberg effect into the air flow model introduces nonlinear terms that preclude the development of analytical solutions. Thus the conditions when Klinbenberg effect can be neglected must be identified. Baehr [7] estimated the error caused by omission of the Klinkenberg effect as below,

$$\varepsilon_{max} = 100\left[\frac{K(P_w) - K(P_{atm})}{K(P_{atm})}\right] \tag{1.64}$$

where P_w is the actual pressure within porous media, and applied Eq. 1.64 to get the error (Fig. 1.9).

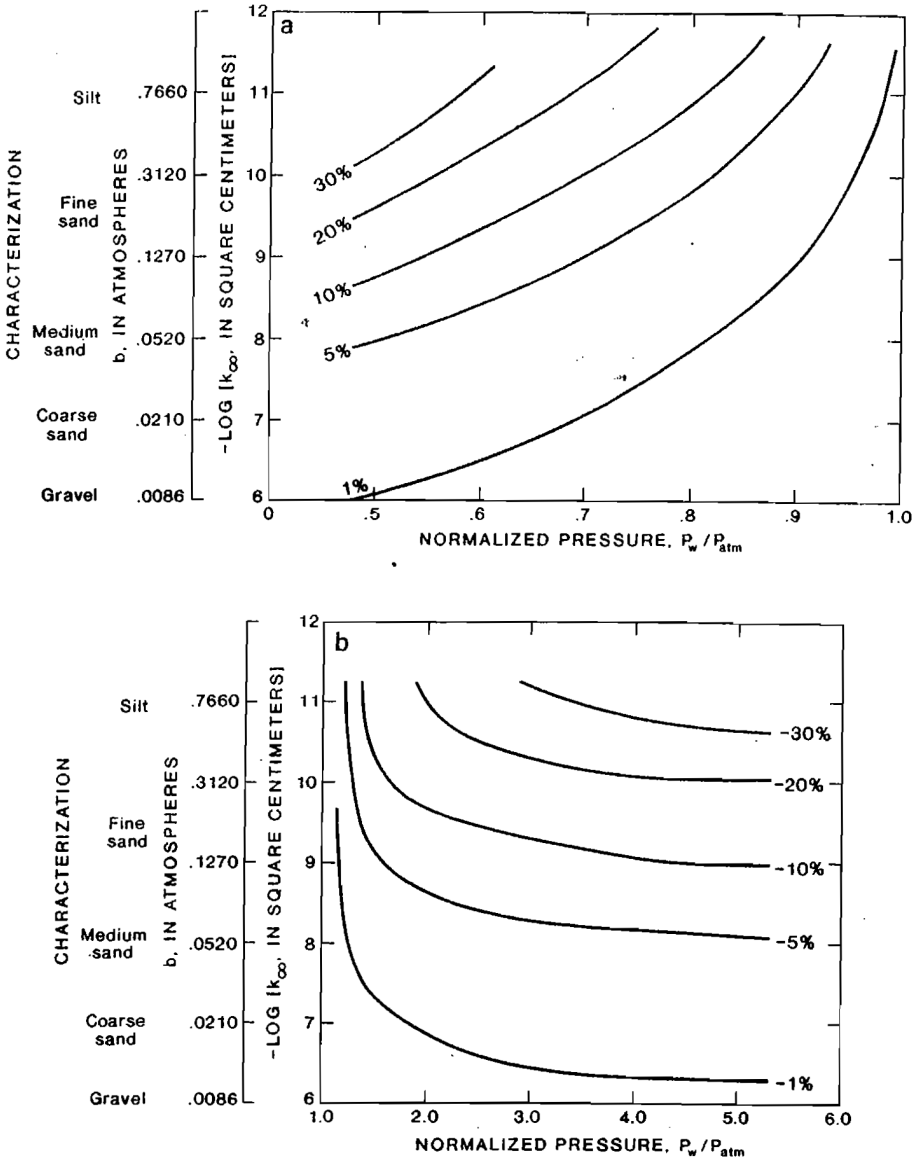

Fig. 1.9: Maximum possible percent error in obtaining air permeability due to neglecting the Klinkenberg effect [7]. (a) Case of air withdrawal and (b) Case of air injection.

Experiments on textile reinforcements at pressure 10^6Pa indicate that permeability is generally a parameter of porous media, and the influence of test fluid is small [98]. Experiments on fabrics with low permeability of the order of 10^{-12}m^2 under lower pressures (10^5 Pa) give the results of permeability between gas and liquid with minor differences, which have the same level as experimental error [85, 8, 87]. Massmann observes that sliding flow may become relevant in soils with permeability of the order of 10^{-12}m^2 [89]. Under low pressure gradients, Moon-Kwang observed that the principal permeability K_1 for gas flow method is a little higher than the one obtained with liquid flow method, and that the values of the other principal permeability K_2 are very close. The differences are attributed to the uniformity of the fabrics by the author. Feser and Advani [8] used water and air in a radial measurement for in-plane permeability of tightly woven glass fabric. The gas permeability value was determined to be $K = 5.89 \times 10^{-13}\text{m}^2$; liquid permeability of the same sample to be $K = 6.02 \times 10^{-13}\text{m}^2$. Pomeroy applied Feser's method in measurement of permeability of continuous filament mat glass fiber reinforcements by saturated radial airflow. Air flow through the samples with various flow rates and differential pressure, and the results show that the values of permeability achieved using radial flow of air have a lower level of scatter than published data for the liquid techniques [87].

In conclusion, the air permeability values of media with finer pores, such as soils and rocks, are higher than the one of liquid due to Klinkenber flow. In this case, a Klinkenberg model can be used. For those media with $K \sim 10^{-12}$m, the differences between permeabilities using liquid and air are observed but are attributed to experimental error (a sumary of the results shown in Tab. 1.10).

Table 1.3: Experiments to compare the gas/liquid permeability

Author	Medium	Fluid	Permeability
Klinkenberg [34]		nitrogen	$K_g = K_\infty (1 + b/P)$
		brine	K_∞
Jones and Owens [35]	tight sand	gas	$b = \alpha_k K_\infty^{-0.36}$
Heid [37]	rock	gas	$b = (3.98 \times 10^{-5}) K_\infty^{-0.39}$
Stonestrom [38]	soil	air	$K_\infty = 1.2 \times 10^{-11}\text{m}^2$ $b = 0.059$
Moon-Kwang [85]	fiber glass fabric ($V_f = 41\%$)	gas	$2.6 \times 10^{-13}\text{m}^2$
		liquid	$2.7 \times 10^{-13}\text{m}^2$
Feser [8]	woven glass fabric	gas	$5.89 \times 10^{-13}\text{m}^2$
		liquid	$6.02 \times 10^{-13}\text{m}^2$

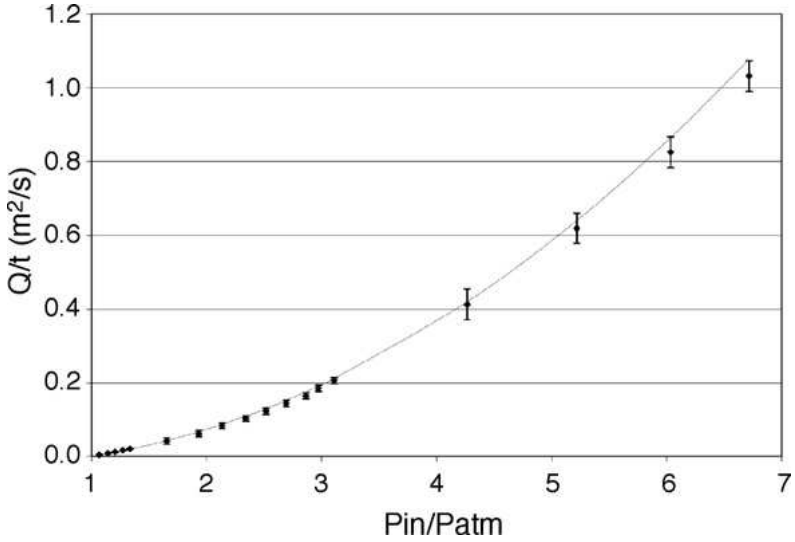

(a) Experimental data points for air as impregnating fluid with tightly woven glass fabric as the porous medium. Solid line represents a nonlinear least-squares fit of Eq. 1.50. Computed in-plane permeability value $K_r = 5.89 \times 10^{-13}\text{m}^2$.

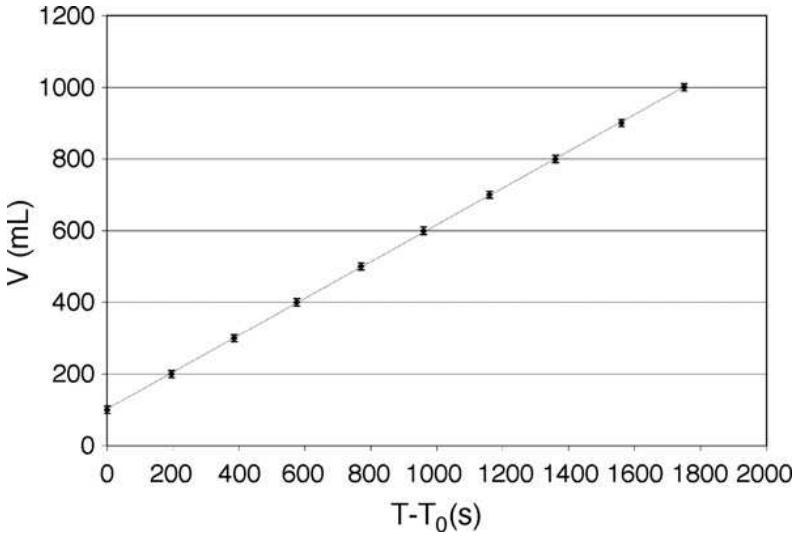

(b) Experimental data points with water as impregnating fluid with tightly woven glass fabric as the porous medium. Solid line represents a least-squares fit of Eq. 1.47. Computed in-plane permeability value $K_r = 6.02 \times 10^{-13}\text{m}^2$.

Fig. 1.10: Permeability measured with air and water [8].

1.9.5 Sources of errors in experiments

1.9.5.1 Fluid continuum

The Navier-Stokes equation assumes that the fluid being studied is a continuum. At very small scales or under extreme conditions, real fluids made out of discrete molecules will produce results different from the continuous fluids modeled by the Navier-Stokes equations. Depending on K_n, a dimensionless parameter defined as the ratio of the molecular mean free path length to a representative physical length scale (Eq. 1.1), statistical mechanics or possibly even molecular dynamics may be a more appropriate approach.

K_n is useful for determining whether statistical mechanics or the continuum mechanics formulation of fluid dynamics should be used: when $K_n \sim 1$, the mean free path of a molecule is comparable to a length scale of the problem and the continuum assumption of fluid mechanics is no longer valid. In this case statistical methods or sliding models must be used.

1.9.5.2 Representative volume element

The conditions on the size of RVE, $l_\phi \ll l_r \ll L$ has to be satisfied, and the symbol $\ll$ generally means the different order of magnitude, or l_ϕ/l_r and l_r/L could be neglected. The order of error brought by l_ϕ/l_r or l_r/L is to be researched.

Feser and Advani [8] considered that in order to have a well defined Darcy permeability, there should be a sufficient number of pores contained within the flow. For example, a typical case of gas diffusion layer, the majority of the void fraction is formed by pores between 10 and $100\mu m$ in diameter; thus, the distance traveled by the flow within the sample of material being tested should be at the length scale of centimeters for a reliable reading.

1.9.5.3 Deviation from Darcy's law in RTM preform

Bruschke and Advani [25] and Gebart [10] demonstrated that predictions of the permeability from the Stokes flow equations for aligned cylinders are accurate. Adams and co-workers [99] and Williams, et al [100] observed that Darcy's law in experiments carried out in both saturated and unsaturated media (in-plane permeability). However, in contrast, Trevino, et al [101] reported that flow behavior in both unsaturated and saturated porous media deviates significantly from Darcy's law. Williams indicated that the permeability measured in unsaturated porous media was about 20% higher than in saturated porous media. Gebart suggested that the apparent permeability of an isotropic material may depend upon the geome-

try of the experiment. They found that saturating flow experiments conducted in both radial and one-dimensional geometries yielded different values of the apparent permeability [10].

1.9.5.4 Sensor's accuracy: P, T, Q

The total error ε_{tot} is determined from the standard error formula [102]

$$\varepsilon_{tot} \approx \sqrt{\sum_{i=1}^{n} \left(\frac{\partial K}{\partial x_i}\right)^2 e_i^2} \tag{1.65}$$

Notice that the error in the slope of a least squares fit can be determined explicitly if the error in the values on which the fit is based is known [103].

Gebart estimated the relative error in the permeability by the theoretical formulas for computation of effective permeability for saturated parallel flow, saturating parallel flow, and radial flow [57].

Porosity is usually estimated by the cavity thickness. Since permeability is sensitive to porosity, cavity thickness should always be carefully controlled with steel shims.

1.9.5.5 Flow issues during impregnation

Race-tracking indicates that resin flows faster through the air channels and higher porosity regions. The air channels exist where the mold gap has lager dimensions than preform or varying thickness around the corners. The higher porosity region could be the tows at the edges of preform which cannot be held together because of the cut between the stitches or weave joints [104].

The flow patterns might be affected very significantly depending on the size of channel. Although these race-tracking cases may be undesirable or unavoidable, sometimes race-tracking is created intentionally to ease the resin flow in order to reduce the injection pressure or reduce filling time.

Racetracking is more significant when the resin flows parallel to the air channels. If the flow is perpendicular to the air channels, the disturbance on the flow pattern will be small [104]. Mold-filling simulations assume that the mold cavity contains a continuous medium. Hence the preform and the air channels should be considered as different sections of a continuous hypothetical preform and the elements of a mesh to be used in the finite element analysis can have different fiber volume fraction and permeability values at different sections.

1.10 Methods of optimization

1.10.1 Introduction

Optimization is to find the "best available" values of several objective functions given in a defined domain [105]. To solve problems, researchers may use algorithms which terminate in a finite number of steps, or iterative methods that converge to a solution, or heuristics that may provide approximate solutions to some problems although their iterates need not converge.

1. The iterative methods used to solve problems of nonlinear programming differ according to whether they evaluate Hessians (*e.g.*, Newton's method), gradients, or only function values (*e.g.*, interpolation methods and pattern search methods). While evaluating Hessians (H) and gradients (G) improves the rate of convergence, such evaluations increase the computational complexity (or computational cost) of each iteration. In some cases, the computational complexity may be excessively high.

2. Heuristic algorithm, besides (finitely terminating) algorithms and (convergent) iterative methods, there are heuristics that can provide approximate solutions to some optimization problems: Memetic algorithm, Differential evolution, Dynamic relaxation, Genetic algorithms, Hill climbing, Nelder-Mead simplicial heuristic (a popular heuristic for approximate minimization without calling gradients), Particle swarm optimization, Simulated annealing, Tabu search.

The optimization methods using Hessian matrix and gradients are not proposed in back-calculation of permeability combined with finite element simulation, because simulation error induces a difficulty to converge and also a degeneration problem in 2D cases. Nelder-Mead's algorithm, having the advantage of stability and efficiency, is chosen in this thesis.

1.10.2 Nelder-Mead's algorithm

The Nelder-Mead technique was proposed by John Nelder & Roger Mead (1965) and is a technique for minimizing an objective function in a many-dimensional space [106].

The method uses the concept of a simplex, which is a special polytope of N + 1 vertices in N dimensions. Examples of simplices include a line segment on a line, a triangle on a plane, a tetrahedron in three-dimensional space and so forth. The

downhill simplex method starts from an initial simplex and continues with iterative steps until the objective function reaches its minimum. Each step of the method consists in an update of the current simplex. These updates are carried out using four operations: reflection, expansion, contraction, and multiple contraction.

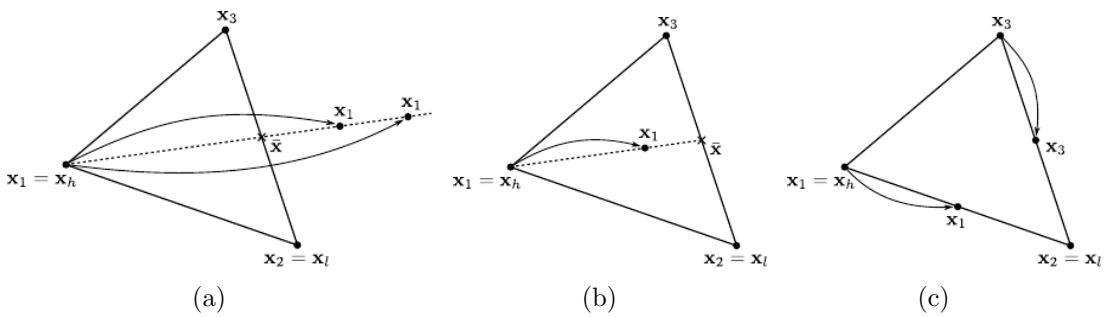

Fig. 1.11: Illustration in 2 dimensions of the four fundamental operations applied to the current simplex by the downhill simplex method: (a) reflection and expansion, (b) contraction, and (c) multiple contraction.

1.11 Conclusion and research roadmap

The stationary flow methods are based on steady-state flow. Based on the governing equation and sample geometry, the relationship of flux q dependent on permeability K and boundary pressure P can be predicted and given as a function $q = f(K, P)$ and a corresponding $K = g(q, P)$. In permeability measurement, q and P are recorded and K can be calculated directly by the function $g(q, P)$ [107, 108, 76, 38, 109, 79, 77], while the transient experiment allows for the acquisition of continuous time-varying pressure data from multiple ports during a single test [92, 82, 110].

The main issue of the techniques using stationary flow through fabric, relies on the fact that depending on the level of permeability to measure, the flow meter and pressure transducers have to be changed to comply with the pressure and flow rate levels to match low Reynolds number Re_ϕ during the experiment. Also, techniques using annular domains limit their use to in-plane isotropic media.

One way to overcome the issue of measuring flow rates is to use transient techniques as presented by Kim *et al.* and Sequeira Tavares *et al.* [92, 6]. The transient evolution of the pressure levels at different locations during the experiments are used to extract a value of permeability. Kim has deduced an analytical solution for transient gas flow with the assumptions: $P\partial^2 P/\partial x^2 \ll (\partial P/\partial x)^2$ and $P/P_0 \approx 1$, where P_0 is the initial pressure. These assumptions are valid only when the variation of pressure is negligible compared with the magnitude of the pressure. In most

transient measurements using gas, pressure changes in such a large range that the analytical solution is impossible to obtain. Therefore numerical methods should be used to simulate the flow field under given pressure distribution and then the permeability is back-calculated by minimizing the difference between experimental and simulated data.

Within this context, the main objectives of the thesis are to,

1. design a fast permeability measurement method using air;
2. build models in various flow regimes (continuous, discontinuous and sliding regimes) and validate the corresponding assumptions;
3. compare results between liquid and air;
4. explore the possible extension to anisotropic permeability fabrics.

CHAPTER 2

Measurements using transient gas flow

Abstract of Chap. 2

A methodology to determine in-plane permeability of fibrous media using a transient one dimensional air flow is developed. The chapter will consist of 3 parts:

The first part describes the experimental set-ups and procedure, and models of gas transport through fibrous porous media which can occur during the experimental measurements. Governing equations and boundaries are given for each model and an inverse method is introduced to determine permeability.

Then, tests are performed on several types of fabrics and results are compared with permeability measurement methods using liquid The deviation from Darcy's law caused by gas sliding effect is analyzed and a relative parameter of fabric material shows dependence in permeability, with a similar trend as the Klinkenberg sliding parameter in soils and rocks.

Finally, the experimental errors due to dimensions, thermal effect, pressure variation, sample handling, trapped gas at BC (boundary conditions) are analyzed and the accuracies of pressure sensors and volume of trapped gas at BC are the most important.

Résumé de Chap. 2

Une méthodologie pour déterminer la perméabilité plane d'un milieu fibreux à l'aide d'un flux transitoire d'air unidimensionnel est développée. Le chapitre se compose en 3 parties:

La première partie décrit la mise en place de l'expérience et les modèles de transport du gaz dans les milieux poreux fibreux qui peuvent survenir lors des mesures expérimentales. Les équations et les conditions limites sont données pour chaque modèle et une méthode inverse est présentée pour déterminer la perméabilité.

Ensuite, des tests sont effectués sur plusieurs types de tissus et les résultats sont comparés aux résultats de mesure de perméabilité utilisant un liquide. L'écart avec la loi de Darcy causé par l'effet du glissement du gaz est analysé et un paramètre lié au tissu montre une dépendance avec la perméabilité, avec une tendance similaire à celle du paramètre de glissement de Klinkenberg pour les sols et les roches.

Enfin, les erreurs expérimentales dues aux dimensions, à l'effet thermique, à la variation de pression, à la manipulation des échantillons, et au gaz emprisonné sur les bords sont analysées et montrent que la précision des capteurs de pression et le volume de gaz piégé sont les facteurs les plus importants.

2.1 Introduction

Among liquid injection measurements, those using stationary and transient liquid flow are respectively referred to as "saturated" and "saturating" flow, the corresponding obtained permeability referred to as "saturated" and "saturating" permeability. Significant disagreements between saturated and saturating methods have been attributed to capillary driven flows occurring on the flow front within fabrics with double-scale porosity. There is no typical "flow front" within fabrics when gas "saturates" the fabric, so permeability obtained in gas saturating flow can be identified as the saturated permeability.

2.2 Experiment design

In this section, air flow through fibrous media will be studied. More specifically, glass and carbon fiber preforms used traditionally in structural fiber-reinforced composites will be under investigation and a permeability measurement methodology will be detailed.

2.2.1 Experimental apparatus and methodology

The equipment designed and built to measure air permeability of the fibrous preform by one dimensional flow consists of a bench, a vacuum pump and a data acquisition system (shown in Fig. 2.1). The details of the bench are illustrated in Fig. 2.2. The preform is inserted between a set of top (PMMA) and bottom (metallic) plates, sealed with a rubber o-ring seal. The outlet and inlet are respectively connected to a vacuum pump and the atmosphere, and controlled by valves. Four pairs of 50 mm-thick steel stiffeners are screwed so as to compact the preform and to force the PMMA and steel platens to be in contact with the spacer plate. The latter ensures the final cavity thickness. The PMMA top platen is 30 mm thick. The application of vacuum leads to less than 0.05 mm deflection during the test. The pressures P_1 and P_2 are monitored by pressure sensors (Kistler 4260A Series, 0-1 bar absolute, 1% accuracy, shown in Fig. 2.3) at room temperature, and recorded with the help of a data acquisition system with a data aquisition rate 10^5 points/s and values are averaged on a sampling number 10^3 to erase data vibrations or noise due to eniviroment. The laboratory vacuum pump delivers a vaccuum level of 3×10^3Pa (absolute).

Pressure sensors are affected by the humidity and temperature. P_1 should be the same as P_2 when no flow takes place. To fix the difference caused by the

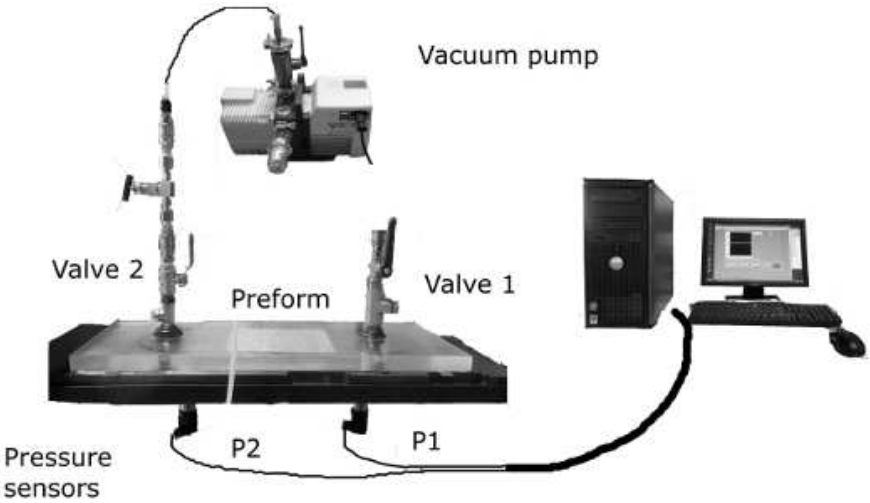

Fig. 2.1: The experimental equipments to measure in-plane permeability using one dimensional air flow.

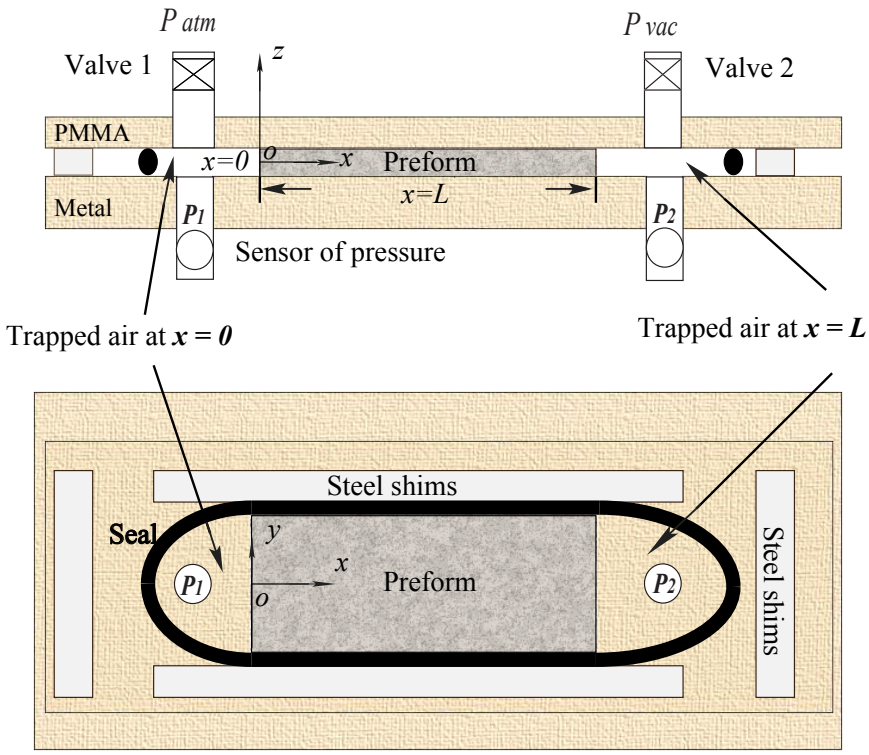

Fig. 2.2: The details of bench for in-plane permeability measurement using one dimensional air flow.

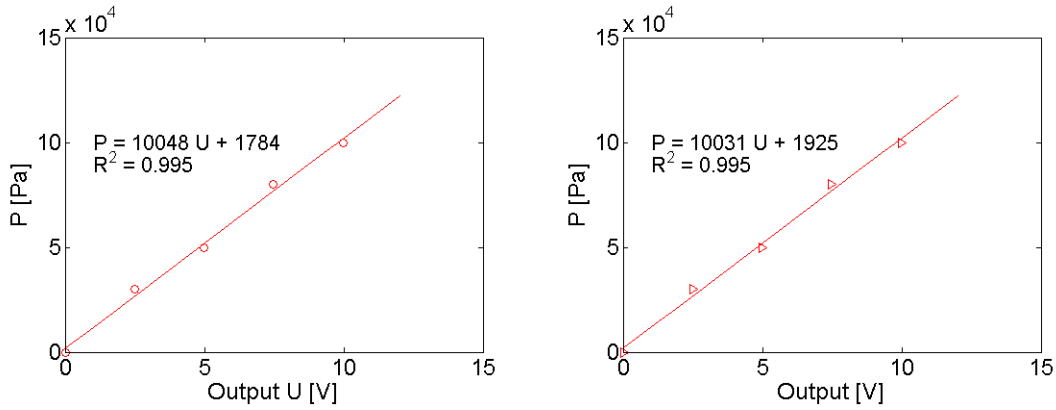

(a) Sensor1 (b) Sensor2

Fig. 2.3: Calibration curves of pressure sensors.

inaccuracy of pressure sensors, $P_1(t)$ is modified as $\hat{P}_1(t) = P_1(t)a + b$, where a and b are calculated based on the initial and ultimate pressures ($P(0)$ and $P(\infty)$ respectively),

$$\begin{bmatrix} a \\ b \end{bmatrix} = \begin{bmatrix} P_2(0) - P_1(\infty) \\ -P_1(\infty)P_2(0) + P_1(0)P_2(\infty) \end{bmatrix} \frac{1}{P_1(0) - P_1(\infty)} \tag{2.1}$$

Such modification will change the value of permeability obtained in the inverse method (to be discussed). Hence this modification is used only when the pressure difference becomes significant, such as in experiments where pressure changes between 2×10^3Pa and 2×10^4Pa.

When atmosphere pressure P_a is used in measurements, the sensors will fail to record accurately once P_a is higher than 1.02×10^5Pa (standard atmosphere pressure 1.013×10^5Pa), and experimental pressure curves will show a truncation on the top where the pressure is about 1.02×10^5Pa. Back-calculated permeability based on this type of data could be underestimated up to 25% when the truncation becomes obvious.

2.2.2 Transient flow tests

Two types of 1D-transient flows are studied: the dropping or raised pressure method (DPM or RPM). To create a flow using the DPM, the test begins by setting the initial pressure within the cavity and the sample to the atmospheric pressure P_a. This is obtained by closing valve 2 and opening valve 1 until the values of P_1 and P_2 become equal. Then, a dropping pressure at the boundary 2 is applied while closing valve 1 and opening valve 2 to let the vacuum in (or

the gas out). Typical pressure responses during DPM are given in Fig. 2.4(a). In conclusion, the boundary conditions for the DPM should be:

$$\begin{cases} P_1 = P_a, \nabla P_2 = 0 & \text{when } t < 0 \\ P_1 = P_2 = P_a & \text{when } t = 0 \\ \nabla P_1 = 0, P_2 = P_2(t) & \text{when } t > 0 \end{cases} \tag{2.2}$$

The experiment can also begin with vacuum initial pressure within the preform and cavity, then valve 1 is opened to let the gas in. This test is referred to as RPM (Fig. 2.4(b)).

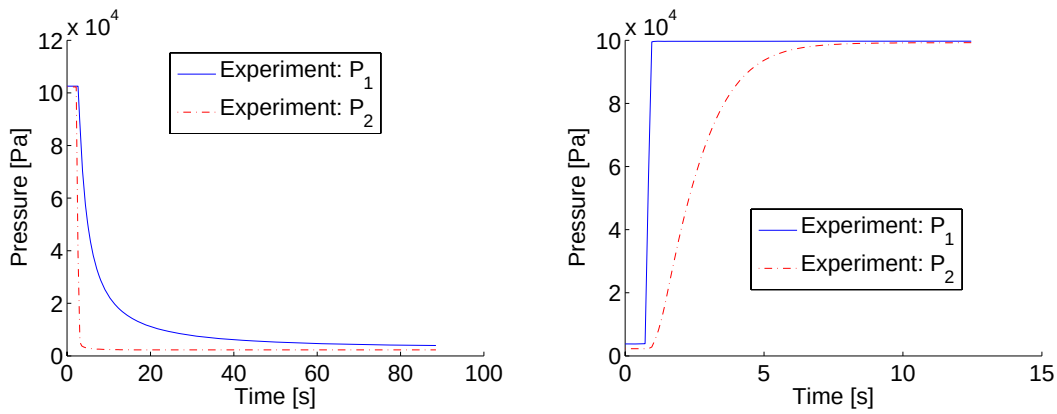

(a) DPM (b) RPM

Fig. 2.4: The pressure curves recorded at the inlet and outlet during DPM and RPM.

2.2.3 Materials

Four kinds of fabrics with fiber volume fractions varying from 0.4 to 0.59 are tested. The fiber volume fraction is calculated as,

$$V_f = \frac{N_p W_f}{\rho_f h} \tag{2.3}$$

where N_p is the number of plies constituting the preform, W_f the ply areal weight, ρ_f the fiber density and h the cavity thickness. Glass- and carbon-based reinforcement combined with representative architectures (woven, unidirectional and bidirectional, some are shown in Fig. 2.5) have been selected. The main features of the materials are given in Tab. 2.1 and the preform configurations are listed in Tab. 2.2. The average size of the samples were 250 mm in length and 150 mm in width. As it can been seen on Fig. 2.2, there are trapped air volumes between the

sample edges and the inlet and outlet valves. This volume has been measured and was on average 30 cm^3.

(a) GTW (b) CTW (c) CUD

Fig. 2.5: Fabrics used in this study, (a) GTW: glass twill weave, (b) CTW: carbon twill weave, (c) CUD: carbon unidirectional fabric.

The same set-up has also been used in permeability measurements using liquid flow. No race-tracking with liquid was observed at the boundaries, which means the eventual gap between fabric and seal is small enough so that race-tracking is negligible. Similar care has been taken with gas flow measurement in this setup to limit race-tracking. With respect to the repeatability of the results for each type of materials, each experiment for a given fiber volume fraction has been repeated between 2 to 5 times with up to 4 types of loading pressures.

Label	GTW	CTW	CBD	CUD
Architecture	Twill weave 2×2	Twill weave 2×2	Bidirectional stitched	Unidirectional
Fiber type	Glass	Carbon	Carbon	Carbon
Areal Weight (g/m^2)	1500	285	548	150
Manufacturer	Chomarat Composites	Hexcel	Saertex	Hexcel
Reference	1500S3	G986	Confidential	Hexforce 43151

Table 2.1: References of the materials tested in the study

Material	GTW	CTW	CBD	CUD
Stacking	$[0,90]_2$	$[0]_6$	$[+/-45]_4$	$[0]_{15}$ and $[90]_{15}$
V_f range in %	[48;53]	[44;55]	[52;59]	[55;57]

Table 2.2: Material configurations tested in the study

2.2.4 Stationary measurement design

The same set-up (shown in Fig. 2.2) to measure permeability using transient gas flow could also be used for stationary gas flow experiments. Although in our work these stationary gas flow experiments are not performed considering the large range of values of permeability, it is still interesting to present the stationary flow experimental design.

For stationary flow, the input pressure P_1 and the output pressure P_2 can be acquired with the corresponding flow rate Q, hence the permeability can be calculated by the analytical solution.

2.2.4.1 Analytical solution

The steady state is characterized by the vanishing of the partial time derivatives of physical quantities. The governing equation of Darcy's flow of gas (Eq. (2.16), in a case of invariability of permeability and viscosity reduces to,

$$\frac{\partial}{\partial x}\left(P\frac{\partial P}{\partial x}\right) = 0 \tag{2.4}$$

which admits a general solution,

$$P = (C_1 + C_2 x)^{1/2} \tag{2.5}$$

where C_1 and C_2 are the coefficients to be determined by the boundary conditions.

Fig. 2.6 shows a case when the fabric of the permeability K along the x direction, dimension 0.2m$\times$0.2m, is placed in a mold to make sure that no flux will arise along the boundary $y = 0, y = 0.2$ and the pressure at the other two edges, $P|_{x=0} = P_a$, and $P|_{x=0.2} = P_{vac}$.

For such 1D steady flow under constant input and output pressures, the coefficients C_1 and C_2 can be determined,

$$C_1 = P_1^2 \tag{2.6}$$

$$C_2 = \left(P_2^2 - P_1^2\right)/L \tag{2.7}$$

where L is the fabric length (here $L = 0.2$m). Pressure distributions over x calculated by the Comsol software fits well with the analytical solution (Fig. 2.7).

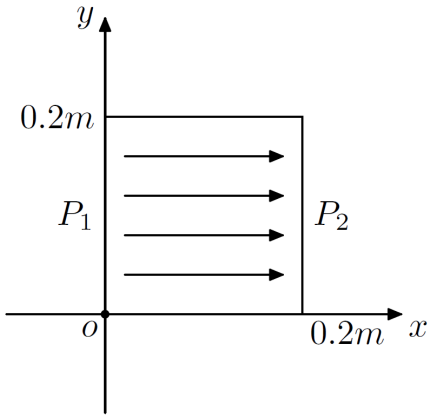

Boundary conditions

$y = 0, y = 0.2\text{m}$	No flux
$x = 0$	$P\|_{x=0} = P_1$
$x = 0.2$	$P\|_{x=0.2} = P_2$

Fig. 2.6: Geometry and boundary conditions in one dimension flow for a 0.2×0.2 m^2 fabric sample.

The analytical solution of velocity can be determined with 1D Darcy's law,

$$q = -\frac{K}{2\mu}\frac{P_2^2 - P_1^2}{L}\left[P_1^2 + \frac{(P_2^2 - P_1^2)\,x}{L}\right]^{-1/2} \tag{2.8}$$

which gives the velocity q at the inlet ($x = 0$) and outlet ($x = L$),

$$q|_{x=0} = \frac{K}{2\mu L}\frac{P_1^2 - P_2^2}{P_1} \tag{2.9a}$$

$$q|_{x=L} = \frac{K}{2\mu L}\frac{P_1^2 - P_2^2}{P_2} \tag{2.9b}$$

To determine permeability using stationary gas flow, pressures at the input and output gates, respectively P_1 and P_2, are measured, and K can be obtained with $q(x)$ at any point and the corresponding $P(x)$,

$$K = \mu L\frac{2q(x)P(x)}{P_1^2 - P_2^2} \tag{2.10}$$

We have to keep in mind that $q(x)$ is not constant over all flow field but $q(x)P(x)$ is constant. Replacing P with density ρ using ideal gas law Eq. 1.36 yields,

$$q(x)P(x) = Q_m\frac{RT}{\omega A} = \frac{K}{\mu}\frac{P_2^2 - P_1^2}{2L} \tag{2.11}$$

where the whole discharge Q_m ($= q\rho A$ [kg/s]) could be measured by a flow rate meter in 1D permeability measurements.

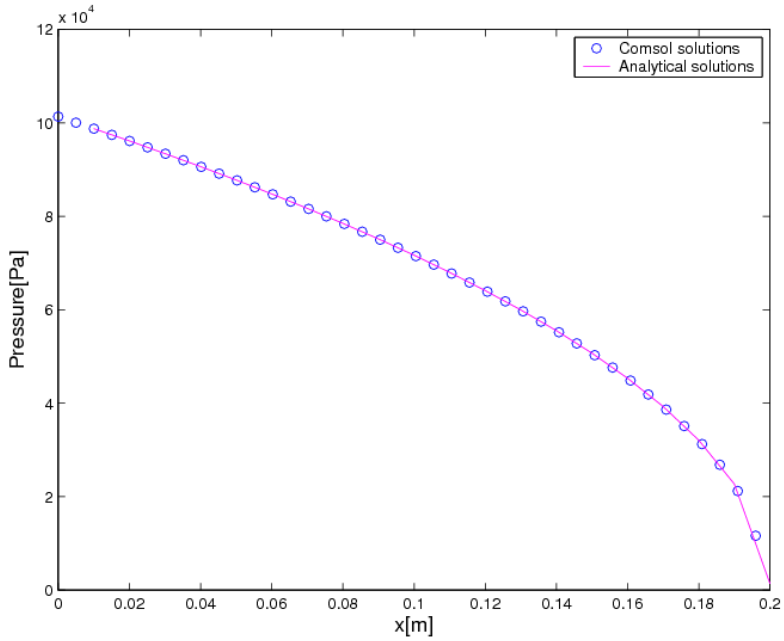

Fig. 2.7: Pressure distributions over flow direction x in one dimensional stationary flow.

2.2.4.2 Validity of Darcy's flow

In-plane permeability range of the glass fiber twill-weave: 10^{-9} - 10^{-11}m^2 can be used to estimate the range of Reynolds number and flow rate. Let's recall that Reynolds number is defined for porous media as,

$$Re_\phi = \frac{\rho v l_\phi}{\mu} = \frac{\rho q l_\phi}{\phi \mu} \tag{2.12}$$

where ϕ is the porosity, and l_ϕ is the characteristic length of pores. The range of velocity is illustrated in Fig. 2.9 for a permeability $K = 10^{-9}\text{m}$, viscosity $\mu = 1.65 \times 10^{-5}\text{Pa} \cdot \text{s}$, and a temperature $T = 273.15\text{K}$, *i.e.* 0°C. The analytical solution for stationary flows shows that the velocity is proportional to permeability and varies inversely with viscosity. The corresponding Reynolds number is determined (Fig. 2.8). The assumption of laminar flow for Darcy's flow, can be satisfied with proper inlet and outlet pressures provided. When the temperature is higher or when the permeability is smaller than 10^{-9}m^2, Re_ϕ will be smaller, which means a laminar flow assumption is guaranteed for gas flowing through fabrics at room temperature.

Once inlet and outlet pressures are chosen, the ranges and accuracy of flow rate meters can be determined by the estimated permeability value and velocity range depending on inlet and outlet pressures (Fig. 2.9) . Since permeability could change by 10 to 100 times for a fabric with porosity ranging from 40% to 60%, for

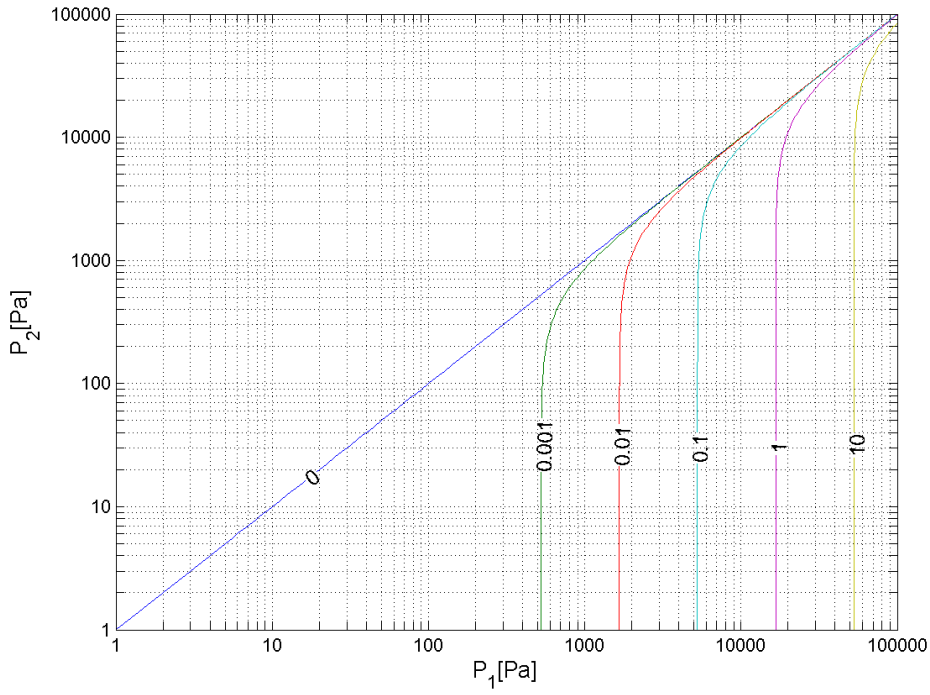

Fig. 2.8: Re_ϕ contour, $Re_\phi = 0, 10^{-3}, 10^{-2}, 10^{-1}, 1, 10^1$, under various inlet pressure P_1 and outlet pressure P_2 in one dimensional stationary flow: permeability $K = 10^{-9}$m, viscosity $\mu = 1.65 \times 10^{-5}$Pa $\cdot$ s, temperature $T = 273.15$K, and sample length 0.18m.

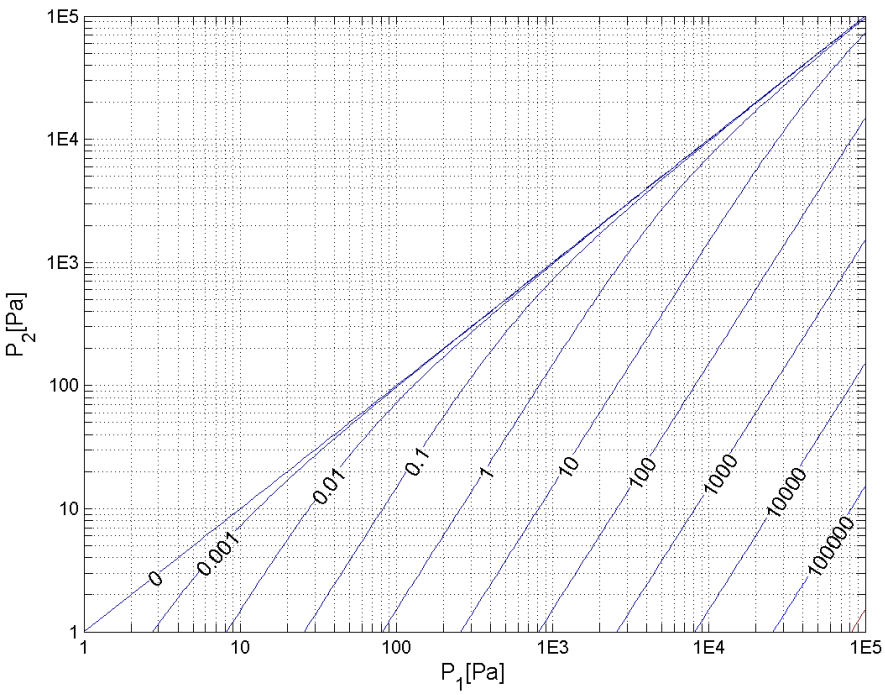

Fig. 2.9: Velocity contour, $v = 0, 10^{-3}, 10^{-2}, 10^{-1}, 1, 10^{1}, 10^{2}, 10^{3}, 10^{4}, 10^{5}$[m/s], under various inlet pressure P_1 and outlet pressure P_2 in one dimensional stationary flow: permeability $K = 10^{-9}\mathrm{m}^2$, viscosity $\mu = 1.65\times10^{-5}\mathrm{Pa}\cdot\mathrm{s}$, temperature $T = 273.15\mathrm{K}$, and sample length 0.18m.

different fabrics permeability varies significantly too. While the range of gas flow rate meter is usually 10 to 100 times of the sensitivity (or minimum scale value), it is necessary to have at least two flow rate sensors to secure the accuracy and test range during stationary measurements.

2.2.4.3 Characteristic time

Combining mass conversation equation and Darcy's law (respectively Eqs. 1.6 and 1.15) with the ideal gas law Eq. 1.36, and considering a 1D viscous flow with neglected gravity, the governing equation is,

$$\frac{\partial P}{\partial t} = \nabla \cdot \frac{K_v}{\phi \mu} \cdot P \nabla P \tag{2.13}$$

Let P^*, t^* and x^* to be the dimensionless variables: $P^* = P/P_{avg}$, $t^* = t/t_0$, $x^* = x^*/L$, where P_{avg} is the average pressure, L is the sample length and t_0 is the characteristic time, and the dimensionless operator $\nabla^* = L\nabla$, then the governing equation is nondimensionized as,

$$\frac{\partial P^*}{\partial t^*} \frac{1}{t_0} = \frac{K_v P_{avg}}{\phi \mu L^2} \cdot \nabla^* \cdot P^* \nabla^* P^* \tag{2.14}$$

The characteristic time t_0 equals to the term $\phi \mu L^2 / K_v P_{avg}$ so that the equation becomes dimensionless. The transient effect can be neglected when $t > t_0$. For the case $L = 0.2\text{m}$, $\mu = 1.8 \times 10^{-5}\text{Pa} \cdot \text{s}$, $K = 10^{-12}\text{m}^2$, $P_0 = 10^5\text{Pa}$, $\phi = 1$, the characteristic time $t_0 \approx 7.2\text{s}$; $t_0 \approx 0.7\text{s}$ for $K = 10^{-11}\text{m}^2$. The estimation is valid according to the simulated pressure distributions after different durations, see Fig. 2.10.

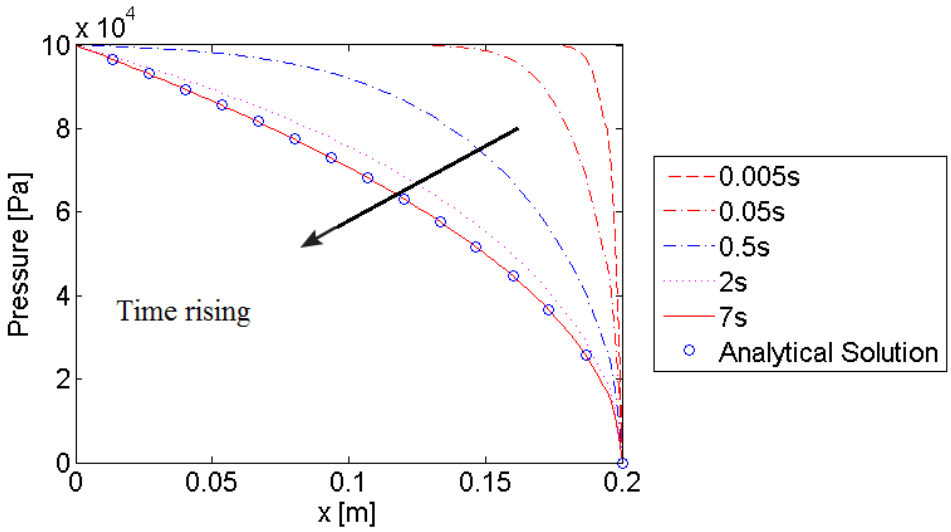

(a) $K = 10^{-12}\mathrm{m}^2$

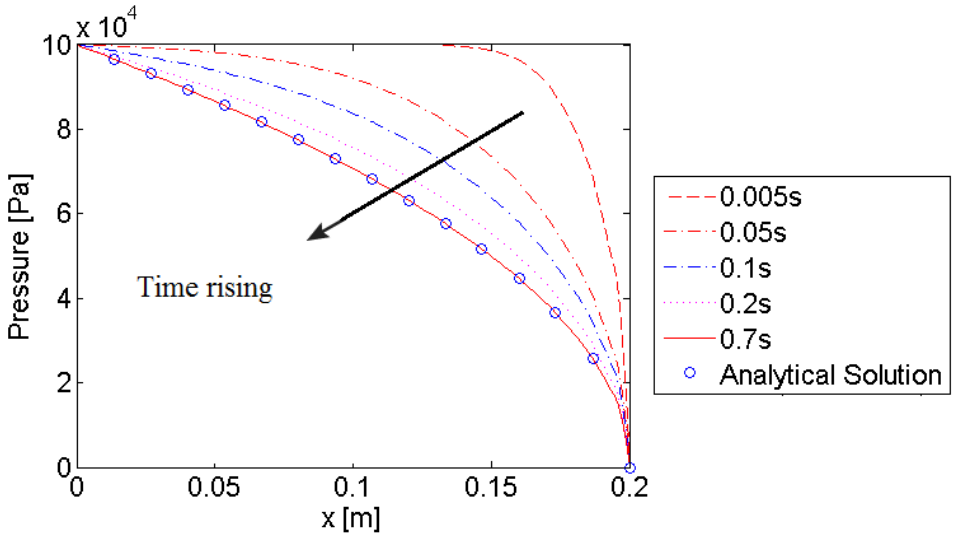

(b) $K = 10^{-11}\mathrm{m}^2$

Fig. 2.10: Transient 1D flow of nitrogen gas: (a) $K = 10^{-12}\mathrm{m}^2$, predicted pressure profile over x, at the time 0.005s, 0.05s, 0.5s, 2s, 7s; (b) $K = 10^{-11}\mathrm{m}^2$: predicted pressure profiles over x, at the time 0.005s, 0.05s, 0.1s, 0.2s, 0.7s.

2.3 Theoretical models

In this section, the models of gas transport based on various theories (as introduced in § 1.2 `Gas transport through porous media`) are built, and boundary conditions with a consider of gas compressibility are proposed for 1D set-up.

2.3.1 Governing equations

Governing equations of gas transport through porous media are deduced by combining mass conversation equation and constitutive equation with the ideal gas law Eq. 1.36.

2.3.1.1 Darcy's flow

Combining mass conversation equation and Darcy's law (respectively Eqs. 1.6 and 1.15) with the ideal gas law Eq. 1.36, and considering a flow in viscous regime with neglected gravity, the governing equation is,

$$\frac{\partial P}{\partial t} = \nabla \cdot \frac{\boldsymbol{K}_v}{\phi\mu} \cdot P \nabla P \tag{2.15}$$

For one-dimensional gas flow in a medium of constant permeability K_v, Eq. 2.20 writes,

$$\frac{\partial P}{\partial t} - \frac{K_v}{\phi\mu}\frac{\partial}{\partial x}\left(P\frac{\partial P}{\partial x}\right) = 0 \tag{2.16}$$

2.3.1.2 Non-Darcian viscous flow

When Re_ϕ is large, therefore the inertial term is no longer negligible, Darcy's flow is not valid. Darcy-Forchheimer equation provides a simple governing equation which is similar to Eq. 2.16 in Darcy's flow,

$$\frac{\partial P}{\partial t} - \frac{f_\beta}{\phi}\frac{\partial}{\partial x}\left(P\frac{\partial P}{\partial x}\right) = 0 \tag{2.17}$$

where f_β is a function of the pressure gradient, viscosity, permeability and Forchheimer parameter β (defined in Eq. 1.22).

2.3.1.3 Knudsen model

When $K_n > 1$, the flow can be described by the Knudsen model and the governing equation becomes,

$$\frac{\partial P}{\partial t} - \frac{1}{\phi}\frac{\partial}{\partial x}\left[(K_m\bar{v})\,\frac{\partial P}{\partial x}\right] = 0 \tag{2.18}$$

Although the above equation is almost the same as liquid governing equation, the physics is totally different.

2.3.1.4 Sliding model

When $K_n \sim 1$, Knudsen and viscous flows are present, Eq. (1.30) can be used. The governing equation in this case becomes,

$$\frac{\partial P}{\partial t} - \frac{1}{\phi}\frac{\partial}{\partial x}\left[\left(K_m\bar{v} + \frac{K_v P}{\mu}\right)\,\frac{\partial P}{\partial x}\right] = 0 \tag{2.19}$$

2.3.1.5 General model

Considering permeability in Darcy's law is not just a porous media property but also a function of pressure or pressure gradient, Darcy's law can be used as a general model for all the cases,

$$\frac{\partial P}{\partial t} = \nabla \cdot \frac{\boldsymbol{K}_g}{\phi\mu} \cdot P\nabla P \tag{2.20}$$

where K_g is the apparent permeability, which depends on various parameters in different models, as for Darcy-Forchheimer model,

$$K_g = \mu f(\beta) \tag{2.21}$$

Knudsen model,

$$K_g = \frac{\mu K_m \bar{v}}{P} \tag{2.22}$$

the sliding model, which is explained by Knudsen flow and deduced from DGM theory [13],

$$K_g = \frac{\mu K_m \bar{v}}{P} + K_v \tag{2.23}$$

or explained by Klinkenberg sliding effect [34],

$$K_g = \left(\frac{b}{P} + 1\right) K_v \tag{2.24}$$

Although the two sliding models come from different hypotheses and theories, the apparent permeability can be expressed equivalently with Eq. 2.23 and Eq. 2.24, and $[K_m, K_v]$ and $[b, K_\infty]$ are related by,

$$K_\infty = K_v, \quad b = \frac{K_m}{K_v}\bar{v}\mu \tag{2.25}$$

2.3.2 Boundary conditions

The sample is sealed along both edges in the flow direction to create a 1D flow. Since 1D governing equation Eq. 2.16 is used, the boundary conditions at the two extremities are considered. Since air is compressible, the air trapped between the valve and the edge of the preform, as shown in Fig. 2.2, may cause a flux at the boundary when pressure evolves. The gas present in pipes and tubing outside the valves do not affect the test.

Assuming a quasi-static flow, the trapped air shares the same values of pressure, density and temperature. For the points $x = 0$ and $x = L$, the mass conservation gives,

$$\begin{cases} \dfrac{\partial \rho}{\partial t} V + \rho A q = 0 & x = 0 \\ \dfrac{\partial \rho}{\partial t} V - \rho A q = 0 & x = L \end{cases} \tag{2.26}$$

where V is the volume of air trapped, A is the cross-sectional area for the gas flow, and L is the length of the fabric sample. Combining Eq. 2.26 with the ideal gas law (Eq. 1.36) and Darcy's law (Eq. 1.15), the boundary conditions can be obtained in terms of pressure P,

$$\begin{cases} \dfrac{K_v}{\mu} P \dfrac{\partial P}{\partial x} - \dfrac{\partial P}{\partial t}\dfrac{V}{A} = 0 & x = 0 \\ \dfrac{K_v}{\mu} P \dfrac{\partial P}{\partial x} + \dfrac{\partial P}{\partial t}\dfrac{V}{A} = 0 & x = L \end{cases} \tag{2.27}$$

where the volume to area ratio V/A is the dominant parameter. The inward flux N_0 equal to $-(V/A\mu)\partial P/\partial t$ at the boundary where the valve is closed (see the BC for Comsol simulation, Eq. 2.42b). For a set of experimental pressures P_1 and P_2, the permeability obtained by inverse method could change remarkably with different volume area ratio. The variation of the calculated permeability can be estimated as,

$$\frac{K_v}{K_o} = 1 + C_k \frac{V}{AL\phi} \tag{2.28}$$

where K_o is the permeability obtained by inverse method with unmodified boundary conditions, and C_k does not depend on the types of samples, but only varies slightly for different loading patterns: $C_k \approx 1.7, 1.9$ and 2.0 respectively for RPM:

1×10^3Pa $\rightarrow 1 \times 10^5$Pa, RPM: 1×10^4Pa $\rightarrow 1 \times 10^5$Pa and DPM 1×10^5Pa $\rightarrow 2 \times 10^3$Pa. This empirical relationship is confirmed by sets of experiments on samples of different sizes and fabrics (CTW with a length of 0.095 m; GTW with a length of 0.18 m; CBD with a length of 0.235 m; CUD with a length of 0.275 m). For each sample, K_x is obtained by back-calculation with changing V/A and constant L. An example for GTW is shown in Fig. 2.11.

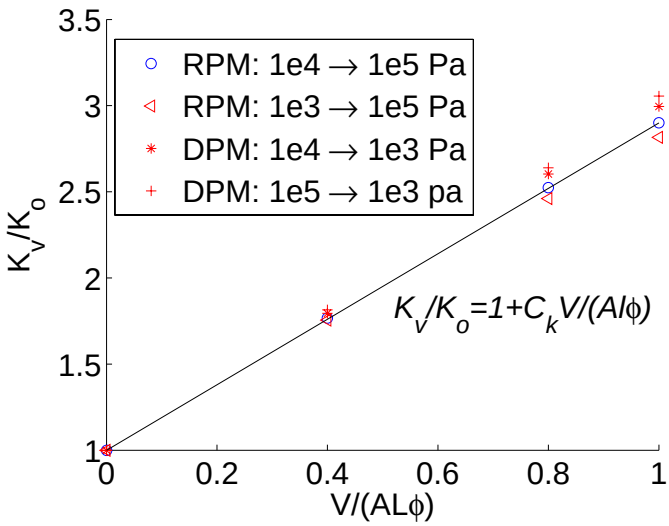

Fig. 2.11: Variation of permeability obtained by inverse method using different volume to area ratios, based on experimental pressures for 4 types of samples and procedures.

It is reasonable to consider temperature as a constant parameter within fabric media, while for the air trapped at the boundary side, temperature variation could be up to 3%. Assuming the relationship between pressure P and volume V as,

$$PV^{\hat{\gamma}} = \text{const} \tag{2.29}$$

where $\hat{\gamma}$ is the efficient adiabatic index, with a value between 1 and 1.4 for air. The $\hat{\gamma}$ for a constant temperature variation of 3% equals to 1.013. Substituting Eq. 2.29 into the mass conservation equation at boundaries (Eq. 2.26) gives,

$$\begin{cases} \dfrac{\partial P^{1/\hat{\gamma}}}{\partial t} V + P^{1/\hat{\gamma}} A v = 0 & x = 0 \\ \dfrac{\partial P^{1/\hat{\gamma}}}{\partial t} V - P^{1/\hat{\gamma}} A v = 0 & x = L \end{cases} \tag{2.30}$$

Therefore the boundary conditions can be written in terms of pressure P as

$$\begin{cases} \frac{K_v}{\mu} P \frac{\partial P}{\partial x} - \frac{\partial P}{\partial t} \frac{V}{A\hat{\gamma}} = 0 & x = 0 \\ \frac{K_v}{\mu} P \frac{\partial P}{\partial x} + \frac{\partial P}{\partial t} \frac{V}{A\hat{\gamma}} = 0 & x = L \end{cases} \tag{2.31}$$

The permeability K_e, affected by gas state equation, can be estimated according to the empirical relationship in Eq. 2.28, as below,

$$K_e = K_0 \frac{1 + 2V/(AL\phi)}{1 + 2V/(AL\phi\hat{\gamma})} \tag{2.32}$$

For example, the difference $(K_e - K_0)/K_0$ is less than 0.7% when $V/(AL\phi) \sim 0.5$ and $L = 0.2$m. The above estimation is based on the assumption that γ is constant, and in real case, the variation of temperature is concentrated on the first stage of loading, and the effect can be neglected.

2.3.3 Validation

2.3.3.1 Capillary effect

Since perfect vacuum does not exist, partial vacuum (or pressure) is of concern in this study. The medium is therefore saturated with gas molecules. When the pressure increases or decreases, gas molecules are added or removed. The gas density varies along the sample due to the movement of molecules. The notion of impregnated/not impregnated region that define a fluid flow front does not exist with gas.

2.3.3.2 Viscous flow regime

It has been seen in § 1.2 that the K_n number is used to determine whether statistical mechanics (Knudsen flow) or the continuum mechanics (viscous flow) dominate the gas flow. Using the definition equation Eqs. 1.1 and 1.2, and considering that $l_\phi \simeq \sqrt{K_v}$ (where l_ϕ is the characteristic length of porous media for viscous flow), the K_n number field can be plotted in the absolute gas pressure and permeability domain (Fig. 2.12). The domain is chosen based on the fibrous materials of interest ($K_v \in [10^{-15}; 10^{-6}]$ m^2 and $P \in [10^0; 10^6]$ Pa.)

When $K_n \ll 1$, viscous flow regimes are considered, and these regimes (laminar or turbulent) are governed by the Reynolds number. In the case of porous or fibrous media, a modified Re_ϕ can be defined in Eq. 2.12. Typical fiber preforms of interest in structural composites exhibit an in-plane permeability in a range of 10^{-13} m^2 to 10^{-8} m^2. Fig. 2.13 shows the Re_ϕ field for given gas velocity v and pressure P, in

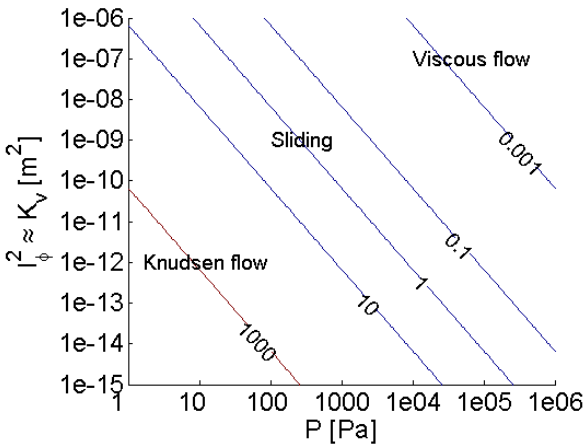

Fig. 2.12: K_n field in the absolute pressure and permeability domain.

the two extreme cases of $K = 10^{-13}$ m^2 and $K = 10^{-8}$ m^2. For a cavity volume of 0.25 m $\times$ 0.15 m $\times$ 0.002 m (corresponding to our apparatus dimensions), a porosity of 0.5, and considering that the gas fills the cavity or is removed from the cavity in 3 seconds, the average gas velocity is around 0.04 m/s.

The rectangular gray regions in Fig. 2.13 show the region of interest for the materials and test conditions of this study. Therefore, for this type of flow, Fig. 2.13 shows that $Re_\phi < 1$ for a maximum absolute pressure of 10^5 Pa. The flow remains laminar and therefore governed by Darcy's law. The non-linearities involved with higher Re_ϕ, that would require the use of Forchheimer's relationship, are not of concern for most of fibrous preforms of interest in this study.

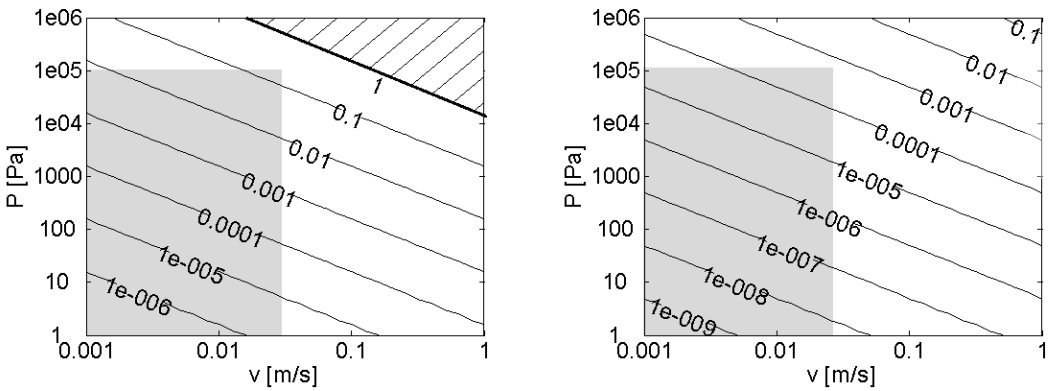

(a) $K_v = 1 \times 10^{-8}$ m^2 (b) $K_v = 1 \times 10^{-13}$ m^2

Fig. 2.13: Re_ϕ related to pressure and velocity.

2.3.3.3 Thermal analysis

The flow of gas in the fibrous preforms, governed by Darcy's law, can be compressed or dilated depending on the type of experiments that will be performed. This eventual temperature change is important to be checked because: first, the viscosity of gases is temperature dependent and is described by the Sutherland's relationship,

$$\mu_a = \mu_0 \left(\frac{T_0 + C}{T + C}\right) \left(\frac{T}{T_0}\right)^{3/2} \tag{2.33}$$

where, e.g. for air, $\mu_0 = 1.81 \times 10^{-5}$ Pa.s, $T_0 = 293$ K and $C = 117$ K.

Second, temperature change determines the way to simplify the state equation of gas. For gas at low pressure and high temperature, an ideal gas law is used as the state equation,

$$PV = nRT \tag{2.34}$$

where n is the number of moles, and R is the ideal gas constant, 8.314 $J/(mol \cdot K)$.

For air trapped in the cavity, as shown in Fig. 2.2, temperature could change a lot when the valve is closed and pressure decreases or increases rapidly. It is important to research on thermal effect of trapped air in order to check the effect on viscosity and boundary conditions proposed in §2.3.2. A simple model is built to predict the approximate temperature variantion.

The first law of thermodynamics for open systems gives,

$$dU = \delta Q_h + dH_{in} - dH_{out} \tag{2.35}$$

where U is the average internal energy, Q_h the heat from out of the system, H_{in} is enthalpy entering the system and H_{out} is the enthalpy internal energy leaving the system (equals to zero here since the valve is closed). Internal energy and enthalpy changes are related to temperature T as,

$$dU = \hat{C}_v R\, d(nT) \tag{2.36}$$

$$dH_{in} = (1 + \hat{C}_v) RT\, dn \tag{2.37}$$

where $\hat{C}_v$ is the dimensionless isochoric specific heat capacity, $\approx 3/2$ for monatomic gas, 5/2 for diatomic gas and 3 for more complex molecules. Heat Q_h is determined by the surface of air contacted with two plates, referred to as A_1,

$$\delta Q_h = h_c A_1 (T_0 - T) \delta t \tag{2.38}$$

where h_c is the heat transfer coefficient, from $10 \sim 100W/(m^2K)$ for air, T_0 is the environment temperature. Substituting Eqs. 2.36, 2.37 and 2.38 into Eq. 2.35, and replacing n and dn with PV/RT and $V/R\,d(P/T)$ respectively, after reorganization the following differential equation is obtained,

$$(1+\hat{C}_v)\frac{PH}{2T}\frac{dT}{dt} + h_cT - \left(\frac{H}{2}\frac{dP}{dt} + h_cT_0\right) = 0 \tag{2.39}$$

where H is the cavity thickness, which equals to $V/2A_1$, and $\hat{C}_v$ equals to 5/2. Since steel plate has high thermal conductivity (43 W/m · K compared with 0.024 W/m · K for atmosphere air), the heat resistance of steel can be ignored. For air in the cavity, the heat transfer is carried out in two ways: conduction and convection. In out-of-plane direction, the thickness is too small and no convection will develop. Hence the heat transfer coefficient h_c is calculated as,

$$h_c = \kappa\frac{\left.\frac{\partial(T_s-T)}{\partial y}\right|_{y_0}}{T_s - T_\infty} \tag{2.40}$$

where the meaning of y_0 and T_∞ are given in Fig. 2.14. From the figure, we can learn that,

$$\left.\frac{\partial(T_s-T)}{\partial y}\right|_{y_0} > \frac{T_s - T_\infty}{y_\infty - y_0} \tag{2.41}$$

Hence h_c in Eq. 2.40 should be less than $\kappa/(y_\infty - y_0)$.

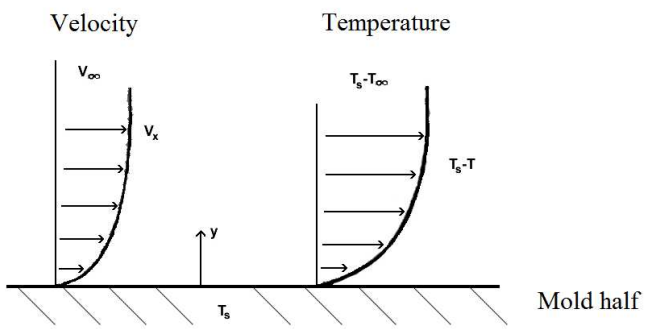

Fig. 2.14: Thermal boundary layer

Since there are two plates, half of the thickness is used as $y_\infty - y_0$, and hence the minimum of h_c is 20 $W/(m^2K)$, and air's thermal conductivity $\kappa = 0.024\ W/mK$. Eq. 2.39 is a first-order differential equation which can be solved with the variable order method. Several pressures given by the experimental configurations are used and the corresponding temperature are calculated from Eq. 2.39, showing variations less than 3% (Fig. 2.15 and Fig. 2.16). Reducing the flow rate by flow rate

controllers can keep temperature change below 1%, and cosrresponding viscosity variation below 0.7%.

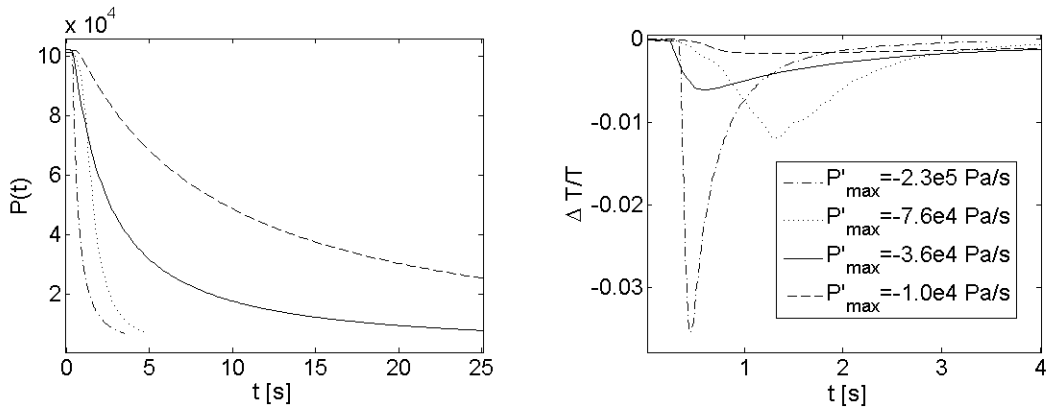

(a) P_{exp} (b) Temperature variations

Fig. 2.15: Temperature variations corresponding to experimental pressure drops in DPM: (a) loading pressure curves for 4 DPM experiments; (b) the temperature variations due to gas evacuations.

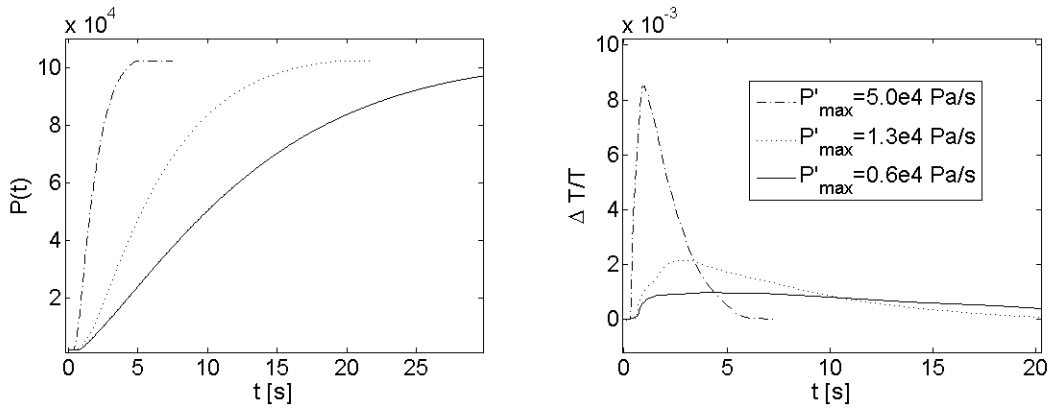

(a) P_{exp} (b) Temperature variations

Fig. 2.16: Temperature variations corresponding to experimental pressure rises in RPM: (a) loading pressure curves for 4 RPM experiments; (b) the temperature variations due to gas infusions.

2.4 Inverse method

Simulation is based on solving fundamental equations for P (Eqs. 2.16 or 2.19), with proper boundary (Eq. 2.27) and initial conditions. Darcy's law in Earth Science Module of Comsol is used and the standard form, which is adopted for our problems, is given as,

$$\delta_s S \frac{\partial P}{\partial t} + \nabla \cdot \left[-\delta_K \frac{K_s}{\mu} (\nabla P + \rho g \nabla D) \right] = \delta_Q Q_s \qquad \text{Flowing domain} \tag{2.42a}$$

$$\boldsymbol{n} \cdot \left[-\delta_K \frac{K_s}{\mu} (\nabla P + \rho g \nabla D) \right] = N_0 \qquad \text{BC: valve closed} \tag{2.42b}$$

$$P = P_0 \qquad \text{BC: loading pressure} \tag{2.42c}$$

where the storage term S is set to be 1, liquid source Q_s is 0, ρg is 0 since gravity is neglected; the scaling coefficients for storage, flux and source δ_s, δ_K and δ_Q respectively are set to be 1; viscosity μ is set to be 1 since viscosity will be combined into K_s. For Darcy's model, the saturated K_s is set to be,

$$K_s = \frac{K_v}{\mu \phi} P \tag{2.43}$$

to match the governing equation of 1D Darcy's flow (Eq. 2.16). For boundary conditions, at the point $x = 0$, pressure is set to be the experimental pressure recorded where the valved is opened (referred to as P_{Iexp}, which is $P_1(t)$ in RPM and $P_2(t)$ in DPM; the experimental pressure at the other side is referred to as P_{Oexp}); at the point $x = L$, the inward flux N_0 equals to zero and the pressure at this point (referred to as P_{Osim}) will be computed and compared with P_{Oexp}.

The room temperature T_o is recorded before each experiment, and since the fabric is thin and in contact with the metallic lower mold, the temperature T of gas within the fabric is considered to be constant and equal to T_o. The pressures $P_1(t)$ and $P_2(t)$ are recorded during experiments, and other parameters are determined: viscosity μ is calculated from the room temperature T_o (Eq. 2.33); the porosity ϕ of the sample is provided by the sample thickness h, number of fabric plies N_p, its areal weight W_f and density of fiber material ρ,

$$\phi = 1 - \frac{W_f N_p}{h \rho} \tag{2.44}$$

Then the viscous permeability K_v is estimated by inverse method while minimizing the residual ε between experimental and simulated results obtained for $P_O(t)$, under the prescribed pressure $P_I(t)$. The fitting error is evaluated as,

$$\varepsilon = \frac{1}{P_a} \sqrt{\frac{1}{N} \sum_{i=1}^{N} \left(P_{Oexp}^i - P_{Osim}^i \right)^2} \tag{2.45}$$

where N is the number of data points i, and P_a is the atmosphere pressure. The

accuracy of pressure sensors is around 1%, so the error of K_v can be estimated according to the dependance of ε on K_v, as shown in Fig. 2.19.

When ε is larger than 1% (the error due to data acquisition accuracy in experiments), the flow may not be in the Darcy's flow regime any more, and the permeability obtained with Darcy's model could have other effects inside and hence be referred to as K_g. If the deviation is caused by non-Darcian flow (Re_ϕ larger than 1), the Forchheimer model (Eq. 1.21) can be applied by setting the saturated permeability K_s used in Comsol earth science module, as,

$$K_s = \frac{2P}{\left(\alpha + \sqrt{\alpha^2 + 4\beta\nabla P}\right)\phi} \tag{2.46}$$

where α and β have the same meaning as in Eq. 1.22; if $K_n \simeq 1$ and gas shows a higher flow rate at low pressure than predicted, there could be a sliding effect, and K_s is set as,

$$K_s = \frac{K_v}{\mu}P + K_m\bar{v} \tag{2.47}$$

which can describe sliding model (Eq. 2.19) and also Darcy's model when K_m vanishes.

In Comsol simulation mesh of 20 elements is sufficient to produce accurate results, with an error less than 0.5%, as shown in Fig. 2.17.

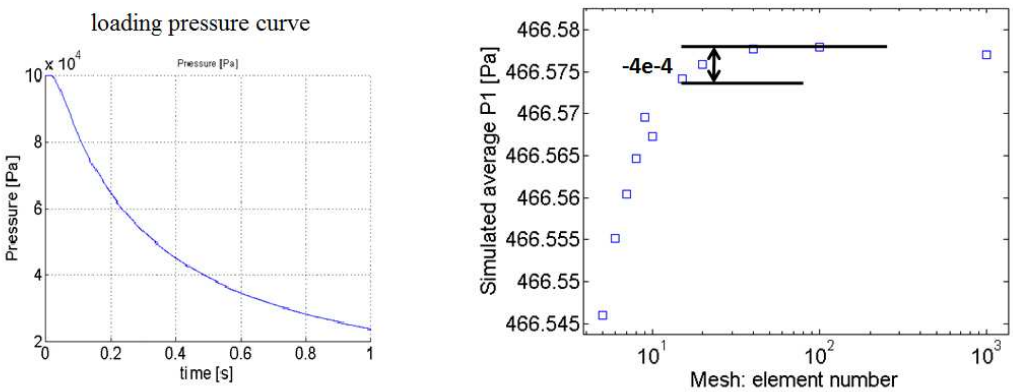

Fig. 2.17: Simulated pressure values based on meshes of various element numbers.

2.5 Results

2.5.1 Evaluation of measurements for Darcy's flow

When $K_n \ll 1$ and $Re_\phi \ll 1$, simulations of flow based on Darcy's law fits well experimental data (Fig. 2.18). Since gas has very low density, $Re_\phi \ll 1$ is satisfied for fabrics used in this study(§ 2.5.1.1). Experimental cases when sliding ($K_n \simeq 1$) and Knudsen flow occur ($K_n > 1$) will be introduced in § 2.5.2.

2.5.1.1 Velocity profile and Re_ϕ

Since no flow rate meter is used in the experiment, the flow rate can be obtained indirectly by simulation with Darcy's model with K_v obtained by inverse method. An example of measurements on GTW is given in Fig. 2.18. $P(x,t)$ is non-linear over x or t (pressure profiles over x at different times shown in Fig. 2.18(c) and Fig. 2.18(d)). Velocity and Re_ϕ can be calculated using Eq. 3.2. The Re_ϕ (the maximum point over x) evolution with respect to time is given for different flow rates (Fig. 2.18(e) and Fig. 2.18(f)). Although the velocity can be up to 1.4 m/s locally, Re_ϕ remains low (< 0.4) since the gas density is low.

2.5.1.2 Flow rate

A better fitting can be obtained at a lower flow rate: ϵ is approximately 0.27%, while 1.1% at high flow rate, which is slightly higher than the pressure sensors a at room temperature (Fig. 2.19). Although measurements at low flow rate give a better fitting between experimental and predicted P_2 because of lower Re_ϕ, lower flow rate will reduce the accuracy of back-calculation, as shown in Fig. 2.19. Also the curves of P_1 and P_2 would be too close to obtain a correct K_v at extreme slow flow rates; that scenario has no interest since the test would last too long.

2.5.1.3 Repeatability and comparison of various loading patterns

In order to check the effect of initial pressure during measurements, a series of experiments using RPM have been applied to one GTW preform at 51% fibre volume fraction. All the experiments are done on one set-up with one sample unreplaced. For each initial pressure, the measurements are repeated 3 to 6 times, and the variation coefficient is less than 5%. For values of permeability obtained under various initial pressure are also quite close with a maximun difference 4.5% (as shown in Tab. 2.3, where $P_{vac} = 2 \times 10^3$Pa and $P_a = 1.017 \times 10^5$Pa, experiments performed on a sample unreplaced). When the initial pressure is high (such as

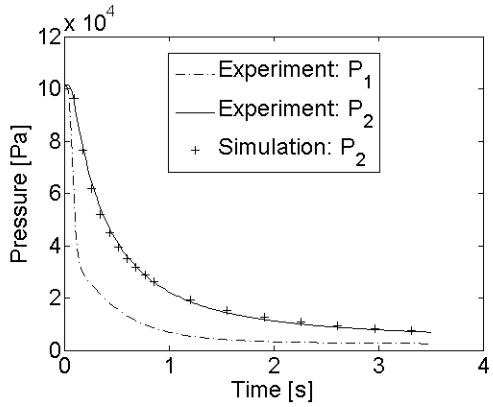

(a) High flow rate, $K_{=}7.4(\pm 7\%) \times 10^{-11}$ m^2

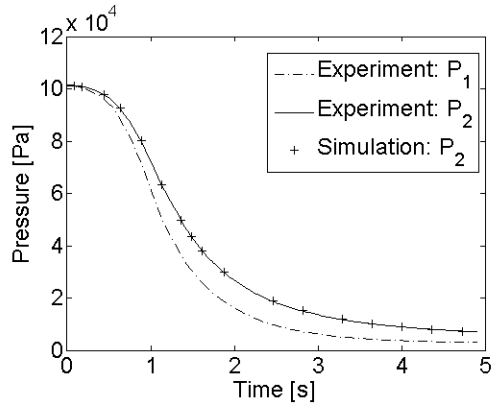

(b) Low flow rate, $K_{=}8.2(\pm 13\%) \times 10^{-11}$ m^2

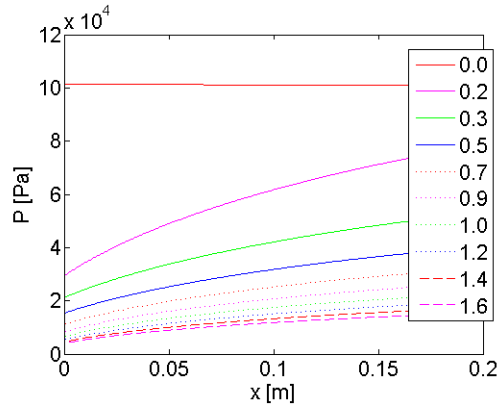

(c) High flow rate: $P(x,t)$

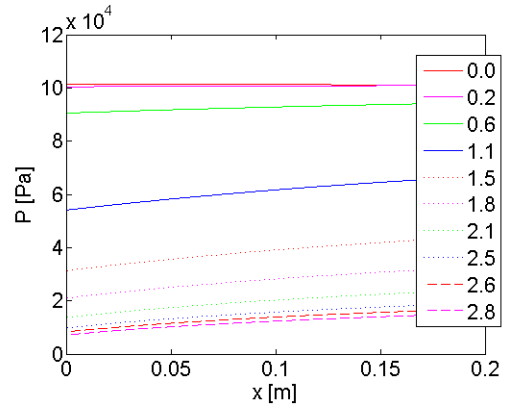

(d) Low flow rate: $P(x,t)$

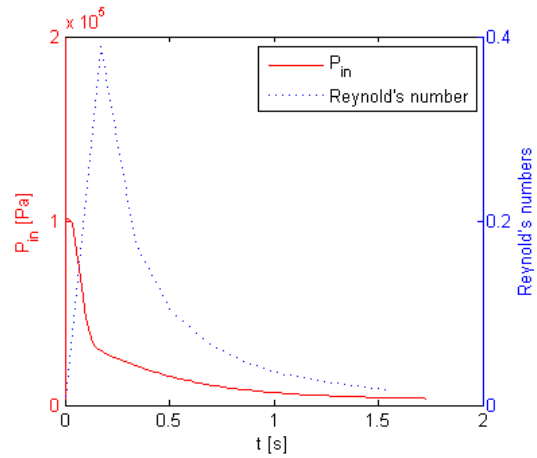

(e) High flow rate: Re_ϕ

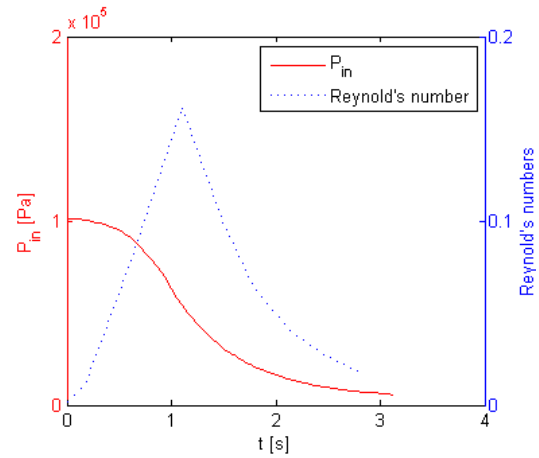

(f) Low flow rate: Re_ϕ

Fig. 2.18: Comparison between experimental and computed P_2 in dropping pressure measurement at different flow rate for a GTW preforms at 51 % fibre volume fraction: figures in the left are for high flow rate and those in the right for low flow rate. (a,b) loading pressure and responses (c,d) the corresponding pressure profiles at different times (e,f) the corresponding Reynolds number.

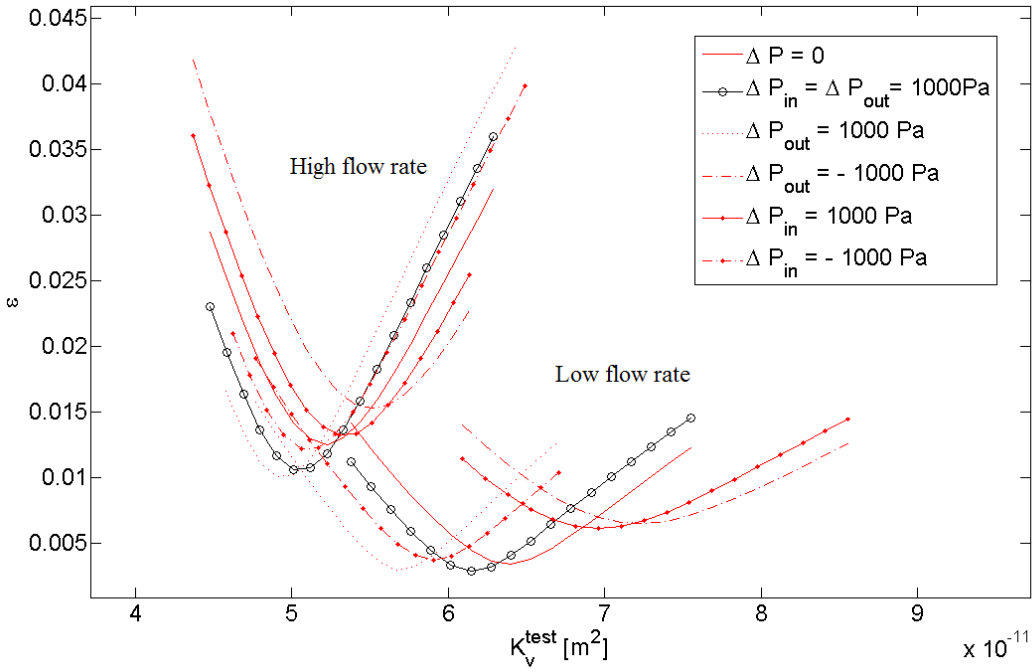

Fig. 2.19: Back-calculation errors with input viscous permeabilities K_v^{test} for various pressure sensor scatters ΔP; K_v is obtained where ε reaches the minimum value for certain input P_{exp}. Two cases shown in this figure are from Fig. 2.18(a): high flow rate and Fig. 2.18(b): low flow rate.

2.7×10^4Pa), the resolution is quite low (P_1 and P_2 curves are too close) and the result is less accurate. Although measurements in the range of [P_{vac}, 1×10^4Pa] have good resolution, the relative accuracies of pressure sensors become as large as 10%. As mentioned earlier, in oder to make the P_1 and P_2 equivalent at the initial and ultimate stages, P_1 is modified by $\hat{P}_1(t) = P_1(t)a + b$, where a and b are calculated by Eq. 2.1.

The repeatability is less than 5% for one sample unreplaced, and when the same sample is reloaded, the difference on results could be up to 15%, which means the permeability is quite sensitive to the micro-structure and experimental set-up.

2.5.1.4 Comparison between DPM and RPM

DPM and RPM have been applied to GTW preforms at 51% fibre volume fraction, and CTW preforms at 48.6% fibre volume fraction (Fig. 2.20). Measurements on the GTW with DPM or RPM (Figs. 2.20(a) and 2.20(b)) give very similar in-plane permeabilities 8.1×10^{-11} m^2 and 7.7×10^{-11} m^2 respectively, with a standard-deviation lower than 10% for 7 sets of experiments with different flow rates.

	Loading pressures [Pa]	K_v[m^2]	C_{vr}	Number of tests
RPM	$0.2 \times 10^4 \rightarrow P_a$	8.5×10^{-11}	1.6%	6
RPM	$0.7 \times 10^4 \rightarrow P_a$	8.7×10^{-11}	0.9%	4
RPM	$1.0 \times 10^4 \rightarrow P_a$	8.5×10^{-11}	4.5%	3
RPM	$1.7 \times 10^4 \rightarrow P_a$	8.8×10^{-11}	1.4%	3
RPM	$2.4 \times 10^4 \rightarrow P_a$	8.9×10^{-11}	0.2%	3
RPM	$2.7 \times 10^4 \rightarrow P_a$	8.8×10^{-11}	1.0%	3
RPM	$P_{vac} \rightarrow 1 \times 10^4$	8.4×10^{-11}	1.3%	3
DPM	$P_a \rightarrow P_{vac}$	8.7×10^{-11}	3.6%	5
DPM	$1.0 \times 10^4 \rightarrow P_{vac}$	8.3×10^{-11}	0.9%	3

Table 2.3: Permeability measured in RPM for GTW with various loading pressure cases, where C_{vr} is the coefficient of variation (standard deviation divided by the mean).

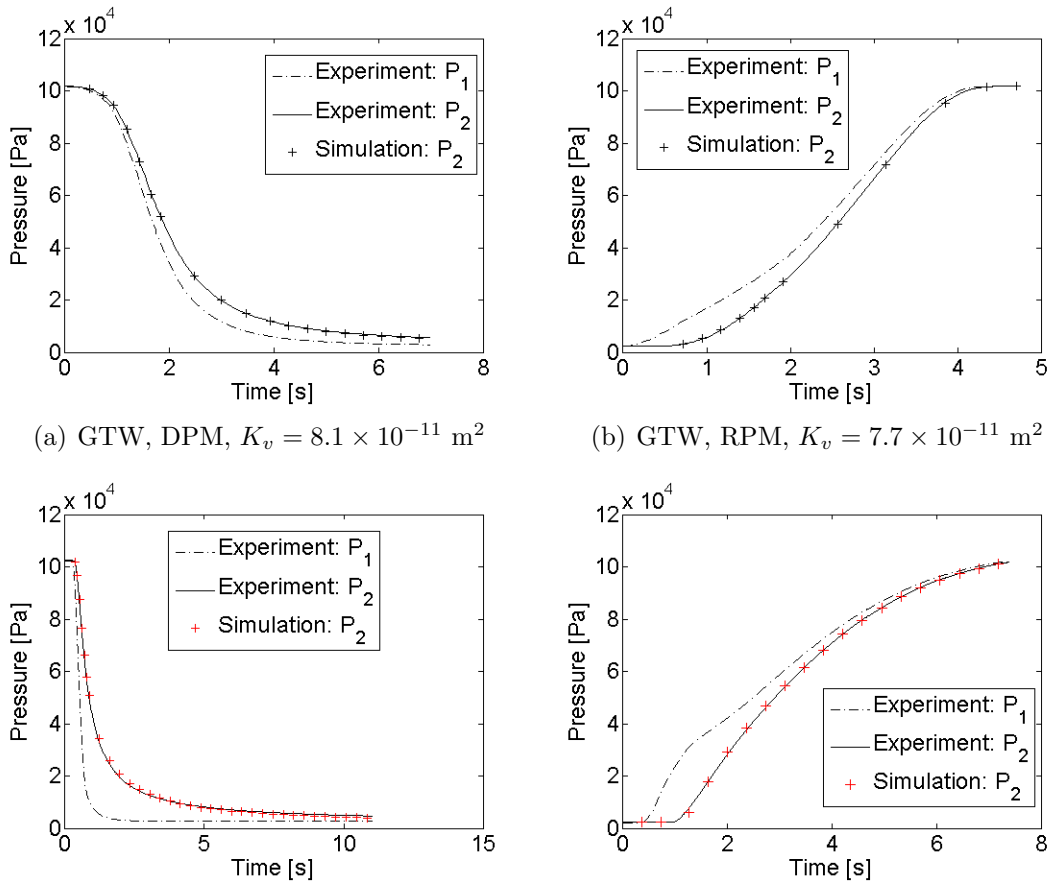

(a) GTW, DPM, $K_v = 8.1 \times 10^{-11}$ m^2

(b) GTW, RPM, $K_v = 7.7 \times 10^{-11}$ m^2

(c) CTW, DPM, $K_v = 4.9 \times 10^{-11}$ m^2

(d) CTW, RPM, $K_v = 5.2 \times 10^{-11}$ m^2

Fig. 2.20: Comparison between experimental and computed pressures P_2 for the GTW preforms at 51% fibre volume fraction and CTW preforms at 48.6% fibre volume fraction.

2.5.1.5 Permeability measured using gas and liquid

The air transient measurements of GTW and CTW are carried out for various volume fractions. Results show that permeability has a similar trend as those extracted from liquid injection and compression tests [9] (Fig. 2.21). Fluid type to determine permeability has no significant effect on results: the difference between permeability values measured are less than 25% between the transient gas flow and liquid injection methods for both fabrics, and the difference is less than 5% between air and nitrogen gas. The permeability measured with gas on CTW with a high fiber volume fraction (about 55%) is higher than the values measured with liquid. This error could be due to gas sliding effect and remains to be verified in the following sections.

2.5.1.6 Effect of trapped gas on permeability

When the trapped gas at boundary is not considered in back-calculation simulations, the obtained values of permeability will be significantly lower than the correct ones. As shown in Fig. 2.22, there is a ratio of 5 times difference for GTW and 2 times for CTW. The ratio is lower for CTW samples because there is a reduced volume of trapped air ($V/A \approx 0.1$ for CTW and ≈ 0.2 for GTW) and longer length (0.27m for CTW and 0.18m for GTW). When a correct boundary condition (Eq. 2.27) is used, the effect due to gas trapped volume is negligible.

2.5.2 Sliding effect in air transport through porous media

2.5.2.1 Validation of models

It has been seen in Sec. 1.2 that gas flow in porous media is governed by the Knudsen number K_n. Using the definition of K_n (Eqs. 1.1 and 1.2), and considering that $l_\phi \simeq \sqrt{K_v}$ (where l_ϕ is the characteristic length of porous media for viscous flow), the K_n number field can be plotted in the absolute gas pressure and permeability domain (Fig. 2.23). The domain is chosen based on the fibrous materials of interest ($K_v \in [10^{-15}; 10^{-6}]$ m^2 and $P \in [10^0; 10^6]$ Pa. For instance, as it can be seen in Fig. 2.23, for CTW and GTW preforms ($K_v \in [10^{-11}; 10^{-9}]$ m^2), and a pressure drop from 10^5 to 10^3 Pa in a DPM test, the flow is mostly viscous and governed by Darcy's law. However for CUD with $K_v \in [10^{-14}; 10^{-12}]$ m^2, the flow is mostly governed by the sliding and Knudsen regimes.

Consequently, the sliding model deduced by DGM (Eq. 2.19) is applied in this case and a better fitting can be obtained, relatively to using Darcy's law (viscous flow) as shown in Fig. 2.24.

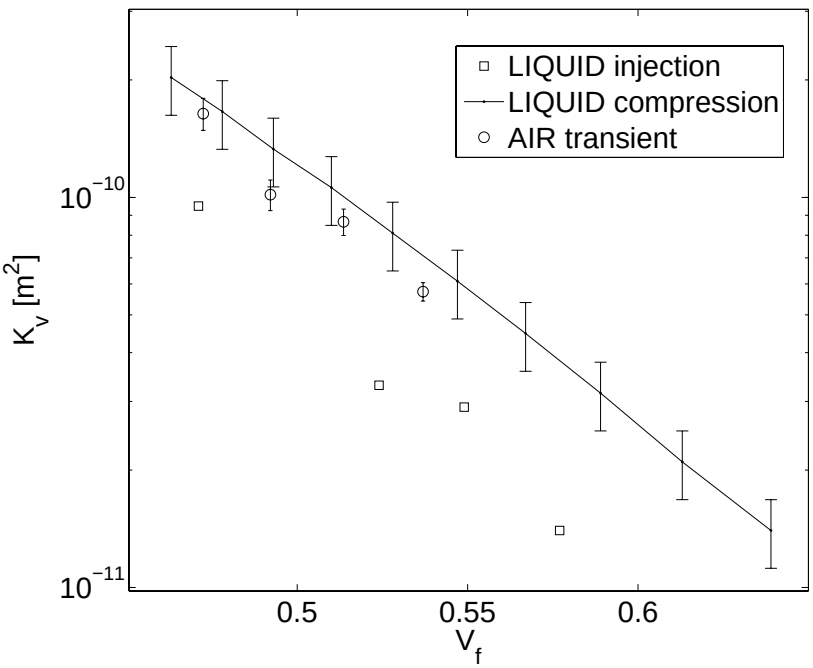

(a) GTW

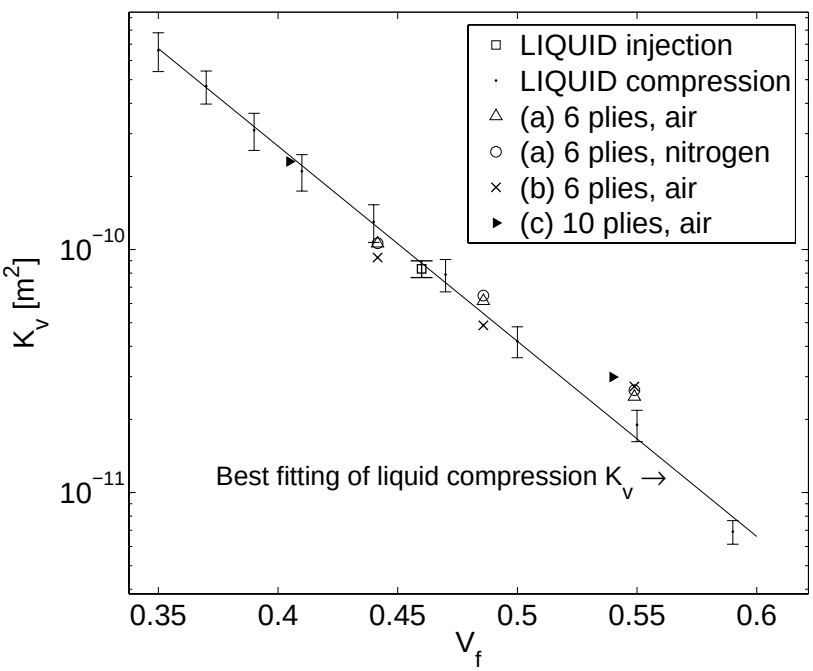

(b) CTW

Fig. 2.21: Comparison of permeability K_v obtained by transient air flow (back-calculated based on Darcy's law: $\varepsilon < 0.7\%$, $\bar{K_g} \approx K_v$), liquid compression and liquid unidirectional injection measurement methods on GTW and CTW for different volume fractions [9].

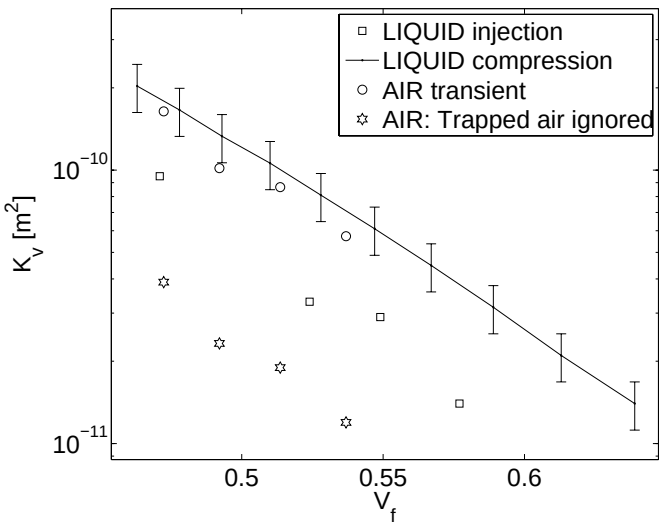

(a) GTW

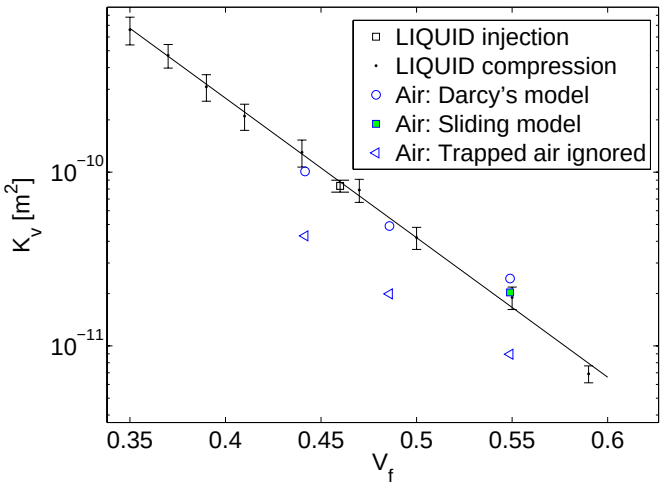

(b) CTW

Fig. 2.22: Values of permeability obtained with no consideration of trapped air at the boundaries.

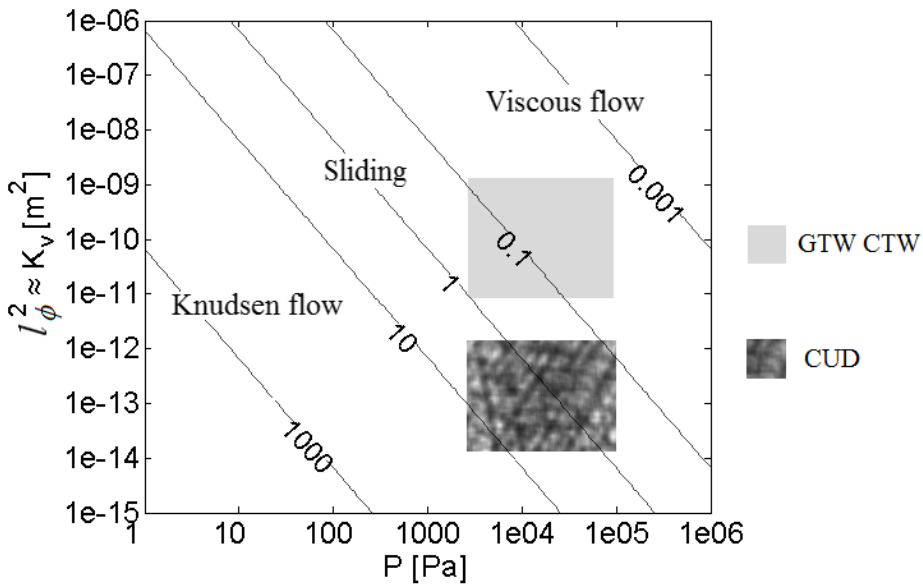

Fig. 2.23: K_n field in the absolute pressure and permeability domain.

2.5.2.2 Experimental results on CTW

There is a slight sliding effect for CTW with high V_f (permeability back-calculated by sliding model is compared with the one obtained by Darcian model, as shown in Fig. 2.22(b).)

2.5.2.3 Experimental results on CUD

The sliding effect will cause the apparent permeability K_g to increase with the decreasing pressure during the measurements, and hence the back-calculated $\bar{K}_g$ using Darcian model is in fact the average value of the apparent permeability (Fig. 2.25).

The gas flow through CUD is measured by DPM and RPM, and permeability is back-calculated using Darcy's model (apparent $\bar{K}_g$ obtained) and sliding models (viscous permeability K_v obtained, also refer to as intrinsic permeability K_∞ in Klinkenberg model Eq. 1.31), as shown in Fig. 2.26. Since $\bar{K}_g$ includes the sliding effect, apparent $\bar{K}_g$ (the average value of K_g over time) is always larger than K_v. When permeability is large, the sliding effect is less significant and hence $\bar{K}_g \approx K_v$ (at the points $V_f \approx 0.56$ in Fig. 2.26). Higher pressure can always help to get more accurate K_v. Theoretically, sliding effect does not depend on permeability but depends on the micro-structures of porous media, this phenomenon is also revealed in experiments (Fig. 2.27), and Klinkenberg parameter b of the cylindrical *tubes* is usually higher than *granular* porous media or *woven* fabric.

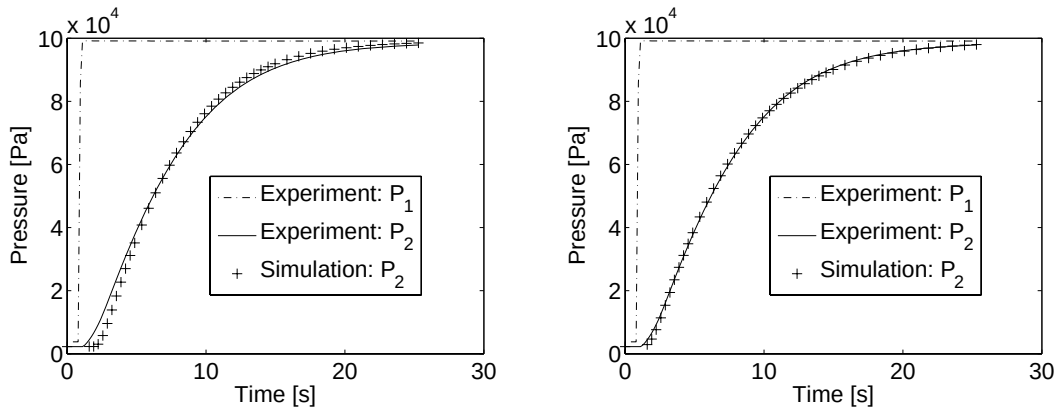

(a) Darcy's law, $\varepsilon = 2.2\%$, $\bar{K_g} = 1.7 \times 10^{-12}$ m^2 (b) Sliding model, $\varepsilon = 0.6\%$: $K_\infty = K_v = 9.3 \times 10^{-13}$ m^2; $K_m = 5.5 \times 10^{-6}$ m, $b = 0.5 \times 10^5$ Pa.

Fig. 2.24: Comparison between experimental and simulation pressures P_2 using Darcy's law (a) and sliding model (b), in RPM for CUD preforms in the direction parallel to the fibers at 60.8% fibre volume fraction.

Results of experiments using two types of gases and four types of loading patterns are compared (permeability obtained by Darcy's model) in Fig. 2.28. Results using air and nitrogen show slight difference. Permeability obtained by different loading patterns at high V_f shows a bigger scatter than those at low V_f.

2.5.2.4 K_g/K_v values with respect to optimization error

For CBD and CUD$\perp$, the loading pressures exceed the range of pressure sensors, because the sensor range is 0-1 bar absolute. Hence there is a truncation at the top of the loading curves, which brings more error and disturbs the back-calculations on b. For CTW, the loading pressure rises gradually, and hence the effect of truncation is not significant. For CUD$_{||}$, the back-calculation error based on Darcy's model is mostly due to sliding effect (Fig. 2.29).

2.5.2.5 Klinkenberg parameter b

For a tube, theoretical values of K_v and K_m predicted by Mason [13] are available, (Eqs. 1.29 and 1.19), from which b can be deduced,

$$b = \frac{32\sqrt{2}}{3} K_v^{-0.5} \tag{2.48}$$

A comparison of b related to K_v for different structures shows that the way b depends on K_v is determined by the local microstructure (Fig. 2.27: tube by Mason's theoretical prediction [13], granular media revealed from experiments on soils and

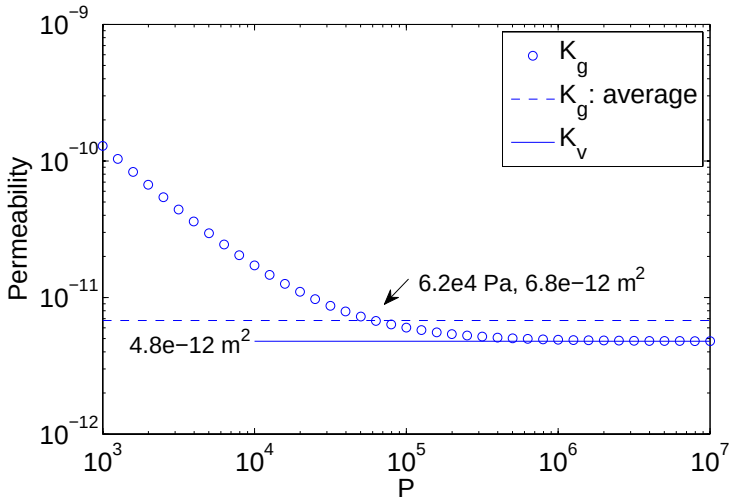

(a) $V_f = 55\%$

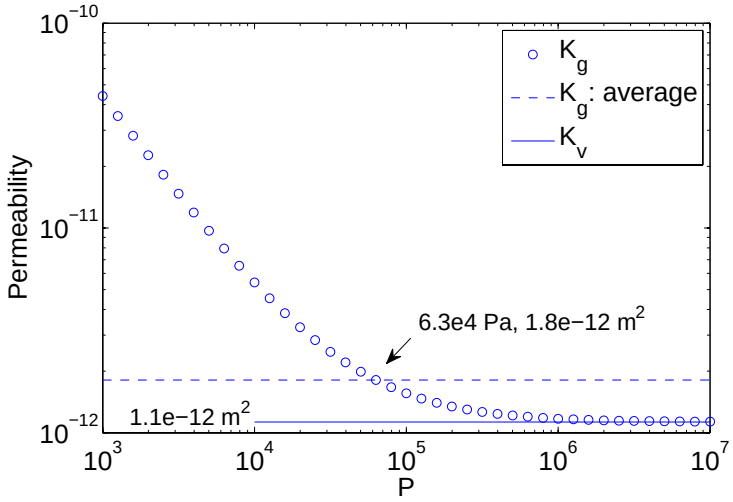

(b) $V_f = 60\%$

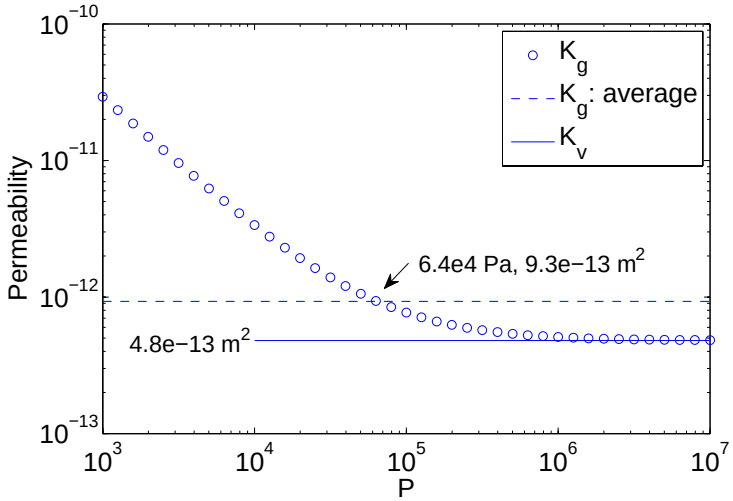

(c) $V_f = 67\%$

Fig. 2.25: The apparent permeability (K_g) compared to viscous permeability (K_v) for $\text{CUD}_{||}$.

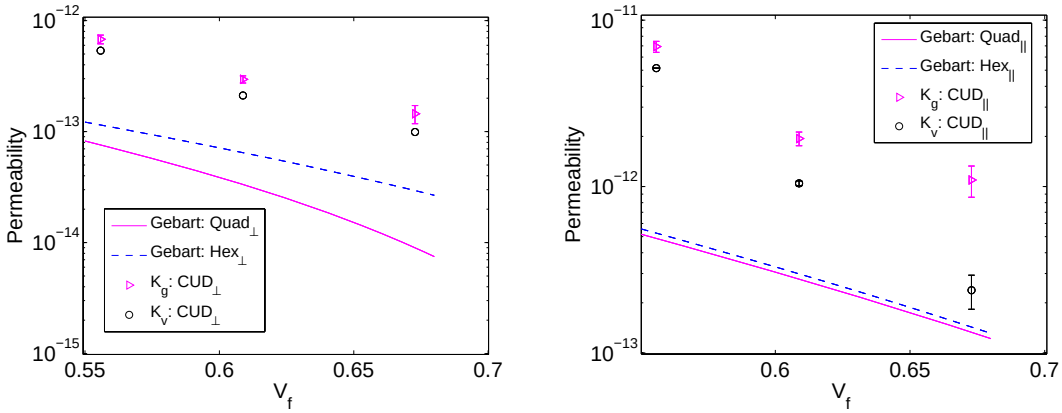

(a) $CUD_{\perp}$ (b) $CUD_{||}$

Fig. 2.26: Comparison of permeability obtained by transient gas measurements (with Darcy or sliding model) and Gebart's models [10].

rocks by Jones and Owens [35], and fibrous media from experiments of the present study). The b Klinkenberg coefficients obtained for the fibrous materials of the study lies between the 2 extreme cases of tubular and granular microstructures; for $CUD_{||}$ (CUD in the direction parallel to fibers), of which the micro-structures can be considered roughly as parallel irregular "tubes" between fibers (Fig. 2.30), the relationship of b and K_v is close to the one for tubular micro-structures . Also, Klinkenberg coefficient is a tensor ($\boldsymbol{b}$) for anisotropic micro-structures (micro-scope pictures shown in Fig. 2.30), *i.e.*, b of $CUD_{\perp}$ is much lower than $CUD_{||}$ for a sample with the same volume fraction V_f.

Fig. 2.27 can also show flow regimes: viscous flow dominates when b is smaller than 3×10^3 Pa and becomes undetectable. Sliding model can explain this clearly: once $b \ll P$, the sliding term in Eq. 1.31 is negligible. On the contrary, when b is much larger than the maximum loading pressure (such as 1×10^6 Pa in DPM using atmosphere pressure as the initial pressure), Darcy's flow term is negligible and Knudsen flow dominates, and hence K_v will be undetectable experimentally. According to Klinkenberg's model (Eq. 1.31), once b is estimated, the flow regime can be determined by a comparison between b and experimental pressures.

2.5.3 Effect of preforming

Bidirectional stitched carbon fabrics (CBD) are spread out with a powder on the surface. After consolidation of preforms (laid in an oven under vacuum to melt the powder), values of permeability are remarkably increased (Fig. 2.31). For high V_f, it means that the dry powder (unconsolidated) hinders the flow, whereas once

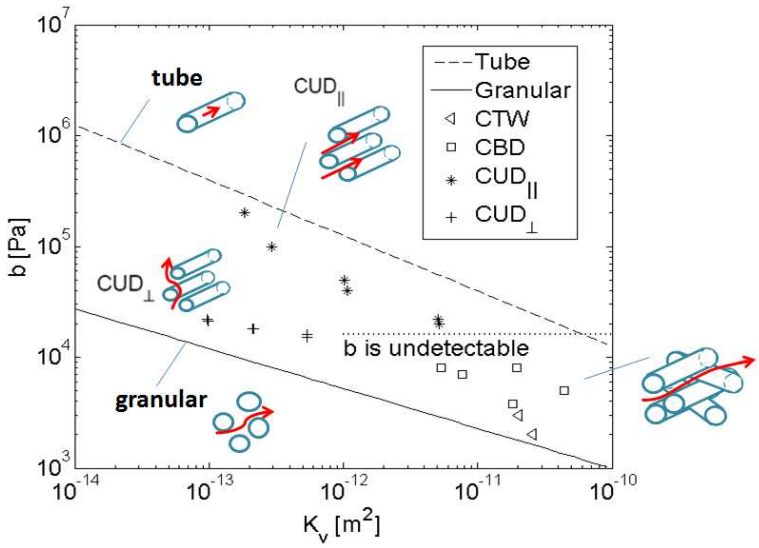

Fig. 2.27: Comparison of the coefficient b related to K_v for the materials of the study.

molten and re-solidified, the flow is eased. Micro-tomographies should be employed to verify this fact. For low V_f, the high values of permeability (consolidated) are due to the fact that the cavity thickness is slightly greater than the preform thickness and creates a thin gap, therefore race-tracking occurs.

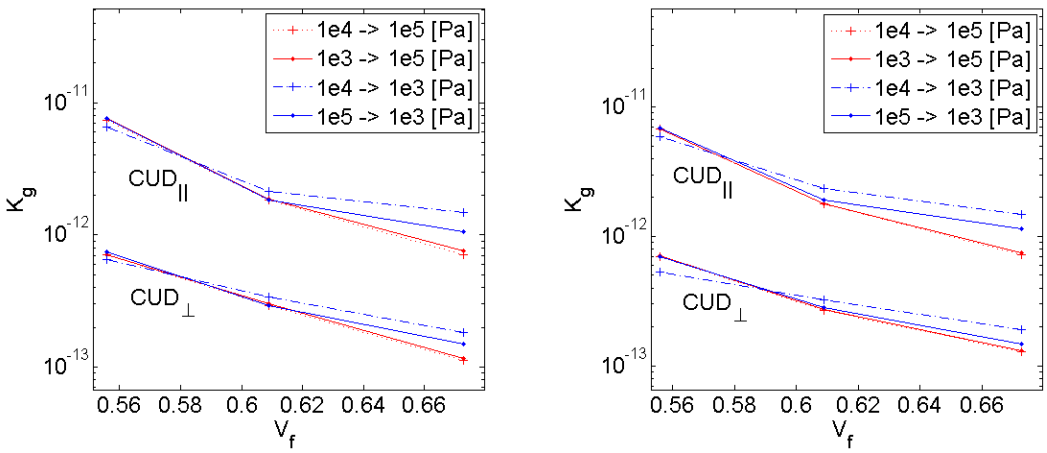

(a) Air (b) Nitrogen

Fig. 2.28: Results of experiments using two types of gases and four types of loading patterns (the permeability is obtained by Darcy's model).

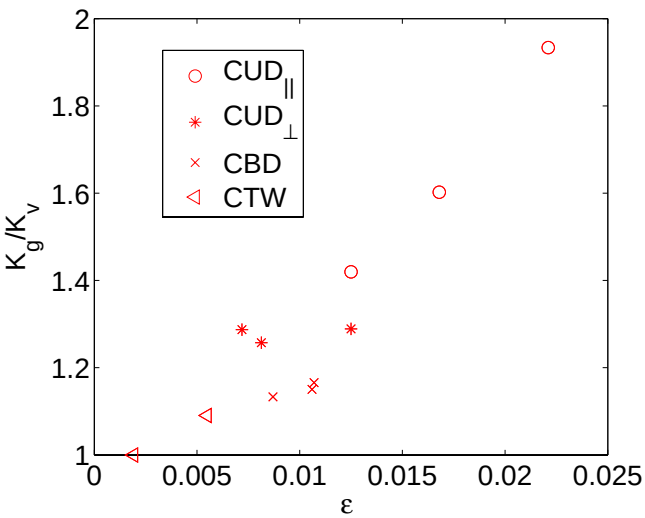

Fig. 2.29: K_g/K_v with respect to the calculation error

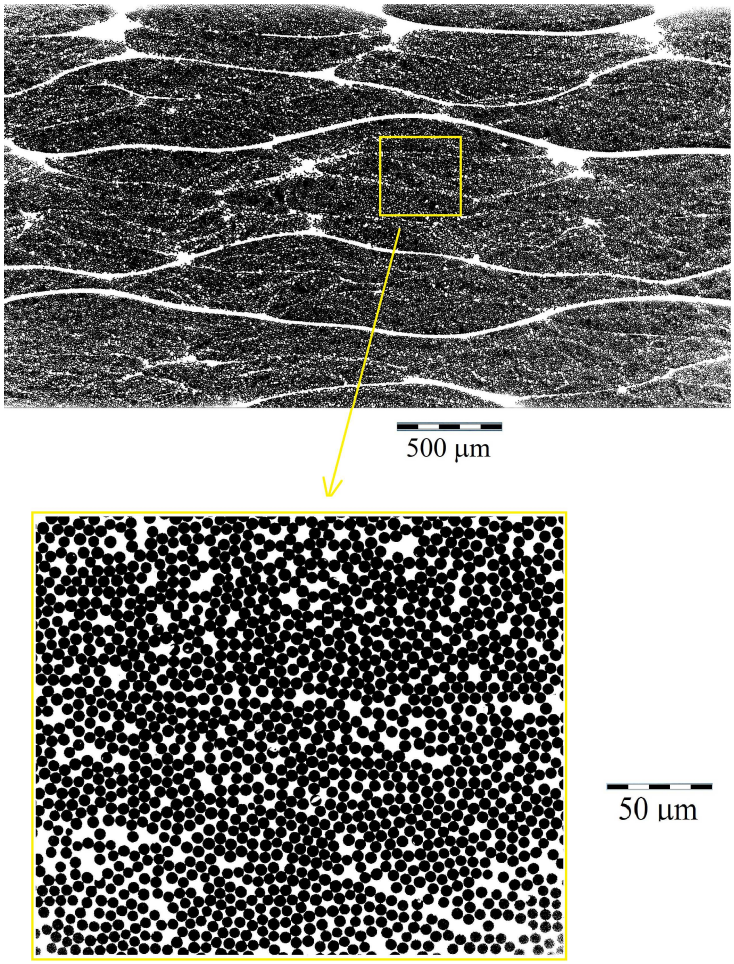

(a) Micro-structure perpendicular to the fiber direction

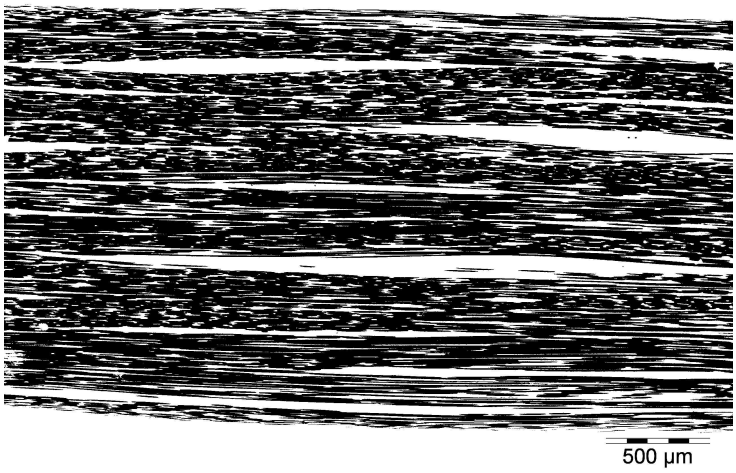

(b) Micro-structure parallel to the fiber direction

Fig. 2.30: The micro-scope pictures of CUD (a) section perpendicular to the fiber direction (b) section parallel to the fiber direction.

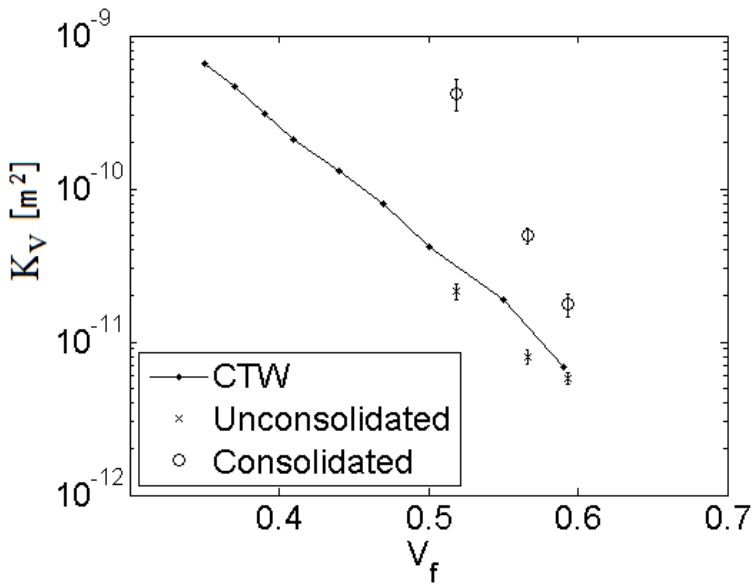

Fig. 2.31: Comparison of permeability K_v after consolidation of CBD (a curve of CTW is shown for a comparison).

2.6 Sources of error

The error in measurements can be caused by various factors, such as atmosphere temperature change, pressure variation, inaccuracy of dimensions and placement of samples. Tab. 2.4 summaries the error caused by the inaccuracy of recorded parameters X, the accuracy and the effect on measurement error. The details will be introduced in the following subsections.

Recorded parameters X	Accuracy dX	Relative dX/X	Effect factor $(\partial K_v/\partial X)/(K_v/X)$	Error dK_v/K_v
ΔT	0.5[K]	0.2%	0.55	0.1%
ΔV	2[cm^3]	10%	< 1	10%
ΔA	$1\times$ 0.1[mm^2]	5%	< 1	5%
Δh	0.1[mm]	5%	< 1	5%
ΔL	1[mm]	0.5%	< 2	1%
ΔP	1000[Pa]	1%		15%
α	$\pi/18$	1%		5%

Table 2.4: Error of measurement

2.6.1 The fabric's misalignment for unidirectional carbon fabric (CUD)

Assuming there is a misalignment angle α between the flow direction and the principal direction of permeability of interest K_1 (illustrated in Fig. 3.1 and detailed in Chapter 3), the obtained permeability K_1^{opt} should be effected by the other permeability K_2, which lays perpendicular to the flow direction. In order to analyze the effect of α, consider a set of permeabilities obtained from transient air measurements (introduced in this thesis) of the anisotropic fabrics CUD: $K_1 = 8.93 \times 10^{-13}\text{m}^2$ and $K_2 = 1.28 \times 10^{-13}\text{m}^2$. Let α be $\pi/18$ (*i.e.,* 10°), a 2D model based on 1D set-up (see Chapter 3) will be used to back-calculate K_1^{opt} with K_2 and α provided. The obtained K_1^{opt} is $K_x = 9.05 \times 10^{-13}\text{m}^2$, so when there is a misaligned angle $\alpha = \pi/18$, the obtained permeability will be underestimated by 1.3%. In another case, when K_2 is much bigger than K_1 such as $K_2 = 1.28 \times 10^{-13}\text{m}^2$ and $K_2 = 8.93 \times 10^{-13}\text{m}^2$, the obtained permeability could be overestimated by 5% when $\alpha = \pi/18$.

For CTW and GTW fabrics, the effect will be quite small and can be ignored.

2.6.2 Boundary condition

Among all the factors intrinsic to the physic, those concerning the trapped gas at the boundary are the most important ones. The empirical relationship Eq. 2.28 (Page. 63) helps estimate the error caused by inaccurate values of volume of the trapped gas at the boundaries,

$$\frac{\partial K_v}{\partial V} = \left(1 + \frac{1}{C_k V/AL\phi}\right)^{-1} \frac{K_v}{V} \tag{2.49}$$

and sectional area of gas flow through porous media,

$$\frac{\partial K_v}{\partial A} = -\left(1 + \frac{1}{C_k V/AL\phi}\right)^{-1} \frac{K_v}{A} \tag{2.50}$$

2.6.3 Cavity thickness

One-dimensional flow through porous media is ensured by constant sample thickness, which is controlled by 4 sets of steel shims at the four sides of the apparatus. The accuracy of the thickness is below 0.1mm, the length and width of samples are around 0.2m, and hence the thickness deflection is less than 0.05%, so the deviation from one-dimensional flow caused by thickness change is neglected. Although thickness h will not be used directly in one-dimentional flow simulation, h would

change the porosity ϕ which subsequentially changes K_v according to the linear relationship between K_v and $V/A\phi$ (Eq. 2.28),

$$\frac{\partial K_v}{\partial \phi} = -\left(1 + \frac{1}{C_k V/AL\phi}\right)^{-1} \frac{K_v}{\phi} \tag{2.51}$$

and since the porosity of sample is estimated by areal weight of the fabric W_f, number of layers N_p, density of fiber material, and thickness of the sample h according to the relationship Eq. 2.44, the error of permeability caused by preform thickness h can be determined as,

$$\frac{\partial K_v}{\partial h} = -\left(1 + \frac{1}{C_k V/AL\phi}\right)^{-1} \frac{1-\phi}{\phi} \frac{K_v}{h} \tag{2.52}$$

2.6.4 Length of sample

The length of sample L is around 0.20m. The effect of ΔL consists of two parts: the length of flow field and the boundary condition. The first part can be estimated by the fundamental equation of 1D Darcy's flow (Eq. 2.16), which shows $(K_v + \Delta K_v)/K_v = [(L+\Delta L)/L]^2$; the second part is difficult to deduce from the boundary condition Eq. 2.27, but can be estimated by the empirical relationship Eq. 2.28. Hence, $K_v + \Delta K_v$ can be obtained by a multiplication of both effects,

$$(K_v + \Delta K_v)/K_v = \left(1 + \frac{\Delta L}{L}\right)^2 \left(1 + \frac{C_k \frac{V}{A\phi}\left(\frac{1}{L+\Delta L} - \frac{1}{L}\right)}{1 + C_k \frac{V}{AL\phi}}\right) \tag{2.53}$$

and $\Delta K_v/K_v$ is estimated as,

$$\frac{\Delta K_v}{K_v} = \left(1 + \frac{1}{1 + C_k V/AL\phi}\right) \frac{\Delta L}{L} \tag{2.54}$$

which reveals that ΔK reaches its maximum when V/A equals to zero, or the boundary condition is ideal. Hence the upper bound of $\Delta K/K$ is two times $\Delta L/L$. Eq. 2.54 can also be written as,

$$\frac{\partial K_v}{\partial L} = \left(1 + \frac{1}{1 + C_k V/AL\phi}\right) \frac{K_v}{L} \tag{2.55}$$

As an example, for a series of experimental data for GTW at $V_f = 51\%$, where the sample length $L = 0.18$m and trapped volume fraction $V/A = 0.3$, the back-calculated permeability are used as a reference values. When a false sample length $L = 0.16$m is used, the back-calculated values of permeability will be amplified

with a ratio from 1.143 to 1.157 times, which varies slightly for various loading pressure curves, but still close to the estimated value 1.151 which can be given by Eq. 2.54.

2.6.5 Temperature

The temperature will not have direct effect on permeability, but will cause viscosity inaccuracy in simulation. The viscosity error can be estimated from the Sutherland's equation (Eq. 2.33),

$$\frac{\partial \mu}{\partial T} = \left(\frac{3}{2} - \frac{T}{T+C}\right)\frac{\mu}{T} \tag{2.56}$$

Since the ratio K_v/μ always appears in such a form in the fundamental equations and boundary conditions, one free variable $x_{p\mu} = K_v/\mu$ can be used instead. Therefore, when only the error on viscosity μ is considered, the sensitivity of the permeability with respect to the viscosity reads $\partial K_v/\partial\mu = d(x_{p\mu}\mu)/d\mu = x_{p\mu} = K_v/\mu$. It means that the temperature variation affects the back-calculated K_v since μ depends on temperature, in the following way,

$$\frac{\partial K_v}{\partial T} = \left(\frac{3}{2} - \frac{T}{T+C}\right)\frac{K_v}{T} \tag{2.57}$$

For room temperature, the ratio of the permeability error over the viscosity error is about 0.55. The temperature accuracy is 0.2%, so the corresponding permeability error is 0.1%, which is negligible in measurement and simulation.

2.6.6 Pressure variation

2.6.6.1 Effect on measured viscous permeability K_v

As mentioned in §2.4, P_I is the loading pressure and P_O is the output pressure. The inverse procedure consists in finding the proper K_v (or K_v, b) where the difference between P_{Oexp} and P_{Osim} reaches its minimum. To represent a series of P_{Oexp} over time, an Einstein notation i is used as a superscript. The simulated P_{Osim} is based on boundary condition P_{Iexp} and K_v.

Briefly, permeability K_v is back-calculated by minimizing the error $\varepsilon(P^i_{Oexp}, P^i_{Osim})$ (Eq. 2.45), where P^i_{Osim} is a function of P^i_{Iexp} and K_v. Hence P^i_{Oexp}, P^i_{Iexp} and K_v are the 3 independent variables which will effect ε, and the partial derivatives are

written as,

$$\frac{\partial \varepsilon}{\partial P^i_{Oexp}} = \frac{1}{\varepsilon N P_a^2}(P^i_{Oexp} - P^i_{Osim}) \tag{2.58a}$$

$$\frac{\partial \varepsilon}{\partial P^i_{Osim}} = \frac{1}{\varepsilon N P_a^2}(P^i_{Osim} - P^i_{Oexp}) \tag{2.58b}$$

and,

$$\frac{\partial \varepsilon}{\partial K_v} = \frac{1}{\varepsilon N P_a^2}\frac{\partial P^i_{Osim}}{\partial K_v} \tag{2.59a}$$

$$\frac{\partial \varepsilon}{\partial P^i_{Iexp}} = \frac{1}{\varepsilon N P_a^2}(P^i_{Osim} - P^i_{Oexp})\frac{\partial P^j_{Osim}}{\partial P^i_{Iexp}} \tag{2.59b}$$

where Einstein notation is used instead ($x^i y^i = \Sigma_{i=1}^N x^i y^i$), and this notation will be maintained in the rest of thesis. Permeability is determined upon the satisfaction of the relationship,

$$f = \frac{\partial \varepsilon}{\partial K_v} = 0 \tag{2.60}$$

with the partial differentials (Eq. 2.58 and Eq. 2.59) substituted and a non-zero constant ($\varepsilon N P_a^2$) eliminated, the above function can be simplified as,

$$\widetilde{f} = (P^i_{Osim} - P^i_{Oexp})\frac{\partial P^i_{Osim}}{\partial K_v} = 0 \tag{2.61}$$

In a case when P^i_{Oexp} have an error ΔP^i_{Oexp} caused by experimental measurement, the input variables are P^i_{Oexp} and K_v is back-calculated based on P^i_{Oexp} and P^i_{Iexp} are accurate and considered to be constant. The error ΔK_v is estimated by,

$$\Delta K_v = \frac{\partial K_v}{\partial P^i_{Oexp}}\Delta P^i_{Oexp} \tag{2.62}$$

where $\partial K_v / \partial P^i_{Oexp}$ can be calculated by partial derivation of $\widetilde{f}$ (Eq. 2.67).

$$\begin{aligned}\frac{\partial K_v}{\partial P^i_{Oexp}} &= -\frac{\partial \widetilde{f}}{\partial P^i_{Oexp}}\left(\frac{\partial \widetilde{f}}{\partial K_v}\right)^{-1} \\ &= \frac{\partial P^i_{Osim}}{\partial K_v}\left[\left(\frac{\partial P^j_{Osim}}{\partial K_v}\right)^2 + (P^k_{Osim} - P^k_{Oexp})\frac{\partial^2 P^k_{Osim}}{\partial K_v^2}\right]^{-1}\end{aligned} \tag{2.63}$$

where P^i_{Osim} is simulated with input K_v and P^I_{iexp}, and the corresponding partial derivatives are calculated as,

$$\frac{\partial P^i_{Osim}}{\partial K_v} = \frac{P^i_{Osim}|_{K_v+\Delta K_v} - P^i_{Osim}|_{K_v-\Delta Kv}}{2\Delta K_v} \tag{2.64a}$$

$$\frac{\partial^2 P^k_{Osim}}{\partial K_v^2} = \frac{P^i_{Osim}|_{K_v+\Delta K_v} + P^i_{Osim}|_{K_v-\Delta Kv} - 2P^i_{Osim}|_{K_v+\Delta K_v}}{\Delta K_v^2} \tag{2.64b}$$

where ΔK_v should be larger than 0.1% of K_v to reduce the effect of truncation error in numerical simulation.

The obtained $\partial K_v/\partial P^i_{Oexp}$ will be a series of values. In order to check the error caused on K_v, a certain series of pressure error should be provided. An assumed constant pressure error $\Delta P^i_{Oexp} = 1000$Pa is applied to the experimental values of each point (Eq. 2.62), the error on K_v is calculated. The other error patterns can be tested similarly.

In order to verify the results, permeability is back-calculated for a RPM test on CTW sample with a loading pressure P_{Iexp} from 1×10^4 to 1×10^5Pa. The calculated $\Delta K_v/K_v$ is within 12%. Some results for measurements in Fig. 2.32 are shown in Tab. 2.5. Slower flow rate will introduce more error in the back-calculation; for DPM with a loading pressure from 1×10^4Pa to 1×10^3Pa in order to check the sliding effect at low pressure, since the error becomes extremely high (50%), the observation becomes unreliable; for most of the tests in the study, the error is less than 10%. Low permeability usually can create a big difference between the pressures at both sides P_1 and P_2, and hence have less back-calculation error; while for high permeability, the error can be reduced by increasing the flow rate.

Material(V_f)	$K_v[\times 10^{-11}\text{m}^2]$	Loading pattern [Pa]	$\Delta K_v/K_v$	Fig.
CTW (44%)	10.1	$1 \times 10^4 \rightarrow 1 \times 10^5$	29%	Fig. 2.32(a)
CTW (44%)	9.41	$1 \times 10^4 \rightarrow 1 \times 10^5$	12%	Fig. 2.32(b)
CTW (44%)	7.68	$1 \times 10^4 \rightarrow 1 \times 10^3$	55%	Fig. 2.32(c)
CTW (44%)	9.52	$1 \times 10^5 \rightarrow 1 \times 10^3$	3%	Fig. 2.32(d)
CTW (47%)	5.00	$1 \times 10^4 \rightarrow 1 \times 10^5$	11%	Fig. 2.32(e)
CTW (55%)	2.21	$2 \times 10^3 \rightarrow 1 \times 10^5$	5.3%	Fig. 2.32(f)

Table 2.5: The error on back-calculated permeability caused by the pressure inaccuracy (pressure curves of the first 4 tests are shown in Fig. 2.32).

2.6.6.2 Effect on the Klinkenberg parameter b

The Klinkenberg parameter b is back-calculated by minimizing the error $\varepsilon(P^i_{Oexp}, P^i_{Osim})$ (Eq. 2.45), where P^i_{Osim} is the function of P^i_{Iexp} and $[K_v, b]$. Starting from the par-

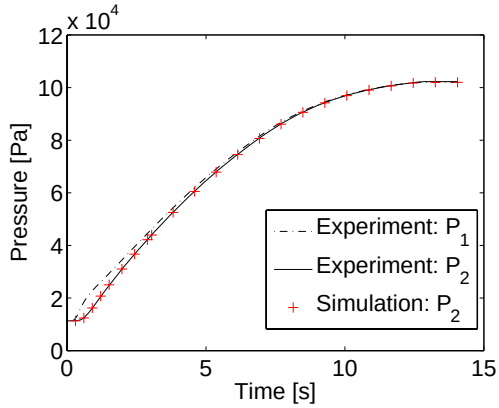

(a) $K_v = 1.01_{\pm 29\%} \times 10^{-10}\mathrm{m}^2$, $V_f = 44\%$

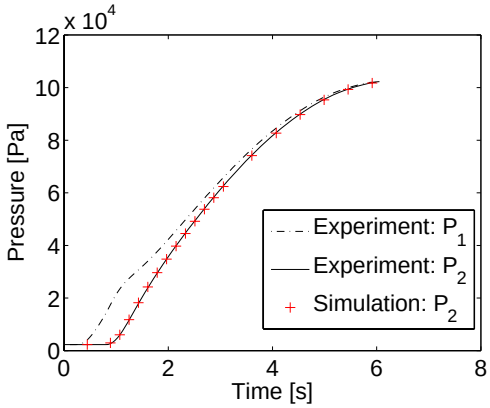

(b) $K_v = 9.41_{\pm 12\%} \times 10^{-11}\mathrm{m}^2$, $V_f = 44\%$

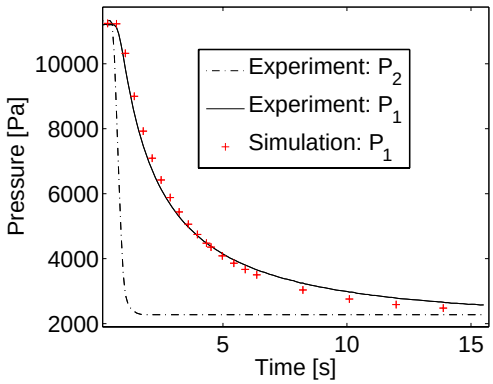

(c) $K_v = 7.68_{\pm 55\%} \times 10^{-11}\mathrm{m}^2$, $V_f = 44\%$

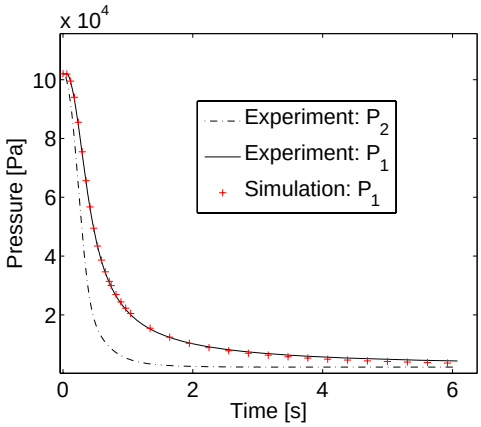

(d) $K_v = 9.52_{\pm 3\%} \times 10^{-10}\mathrm{m}^2$, $V_f = 44\%$

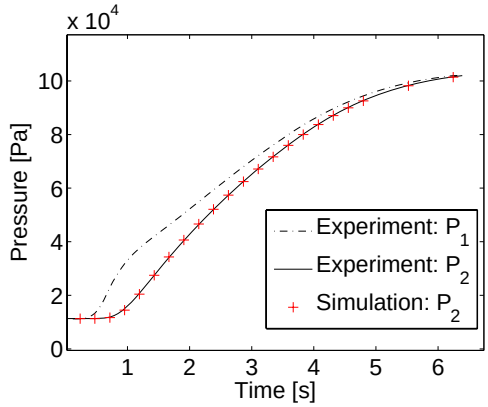

(e) $K_v = 5.00_{\pm 11\%} \times 10^{-11}\mathrm{m}^2$, $V_f = 47\%$

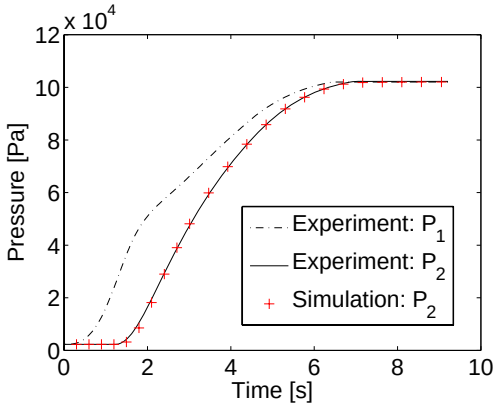

(f) $K_v = 2.21_{\pm 5\%} \times 10^{-11}\mathrm{m}^2$, $V_f = 55\%$

Fig. 2.32: Pressure curves of CTW with different loading pressure. The error of K_v is calculated using Eq. 2.63 for a constant pressure error (results shown in Tab. 2.5).

tial derivatives in Eq. 2.58,

$$\frac{\partial \varepsilon}{\partial b} = \frac{1}{\varepsilon N P_a^2} \frac{\partial P_{Osim}^i}{\partial b} \tag{2.65a}$$

$$\frac{\partial \varepsilon}{\partial P_{Iexp}^i} = \frac{1}{\varepsilon N P_a^2} (P_{Osim}^i - P_{Oexp}^i) \frac{\partial P_{Osim}^j}{\partial P_{Iexp}^i} \tag{2.65b}$$

where Einstein notation is used instead ($x^i y^i = \Sigma_{i=1}^N x^i y^i$). Permeability is determined upon a satisfaction of the relationship below,

$$f = \frac{\partial \varepsilon}{\partial b} = 0 \tag{2.66}$$

which can be simplified since $\varepsilon N P_a^2 \neq 0$,

$$\widetilde{f} = (P_{Osim}^i - P_{Oexp}^i) \frac{\partial P_{Osim}^i}{\partial b} = 0 \tag{2.67}$$

In a case when P_{Oexp}^i have an error ΔP_{Oexp}^i caused by measurement inaccuracies, and P_{Iexp}^i are accurate and considered to be constant. The input variables are P_{Oexp}^i and K_v is back-calculated based on P_{Oexp}^i. The error ΔK_v is estimated by,

$$\Delta K_v = \frac{\partial K_v}{\partial P_{Oexp}^i} \Delta P_{Oexp}^i \tag{2.68}$$

where $\partial K_v / \partial P_{Oexp}^i$ can be calculated by partial derivation of $\widetilde{f}$ (Eq. 2.67).

$$\begin{aligned} \frac{\partial b}{\partial P_{Oexp}^i} &= -\frac{\partial \widetilde{f}}{\partial P_{Oexp}^i} \left(\frac{\partial \widetilde{f}}{\partial b} \right)^{-1} \\ &= \frac{\partial P_{Osim}^i}{\partial b} \left[\left(\frac{\partial P_{Osim}^j}{\partial b} \right)^2 + (P_{Osim}^k - P_{Oexp}^k) \frac{\partial^2 P_{Osim}}{\partial b^2} \right]^{-1} \end{aligned} \tag{2.69}$$

where P_{Osim}^i is simulated with input b and P_{Iexp}^i, and the corresponding partial derivatives are calculated as,

$$\frac{\partial P_{Osim}^i}{\partial b} = \frac{P_{Osim}^i|_{b+\Delta b} - P_{Osim}^i|_{b-\Delta b}}{2\Delta b} \tag{2.70a}$$

$$\frac{\partial^2 P_{Osim}^k}{\partial b^2} = \frac{P_{Osim}^i|_{b+\Delta b} + P_{Osim}^i|_{b-\Delta b} - 2P_{Osim}^i|_{b+\Delta b}}{\Delta b^2} \tag{2.70b}$$

where Δb should be larger than 0.1% of b to reduce the effect of truncation error in the numerical simulation.

2.6.7 Overall error sources

As a conclusion, the error sources from 2 parts,

- Model assumptions: deviation from isothermal flow cause viscosity variation less than 1% and hence permeability error less than 1%, which can be neglected; Renolds' number is always less than 0.1 and the non-Darcian effect such as described in Forchheimer equation is not considered for gas transport here; sliding effect is important and should be verified with Knudsen number.
- Experimental measurements: the most important factors are the gas volume trapped at boundary and pressure sensor accuracy.

Generally the measurement using transient gas flow gives a variation coefficient less than 25% with a proper model considered.

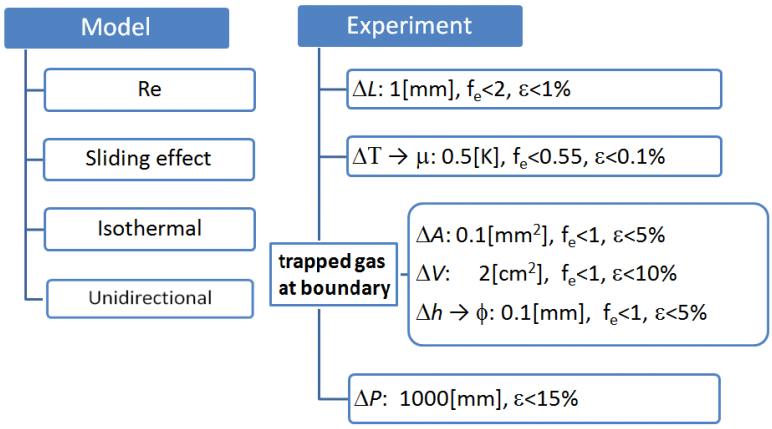

Fig. 2.33: The error sources in 1D permeability measurement methods.

2.7 Conclusions

A methodology to measure fabric in-plane permeability using a transient air flow has been described. The method, based on the simple measurement of gas pressure throughout the transient flow, is convenient, clean and fast, avoids usage of a gas flow meter and offers a way to study the air transport within porous media.

The equipment described here has been used to measure permeability from 10^{-10}m^2 to 10^{-14}m^2. The results match well the permeability measured with liquid techniques (compression and injection), but there are several factors which should be checked carefully.

The first one is gas compressibility, which is sometimes neglected but has to be considered under a high pressure gradient [76]. Since pressure changes from

3000 to 10^5Pa, compressibility becomes very important. Fundamental equations and boundary conditions for gas flow in fibrous media have been proposed. At the boundary where gas flow is cut off by a closed valve, a slight flux could exist due to compressibility of the gas trapped between the sample and valve. This could change the overall gas flow field of the sample, leading to a significantly underestimated permeability. To estimate the error of permeability ignoring gas compressibility at the boundaries, an empirical relationship of the permeability related to trapped gas volume and cross-section area of gas flow is proposed.

The second one is thermal effect. An isothermal process is assumed in the work, while in real case the temperature variation at the boundaries could be up to 3% with a maximum pressure changing rate $P' = dP/dt \approx 2 \times 10^5$Pa/s. The temperature variation will introduce a different BC from the model, and hence changes permeability. This problem happens when permeability is high and hence experimental time is short, so it is better to keep the pressure dropping or rising rate lower than 5×10^4Pa/s to avoid any thermal effects.

The third one is the sliding effect. Darcy's law for viscous flow can be applied to air flow through fabric with larger pore size and higher pore pressure. While for smaller pore size and lower pore pressure, gas molecules slides on pore walls. The sliding effect, also called Klinkenberg effect [34, 36, 111], reveals a dependence of apparent permeability on pressure in porous media. In rocks and soils, the Klinkenberg effect is considered important when permeability is lower than 10^{-18}m^2 [111], while in this study, the Klinkenberg effect is important although the permeability is much higher since the loading pressure is low, which could be explained by Knudsen theory. Also in this measurement it is possible to capture small sliding effect. Since klinkenberg parameter b and permeability K_v are obtained in one test, some sources of experimental error are avoided, such as micro-structures of porous media, temperature and humidity.

In experiments, the Klinkenberg parameter b is used here, since b is easy to measure and the ratio of b to P indicates the error caused by sliding effect. In permeability measurement using transient gas flow, gas sliding effect occurs, when b is higher than the vacuum pressure. When b is 10% of the highest pressure P_{max}, sliding model should be used instead of Darcy's model. If $b \gg P_{max}$, Knudsen flow will override viscous flow. Based on experiments of different fabrics, we proposed a relationship between b and K_v, which helps to design experiments or choose proper models. b in fibrous material is lower than the one from tubular structure and higher than the one from granular media with the same value of K_v. Hence an estimation about b could be made based on the type of porous media, and a comparison between b and the pore pressure could give indication on whether

Darcy's law fits the conditions or how much error exists between Darcy's law and the actual air flow. Also b shows a dependence on fibrous microstructure.

Once the flow is viscous, Re_ϕ is checked to ensure a Darcy's flow. Reynolds number of gas flow through fabrics tested in this study, and representative of usual fiber reinforcement of composite materials, is always lower than 1 since gas has quite low density and viscosity.

This measurement could be quite stable, once all the factors which affect permeability are fixed: such as dimensions of bench and sample, temperature and humidity.

CHAPTER 3

Measurement design using 2D transient gas flow

Abstract of Chap. 3

A 2D measurement using gas to obtain 2D permeability tensor in one single test is proposed, and two set-ups are discussed: one based on 1D measurement set-up with sample misalignment orientations considered, and the other designed to get rid of the issues of trapped gas at boundaries. Simulated experiments are carried out and the results show that the measurements based on points at three proposed locations could provide robust and accurate permeability determinations for fabrics of anisotropic permeability ratios (K_1 /K_2) ranging from 0.1 to 10, with various misalignment angles.

Résumé de Chap. 3

Une mesure 2D à l'aide d'un gaz a été mise en place pour déterminer le tenseur de perméabilité 2D en un seul test, et deux systèmes sont présentés: l'un basé sur la mesure 1D considérant des échantillons avec des orientations de désalignement, et l'autre visant à s'affranchir des problèmes de gaz piégés sur les bords. Des expériences simulées sont considérées et les résultats montrent que les mesures basées sur des points répartis sur trois positions pourraient permettre la détermination robuste et précise des perméabilités des préformes ayant des rapports d'anisotropie perméabilité (K_1 / K_2) allant de 0,1 à 10, avec quelconques angles de désalignement.

3.1 Introduction

2D or even 3D fiber preform permeability tensor can be determined in radial liquid saturating flow using an inverse algorithm based on sensors and simulation. For anisotropic materials, the 2D set-up is generally not suitable for saturated permeability measurement using liquid flow since the flow rate and pressure drop are not sufficient to determine 2 different permeability components. Another disadvantage of the traditional central injection method based on the direct observation of the flow front is that the flow front has to be visible [60, 71, 57, 63]. The contrast of the images or videos may not be good enough for resin through carbon fabric, and the transparent top plate (made of glass or plastic) which is usually of low bending stiffness, leads to non-uniform cavity thickness and thus to unproper measurements [57]. To overcome the mold deflection problem, the transparent top plate is often covered with a steel frame [99, 57, 71], but the visibility is then reduced. Also, sensors can be used instead of pictures to track the flow front, such as electrical based sensors, which implies an electrically conductive test-fluid and an isolated tested material [69, 70, 112]. This is a distributed measurement and the number of sensors should be large enough to cover the several directions and distance to record the flow front progression. In addition when the ratio of principal in-plane permeabilities, referred to as anisotropy ratio, exceeds 10, the sensors in one direction will be triggered only after all the sensors in the other direction are fully saturated. This will not provide sufficient information for permeability calculations [68].

For gas diffusion layers materials, the in-plane permeability is determined by forcing stationary air flow through an annulus sample and measuring the flow rate and pressure drop across the layers [8]. However this method is not suitable for anisotropic in-plane permeability. Um et al. [85] and Kim [86] proposed a method to estimate the permeability by measuring the nitrogen flow rate under constant inlet pressure and combining the results of two tests with different sets of vent locations.

This section chapter aims at building a measurement methodology for non-isotropic in-plane permeability characterization in one test, using two-dimensional transient gas flow. First, the idea of placing complementary pressure sensors in the existing 1D set-up will be studied regarding the accuracy of the identified 2D permeability. Then, a fully 2D design solution will be proposed to show the potential of inducing 2D flows in transient regime for permeability identification.

3.2 Anisotropic permeability measurement on 1D set-up

In permeability measurement using the 1D set-up (Fig 2.2), assume that a sample with anisotropic permeability is placed in the mold, with an angle α between the $\boldsymbol{e}_x$ flow direction and the principal direction $\boldsymbol{e}_1$ of the permeability, as shown in Fig. 3.1. The permeability tensor $\boldsymbol{K}$ is represented by a 2×2 symmetrical matrix in 2D $[K]_{(O,\boldsymbol{e}_x,\boldsymbol{e}_y)}$ in the $(O,\boldsymbol{e}_x,\boldsymbol{e}_y)$ reference frame of the apparatus, and its principal permeabilities are K_1 and K_2, related by :

$$\begin{aligned}
\boldsymbol{K} &= \begin{bmatrix} K_x & K_{xy} \\ K_{xy} & K_y \end{bmatrix}_{(O,\boldsymbol{e}_x,\boldsymbol{e}_y)} \\
&= \begin{bmatrix} C & -S \\ S & C \end{bmatrix}_{(O,\boldsymbol{e}_1,\boldsymbol{e}_2)\to(O,\boldsymbol{e}_x,\boldsymbol{e}_y)} \begin{bmatrix} K_1 & 0 \\ 0 & K_2 \end{bmatrix}_{(O,\boldsymbol{e}_1,\boldsymbol{e}_2)} \begin{bmatrix} C & S \\ -S & C \end{bmatrix}_{(O,\boldsymbol{e}_1,\boldsymbol{e}_2)\to(O,\boldsymbol{e}_x,\boldsymbol{e}_y)} \\
&= \begin{bmatrix} C^2K_1 + S^2K_2 & CS(K_1-K_2) \\ CS(K_1-K_2) & S^2K_1 + C^2K_2 \end{bmatrix}_{(O,\boldsymbol{e}_x,\boldsymbol{e}_y)}
\end{aligned} \tag{3.1}$$

where $C = \cos\alpha$ and $S = \sin\alpha$ define the projection matrix from the principal basis $(O,\boldsymbol{e}_1,\boldsymbol{e}_2)$ to the lab frame of reference $(O,\boldsymbol{e}_x,\boldsymbol{e}_y)$. Substituting $\boldsymbol{K}$ into Darcy's law,

$$\boldsymbol{q} = -\frac{1}{\mu}\begin{bmatrix} K_x & K_{xy} \\ K_{xy} & K_y \end{bmatrix}_{(O,\boldsymbol{e}_x,\boldsymbol{e}_y)} \cdot \nabla P = \frac{\boldsymbol{K}_v}{\mu}\cdot\nabla P \tag{3.2}$$

where K_{xy} is not equal to 0, and therefore the pressure drop in $\boldsymbol{e}_x$ direction will cause a gas flow in $\boldsymbol{e}_y$ direction. Also, the normal velocity should be zero at the upward and downward boundaries ($y = 0$ and $y = L_b$), which are sealed as shown in Fig 2.2. Hence the velocity must be inhomogeneous and non-linear, which means the misalignment of fabric with a forced 1D boundary condition leads to a 2D flow.

Simulations both in 1D and 2D will consist in solving Eq. 2.20, representing the combination of Darcy's law and mass conservation for viscous flow of a compressible fluid. Comsol will be used to discretize the problem and solve it by FE.

3.2.1 Boundary conditions for 2D computations

The boundary conditions for 1D gas flow are given in Eq. 2.27, while for 2D gas flow, the BC (boundary condition) equation in the other direction y should be

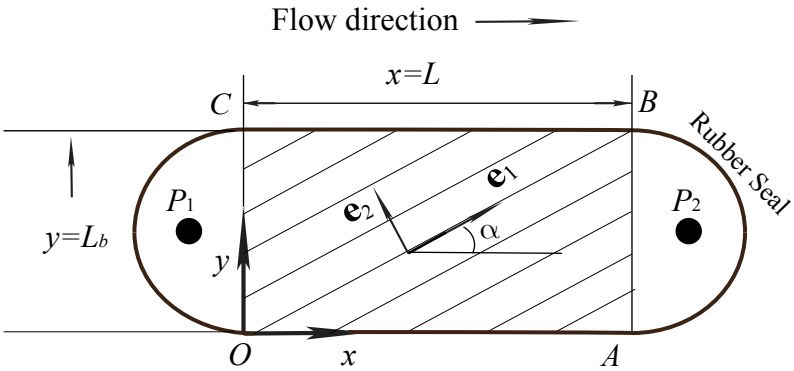

Fig. 3.1: The deviation angle α between the $\boldsymbol{e}_x$ direction (forced 1D flow direction) and the first principal direction of fabric permeability $\boldsymbol{e}_1$.

provided at the boundaries $y = 0$ and $y = L_b$,

$$\boldsymbol{q} \cdot \boldsymbol{n}|_{y=0} = \boldsymbol{q} \cdot \boldsymbol{n}|_{y=L_b} = 0 \tag{3.3}$$

The boundary $x = L$ is given a loading pressure $P(t)$ and the other boundary ($x = 0$) is connected to a closed valve. Considering that there is still gas trapped in the cavity at the boundary, BC equation $K_v/\mu(P\partial P/\partial x) - V/A(\partial P/\partial t) = 0$ at the boundary $x = 0$ (from 1D BC Eq. 2.27) are only valid for 1D simulations. For the present 2D numerical approach, in order to build an equivalent boundary condition, an extra isotropic medium with much higher permeability (1000 times the one of the sample) is attached to the sample edges to play the role of "trapped air" (Fig. 3.2). The width of this extra medium is set equivalent to V/A (ratio of trapped air volume and flow sectional area), and the corresponding boundary condition is,

$$\boldsymbol{q} \cdot \boldsymbol{n}|_{x=-V/A} = 0 \tag{3.4}$$

In order to validate this new BC, the pressure $P(t)$ at $x = (0, 0)$ in both 1D and 2D cases is computed for a 1D flow (that is, α equals to 0). The sample size is $0.2 \times 0.2\text{m}^2$; permeabilities are $K_1 = 1 \times 10^{-11}\text{m}^2$, $K_2 = 5 \times 10^{-12}\text{m}^2$. A pressure loading distribution $P(t)$ corresponding to GTW measurements in RPM conditons will be considered (Fig. 3.3), and if not specified, this loading pressure is also used for the following simulations.

The good match of the pressure curves obtained for 2 V/A ratios indicates that adding an extra medium with higher permeability in the 2D simulations can represent the effect of "trapped gas" (Fig. 3.3). Volume to sectional area ratio V/A

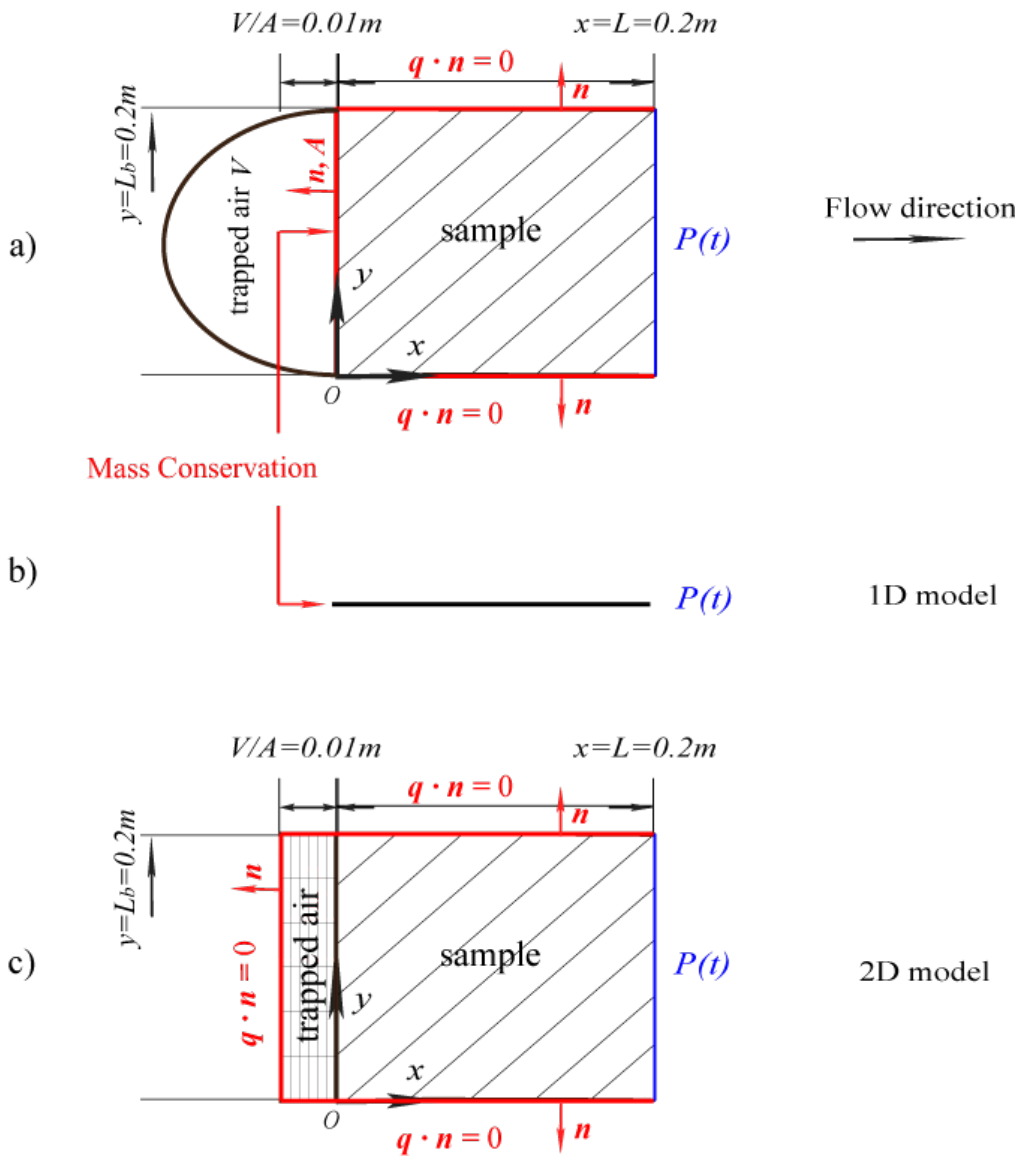

Fig. 3.2: The representative graphs of boundary conditions: (a) the physical case, (b) 1D model and (c) the equivalent boundary conditions for the 2D model.

is set to be 0.01 in the following simulations.

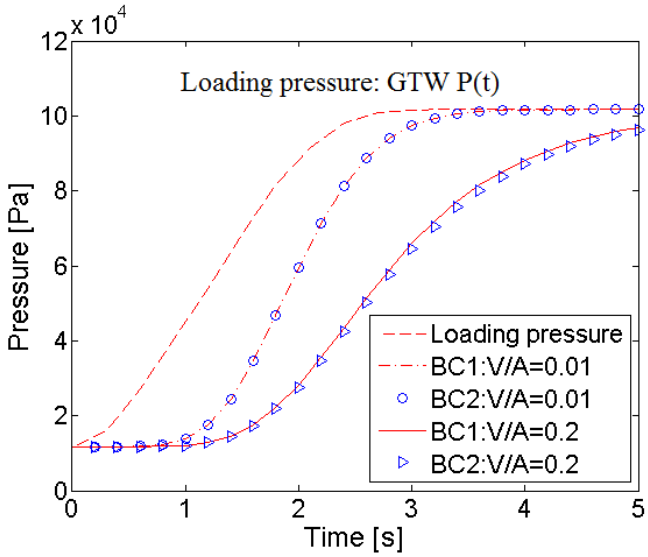

Fig. 3.3: BC1: modification in Eq. 2.27; BC2: attaching to the sample edge an extra medium of much higher permeability (1000 times the fabric permeability).

3.2.2 Pressure distributions

Fig. 3.4 and Fig. 3.5 show respectively the pressure distributions and the velocity fields of transient gas flow through anisotropic samples ($K_1 = 1 \times 10^{-11}\text{m}^2$, $K_2 = 5 \times 10^{-12}\text{m}^2$, and $\alpha \in [0.1; \pi/6; \pi/4; \pi/3]$) at the moment of time when pressure drop across the sample (difference between loading pressure and responses) reaches its maximum. During the flowing process, the pressure distribution is quite similar for a given sample, only the magnitude of pressure varies with time.

Analyzing pressure curves at several points will help to choose the best locations to place pressure sensors (Fig. 3.6). The pressure at point ① is the loading pressure at boundary $x = L$. Along boundary $x = 0$ pressure is always equivalent (curves of points ② and ③ coincide with each other). The deviation angle α leads to a pressure change over the flow cross-section (such as in points ④, ⑤ and ⑥). Since the difference between ① and ② is the largest among all the points, and that the pressure profiles difference due to α is significant over the middle cross-section, three locations ② (0,0), ④ (0.1,0.0), ⑥ (0.1,0.2) (corresponding to the middle points of the 3 edges except for the loading edge) are chosen to measure pressure data for back-calculation of the three parameters [K_1, K_2, α].

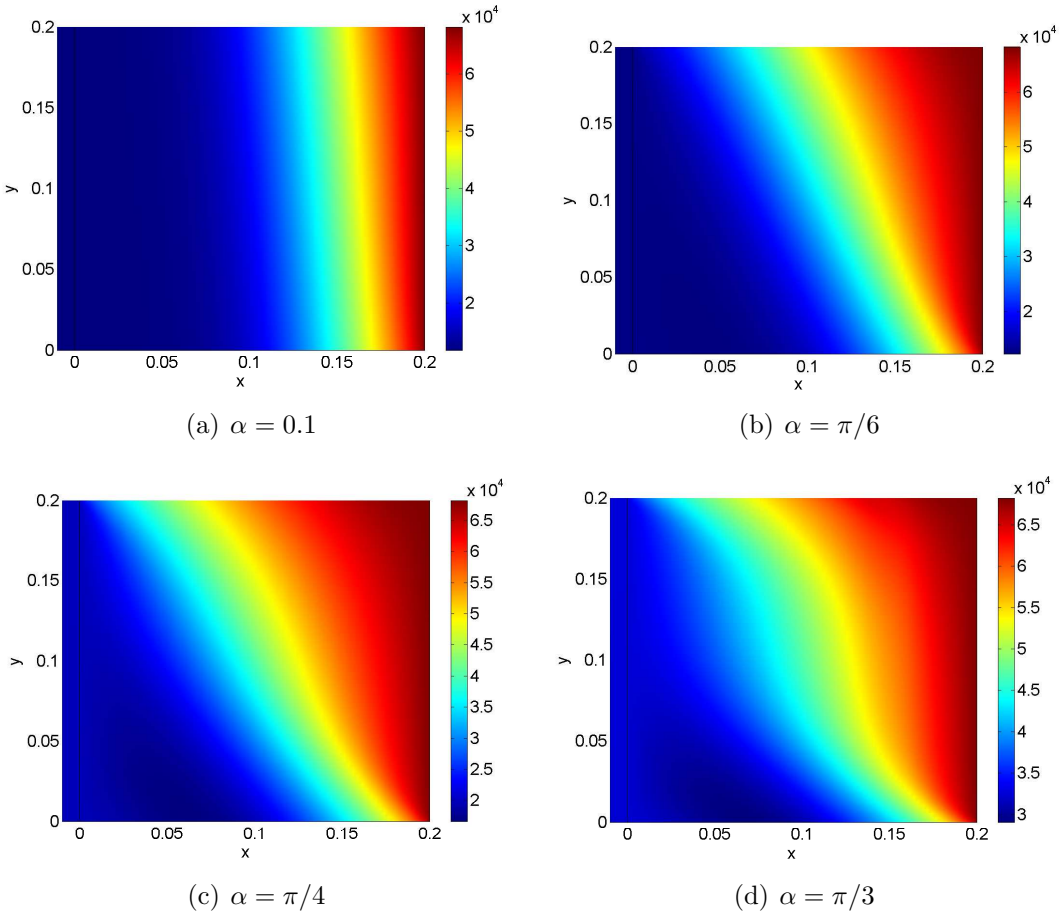

(a) $\alpha = 0.1$

(b) $\alpha = \pi/6$

(c) $\alpha = \pi/4$

(d) $\alpha = \pi/3$

Fig. 3.4: Pressure distributions of gas flow through samples where the principal permeability directions are deviated from the set-up directions; sample size is $0.2 \times 0.2\text{m}^2$; permeabilities are $K_1 = 2 \times 10^{-11}\text{m}^2$, $K_2 = 5 \times 10^{-12}\text{m}^2$.

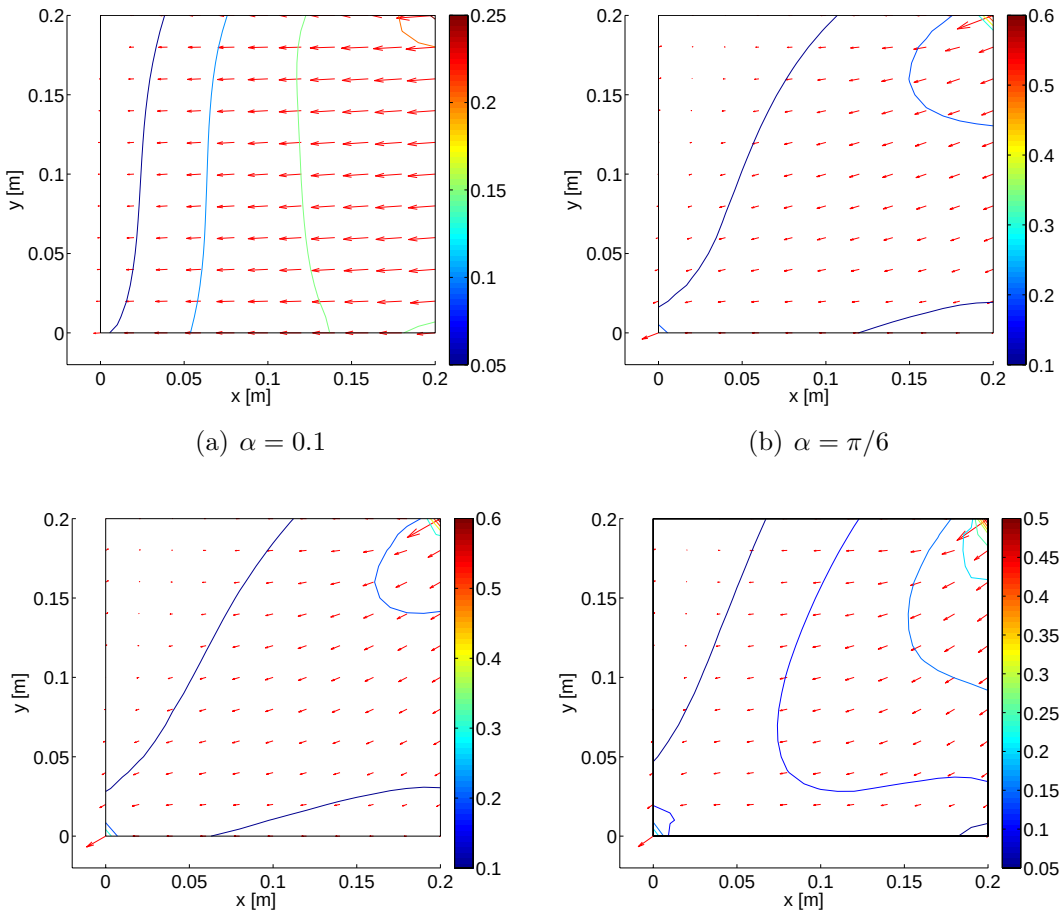

(a) $\alpha = 0.1$

(b) $\alpha = \pi/6$

(c) $\alpha = \pi/4$

(d) $\alpha = \pi/3$

Fig. 3.5: Gas flow velocity fields (m/s) through samples where the principal permeability directions are deviated from the set-up directions; sample size is $0.2 \times 0.2\text{m}^2$; permeabilities are $K_1 = 2 \times 10^{-11}\text{m}^2$, $K_2 = 5 \times 10^{-12}\text{m}^2$.

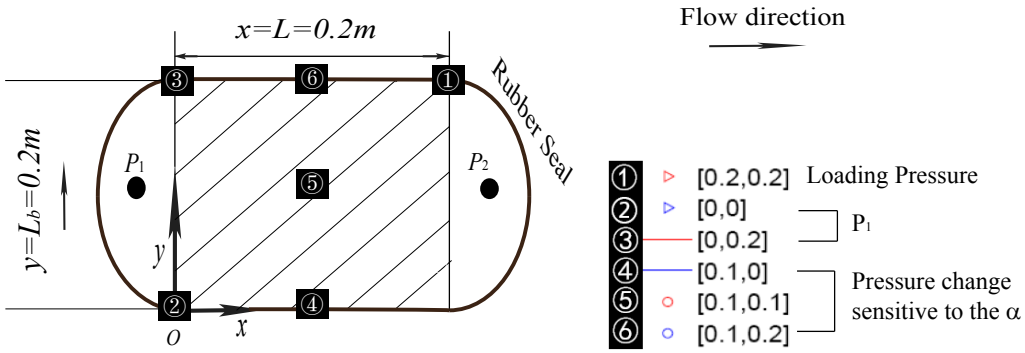

(a) Locations with pressure recorded

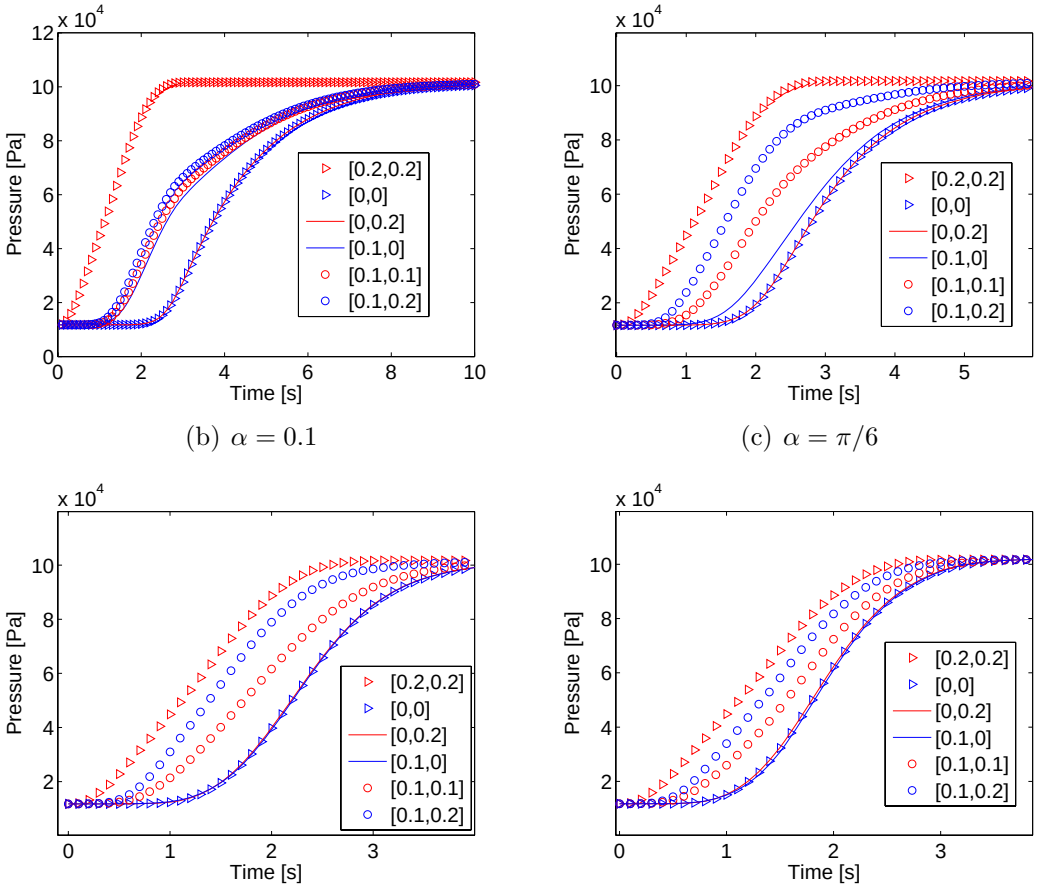

(b) $\alpha = 0.1$ (c) $\alpha = \pi/6$

(d) $\alpha = \pi/4$ (e) $\alpha = \pi/3$

Fig. 3.6: Pressure curves at several points for gas flow through samples with principal permeability directions deviated from the set-up directions. Sample size $0.2 \times 0.2\text{m}^2$; permeabilities $K_1 = 1 \times 10^{-11}\text{m}^2$, $K_2 = 5 \times 10^{-12}\text{m}^2$.

3.2.3 Back-calculations

For this 2D approach, "simulated experiments" will be considered as experimental measurements used in the back-calculation process. A 2D pressure field is generated using permeability data $[K_1', K_2', \alpha']$, and various combinations of virtual pressure sensors measurements are considered to assess this permeability measurement solution. Input permeability and angle values in "simulated experiments" are denoted by $(\cdot')$, in order to be distinguishable from those used in back-calculation processes.

There are two sets of variable available for the optimization process: $[K_1,\ K_2,\ \alpha]$ or $[K_x,\ K_y,\ K_{xy}]$. The Nealder-Mead method is used as an optimization method to search the local minimum solution of the fitting error ϵ, given as,

$$\epsilon = \frac{1}{P_a N'} \sum_{j=1}^{N'} \sqrt{\frac{1}{N} \sum_{i=1}^{N} \left(P_{Oexp}^{i} - P_{Osim}^{i}\right)^2} \tag{3.5}$$

where N' is the number of virtual output pressures and N is the number of data points on one pressure curve. Fig. 3.7 shows the distribution of fitting error over K_1 (varying from $0.05 \times 10^{-11}\mathrm{m}^2$ to $1.5 \times 10^{-11}\mathrm{m}^2$) and α (from $-\pi/9$ to $\pi/9$) with a fixed $K_2' = 1 \times 10^{-10}\mathrm{m}^2$.

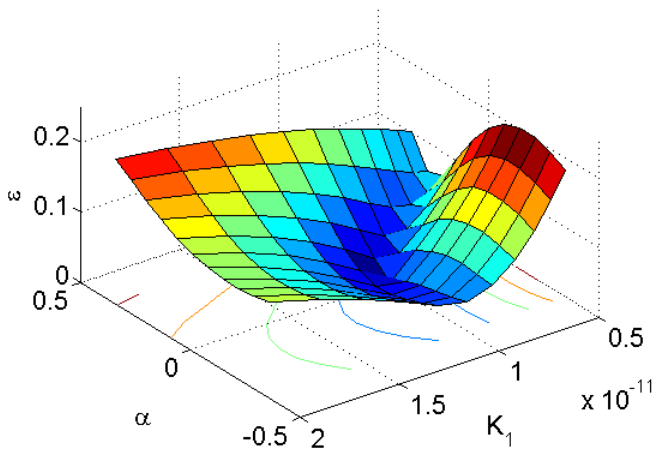

Fig. 3.7: Distribution of optimization error for $[K_1,\ \alpha]$ using the virtual output pressure at ⑥ (0.1m,0.2m). $K_1 \in [0.05, 1.5] \times 10^{-11}\mathrm{m}^2$, $\alpha \in [-\pi/9, \pi/9]$ and K_2' is fixed to $1 \times 10^{-10}\mathrm{m}^2$.

Alternatively the $[K_x, K_y, K_{xy}]$ variable space can be used to describe the permeability. In order to make sure the matrix $[K]_{(O,\boldsymbol{e}_x,\boldsymbol{e}_y)}$ is positive-definite, the

eigenvalues are calculated,

$$K_1 = \frac{1}{2\hat{D}}\left[K_x + K_y - \sqrt{(K_x - K_y)^2 + 4K_{xy}^2}\right] \qquad > 0 \tag{3.6a}$$

$$K_2 = \frac{1}{2\hat{D}}\left[K_x + K_y + \sqrt{(K_x - K_y)^2 + 4K_{xy}^2}\right] \qquad > 0 \tag{3.6b}$$

where

$$\hat{D} = -\frac{\sqrt{K_x^2 - 2K_xK_y + 4K_{xy}^2 + K_y^2}}{K_{xy}} \tag{3.7}$$

In simulation, [$\log_{10}(K_x)$,$\log_{10}(K_y)$,$\log_{10}(-K_{xy})$] are used, which imposes $K_x > 0$, $K_y > 0$ and $K_{xy} < 0$, reducing Eq. 3.6 to the constraint of $K_xK_y > K_{xy}^2$ or $\log_{10}(K_x) + \log_{10}(K_y) > 2\log_{10}(K_{xy})$. Fig. 3.8 shows the distribution of fitting error over K_x and K_{xy} with a fixed K_y (the result is plotted in an area where K_{xy}^2 is smaller than K_xK_y). The sensitivity over K_x is much higher than over K_{xy}.

Globally, the idenfication procedure based on the set [K_x,K_y,K_{xy}] is robust and accurate (several results of optimization are shown in Tab. 3.1). However, this process of optimization is not convenient because of the constraints to be verified for the permeability tensor. Consequently, the first set [K_1,K_2,α] will be used in the following.

α'	[K'_x, K'_y, K'_{xy}] ($\times 10^{-12}$m^2)	[K_x^{opt}, K_y^{opt}, K_{xy}^{opt}] ($\times 10^{-12}$m^2)
0.1	[1.09, 9.91, -0.89]	[1.09, 9.91, -0.89]
$\pi/6$	[3.25, 7.75, -3.90]	[3.25, 7.75, -3.90]
$\pi/4$	[5.50, 5.50, -4.50]	[5.50, 5.49, -4.51]
$\pi/3$	[7.75, 3.25, -3.90]	[7.76, 3.25, -3.89]

Table 3.1: Optimization results for various deviation angles α, with the same principal permeability values $K'_1 = 1.0\times10^{-12}$m^2, $K'_2 = 1.0\times10^{-11}$m^2 used for the simulated experiments generation.

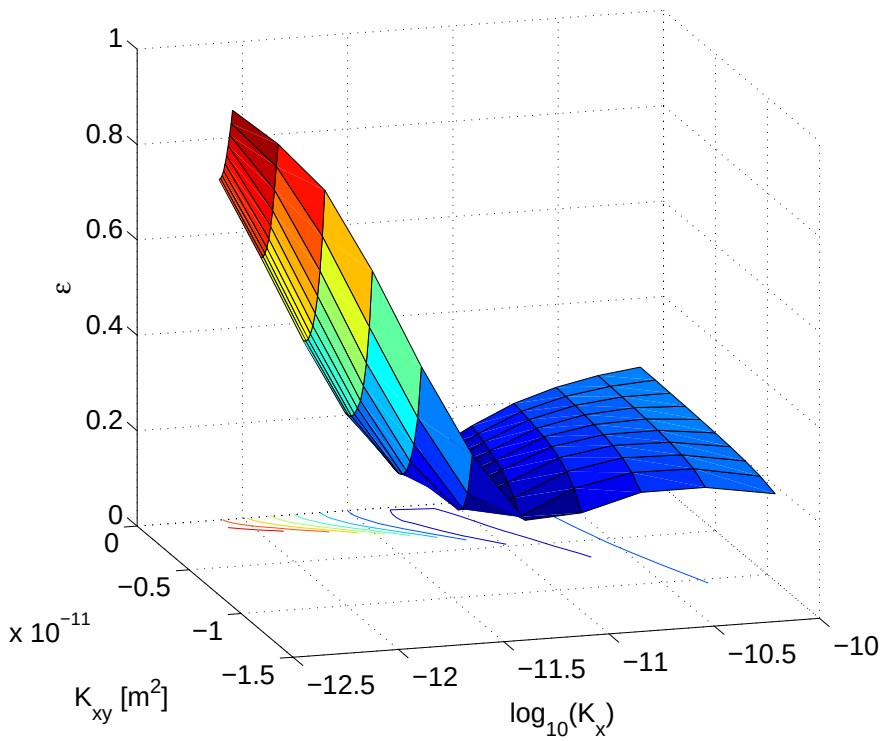

Fig. 3.8: The distribution of optimization error for K_x, K_{xy} and fixed K_y ($K'_y = 1 \times 10^{-11}\mathrm{m}^2$).

3.2.4 Assessment of the method efficiency

As explained earlier, this chapter is devoted to 2D measurements, relying so far on 1D set-up. In order to assess the efficiency of the physics and inverse methods to identify 2D permeabilities, a sensitivity analysis has to be performed, and then locations for potential pressure sensors placements have to be determined regarding the robustness and accuracy inherent to the method.

Although robustness and accuracy can be used to qualify the method, one has first to properly define these characteristics. Relying on the error made in the identification process, *i.e.* the objective function, they can be expressed as the following :

- *Robustness* is the capability of the system to reach the "real" permeability (the input permeability in "simulated experiments") in presence of perturbed data. The partial derivatives of the objective function ε, also called *sensitivities* ($\partial\varepsilon/\partial\alpha$, $\partial\varepsilon/\partial K_1$, and $\partial\varepsilon/\partial K_2$, at the input points $[\alpha', K_1', K_2']$, referred to as O'), can qualify the robustness of the method to resist data perturbation (Fig. 3.9(a)). The smaller the sensitivity, the lower the influence of data perturbation, and the more robust the methodology.

- *Accuracy* is the capability of the system (set-up and optimization process) to get a permeability that is as close as possible to the "real" permeability (the input permeability in "simulated experiments"). It can be characterized by the values of the lowest partial derivative near the input point $\boldsymbol{O'}$. Assuming a limited variable $\boldsymbol{s} = s\boldsymbol{e}_s$ in space $[\alpha, K_1, K_2]$, where $\boldsymbol{e}_s$ is an unit vector and hence,

$$\left.\frac{\partial\varepsilon}{\partial\boldsymbol{s}}\right|_{\boldsymbol{O'}} = \left.\frac{\partial\varepsilon}{\partial s}\right|_{\boldsymbol{O'},\boldsymbol{e}_s} = \frac{\varepsilon|_{\boldsymbol{O'}+d\,\boldsymbol{s}} - \varepsilon|_{\boldsymbol{O'}}}{d\,\boldsymbol{s}} \tag{3.8}$$

  where ds is an infinitesimal increment of s. The lowest partial derivative, or the minimum slope near the input values $\boldsymbol{O'}$ ($min(\partial\varepsilon/\partial\boldsymbol{s})$) is then defined as the system accuracy, and the corresponding unit vector $\boldsymbol{e}_s$ is calculated for each case and referred to as $\boldsymbol{e}_s'$. The higher the accuracy (or slope in the direction $\boldsymbol{e}_s'$ at $\boldsymbol{O'}$), the higher the sensitivity for any back-calculation solutions fitting the vector $\boldsymbol{s}$ components relationship. The extreme case being flatness meaning a poor accuracy to be expected for data in the direction $\boldsymbol{e}_s'$.

3.2.5 Parameter reduction - permeability anisotropy

Like noticed in 1D experiments, for a real loading pressure in 2D, permeability measurements will lead to better accuracies for lower permeability samples due to

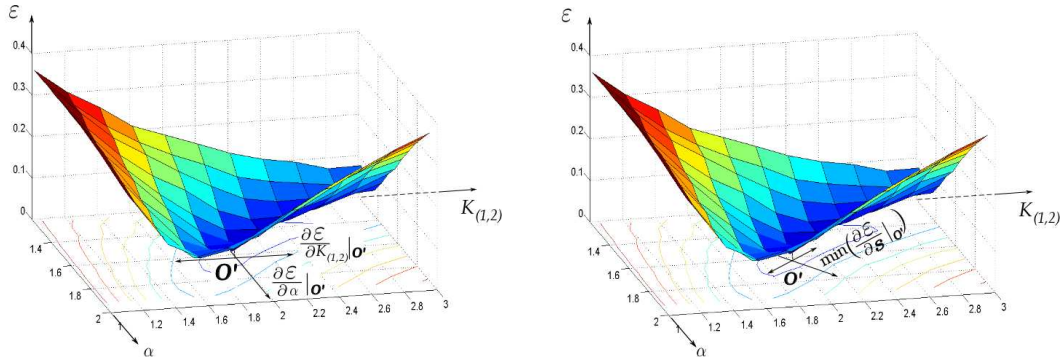

(a) Robustness (b) Accuracy

Fig. 3.9: Definition of the robustness and accuracy from the error surface response in the 3D $[\alpha, K_1, K_2]$ space (simplified in 2D here).

the larger difference between loading pressure and response pressures (Fig. 3.10(b)). Moreover, in order to get rid of the loading pressure profile effect, an ideal step loading pressure may be used, written as,

$$P(t = 0) = 1 \times 10^4 \text{Pa} \tag{3.9a}$$

$$P(t > 0) = 1 \times 10^5 \text{Pa} \tag{3.9b}$$

which will give the highest accuracy among the possible loading pressure patterns. Indeed, with this ideal loading, only the characteristic time of the transient regime, which depends on the physics of the problem, will be of importance. This makes the difference in the output pressure profiles that can be observed between Fig. 3.10(a) and Fig. 3.10(b).

Let us recall that, for 1D transient flows, the time after which transient effects can be neglected is given by :

$$t_0 = \frac{\mu\ L^2}{K\ P_0} \tag{3.10}$$

Obviously, for any parameter inducing a 2D flow, like $\alpha \neq 0$, this characteristic time will not be strictly verified. This is illustrated for instance in Fig. 3.11 where pressure responses are plotted against the dimensionless time considering K_1' as the permeability of interest in Eq. 3.10. In Fig. 3.11(a) one can verify that for $\alpha = 0$ a 1D flow is induced which fits the 1D characteristic time (Eq. 3.10) whereas for $\alpha \neq 0$ a 2D flow is induced with a characteristic time different from t_0.

Second, Figures 3.11 show that for 2D flows, the value of K_1' or K_2' alone do not control the flow, but the permeability ratio $R_k' = K_1'/K_2'$ is the key parameter. In Fig. 3.11(a) plotted for $R_k' = 10$ and $K_1' \in [1; 5] \times 10^{-11}$ m^2, it can be verified that output pressure profiles over dimensionless time perfectly fit for constant ra-

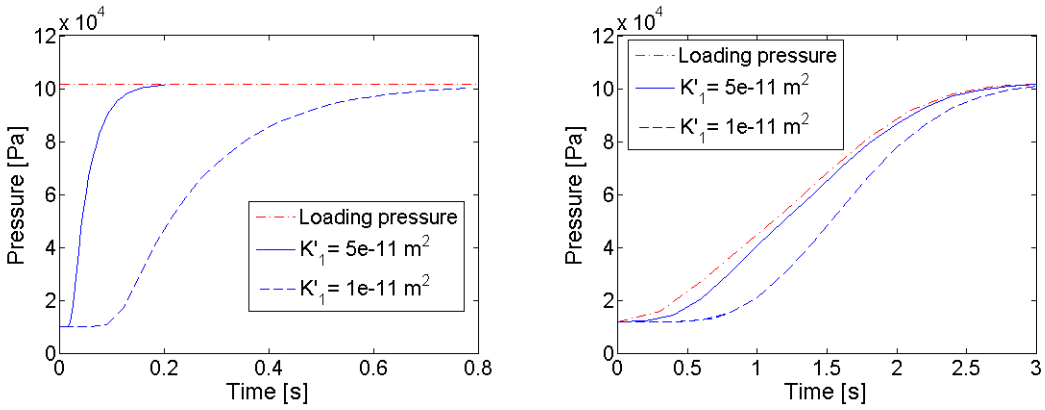

(a) (b)

Fig. 3.10: Comparison of response pressures for 2D air flow at the boundary $x = 0$, with two types of loading pressure provided ($\alpha' = \pi/6$ and $R'_k = 10$) at the boundary $x = L$: (a) step loading pressure and (b) real loading pressure for GTW.

tios. Complementary, in Fig. 3.11(a) plotted for K'_1 constant and $R'_k \in [0.1; 1; 10]$, it is clear that changing the permeability ratio by varying K'_2 will modify the response. Consequently, from now on, only 2 variables will be used to describe the 2D permeability identified in the 1D set-up loaded with an ideal step-like pressure: $[\alpha, R_k]$.

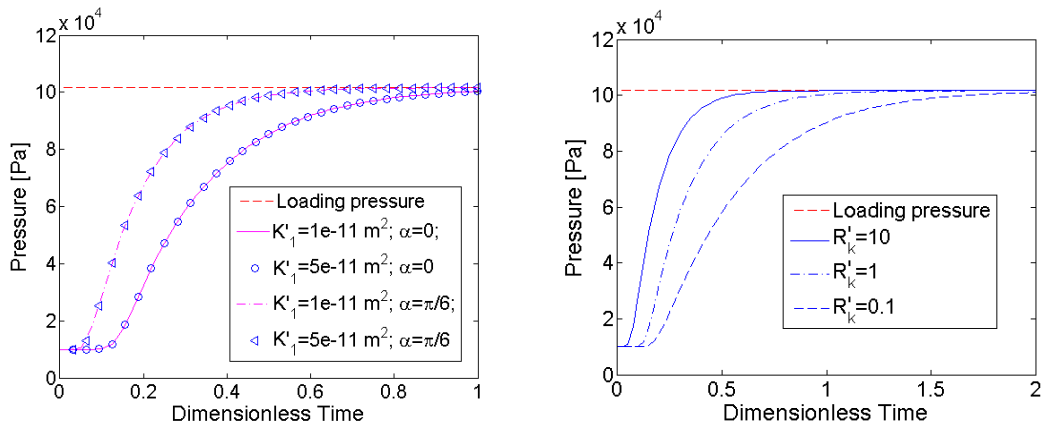

(a) (b)

Fig. 3.11: Comparison of output pressures for 2D air flow *vs* dimensionless time (Eq. 3.10), for various permeability ratios : (a) $\alpha' \in [0; \pi/6]$ and permeability ratio $R'_k = K'_1/K'_2 = 10$, and (b) $R'_k \in [0.1; 1; 10]$ with $K'_1 = 1 \times 10^{-11}$ m^2 for $\alpha' = \pi/6$.

3.2.6 Virtual sensor locations - selection and validation

3.2.6.1 Objective function analysis

We can now go farther in the analysis of the 2D response, by considering possible sensor locations, thereafter referred to as *locations*, to back-calculate permeabilities. From the pressure response studied in §3.2.2, 5 possible locations have been defined which are placed (*see* also Fig. 3.12(a)):

① is at the loading inlet $x = L$

② at the outlet boundary (0,0) - equivalent to ③ in (0,0.2)

⑤ in the middle of the preform

④, ⑥ placed respectively at half-length of both sides along the flow, at (0.1,0.0) and (0.1,0.2) respectively

Let us observe the effect of the location on the objective function ε which thereafter will be computed in the space $[\alpha, R_k]$, with $[\alpha', R'_k = K'_1/K'_2]$ the input values, for a varying $K_1 \in [0.5K'_1, 1.5K'_1]$, varying $\alpha = \alpha' \pm 20°$ and a fixed K'_2. Fig. 3.12 shows the objective function for virtual pressure sensors located at the 5 possible places, but also a combination of locations ②, ④, ⑥, for the case corresponding to $K'_1 = 1 \times 10^{-11}\text{m}^2$, $K'_2 = 1 \times 10^{-10}\text{m}^2$ with $\alpha' = 0$. One can first verify that the objective function has 1 minimum which is well defined for any sensor location.

Then, regarding the effect of the angle on the objective function, one can first verify that the objective function for location ④ (Fig. 3.12(c)) and for location ⑥ (Fig. 3.12(e)e) are totally symmetric around the line $\alpha' = 0$ since the flow remains unidimensionnal (*see* Fig. 3.4(a) on page 107 and *see* Fig. 3.5(a)). Conversely, for the case where $\alpha' = \pi/6$ shown in Fig. 3.13, this is no longer true although ④ and ⑥ are placed on either edge of the 1D set-up, since a real 2D flow is induced as shown in Fig. 3.4(b)). The 2D flow induced by $\alpha = \pi/6$ has hence to be characterized by more than one pressure sensor: the one at the output (location ②) plus another on a edge (④ or ⑥). That is why we can propose to consider the combination of sensors ②, ④, and ⑥ to characterize the permeability with confidence, as explained below.

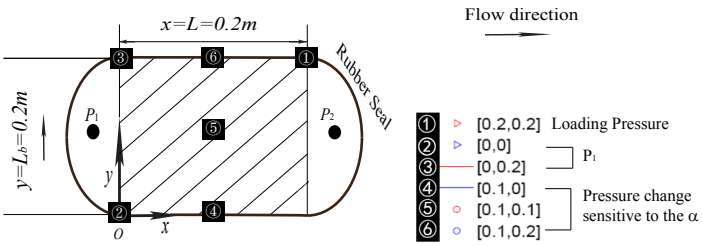

(a) Locations

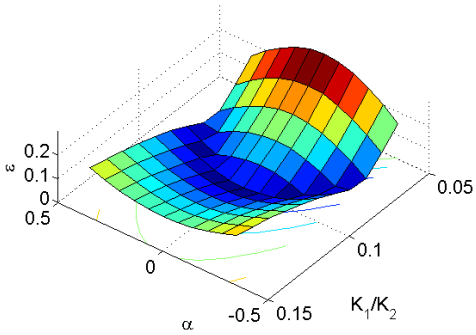

(b) $\alpha' = 0$, point ②

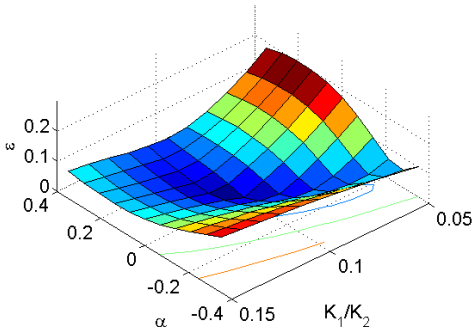

(c) $\alpha' = 0$, point ④

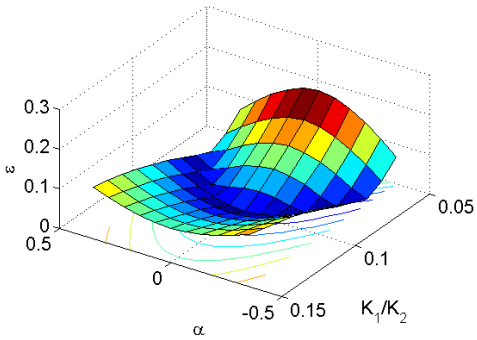

(d) $\alpha' = 0$, point ⑤

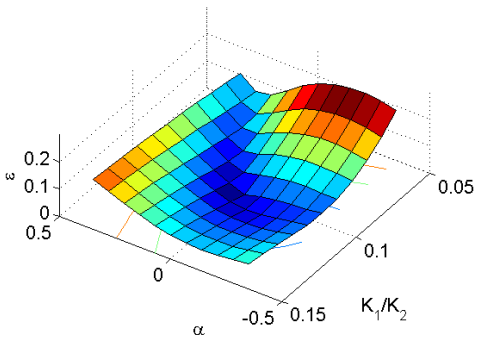

(e) $\alpha' = 0$, point ⑥

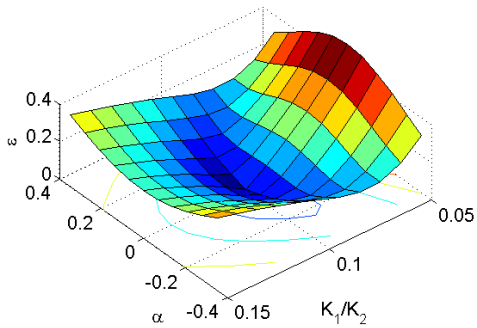

(f) $\alpha' = 0$, point ② ④ ⑥

Fig. 3.12: Objective function ε at different tested locations (input parameters: $R'_k = 0.1$ - $K'_1 = 1 \times 10^{-11}$ m^2, $K'_2 = 1 \times 10^{-10}$ m^2 and $\alpha' = 0$).

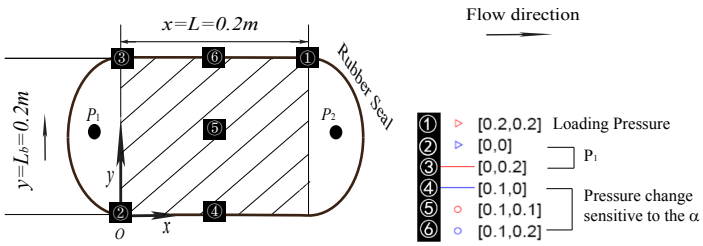

(a) Locations

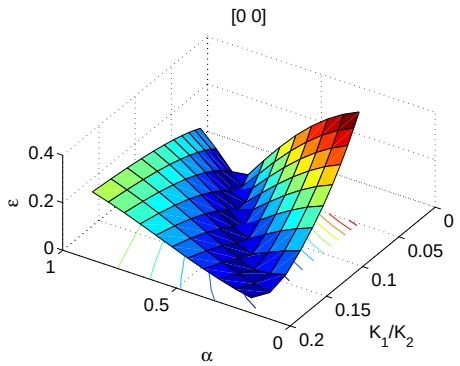

(b) $\alpha' = \pi/6$, point ②

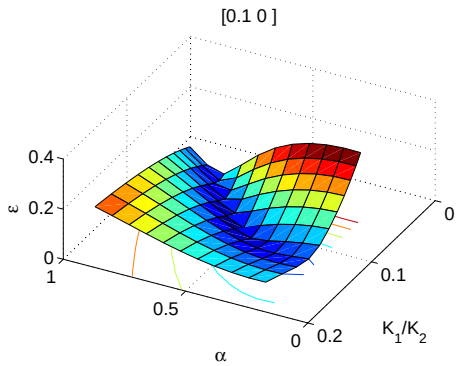

(c) $\alpha' = \pi/6$, point ④

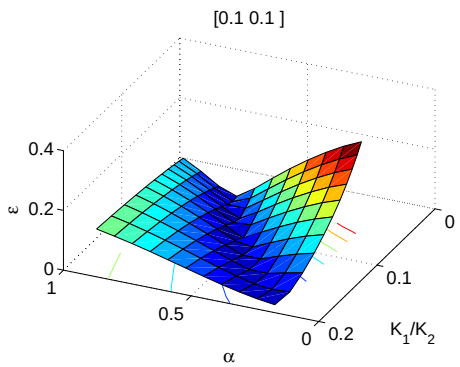

(d) $\alpha' = \pi/6$, point ⑤

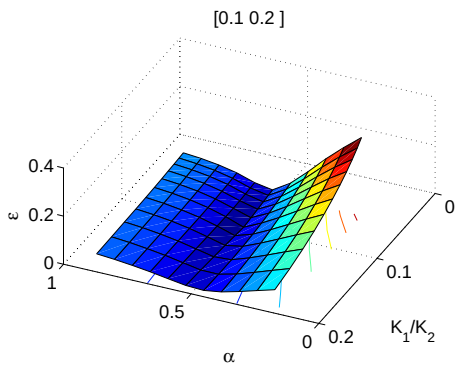

(e) $\alpha' = \pi/6$, point ⑥

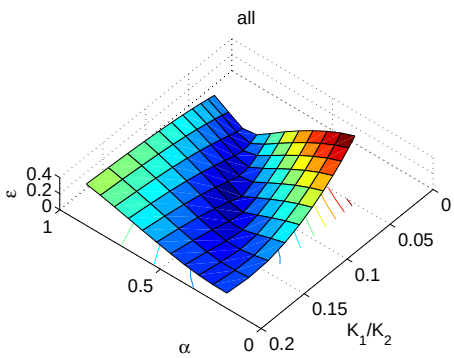

(f) $\alpha' = \pi/6$, point ② ④ ⑥

Fig. 3.13: Objective function ε at different tested locations (input parameters: $R'_k = 0.1$ - $K'_1 = 1 \times 10^{-11}$ m^2, $K'_2 = 1 \times 10^{-10}$ m^2 and $\alpha' = \pi/6$).

3.2.6.2 Sensor selection and combination

Let us consider the combination of sensors ②, ④, and ⑥ to characterize the permeability properly. Rather than relying on the visualization of this function ε, the sensitivities and accuracy must be extracted from these data to select the sensor locations. Table 3.2 summarizes both robustness (sensitivities $\partial\varepsilon/\partial\alpha$ and $\partial\varepsilon/\partial R_k$ at $\boldsymbol{O'}$, point of minimum ε) and accuracy ($min(\partial\varepsilon/\partial\boldsymbol{s})$) for the cases corresponding to the configurations presented above (Figs. 3.12 and 3.13).

It can be seen that the lowest accuracy corresponds to sensor locations at the outlet ② and in the middle of the apparatus ⑤. More precisely, when the principal permeability K_1' lies in the experimental direction $\boldsymbol{e}_x$ ($\alpha' = 0$), the pressure curve at ② $(0.0, 0.0)$ will not contain any information on angle α' and it is impossible to properly back-calculate the values of the other permeability K_2' and α'. Hence calculations relying on one point (② $(0.0, 0.0)$ and ⑤ $(0.1, 0.1)$) is not robust for this 1D-like case. But pressure information provided at points ② (or ⑤) can give the correct values of permeability and misalignment angle α in an ideal model, although the accuracy is lower than 0.1. However, this could not resist the pressure errors which will appear in experimental measurements. Finally, knowing pressure at the outlet is very easy to implement and will probably yield a "macroscopical" information which will help in reducing the solution of the inverse method as classically verified, even for our $\alpha' = 0$ case.

Fig. No.	$[\alpha', K_1', R_k']$ ([-,m^2,-])	Locations ([m,m])	Robustness		Accuracy	
			$\partial\varepsilon/\partial\alpha^{[+,-]}$	$\partial\varepsilon/\partial R_k^{[+,-]}$	$\partial\varepsilon/\partial s$	$\boldsymbol{e}_s'$
Fig. 3.12(b)	[0,1e-11,0.1]	② [0.0,0.0]	[0.04,0.04]	[0.86,0.94]	0.02	[-0.33,0.95]
Fig. 3.12(c)	[0,1e-11,0.1]	④ [0.1,0.0]	[0.21,0.29]	[0.51,0.55]	0.11	[0.00,1.00]
Fig. 3.12(d)	[0,1e-11,0.1]	⑤ [0.1,0.1]	[0.03,0.03]	[0.51,0.55]	0.02	[-0.28,0.96]
Fig. 3.12(e)	[0,1e-11,0.1]	⑥ [0.1,0.2]	[0.29,0.21]	[0.51,0.55]	0.11	[0.00,-1.00]
Fig. 3.12(f)	[0,1e-11,0.1]	② ④ ⑥	[0.35,0.35]	[0.50,1.64]	0.35	[0.00,1.00]
Fig. 3.13(b)	[$\frac{\pi}{6}$,1e-11,0.1]	② [0.0,0.0]	[0.71,0.71]	[0.60,0.65]	0.04	[0.65,-0.76]
Fig. 3.13(c)	[$\frac{\pi}{6}$,1e-11,0.1]	④ [0.1,0.0]	[0.45,0.40]	[0.56,0.61]	0.10	[-0.75,0.66]
Fig. 3.13(d)	[$\frac{\pi}{6}$,1e-11,0.1]	⑤ [0.1,0.1]	[0.44,0.45]	[0.31,0.34]	0.04	[0.65,-0.76]
Fig. 3.13(e)	[$\frac{\pi}{6}$,1e-11,0.1]	⑥ [0.1,0.2]	[0.39,0.49]	[0.09,0.08]	0.07	[-1.00,0.00]
Fig. 3.13(f)	[$\frac{\pi}{6}$,1e-11,0.1]	② ④ ⑥	[1.25,1.26]	[1.06,1.16]	0.30	[-0.82,0.57]

Table 3.2: Sensitivities and accuracy of the objective function in various cases of sensor locations ($R_k' = 0.1$, $K_1' = 1 \times 10^{-11}\mathrm{m}^2$), $\alpha' \in [0, \pi/6]$).

The second information coming from this Tab. 3.2, is that the highest accuracy can be expected from the combination of sensors at locations ②, ④, and ⑥. This can also be summarized in Fig. 3.14 where sensitivities have been reported as a function of the sensor location. One can verify that the highest accuracy is given by the combination of the 3 sensors, with a strong influence of both angles and permeability ratios.

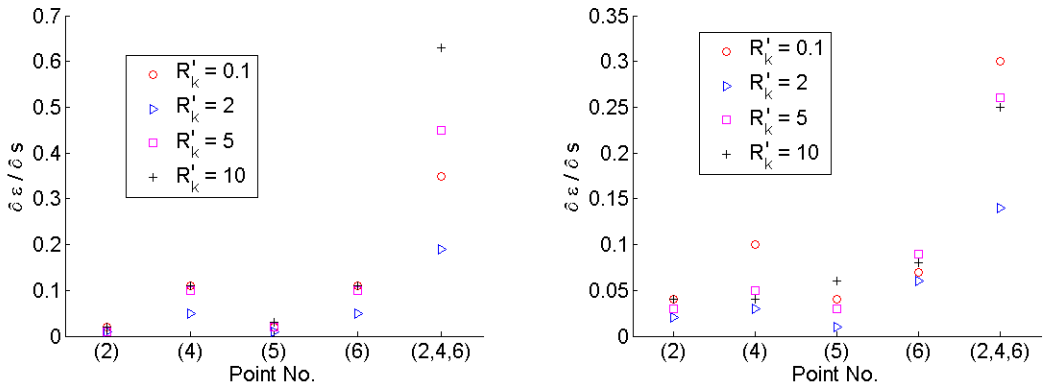

(a) $\alpha' = 0$ (b) $\alpha' = \pi/6$

Fig. 3.14: Accuracy $\partial\varepsilon/\partial s$ for $R'_k \in [0.1; 2; 5; 10]$, with angles (a) $\alpha' = 0$ and (b) $\alpha' = \pi/6$.

3.2.6.3 Effect of the permeability ratio

The permeability ratio has a strong influence on both robustness and accuracy as stated previously (Fig. 3.14). It is worth verifying again the decorrelation of this ratio with respect to the permeabilities themselves. In order to be concise, all the objective functions obtained for the 5 sensor locations and for configurations $R'_k = 0.1$ with $K'_1 = 1 \times 10^{-12}\text{m}^2$ and $\alpha' \in [0; \pi/6]$ are not presented here, they are placed in Appendix A.

Comparisons can be made between the objective function computed for $R_k = 0.1$ but for $K'_1 = 1 \times 10^{-12}\text{m}^2$ and $K'_1 = 1 \times 10^{-11}\text{m}^2$: for $\alpha' = 0$ Fig. 3.12 must be compared with Fig. A.1 page 164 and for $\alpha' = \pi/6$ Fig. 3.12 must be compared with Fig. A.2 page 165. The corresponding robustness and sensitivity are reported in Tab. 3.2 for $K'_1 = 1 \times 10^{-12}\text{m}^2$ and in Tab. A.1 page 160 for $K'_1 = 1 \times 10^{-11}\text{m}^2$.

To summarise, the objective functions obtained when considering 3 sensors locations ②, ④, and ⑥, for the same permeability ratio are similar, for both angles $\alpha' = \pi/6$ (Figs. 3.15(a)-3.15(b)) and $\alpha' = 0$ (Figs. 3.15(c)-3.15(d)). Also, the same accuracy can be expected when the permeability ratio is unchanged as shown in Fig. 3.16, for 2 angles.

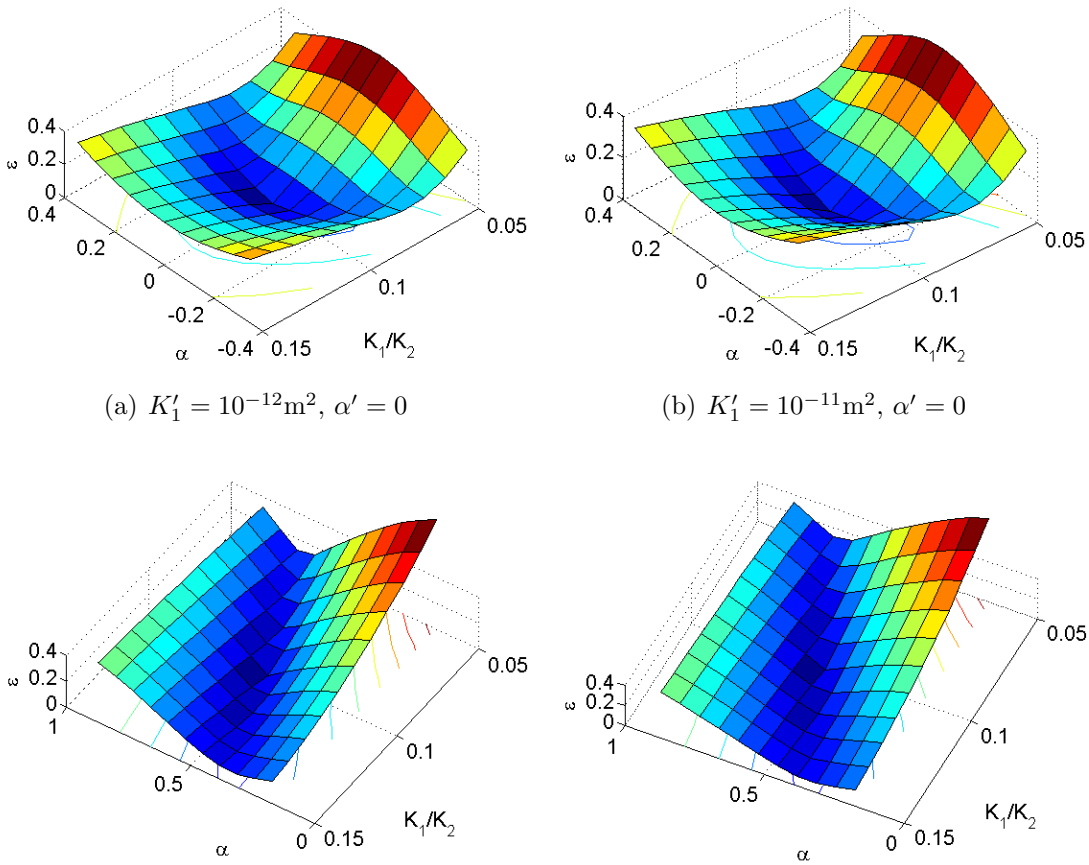

(a) $K_1' = 10^{-12}\mathrm{m}^2$, $\alpha' = 0$

(b) $K_1' = 10^{-11}\mathrm{m}^2$, $\alpha' = 0$

(c) $K_1' = 10^{-12}\mathrm{m}^2$, $\alpha' = \pi/6$

(d) $K_1' = 10^{-11}\mathrm{m}^2$, $\alpha' = \pi/6$

Fig. 3.15: Comparison of the objective functions based on points ② ④ ⑥ for (a-c) $K_1' = 10^{-12}\mathrm{m}^2$ and (b-d) $K_1' = 10^{-11}\mathrm{m}^2$ with $R_k' = 0.1$ and $\alpha \in [0; \pi/6]$.

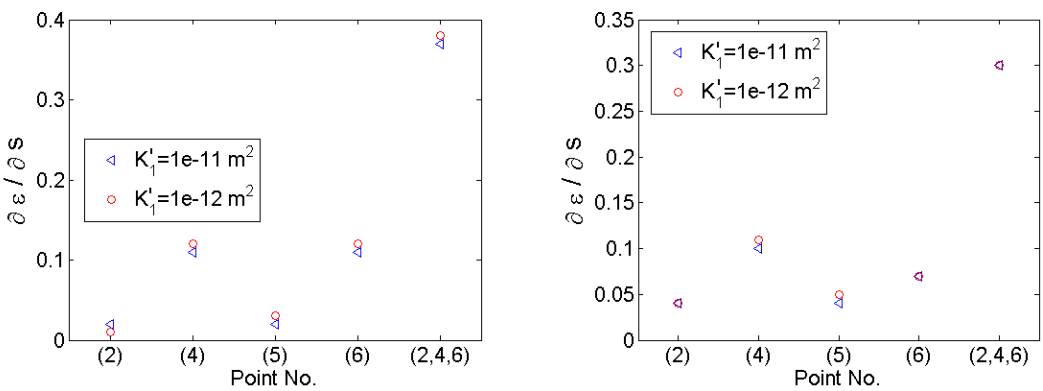

(a) $\alpha' = 0$

(b) $\alpha' = \pi/6$

Fig. 3.16: Accuracy for objective functions based on pressures in points ②, ④, ⑥ for (a) $\alpha' = 0$ and (b) $\alpha' = \pi/6$ with the same permeability ratio $R_k' = 0.1$.

3.2.7 Alignment angles

The fabric to be tested must be placed carefully in the apparatus to get the highest accuracy. This accuracy reaches its maximum when α is null, which means that during experiments the sample has its principal direction parallel with the flow direction $\boldsymbol{x}$, as shown in Fig. 3.17. For most of the woven fabrics the principal direction is close to the fiber direction, and this will help to raise the system accuracy.

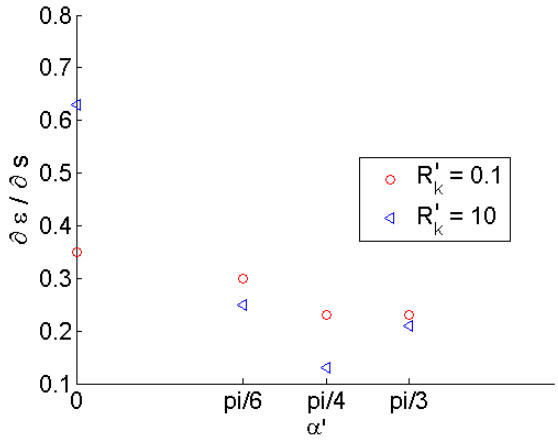

Fig. 3.17: Accuracy for $R'_k \in [0.1; 10]$, with angle $\alpha' \in [0; \pi/6; \pi/4; \pi/3]$.

The objective function profiles are computed for other ratios ($R'_k \in [0.1; 1; 2; 5; 10]$), the results are reported in Appendix A. The profiles for the same ratios R'_k are similar, and the sensitivities vary little (Fig. 3.12 for $K_1 = 1 \times 10^{-11}\text{m}^2$ and $\alpha = 0$, Fig. 3.13 for $K_1 = 1 \times 10^{-11}\text{m}^2$ and $\alpha = \pi/6$, Fig. A.1 for $K_1 = 1 \times 10^{-12}\text{m}^2$ and $\alpha = 0$, and Fig. A.2 for $K_1 = 1 \times 10^{-12}\text{m}^2$ and $\alpha = \pi/6$).

It can be verified that the system based on pressure responses at 3 points can give a good accuracy for R'_k from 0.1 to 10. Globally, it is possible to select some combinations of angles and permeability ratios, even larger than 10, to maintain a good accuracy. This is an advantage compared with 2D permeability using liquid transient flow, which as mentioned in the introduction, will not provide sufficient information for calculation when the anisotropy ratio exceeds 10 [68].

3.2.8 Capabilities of the method

Now that we have established that 3 sensors should be used to properly characterize the 2D permeability, let us investigate the capabilities of this methodology for isotropic and anisotropic fabrics. Since the idealized step loading pressure does not show the improvement of the method accuracy for low permeability materials,

a real loading pressure from 1D measurement on GTW fabrics (Fig. 3.10(b) for instance) will be used in this section.

The ranges of data considered to assess both robustness and accuracy are : $\alpha' \pm 10°$, $0.5(K_1'/K_2') < R_k < 2(K_1'/K_2')$ where α', K_1' and K_2' are the data taken to generate the 'simulated' experiments. Isotropic, and then anisotropic, materials are considered here.

3.2.8.1 Isotropic permeability

The permeability of isotropic material can be represented as $K_r\boldsymbol{I}$, where $\boldsymbol{I}$ is a second order unit tensor. Hence the components in cartesian coordinates should be $K_x = K_y = K_r$ and $K_{xy} = K_{yx} = 0$ (*cf* Eq. 3.1). Consequently, the orientation of the sample has no influence on the material property.

This can be verified since the partial derivative $\partial\varepsilon/\partial\alpha$ equates zero (Tab. 3.3) and the orientation of the principal direction is $[0, 1]$ in $[\alpha, R_k]$ space for these materials. Also, this can be verified in Fig. 3.18(a) to 3.18(c) for any angle considered. Again, changing permeability K_1' will not affect the shape of the objective function if the permeability ratio is constant. However, low permeability can create a larger difference between loading pressure curves (P_i) and pressure response curves (P_o), hence the values of sensitiviy with respect to the permeability anisotropy $\partial\varepsilon/\partial R_k$ are larger (last 2 lines in Tab. 3.3). A higher accuracy can then be expected on materials with lower permeability, as found in 1D experiments from pressure curves analysis.

Fig. No.	$[\alpha', K_1', R_k']$ ([-,m^2,-])	Robustness		Accuracy	
		$\partial\varepsilon/\partial\alpha^{[+,-]}$	$\partial\varepsilon/\partial R_k^{[+,-]}$	$\partial\varepsilon/\partial s$	$\boldsymbol{e}_s'$
Fig.3.18(c)	[π/4,1e-11,1]	[0 , 0]	[0.34, 0.44]	0	[0,1]
Fig.3.18(b)	[π/6,1e-11,1]	[0 , 0]	[0.12, 0.15]	0	[0,1]
Fig.3.18(a)	[0,1e-12,1]	[0 , 0]	[0.87, 1.12]	0	[0,1]
Fig.3.18(d)	[π/6,1e-12,1]	[0 , 0]	[0.78, 0.03]	0	[0,1]

Table 3.3: Robustness and sensitivity in various cases of angles ($\alpha \in [0, \pi/6, \pi/4]$) and permeabilities ($K_1' = 10^{-11}$m^2 and $K_1' = 10^{-12}$m^2) for isotropic materials ($R_k' = 1$).

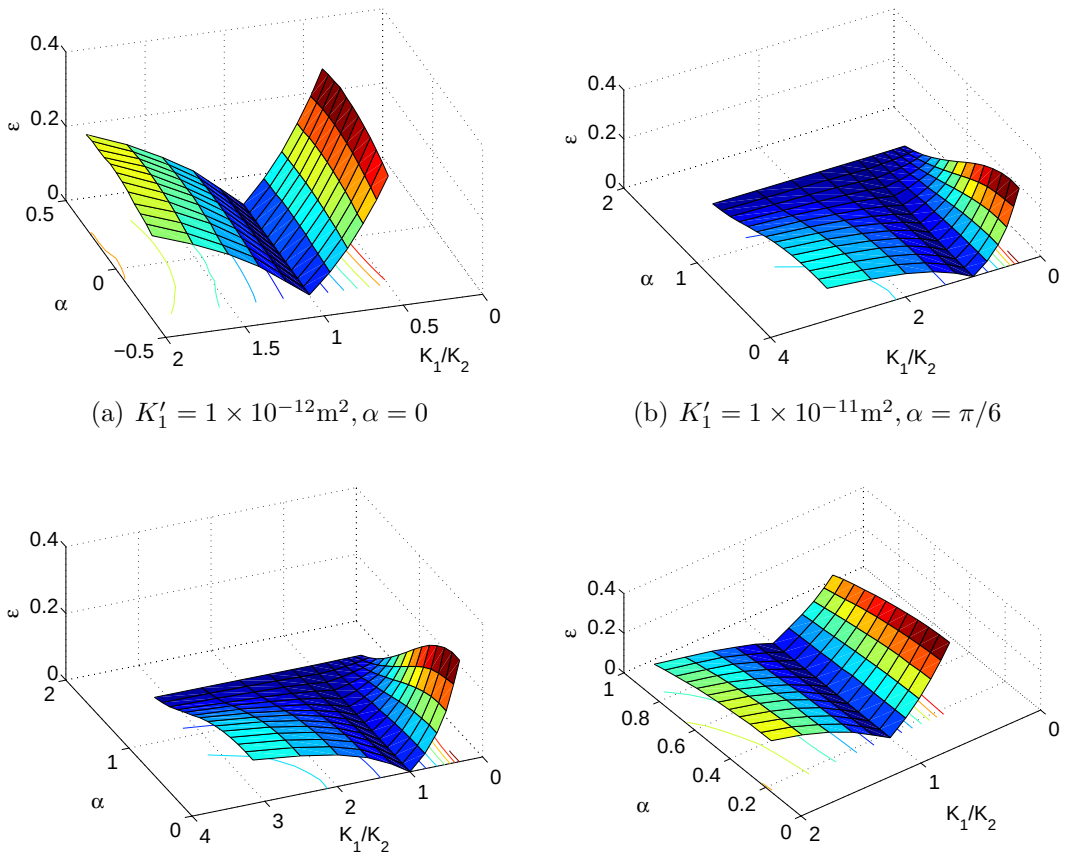

(a) $K_1' = 1 \times 10^{-12}\mathrm{m}^2, \alpha = 0$

(b) $K_1' = 1 \times 10^{-11}\mathrm{m}^2, \alpha = \pi/6$

(c) $K_1' = 1 \times 10^{-11}\mathrm{m}^2, \alpha = \pi/4$

(d) $K_1' = 1 \times 10^{-12}\mathrm{m}^2, \alpha = \pi/6$

Fig. 3.18: Objective function ε for isotropic permeability ($R_k' = 1$) : (a-c) for various angles ($\alpha' \in [0, \pi/6, \pi/4]$) and $K_1' = 10^{-11}\mathrm{m}^2$, and (d) for a lower permeability $K_1' = 10^{-12}\mathrm{m}^2$.

3.2.8.2 Anisotropic permeability

Anisotropic permeability with ratios $R'_k = K'_1/K'_2$ from 0.1 to 10 are tested. Various series of configurations are presented here corresponding to the following Figures 3.19 to 3.22 and the synthetic results in Tab. 3.4. These series correspond to different angles between 0 and $\pi/3$ for permeability ratios of $R'_k = 5$ (Fig. 3.19), $R'_k = 10$ (Fig. 3.20) and $R'_k = 0.1$ (Fig. 3.21) obtained by keeping K'_2 constant. A last series (Fig. 3.22) is considered with a permeability ratio $R'_k = 0.1$ but obtained with $K'_1 = 10^{-12}\text{m}^2$ since with the real loading pressure the permeability will induce higher pressures and this must be assessed.

These results reported in Tab. 3.4 show 2 main facts. First, when the angle increases, for any permeability ratio R'_k and permeability K'_1, sensitivity to angles increases while sensitivity to permeability ratio decreases. The main result being that the highest accuracy is obtained with a perfect alignment of the principal direction, corresponding to K'_1, with the apparatus axis $\boldsymbol{e}_x$.

The second important result is related to both permeability ratio R'_k and permeabilities K'_1 and K'_2. When the permeability ratio R'_k increases one can see that the sensitivity may be affected. But more importantly, when the same ratio is obtained by decreasing K'_1 (Fig. 3.22), both robustness and accuracy increase due to the increase in the experimental pressure which in turn induces a larger contrast between the input and output pressure profiles. This was a conclusion of the 1D experiments, where the larger the profile difference between input and ouput, the higher the identification safety. This is validated here more precisely.

Fig. No.	$[\alpha', K'_1, R'_k]$ ([-,m^2,-])	Robustness		Accuracy	
		$\partial\varepsilon/\partial\alpha^{[+,-]}$	$\partial\varepsilon/\partial R_k^{[+,-]}$	$\partial\varepsilon/\partial s$	$\boldsymbol{e}'_s$
Fig.3.19(a)	[0,5e-11,5]	[0.43,0.32]	[0.80,0.83]	0.32	[0, -1]
Fig.3.19(b)	[π/6,5e-11,5]	[0.48,0.36]	[0.66,0.66]	0.22	[0.71, 0.71]
Fig.3.19(c)	[π/4,5e-11,5]	[0.71,0.34]	[0.28,0.58]	0.06	[-0.71,-0.71]
Fig.3.19(d)	[π/3,5e-11,5]	[0.72,0.55]	[0.11,0.35]	0.05	[-0.71,-0.71]
Fig.3.20(a)	[0,1e-10,10]	[0.46,0.34]	[0.52,0.59]	0.26	[0.78,-0.62]
Fig.3.20(b)	[π/6,1e-10,10]	[0.63,0.41]	[0.30,0.52]	0.18	[0.86, 0.51]
Fig.3.21(a)	[0,1e-10,0.1]	[0.18,0.11]	[0.60,0.77]	0.11	[0, -1]
Fig.3.21(b)	[π/6,1e-10,0.1]	[0.31,0.26]	[0.39,0.38]	0.09	[-0.62, 0.78]
Fig.3.21(c)	[π/4,1e-10,0.1]	[0.41,0.27]	[0.42,0.33]	0.04	[-0.78, 0.62]
Fig.3.22(a)	[0,1e-12,0.1]	[0.29,0.28]	[0.87,1.08]	0.28	[0, -1]
Fig.3.22(b)	[π/6,1e-12,0.1]	[0.38,0.62]	[0.60,0.87]	0.12	[-0.71, 0.71]
Fig.3.22(c)	[π/4,1e-12,0.1]	[0.71,0.51]	[0.67,0.61]	0.05	[-0.80, 0.60]

Table 3.4: Robustness and accuracy in various configuration for anisotropic materials.

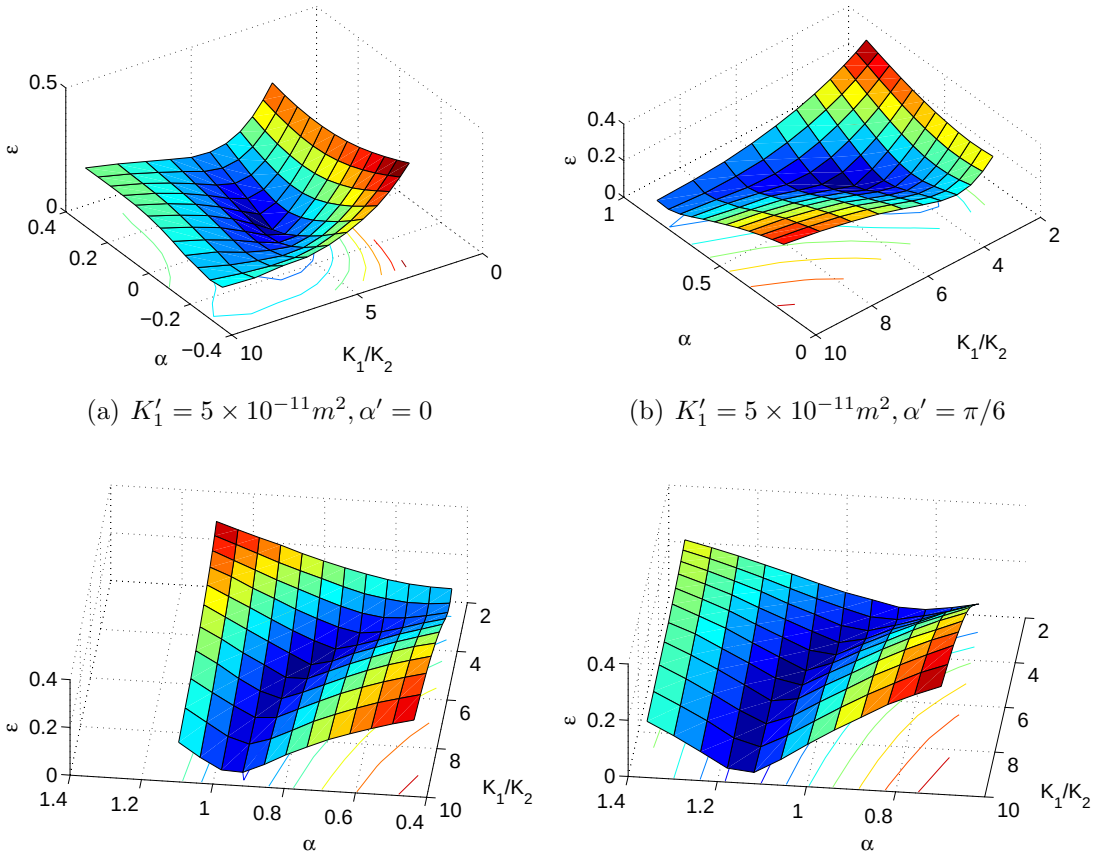

(a) $K_1' = 5 \times 10^{-11} m^2, \alpha' = 0$

(b) $K_1' = 5 \times 10^{-11} m^2, \alpha' = \pi/6$

(c) $K_1' = 5 \times 10^{-11} m^2, \alpha' = \pi/4$

(d) $K_1' = 5 \times 10^{-11} m^2, \alpha' = \pi/3$

Fig. 3.19: Objective function ε for $R_k' = 5$ with $\alpha' \in [0; \pi/6; \pi/4]$.

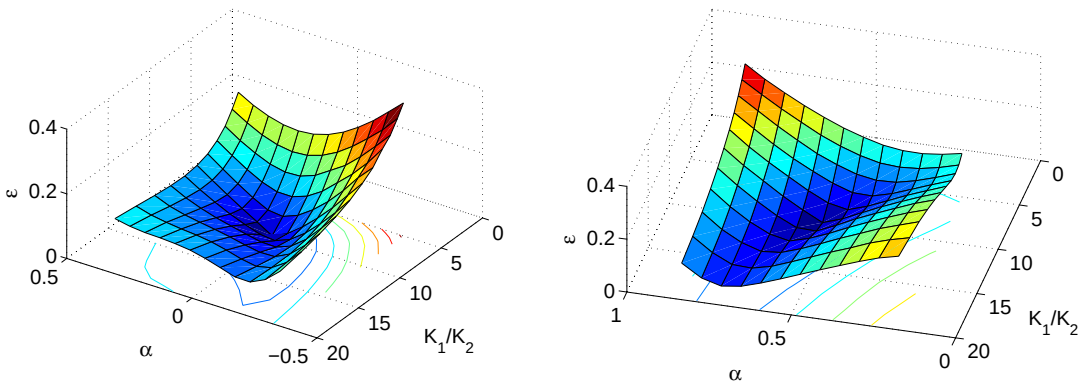

(a) $K_1' = 1 \times 10^{-10} m^2, \alpha' = 0$

(b) $K_1' = 1 \times 10^{-10} m^2, \alpha' = \pi/6$

Fig. 3.20: Objective function ε for $R_k' = 10$ with $\alpha' \in [0; \pi/6]$.

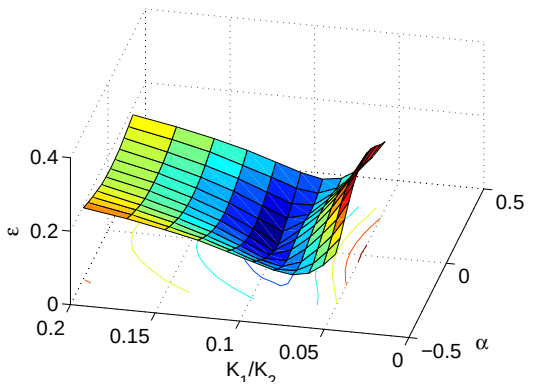

(a) $K_1' = 1 \times 10^{-10} m^2, \alpha' = 0$

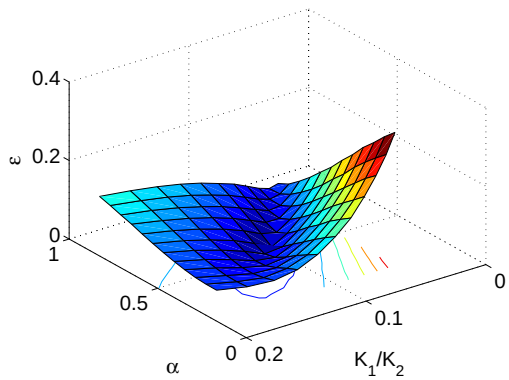

(b) $K_1' = 1 \times 10^{-10} m^2, \alpha' = \pi/6$

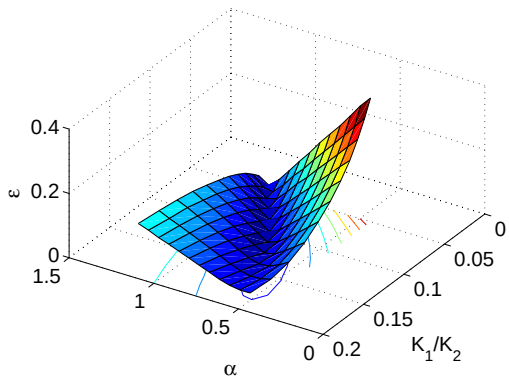

(c) $K_1' = 1 \times 10^{-10} m^2, \alpha' = \pi/4$

Fig. 3.21: Objective function ε for $R_k' = 0.1$ with $\alpha' \in [0; \pi/6; \pi/4]$.

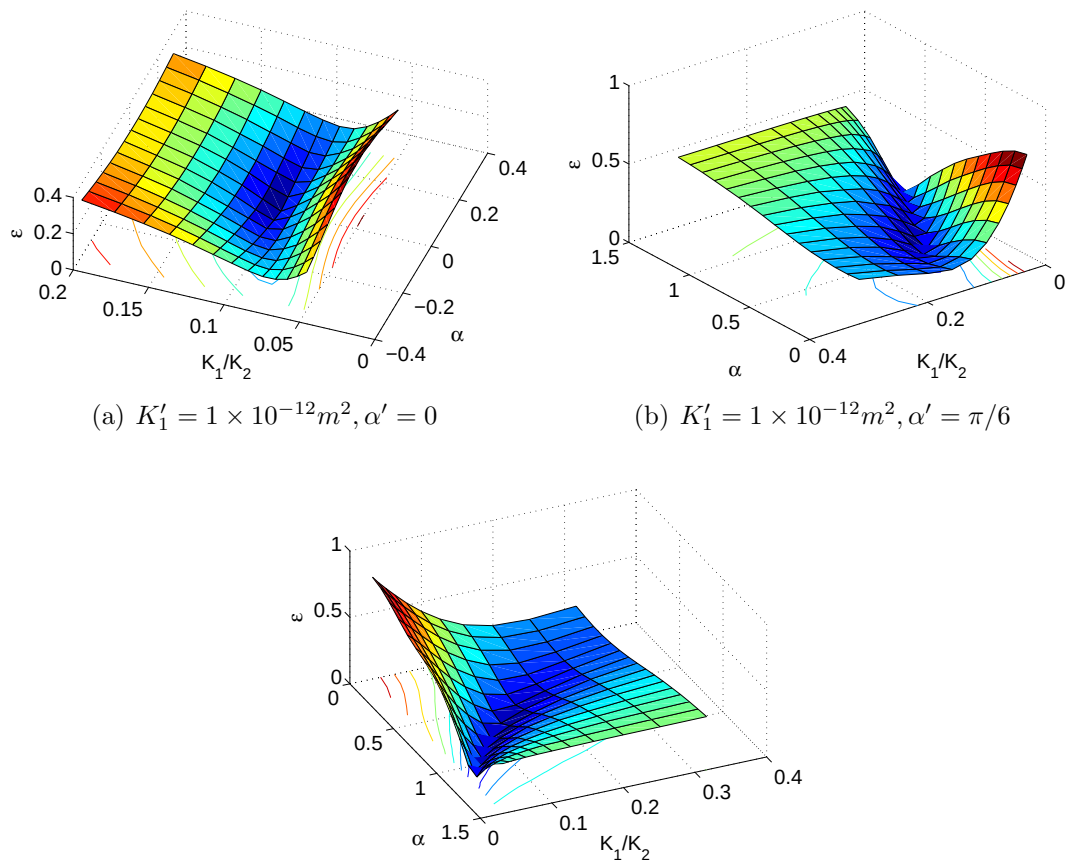

(a) $K_1' = 1 \times 10^{-12} m^2, \alpha' = 0$

(b) $K_1' = 1 \times 10^{-12} m^2, \alpha' = \pi/6$

(c) $K_1' = 1 \times 10^{-12} m^2, \alpha' = \pi/4$

Fig. 3.22: Objective function ε for $R_k' = 0.1$ with $\alpha' \in [0; \pi/6; \pi/4]$.

3.3 2D Set-up design

The knowledge gained in studying the 1D set-up for measuring 2D permeability tensor can now be used to design a fully 2D set-up, with a proper pressure sensor distribution. Especially, the issues of the trapped gas at boundaries, and more generally gaps, will have to be studied before to assess the 2D set-up efficiency.

As introduced in § 2.3.2, the trapped gas at boundaries will affect the overall flow field and may lead to unproper permeability characterization. To overcome this problem, only one vent is proposed here, playing the role of both *loading vent* (where a changing pressure is applied) and *input vent* (used to apply an initial pressure). All the other boundaries are sealed and the seal must tightly fit the sample to avoid other gap in the apparatus (Fig. 3.23). The pressure sensors are flush mounted below the sample without any gap (pressures referred to as P_O).

The pressure at the "loading vent" (referred to as P_I) can be changed by switching between connections of vacuum pump or atmosphere; or directly by a pressure generator. The pressure measurement has to be ensured such that only the gas pressure is measured (with the use of appropriate sensors).

Here are the two main problems left: the position of the loading vent; the number and the positions of test pressure sensors.

3.3.1 Transient gas flow simulation

The position of the loading vent should stimulate an anisotropic flow to the largest extent, so it is placed on one corner. This would ease the fabric placement such that the principal permeability directions, usually corresponding to the fabric structure itself, would correspond to the reference frame of the set-up. This corner is cut to be flat so that a boundary condition can be applied to a line instead of one point. The resulting flow is clearly 2D as can be seen in Fig. 3.23 for an isotropic fabric.

Simulations of 2D transient gas flow in this 2D set-up are modeled on a sample of size $L_a \times L_b = 0.2 \times 0.2\text{m}^2$. The experimental *loading pressures* in RPM and DPM for GTW fabric are used in simulations. Fig. 3.23 shows the pressure distribution for an isotropic sample in RPM at the time point when the pressure difference reaches its maximum. Based on this pressure distribution, four positions are chosen to record pressure changes (Fig. 3.23): $(x, y)_a = (0, 0)$, $(x, y)_b = (0, 0.2)$, $(x, y)_c = (0.2, 0.2)$ and $(x, y)_d = (0.1, 0.1)$ with unit in [m]. Pressure curves of RPM and DPM at the above points are shown respectively in Figs. 3.24 and 3.25.

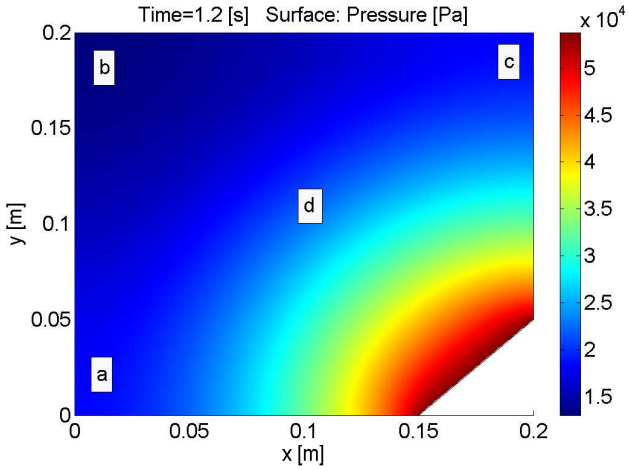

Fig. 3.23: Model of 2D transient gas flow for an isotropic fabric loaded with RPM input pressure.

3.3.2 Pressure sensors locations and combinations

The second issue which must be tackled consists in selecting optimized sensor locations and combinations such that permeability can be properly characterized for anisotropic permeability at optimal angle of placement in the apparatus.

As it was demonstrated in the 1D set-up used for 2D permeability characterization §3.2, one curve is obviously not enough to determine properly the complete permeability tensor. To chose the proper set of locations, pressure profiles over time are analyzed.

The difference in pressure responses (P_O) between points a and b (or c) indicates the anisotropy ratio of permeability. For instance, it can be verified in Figs. 3.24(d) and 3.25(c) that when the material is isotropic, those two curves for a and c coincide with each other. On the contrary, pressure curves in the center (d) always lie between pressure curves at corners a and c for isotropic sample, and does not exhibit a real difference globally for anisotropic permeability. Hence, one can infer that pressure curves at corners a, b and c will give better resolutions for back-calculation of isotropic permeabilities than those in the middle.

In terms of pressure profiles difference, pressure curve in b always exhibits the largest difference with the loading pressure, for both RPM and DPM. However, this pressure in b coincides with other curves for high anisotropic permeability, *i.e.* with curve at a when $K_1'/K_2' = 0.2$ (Figs. 3.24(b) and 3.25(b)), and with curve at c when $K_1'/K_2' > 2 - 3$ (Figs. 3.24(f) and 3.25(d)). Keeping K_2' constant and varying K_1', Fig. 3.26(a) and Fig. 3.26(b) shows that pressure profiles at points a and b change significantly. However pressure profiles at point c will not change much in magnitude but the shape is affected by the permeability ratio, as shown

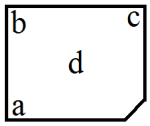

(a) sensor locations

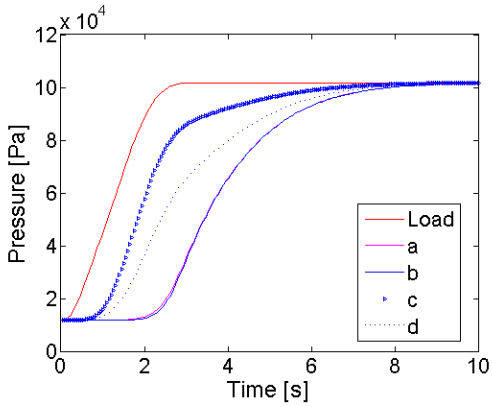

(b) $K_1'/K_y' = 0.2$

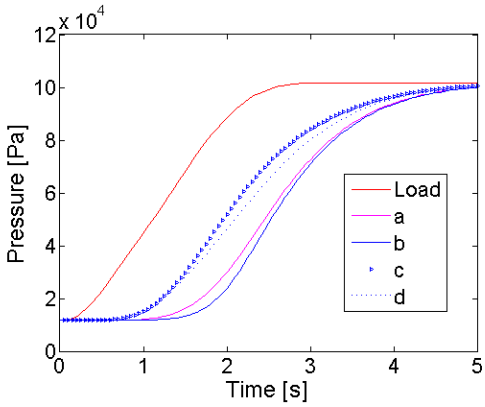

(c) $K_1'/K_2' = 0.5$

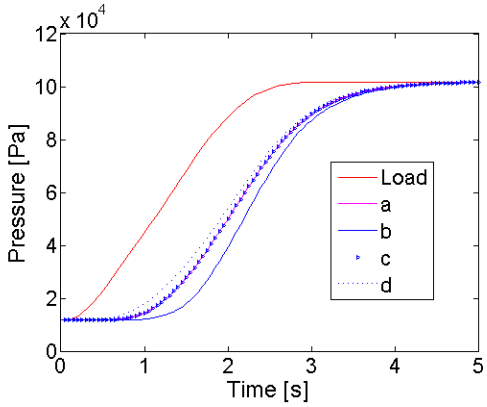

(d) $K_1'/K_2' = 1$

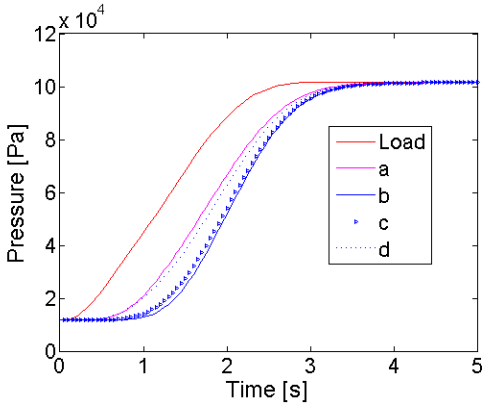

(e) $K_1'/K_2' = 2$

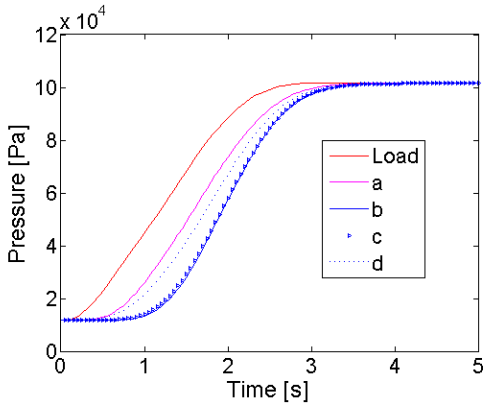

(f) $K_1'/K_2' = 3$

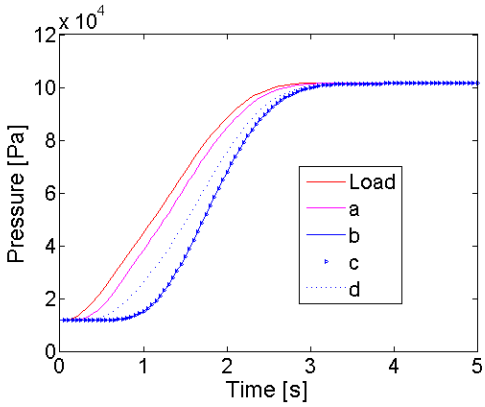

(g) $K_1'/K_2' = 10$

Fig. 3.24: Output pressures P_O at four locations under a given loading pressure P_I corresponding to RPM on GTW fabrics. Permeability ratios $K_1'/K_2' \in [0.2; 0.5; 1; 2; 3; 10]$ with permeability $K_y' = 10^{-11}\text{m}^2$.

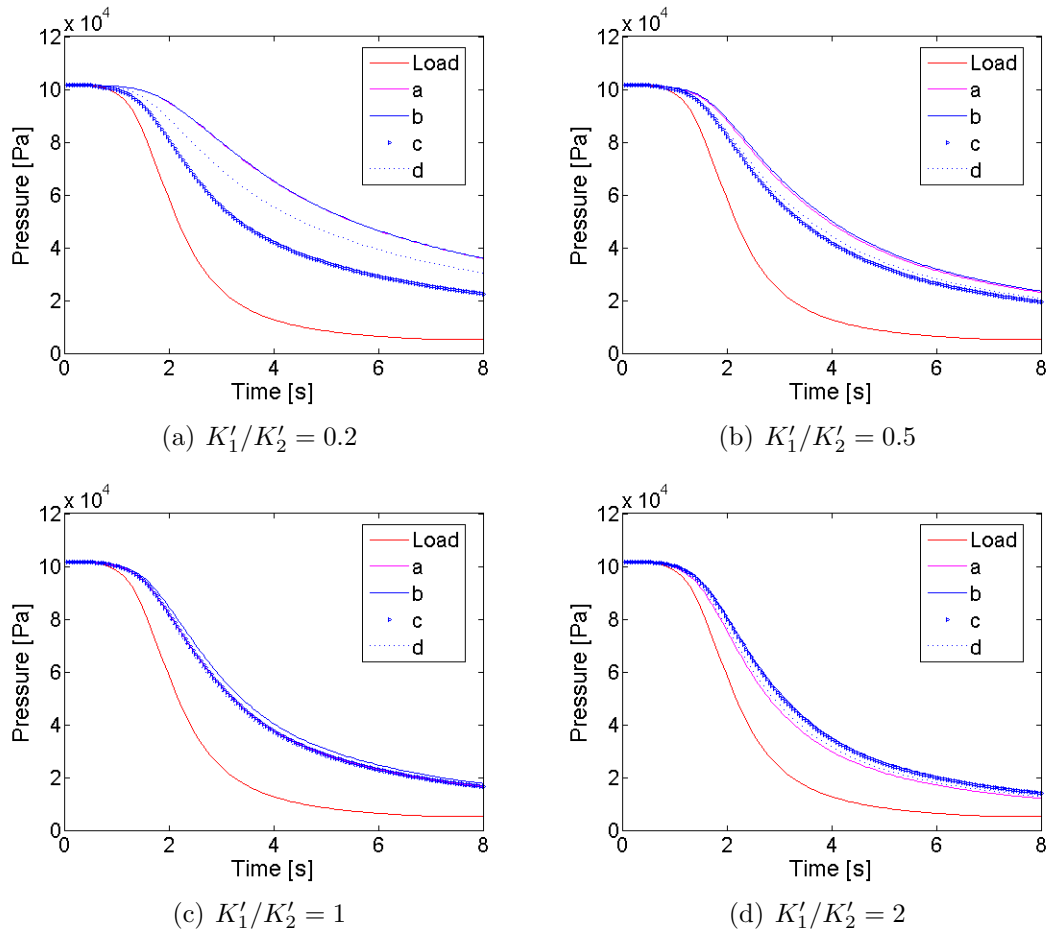

(a) $K_1'/K_2' = 0.2$ (b) $K_1'/K_2' = 0.5$

(c) $K_1'/K_2' = 1$ (d) $K_1'/K_2' = 2$

Fig. 3.25: Output pressures P_O at four locations a, b, c and d, under a loading pressure P_I corresponding to DPM on GTW fabrics. Permeability ratios $R_k' = K_1'/K_2' \in [0.2; 0.5; 1; 2]$, with permeability $K_y' = 10^{-11}\mathrm{m}^2$.

in Fig. 3.26(c).

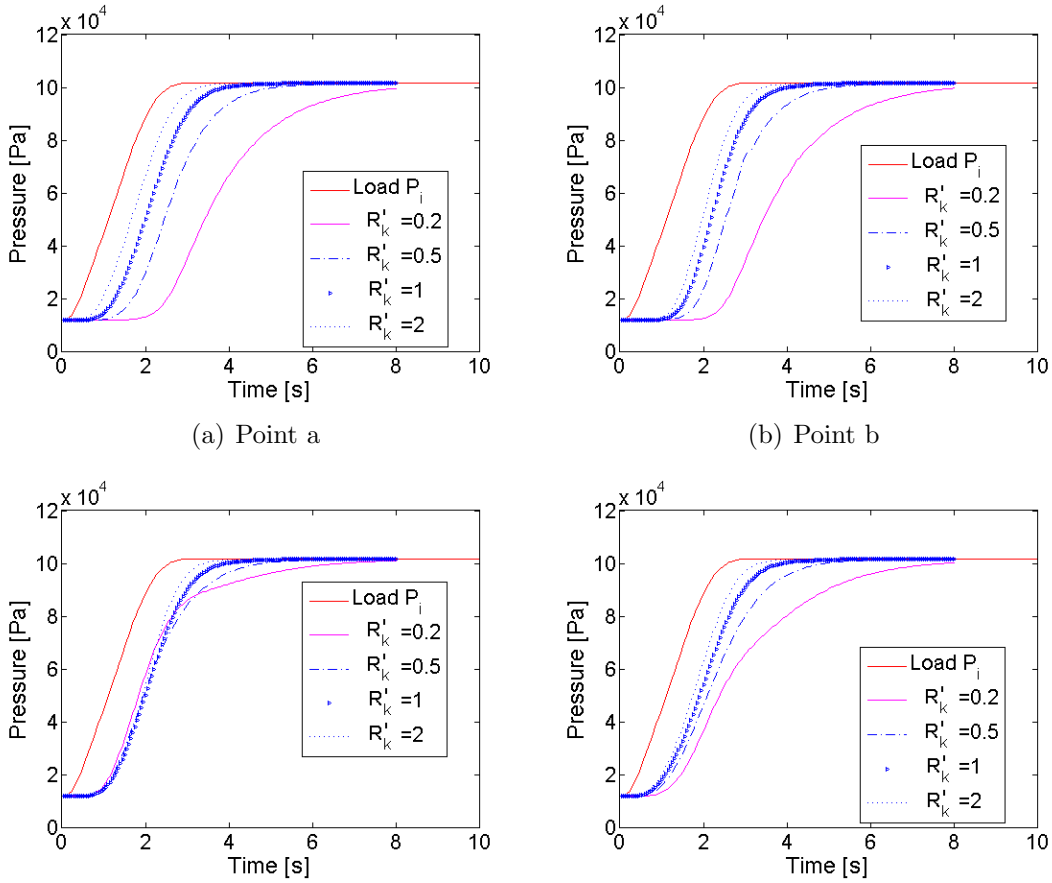

(a) Point a (b) Point b

(c) Point c (d) Point d

Fig. 3.26: Pressure profiles at four locations (Fig. 3.23) for permeability ratios $R'_k = K'_1/K'_2 \in [0.2; 0.5; 1; 2]$.

This influence of the anisotropy which can be observed in the pressure profiles at points a and b corresponds to fully 2D effects. It appears more clearly in the pressure distribution plotted for various permeability ratios $K_1'/K_2' \in [2; 3; 10]$ in Fig. 3.27. One can verify that this region will be less 'activated' for higher ratios, when $K_1'/K_2' > 3$ the pressure will rise quickly in the $\boldsymbol{e}_x$ direction (Fig. 3.27(c)) and hence pressure responses of points with the same y values will coincide, such as pressure curves at point b and c in Fig. 3.24(f) and Fig. 3.24(g). Hence for highly anisotropic fabrics, adding a further sensor placed at the same y coordinate is of no use.

As a conclusion, in order to back-calculate permeability for various anisotropy ratios, pressure curves at locations a and c are essential. Additional points can also be used for measurements to determine the sliding effect (sliding effect will change the pressure profiles) or to get more confidence in measurement, especially for isotropic materials. Point d being in the 'diagonal' of the set-up, at (0.1,0.1), pressure sensor at point c will be preferred. Eventually, the combination of sensors $a + b + c$ should lead to proper characterization for various anisotropy ratios.

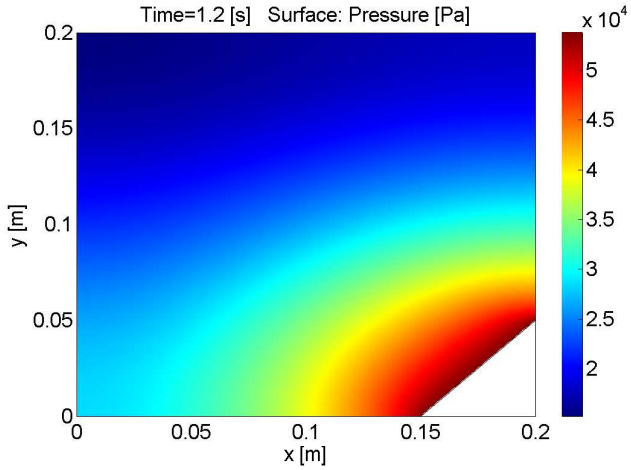

(a) $K_1'/K_2' = 2$

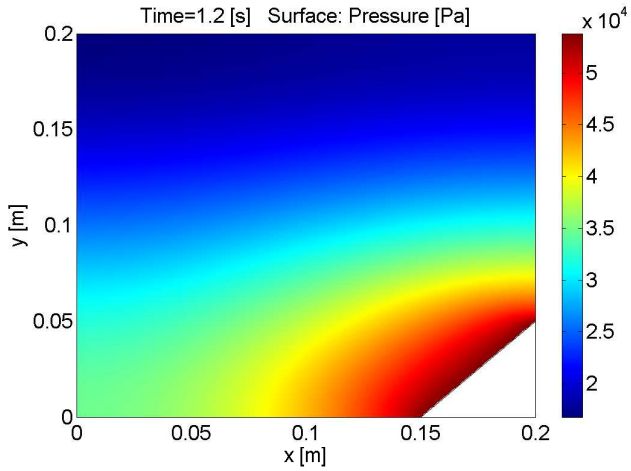

(b) $K_1'/K_2' = 3$

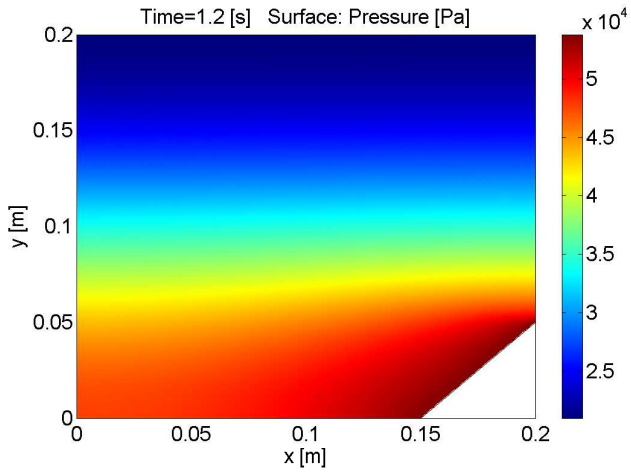

(c) $K_1'/K_2' = 10$

Fig. 3.27: Distributions of pressure in 2D transient gas flow, for $K_1'/K_2' \in [2, 3, 10]$.

3.3.3 Assessment of the method efficiency and capability

In order to characterize the robustness and sensitivity of the back-calculation in the 2D set-up equipped with pressure sensors in a, b, and c, the same objective function as the one proposed for the 1D set-up can be used here. Robustness and accuracy can be determined from the error function ε considered in the ranges : $\alpha' \pm 10°$, $R_k \in [0.5(K'_1/K'_2), 2(K'_1/K'_2)]$ where $[\alpha', K'_1, K'_2]$ are the data selected to generate the 'simulated' experiments. Isotropic, as well as anisotropic, materials are considered here. Cases to be investigated cover the ranges of permeability ratios $R'_k \in [1; 2; 5; 10]$ and angles $\alpha' \in [0; \pi/6; \pi/4; \pi/3; \pi/2]$.

As indicated in §3.2.8, to show the improvement of the back-calculation in case of low permeability materials, a real loading pressure from 1D measurement on GTW fabrics (*see* Fig. 3.10(b) for instance) will be used in this section.

In order to be concise, objective function plots, obtained with RPM loading taken from GTW experiments in Chapter 2 have been placed in Appendix A : error plotted for locations a, b, c, d, and $a + b + c$ for $R'_k = 2$ and $\alpha' = \pi/6$ (Fig. A.11), followed by the plots of error for combination $a + b + c$ for angles $\alpha' \in [0; \pi/6; \pi/4; \pi/3; \pi/2]$ with permability ratios $R'_k = 2$ (Fig. A.12), $R'_k = 5$ (Fig. A.13), and $R'_k = 10$ (Fig. A.14). All the robustness and accuracy data are summarized in Tab. 3.5.

Fig. No.	$[\alpha', K_1', R_k']$ ([-,m^2,-])	Robustness		Accuracy	
		$\partial\varepsilon/\partial\alpha^{[+,-]}$	$\partial\varepsilon/\partial R_k^{[+,-]}$	$\partial\varepsilon/\partial s$	$\boldsymbol{e}_s'$
Fig. A.12(a)	[0,2e-12,2.0]	[0.60,0.43]	[1.03,1.14]	0.20	[0.45,0.89]
Fig. A.12(b)	[π/6,2e-12,2.0]	[0.37,0.41]	[0.46,0.36]	0.09	[-0.41,-0.91]
Fig. A.12(c)	[π/4,2e-12,2.0]	[0.29,0.34]	[0.32,0.25]	0.14	[-0.54,-0.84]
Fig. A.12(d)	[π/3,2e-12,2.0]	[0.32,0.42]	[0.38,0.60]	0.09	[-0.41,0.91]
Fig. A.12(e)	[π/2,2e-12,2.0]	[0.50,0.46]	[1.07,1.20]	0.19	[0.46,-0.89]
Fig. A.13(a)	[0,5e-12,5.0]	[1.01,0.76]	[0.79,0.89]	0.34	[0.78,0.62]
Fig. A.13(b)	[π/6,5e-12,5.0]	[0.64,0.79]	[0.52,0.39]	0.12	[-0.82,-0.57]
Fig. A.13(c)	[π/4,5e-12,5.0]	[1.32,1.28]	[0.44,0.49]	0.23	[1.00,0.00]
Fig. A.13(d)	[π/3,5e-12,5.0]	[0.74,0.74]	[0.30,0.41]	0.11	[-0.91,0.41]
Fig. A.13(e)	[π/2,5e-12,5.0]	[0.85,0.95]	[0.75,1.02]	0.32	[0.85,-0.52]
Fig. A.14(b)	[0,1e-11,10.0]	[1.00,1.28]	[1.02,0.64]	0.35	[0.90,0.43]
Fig. A.14(b)	[π/6,1e-11,10.0]	[1.09,1.17]	[0.30,0.42]	0.13	[-0.97,-0.23]
Fig. A.14(c)	[π/4,1e-11,10.0]	[0.72,0.72]	[0.10,0.23]	0.06	[1.00,0.00]
Fig. A.14(d)	[π/3,1e-11,10.0]	[1.21,1.18]	[0.18,0.55]	0.14	[-0.97,0.23]
Fig. A.14(e)	[π/2,1e-11,10.0]	[1.21,1.16]	[0.70,0.63]	0.34	[0.90,-0.43]

Table 3.5: Robustness and accuracy for various permeability ratios ($R_k' \in [1; 2; 5; 10]$) and angles ($\alpha' \in [0; \pi/6; \pi/4; \pi/3; \pi/2]$) considering locations $a + b + c$. Loading with RPM from GTW measurements in Chapter 2.

Regarding both accuracy and robustness, Tab. 3.5 illustrates the way fabrics can be positioned in the 2D set-up. The highest accuracy corresponds to angles $\alpha' = 0$ and $\alpha' = \pi/2$, symmetrical with respect to the diagonal of the set-up where the inlet pressure is applied. The pressure field distribution in this case would correspond to Fig. 3.27 page 136, and sensors located at points a, b, and c would yield very different information, this difference being directly dependent on the permeability ratio. This was the motivation to place pressure loading at (0.,0.) coordinates, inducing this 2D flow for such configurations ($\alpha' = 0$ and $\alpha' = \pi/2$).

The second highest accuracy is obtained for $\alpha' = \pi/4$, at least for permeability ratios $R'_k \in [2; 5]$. In that special case one of the principal directions of the permeability tensor fits with the diagonal of the 2D set-up, *i.e.* the flow will be controlled along the diagonal of the set-up. But when anisotropy is too large, K_1 is dominant in this direction and the pressure field gradient is mostly orientated between sensors a and c which will tend to deliver similar information. Problems for identifying the 2D permeability can be expected as shown by the very poor robustness and accuracy for this configuration ($\alpha' = \pi/4, R'_k = 10$ in Tab. 3.5).

All this can be verified by plotting accuracy as a function of the angle for permeability ratios $R'_k = 2$ and $R'_k = 10$ (Fig. 3.28). On this same graph, one can verify that the highest permeability ratio will lead to the highest accuracy, especially for angles $\alpha' = 0$ and $\alpha' = \pi/2$, symmetric with respect to the diagonal of the set-up.

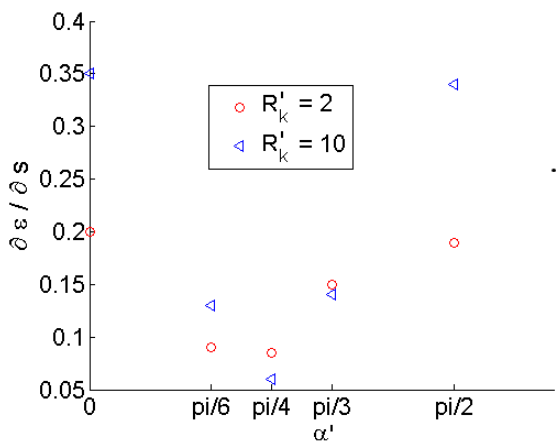

Fig. 3.28: Sensitivity for permeability ratios $R'_k \in [2; 10]$, for angles $\alpha' \in [0; \pi/6; \pi/4; \pi/3]$.

3.3.4 Back calculation of permeabilities

The purpose of this section is to check quickly, on various configurations, the possibility of back-calculation of 2D permeability once the pressures are recorded in experiments. Results obtained are gathered in Tabs. 3.6 and A.4, respectively for RPM and DPM loadings. These results show the same trends, therefore only Tab. 3.6 is presented here.

The main conclusions which come out from these computations is that since the shape of the pressure curves will vary for different values of anisotropic permeability, as presented in §3.3.1, it is possible to back-calculate permeability ($[\alpha,\ K_1,\ K_2]$) with pressure changing at one point. For anisotropic permeability, data at single point a or point c can give accurate results respectively; even though some values obtained at point b or d give the right answers, the directions seem reversed, which is normal since b and d would not change much due to α change. For instance, at b or d locations, the solution in pressure is similar if $K_1' = 10^{-12}\mathrm{m}^2, K_2' = 10^{-11}\mathrm{m}^2$ or $K_1' = 10^{-11}\mathrm{m}^2, K_2' = 10^{-12}\mathrm{m}^2$. For isotropic permeability, the optimization fails to obtain the correct permeabilities based on a single data (*see* the 2 last series in Tab. 3.6). This corresponds to the conclusions drawn for the 1D set-up, since sensitivity towards the angle tends to 0 for isotropic materials.

As a conclusion, it is possible to back-calculate permeability K_1 and K_2 with pressure changing at one point (such as a and c), but the optimization procedure sometimes obtaines wrong values when the tolerances of the Nelder-Mead algorithm are set to be large (such as absolute termination tolerance on the function value 100, and relative termination tolerance 1%), especially for isotropic permeability (Tab. 3.6). Since experimental measurements will always contain some errors, it is not sufficient to have data from only one location. Points a and c are suggested, complemented by point b, as shown in the previous sections devoted to the pressure responses analysis.

Sensor locations	$[K_1', K_2']$ ([m^2, m^2])	Back-calculated $[K_1, K_2]$ ([m^2, m^2])
a	[2e-12, 1e-11]	[1.59e-12 3.10e-11]
b	[2e-12, 1e-11]	[2.04e-11 1.68e-12]
c	[2e-12, 1e-11]	[2.08e-12 1.04e-11]
d	[2e-12, 1e-11]	[9.94e-12 2.00e-12]
a, b	[2e-12, 1e-11]	[1.62e-12 2.63e-11]
a, c	[2e-12, 1e-11]	[2.00e-12 1.00e-11]
a, d	[2e-12, 1e-11]	[2.01e-12 9.95e-12]
a	[5e-12, 1e-11]	[4.94e-12 1.01e-11]
b	[5e-12, 1e-11]	[3.21e-11 3.37e-12]
c	[5e-12, 1e-11]	[5.35e-11 6.09e-12]
d	[5e-12, 1e-11]	[1.15e-11 4.31e-12]
a, b	[5e-12, 1e-11]	[3.39e-12 3.07e-11]
a, c	[5e-12, 1e-11]	[5.01e-12 1.00e-11]
a, d	[5e-12, 1e-11]	[5.00e-12 9.97e-12]
a	[1e-11, 1e-11]	[6.65e-12 4.95e-11]
b	[1e-11, 1e-11]	[2.01e-11 6.28e-12]
c	[1e-11, 1e-11]	[4.85e-11 6.69e-12]
d	[1e-11, 1e-11]	[9.86e-12 1.02e-11]
a, b	[1e-11, 1e-11]	[9.98e-12 1.00e-11]
a, c	[1e-11, 1e-11]	[1.00e-11 1.00e-11]
a, d	[1e-11, 1e-11]	[1.00e-11 1.01e-11]
a	[2e-11, 1e-11]	[2.00e-11 1.03e-11]
b	[2e-11, 1e-11]	[1.07e-11 1.81e-11]
c	[2e-11, 1e-11]	[2.03e-11 9.90e-12]
d	[2e-11, 1e-11]	[1.98e-11 1.01e-11]
a, b	[2e-11, 1e-11]	[2.00e-11 1.00e-11]
a, c	[2e-11, 1e-11]	[2.01e-11 9.93e-12]
a, d	[2e-11, 1e-11]	[2.01e-11 9.81e-12]

Table 3.6: Back-calculated permeabilities for various locations of pressure measurements for RPM loading.

3.4 Conclusion

The 1D set-up has been first considered for a possible identification of 2D permeability using this single set-up. After presenting the 2D permeability, robustness and accuracy of the methodology have been defined and used to assess the need for placing complementary pressure sensors in the 1D set-up. The pressure profiles have been first studied, starting from the conclusion drawn from Chapter 2 that pressure profiles must exhibit the largest difference (between input and ouputs) to guarantee a robust and accurate 2D permeability identification. It was established clearly that relying on 3 pressure sensors measurements placed at the inlet and on either edge of the set-up, at mid-length, will ensure the best accuracy for any permeability ratio, including isotropic fabrics, and any angle of placement.

Then, a fully 2D set-up was proposed, designed to avoid problems of air entrapment, or more generally of 'dead zones' made of gaps. The proposed configuration consists of a rectangular geometry with a corner cut, this place being used for both input and output pressure measurement and control. After assessing the placement and location of pressure sensors, it came out that using 2 sensors could be sufficient for the inverse method to be robust and accurate. However, in order to cover as many cases as possible, including isotropic fabrics and highly anisotropic media, a combination of 3 sensors, placed on the 3 remaining corners of the 2D set-up would be the best combination.

Finally, the identification method used in Chapter 2 has permitted to investigate 2D permeability characterization using air in transient regime. However, the sliding effect, which was shown in Chapter 2 to be quite important for anisotropic fabrics of low permeability at low pressure regimes, should be accounted for to secure a satisfying set-up design. Still remains also to consider technological solutions to build such kind of set-ups.

General conclusion

In the present work, a methodology to measure in-plane permeability of fibrous media using a transient one dimensional air flow with absolute pressures ranging from 10^3 to 10^5 Pa is proposed. The method, based on the measurement of gas pressure at the boundaries throughout the transient flow, is convenient, clean and fast, avoids usage of a gas flow meter and offers a way to study the gas transport within fibrous media.

The gas transport through fibrous porous media is described by several models to comply with different flow regimes. Literature review in the first chapter has introduced that pressure driven flow is the dominant mechanism of the gas transport through gas/carbon fibrous porous media compared with diffusion, adsorption and surface flow. Permeability is a linear parameter relating flow rate and pressure gradient and is considered to depend only on the fibrous structure in Darcy's law (valid for a viscous laminar flow). Many factors lead to a deviation from Darcy's law, such as high Reynolds number leading to non-Darcian effect which can be described by a quadratic momentum equation, Forchheimer equation. For transient experiment using partial gas vacuum on fabrics, Reynolds number is lower than 0.4 during experiments and a linear relationship is enough to describe the flow in viscous regime. Another factor is that, when the Knudsen number is larger than 1, *i.e.*, the mean molecular free path in gas is larger than the characteristic length of pores, the inter-molecular and molecular-wall collisions are not frequent enough to show a viscous flow behavior. In this case a free-molecular model (or Knudsen flow) should be considered. Specific criteria of regimes are given when Darcian or sliding model can be used. For each type of fibrous media one can choose the appropriate set of equations to solve when performing gas flow measurement. A

proper model is chosen based on experimental conditions, and the corresponding parameters can be determined by inverse method, fitting the simulation results to the experimental data obtained using rising or dropping pressure methods.

Measurements performed on several types of fabrics showed that gas flows in Darcy's and sliding regimes depending on the fabrics tested. For large-pore fabrics as CTW (carbon twill weave) and GTW (glass twill weave) with permeability values ranging from 10^{-11} to $10^{-10}\mathrm{m}^2$, the predicted pressure responses match quite well the experimental responses using a Darcy's model. The results of back-calculated viscous permeability also match well the permeability measured with liquid compression and injection techniques on CTW and GTW fabrics. While in CUD fabrics ($K_v \in [10^{-14}, 10^{-12}]\mathrm{m}^2$), the deviation from Darcy's law caused by sliding effect cannot be ignored, and the relative parameter b shows a dependence on permeability, with a similar trend as the Klinkenberg sliding parameter in soils and rocks. The parameter b depends not only on the characteristic length of pores but also on the micro-structure in the flow direction, *i.e.*, values b of $\mathrm{CUD}_\perp$ (in the direction perpendicular with fiber orientation) are much higher than that of $\mathrm{CUD}_{||}$ with the same permeability.

Sliding effect and gas compressibility are the two main differences between liquid flow and gas flow. Gas compressibility is neglected sometimes but has to be considered under a high pressure gradient. Since pressure changes from 3000 to 10^5Pa during the experiments, compressibility becomes very important. Fundamental equations and boundary conditions for gas flow in fibrous media have been proposed. At the boundary where gas flow is cut off by a closed valve, a slight flux could exist due to compressibility of the gas trapped between the sample and valve. This could change the overall gas flow field of the sample, leading to a significantly underestimated permeability. To estimate the error of permeability ignoring gas compressibility at the boundaries, an empirical relationship of the permeability related to trapped gas volume and cross-section area of gas flow was proposed.

The other experimental errors due to dimensions, thermal effect, pressure variation, misalignment angle (the angle between the flow direction and the permeability principal direction) in sample handling were analyzed and the precisions of recorded pressure values and trapped gas volumes at boundaries dominate the measurement accuracy.

In order to cope with the issues of trapped gas at boundaries and the misalignment angle, a 2D measurement using gas to obtain permeability tensor in one single test is proposed. Simulated experiments are performed with responses on selected locations recorded and these data are used as pressure responses P_{Oexp} to back-calculate the permeabilities and misalignment angle. A series of experimental

simulations and back-calculation processes were performed based on data of sensors at three proposed locations, and the system showed good robustness and accuracy for fabrics with permeability anisotropy ratio ranging from 0.1 to 10 with a misalignment angle ranging from 0 to $\pi/2$. Sliding effect, which will make the system even more intricate, is not considered here. As already shown in 1D experiments, this effect, which can be avoided by increasing loading pressure, should not be a problem in measurements.

Although the mechanics of gas transport are intricate, the system of permeability measurement using gas is efficient: it takes 40 min to prepare a set-up and 10s to 2 min to complete a test in 1D (should be the same case for 2D), and 30 min for a back-calculation process with a mesh sizes 20 and 20 time step; 30 min to 2 hours to back-calculate 2D permeability based on a mesh 100×100, and 20 time step. A single-core computer with Matlab and Comsol installed is sufficient and the equipment used for liquid injection method can also be modified as an air measurement set-up.

For a future work, 2D set-up can be built to determine fabrics which have unknown principal directions, and the sliding effect in 2D conditions can also be assessed. Moreover, since measurements using gas will not damage the materials, on-line permeability determination process in industry can be a prospective application to characterize the preforms before composites manufacturing. 3D permeability measurement can also be built using a 3D mold with sensors on walls in various direction.

Bibliography

[1] M. Cieplak, J. Koplik, and J. R. Bavanar. Molecular dynamics of flows in the knudsen regime. *Physica A: Statistical Mechanics and its Applications*, vol. 287(1-2), (2000), pp. 153–160.

[2] M. Cieplak, J. Koplik, and J. R. Banavar. Applications of statistical mechanics in subcontinuum fluid dynamics. *Physica A: Statistical Mechanics and its Applications*, vol. 274(1-2), (1999), pp. 281–293.

[3] R. T. Jacobsen and E. W. Lemmon. Viscosity and thermal conductivity equations for nitrogen, oxygen, argon, and air. *International Journal of Thermophysics*, vol. 25(1), (2003), pp. 21–69.

[4] P. Gibson, D. Rivin, C. Kendrick, and H. Schreuder-Gibson. Humidity-dependent air permeability of textile materials1. *Textile Research Journal*, vol. 69(5), (1999), pp. 311–317.

[5] T. S. Lundstrom, B. R. Gebart, and E. Sandlund. In-plane permeability measurements on fiber reinforcements by the multi-cavity parallel flow technique. *Polymer Composites*, vol. 20(1), (1999), pp. 146–154.

[6] S. S. Tavares, V. Michaud, and J.-A. Manson. Through thickness air permeability of prepregs during cure. *Composites Part A: Applied Science and Manufacturing*, vol. 40(10), (2009), pp. 1587–1596.

[7] A. L. Baehr and M. F. Hult. Evaluation of unsaturated zone air permeability through pneumatic tests. *Water Resources Research*, vol. 27(10), (1991), pp. 2605–2617.

[8] J. Feser, A. Prasad, and S. Advani. Experimental characterization of in-plane permeability of gas diffusion layers. *Journal of Power Sources*, vol. 162(2), (2006), pp. 1226–1231.

[9] S. Comas-Cardona, C. Binetruy, and P. Krawczak. Unidirectional compression of fibre reinforcements. part 2: A continuous permeability tensor measurement. *Composites Science and Technology*, vol. 67(3-4), (2006), pp. 638–645.

[10] B. Gebart. Permeability of unidirectional reinforcements for RTM. *Journal of Composite Materials*, vol. 26(8), (1992), pp. 1100–1133.

[11] J. Bear and M. Y. e. Corapcioglu. *Fundamentals of Transport Phenomena in Porous Media*. Martinus Nijhoff Publ., 1984. ISBN 9789024726899.

[12] M. D. Lepech and V. C. Li. Water permeability of engineered cementitious composites. *Cement and Concrete Composites*, vol. 31(10), (2009), pp. 744–753.

[13] E. A. Mason and A. P. Malinauskas. *Gas transport in porous media : the dusty-gas model*. Chemical engineering monographs 17, Elsevier Scientific Pub. Co, Amsterdam, 1983. ISBN 0444421904.

[14] M. Knudsen. *The kinetic theory of gases*. Methuen & Co., Ltd., London, 1934.

[15] R. A. Serway. *Physics for Scientists and Engineers with Modern Physics*. BrooksCole, 2010. ISBN 9781439048757.

[16] J. Bear. *Dynamics of fluids in porous media*. Courier Dover Publications, 1988. ISBN 9780486656755.

[17] L. Dormieux, D. Kondo, and F.-J. Ulm. *Microporomechanics*. 2006. ISBN 9780470031889.

[18] H. Darcy. Determination des lois d'ecoulement de l'eau a travers le sable. *Les Fontaines Publiques de la Ville de Dijon*, vol. 1, (1856), pp. 590–594.

[19] S. M. Hassanizadeh and W. G. Gray. High velocity flow in porous media. *Transport in Porous Media*, vol. 2(6), (1987), pp. 521–531.

[20] S. Ergun. Fluid flow through packed columns. *Chem. Engng Prog.*, vol. 48(2), (1952), pp. 89–94.

[21] A. E. Scheidegger. *The physics of flow through porous media.* University of Toronto Press, 1974. ISBN 9780802018496.

[22] J. P. Plessis and J. H. Masliyah. Mathematical modelling of flow through consolidated isotropic porous media. *Transport in Porous Media*, vol. 3(2), (1988), pp. 145–161.

[23] G. K. Batchelor. *An introduction to fluid dynamics.* Cambridge University Press, 1967. ISBN 9780521663960.

[24] D. Acheson. *Elementary Fluid Dynamics.* Oxford University Press, USA, 1990. ISBN 019859660X.

[25] M. V. Bruschke and S. G. Advani. A finite element/control volume approach to mold filling in anisotropic porous media. *Polymer Composites*, vol. 11(6), (1990), pp. 398–405.

[26] T. A. K. Sadiq, S. G. Advani, and R. S. Parnas. Experimental investigation of transverse flow through aligned cylinders. *International Journal of Multiphase Flow*, vol. 21(5), (1995), pp. 755–774.

[27] P. Forchheimer. Wasserbewegung durch boden. *Z. Ver. Deutsch Ing.*, vol. 45, (1901), pp. 1782–1788.

[28] H. Brinkman. A calculation of the viscous force exerted by a flowing fluid on a dense swarm of particles. *Applied Scientific Research*, vol. 1(1), (1949), pp. 27–34.

[29] G. S. Beavers and D. D. Joseph. Boundary conditions at a naturally permeable wall. *Journal of Fluid Mechanics*, vol. 30(1), (1967), pp. 197–207.

[30] E. A. Mason. Flow and diffusion of gases in porous media. *The Journal of Chemical Physics*, vol. 46(8), (1967), pp. 3199–3217.

[31] A. Z. Weber and J. Newman. Modeling gas-phase flow in porous media. *International Communications in Heat and Mass Transfer*, vol. 32(7), (2005), pp. 855–860.

[32] R. W. Schofield, A. G. Fane, and C. J. D. Fell. Gas and vapour transport through microporous membranes. i. knudsen-poiseuille transition. *Journal of Membrane Science*, vol. 53(1-2), (1990), pp. 159–171.

[33] R. Datta, S. Dechapanichkul, J. Kim, L. Fang, and U. H. A generalized model for the transport of gases in porous, non-porous, and leaky membranes. i. application to single gases. *Journal of Membrane Science*, vol. 75(3), (1992), pp. 245–263.

[34] L. Klinkenberg. The permeability of porous media to liquids and gases. In *Drilling and Production Practice*, pp. 200–213. American Petroleum Inst., 1941.

[35] F. Jones and W. Owens. A laboratory study of low-permeability gas sands. *Journal of Petroleum Technology*, vol. 32(9), (1980), pp. 1631–1640.

[36] Y.-S. Wu, K. Pruess, and p. Persoff. Gas flow in porous media with Klinkenberg effects. *Transport in Porous Media*, vol. 32(1), (1998), pp. 117–137.

[37] J. G. Heid, J. J. McMahon, R. F. Nielsen, and S. T. Yuster. Study of the permeability of rocks to homogeneous fluids. In *Drilling and Production Practice*. American Petroleum Institute, New York, 1950.

[38] D. A. Stonestrom and J. Rubin. Air permeability and trapped-air content in two soils. *Water Resources Research*, vol. 25(9), (1989), pp. 1959–1969.

[39] S. D. Butt, P. K. Frempong, C. Mukherjee, and J. Upshall. Characterization of the permeability and acoustic properties of an outburst-prone sandstone. *Journal of Applied Geophysics*, vol. 58(1), (2005), pp. 1–12.

[40] C. Valve. *Flow of Fluids Through Valves, Fittings and Pipe TP-410 Metric*. Vervante, 1999, metric Edn. ISBN 1400527139.

[41] N. Epstein. On tortuosity and the tortuosity factor in flow and diffusion through porous media. *Chemical Engineering Science*, vol. 44(3), (1989), pp. 777–779.

[42] C. J. Gommes, A.-J. Bons, S. Blacher, J. H. Dunsmuir, and A. H. Tsou. Practical methods for measuring the tortuosity of porous materials from binary or gray-tone tomographic reconstructions. *AIChE Journal*, vol. 55(8), (2009), pp. 2000–2012.

[43] T. U. Kaempfer, M. Schneebeli, and S. A. Sokratov. A microstructural approach to model heat transfer in snow. *Geophysical Research Letters*, vol. 32(21).

[44] P. Carman. Fluid flow through granular beds. *Transactions of the Institution of Chemical Engineers*, vol. 15, (1937), pp. 150–166.

[45] E. Lord. Air flow through plugs of textile fibres. *Textile Institute Journal*, vol. 46(3), (1955), pp. 191–213.

[46] E. Lord and S. A. Heap. *The origin and assessment of cotton fibre maturity.* Int. Inst. for Cotton, Manchester, England, 1988.

[47] R. E. Collins. *Flow of fluids through porous materials.* Research & Engineering Consultants, Inc, 1990. ISBN 0878140727.

[48] L. E. Nielsen. Models for the permeability of filled polymer systems. *Journal of Macromolecular Science: Part A - Chemistry*, vol. 1(5), (1967), pp. 929–942.

[49] J. A. Wehner, B. Miller, and L. Rebenfeld. Moisture induced changes in fabric structure as evidenced by air permeability measurements. *Textile Research Journal*, vol. 57(5), (1987), pp. 247–256.

[50] C. L. Tucker and R. B. Dessenberger. Governing equations for flow and heat transfer in stationary fiber beds. In *Flow and rheology in polymer composites manufacturing*, pp. 257–323. Elsevier, The Netherlands, 1994, Advani Edn.

[51] W. Zijl and J. Stam. Modeling permeability in imperfectly layered porous media. i. derivation of block-scale permeability tensor for thin grid-blocks. *Mathematical Geology*, vol. 24(8), (1992), pp. 865–883.

[52] M. Li, Y. Gu, Z. Zhang, and Z. Sun. A simple method for the measurement of compaction and corresponding transverse permeability of composite prepregs. *Polymer Composites*, vol. 28(1), (2007), pp. 61–70.

[53] O. Elbouazzaoui and S. Drapier. An experimental assessment of the saturated transverse permeability of non-crimped new concept (NC2) multiaxial fabrics. *Journal of Composite Materials*, vol. 39(13), (2005), pp. 1169–1193.

[54] R. Parnas and F. R. Phelan. The effect of heterogeneous porous-media on mold filling in resin transfer molding. *Sample Quarterly for the Advancement of Material and Process Engineering*, vol. 22(2), (1991), pp. 53–60.

[55] R. S. Parnas, A. J. Salem, T. A. Sadiq, H.-P. Wang, and S. G. Advani. The interaction between micro- and macro-scopic flow in RTM preforms. *Composite Structures*, vol. 27(12), (1994), pp. 93–107.

[56] S. H. Ahn, W. I. Lee, and G. S. Springer. Measurement of the 3-dimensional permeability of fiber preforms using embedded fiber optic sensors. *Journal of Composite Materials*, vol. 29(6), (1995), pp. 714–733.

[57] B. R. Gebart and P. Lidstrom. Measurement of in-plane permeability of anisotropic fiber reinforcements. *Polymer Composites*, vol. 17(1), (1996), pp. 43–51.

[58] Y. D. Parseval, K. M. Pillai, and S. G. Advani. A simple model for the variation of permeability due to partial saturation in dual scale porous media. *Transport in Porous Media*, vol. 27(3), (1997), pp. 243–264.

[59] R. S. Parnas, J. G. Howard, T. L. Luce, and S. G. Advani. Permeability characterization. part 1: A proposed standard reference fabric for permeability. *Polymer Composites*, vol. 16(6), (1995), pp. 429–445.

[60] R. S. Parnas and A. J. Salem. A comparison of the unidirectional and radial in-plane flow of fluids through woven composite reinforcements. *Polymer Composites*, vol. 14(5), (1993), pp. 383–394.

[61] P. Ferland, D. Guittard, and F. Trochu. Concurrent methods for permeability measurement in resin transfer molding. *Polymer Composites*, vol. 17(1), (1996), pp. 149–158.

[62] R. Gauvin, F. Trochu, Y. Lemenn, and L. Diallo. Permeability measurement and flow simulation through fiber reinforcement. *Polymer Composites*, vol. 17(1), (1996), pp. 34–42.

[63] T. Lundstrom, R. Stenberg, R. Bergstrm, H. Partanen, and P. A. Birkeland. In-plane permeability measurements: a nordic round-robin study. *Composites Part A: Applied Science and Manufacturing*, vol. 31(1), (2000), pp. 29–43.

[64] S. Amico and C. Lekakou. An experimental study of the permeability and capillary pressure in resin-transfer moulding. *Composites Science and Technology*, vol. 61(13), (2001), pp. 1945–1959.

[65] G. Neale and W. Nader. Practical significance of brinkman's extension of darcy's law: Coupled parallel flows within a channel and a bounding porous medium. *The Canadian Journal of Chemical Engineering*, vol. 52(4), (1974), pp. 475–478.

[66] R. Parnas and Y. Cohen. Power-law fluids in porous media. *Chemical Engineering Communications*, vol. 53(1-6), (1987), pp. 3–22.

[67] W. B. Young and S. F. Wu. Permeability measurement of bidirectional woven glass fibers. *Journal of Reinforced Plastics and Composites*, vol. 14(10), (1995), pp. 1108–1120.

[68] J. Weitzenbck, R. Shenoi, and P. Wilson. Radial flow permeability measurement. part a: Theory. *Composites Part A: Applied Science and Manufacturing*, vol. 30(6), (1999), pp. 781–796.

[69] K. Hoes, D. Dinescu, H. Sol, M. Vanheule, R. S. Parnas, Y. Luo, and I. Verpoest. New set-up for measurement of permeability properties of fibrous reinforcements for RTM. *Composites Part A: Applied Science and Manufacturing*, vol. 33(7), (2002), pp. 959–969.

[70] Q. Liu, R. S. Parnas, and H. S. Giffard. New set-up for in-plane permeability measurement. *Composites Part A: Applied Science and Manufacturing*, vol. 38(3), (2006), pp. 954–962.

[71] C. Lekakou, M. A. K. Johari, D. Norman, and M. G. Bader. Measurement techniques and effects on in-plane permeability of woven cloths in resin transfer moulding. *Composites Part A: Applied Science and Manufacturing*, vol. 27(5), (1996), pp. 401–408.

[72] P. B. Nedanov and S. G. Advani. A method to determine 3D permeability of fibrous reinforcements. *Journal of Composite Materials*, vol. 36(2), (2002), pp. 241–254.

[73] J. R. Weitzenbock, R. A. Shenoi, and P. A. Wilson. Measurement of three-dimensional permeability. *Composites Part A: Applied Science and Manufacturing*, vol. 29(1-2), (1998), pp. 159–169.

[74] M. J. Buntain and S. Bickerton. Compression flow permeability measurement: a continuous technique. *Composites Part A: Applied Science and Manufacturing*, vol. 34(5), (2003), pp. 445–457.

[75] T. G. Gutowski, T. Morigaki, and Z. Cai. The consolidation of laminate composites. *Journal of Composite Materials*, vol. 21(2), (1987), pp. 172 – 188.

[76] H. V. Groenewoud. Methods and apparatus for measuring air permeability of the soil. *Soil Science*, vol. 106(4), (1968), pp. 275–279.

[77] B. V. Iversen, P. Schjnning, T. G. Poulsen, and P. Moldrup. In situ, on-site and laboratory measurements of soil air permeability: Boundary conditions and measurement scale. *Soil Science*, vol. 166(2), (2001), pp. 97–106.

[78] M. D. M. Innocentini, A. C. Rizzi, L. A. Nascimento, and V. C. Pandolfelli. The pressure-decay technique for air permeability evaluation of dense refractory ceramics. *Cement and Concrete Research*, vol. 34(2), (2004), pp. 293–298.

[79] D. S. Springer, H. A. Loaiciga, S. J. Cullen, and L. G. Everett. Air permeability of porous materials under controlled laboratory conditions. *Ground Water*, vol. 36(4), (1998), pp. 558–565.

[80] J. Massmann and L. Johnson. Exercises illustrating flow in porous media. *Ground Water*, vol. 39(4), (2001), pp. 499–503.

[81] D. B. McWhorter. Unsteady radial flow of gas in the vadose zone. *Journal of Contaminant Hydrology*, vol. 5(3), (1990), pp. 297–314.

[82] H. Li, J. J. Jiao, and M. Luk. A falling-pressure method for measuring air permeability of asphalt in laboratory. *Journal of Hydrology*, vol. 286(1-4), (2004), pp. 69–77.

[83] J. S. Cho and D. Ellett. Soil air permeability measurement with a transient pressure buildup method. *Hazardous Waste & Hazardous Materials*, vol. 12(4), (1995), pp. 365–371.

[84] T. L. Starr and N. Hablutzel. Measurement of gas transport through fiber preforms and densified composites for chemical vapor infiltration. *Journal of the American Ceramic Society*, vol. 81(5), (1998), pp. 1298–1304.

[85] M.-K. Um, I. M. Daniel, and B. W. Childs. A gas flow method for determination of in-plane permeability of fiber preforms. *Polymer Composites*, vol. 22(1), (2001), pp. 47–56.

[86] S. K. Kim, J. G. Opperer, D.-H. Kim, and I. M. Daniel. Determination of in-plane permeability of fiber preforms by the gas flow method using pressure measurements. *Polymer Composites*, vol. 24(1), (2003), pp. 34–44.

[87] R. Pomeroy, S. Grove, J. Summerscales, Y. Wang, and A. Harper. Measurement of permeability of continuous filament mat glass-fibre reinforcements by saturated radial airflow. *Composites Part A: Applied Science and Manufacturing*, vol. 38(5), (2007), pp. 1439–1443.

[88] J. W. Massmann and M. Madden. Estimating air conductivity and porosity from vadose-zone pumping tests. *Journal of Environmental Engineering*, vol. 120(2), (1994), pp. 313–328.

[89] J. W. Massmann. Applying groundwater flow models in vapor extraction system design. *Journal of Environmental Engineering*, vol. 115(1), (1989), pp. 129–149.

[90] C. Shan, R. Falta, and I. Javandel. Analytical solutions for steady-state gas-flow to a soil vapor extraction well. *Water Resources Research*, vol. 28(4), (1992), pp. 1105–1120.

[91] C. J. Joss and A. L. Baehr. *Documentation of AIR2D, a computer program to simulate two-dimensional axisymmetric air flow in the unsaturated zone.* U.S. Dept. of the Interior, U.S. Geological Survey, West Trenton, 1997.

[92] S. K. Kim and I. M. Daniel. Transient gas flow technique for inspection of fiber preforms in resin transfer molding. *Composites Part A: Applied Science and Manufacturing*, vol. 36(12), (2005), pp. 1694–1699.

[93] S. K. Kim, J. G. Opperer, and I. M. Daniel. Gas flow method for detecting local preform defects by inverse estimation of space-varying permeability. *Journal of Composite Materials*, vol. 37(15), (2003), pp. 1367–1383.

[94] G. V. Reklaitis, A. Ravindran, and K. M. Ragsdell. *Engineering Optimization: Methods and Applications.* John Wiley & Sons, New York, 1983, 1st Edn. ISBN 9780471055792.

[95] IMSL Math/Library user's guide, 1994.

[96] H. S. Carslaw and J. C. Jaeger. *Conduction of Heat in Solids.* Oxford University Press, Stock, 1986, 2nd Edn. ISBN 9780198533689.

[97] W. J. Minkowycz, E. M. Sparrow, and J. Y. Murthy. *Handbook of Numerical Heat Transfer.* Wiley-Interscience, 2006, 2nd Edn. ISBN 9780471830931.

[98] Y. Luo, I. Verpoest, K. Hoes, M. Vanheule, H. Sol, and A. Cardon. Permeability measurement of textile reinforcements with several test fluids. *Composites Part A: Applied Science and Manufacturing*, vol. 32(10), (2001), pp. 1497–1504.

[99] K. Adams, B. Miller, and L. Rebenfeld. Forced in-plane flow of an epoxy resin in fibrous networks. *Polymer Engineering and Science*, vol. 26(20), (1986), pp. 1434–1441.

[100] J. G. Williams, C. E. M. Morris, and B. C. Ennis. Liquid flow through aligned fiber beds. *Polymer Engineering & Science*, vol. 14(6), (1974), pp. 413–419.

[101] L. Trevino, K. Rupel, W. B. Young, M. J. Liou, and L. J. Lee. Analysis of resin injection molding in molds with preplaced fiber mats. i: Permeability and compressibility measurements. *Polymer Composites*, vol. 12(1), (1991), pp. 20–29.

[102] J. B. Scarborough. *Numerical Mathematical Analysis*. Oxford & Ibh Publishing Co. Pvt Ltd, Baltimore, 2008. ISBN 9780009780021.

[103] W. H. Press, B. P. Flannery, S. A. Teukolsky, and W. T. Vetterling. *The Art of Scientific Computing*. Numerical Recipes, Cambridge University Press, Cambridge, England, 1989. ISBN 9780521880688.

[104] S. Bickerton, S. G. Advani, R. V. Mohan, and D. R. Shires. Experimental analysis and numerical modeling of flow channel effects in resin transfer molding. *Polymer Composites*, vol. 21(1), (2000), pp. 134–153.

[105] G. B. Dantzig and M. N. Thapa. *Linear Programming: Theory and extensions*. Springer, 2003. ISBN 9780387986135.

[106] J. A. Nelder and R. Mead. A simplex method for function minimization. *The Computer Journal*, vol. 7(4), (1965), pp. 308–313.

[107] M. F. De Boodt and D. Kirkham. Anisotropy and measurement of air permeability of soil clods. *Soil Science*, vol. 76(2), (1953), pp. 127–134.

[108] M. Maasland and D. Kirkham. Theory and measurement of anisotropic air permeability in soil. *Soil Science Society of America Journal*, vol. 19(4), (1955), pp. 395–400.

[109] K. Garbesi, R. G. Sextro, A. L. Robinson, J. D. Wooley, J. A. Owens, and W. W. Nazaroff. Scale dependence of soil permeability to air: Measurement method and field investigation. *Water Resources Research*, vol. 32(3), (1996), pp. 547–560.

[110] S. S. Tavares. *Optimisation of low pressure processing for honeycomb sandwich structures*. Ph.D. thesis, Universidade Nova de Lisboa, 2009.

[111] W. Tanikawa and T. Shimamoto. Comparison of Klinkenberg-corrected gas permeability and water permeability in sedimentary rocks. *International*

Journal of Rock Mechanics and Mining Sciences, vol. 46(2), (2009), pp. 229–238.

[112] G. Morren, S. Bossuyt, and H. Sol. 2D permeability tensor identification of fibrous reinforcements for RTM using an inverse method. *Composites Part A: Applied Science and Manufacturing*, vol. 39(9), (2008), pp. 1530–1536.

APPENDIX A

Set-up design : results tables and objective function plots

A.1 1D set-up design for 2D permeability measurement

A.1.1 Tables

Fig. No.	$[\alpha', K_1', R_k']$ ([-,m^2,-])	Locations ([m,m])	Robustness		Accuracy	
			$\partial\varepsilon/\partial\alpha^{[+,-]}$	$\partial\varepsilon/\partial R_k^{[+,-]}$	$\partial\varepsilon/\partial s$	$\boldsymbol{e}_s'$
Fig. A.1(a)	[0,1e-12,0.1]	② [0.0,0.0]	[0.06,0.07]	[0.90,0.94]	0.01	[-0.21,0.98]
Fig. A.1(b)	[0,1e-12,0.1]	④ [0.1,0.0]	[0.21,0.30]	[0.53,0.55]	0.12	[0.00,1.00]
Fig. A.1(c)	[0,1e-12,0.1]	⑤ [0.1,0.1]	[0.05,0.05]	[0.53,0.55]	0.03	[-0.33,0.94]
Fig. A.1(d)	[0,1e-12,0.1]	⑥ [0.1,0.2]	[0.30,0.21]	[0.53,0.55]	0.12	[0.00,-1.00]
Fig. A.1(e)	[0,1e-12,0.1]	② ④ ⑥	[0.38,0.38]	[1.57,1.63]	0.38	[-0.21,-0.98]
Fig. A.2(a)	[π/6,1e-12,0.1]	② [0.0,0.0]	[0.73,0.70]	[0.62,0.65]	0.04	[0.64,-0.77]
Fig. A.2(b)	[π/6,1e-12,0.1]	④ [0.1,0.0]	[0.47,0.40]	[0.58,0.61]	0.11	[-0.82,0.57]
Fig. A.2(c)	[π/6,1e-12,0.1]	⑤ [0.1,0.1]	[0.45,0.45]	[0.33,0.34]	0.05	[0.72,-0.69]
Fig. A.2(d)	[π/6,1e-12,0.1]	⑥ [0.1,0.2]	[0.39,0.49]	[0.09,0.09]	0.07	[-1.00,0.00]
Fig. A.2(e)	[π/6,1e-12,0.1]	② ④ ⑥	[1.28,1.26]	[1.11,1.15]	0.30	[-0.82,0.57]

Table A.1: Robustness and accuracy in various cases ($R_k' = K_1'/K_2' = 0.1$).

Fig. No.	$[\alpha', K_1', R_k']$ ([-,m^2,-])	Locations ([m,m])	Robustness		Accuracy	
			$\partial\varepsilon/\partial\alpha^{[+,-]}$	$\partial\varepsilon/\partial R_k^{[+,-]}$	$\partial\varepsilon/\partial s$	$\boldsymbol{e}_s'$
Fig. A.3(a)	[0,1e-11,1.0]	② [0.0,0.0]	[-0.00,-0.00]	[0.86,0.94]	0.00	[0.00,1.00]
Fig. A.3(b)	[0,1e-11,1.0]	④ [0.1,0.0]	[0.00,-0.00]	[0.51,0.55]	0.00	[0.00,1.00]
Fig. A.3(c)	[0,1e-11,1.0]	⑤ [0.1,0.1]	[-0.00,-0.00]	[0.51,0.55]	0.00	[0.00,1.00]
Fig. A.3(d)	[0,1e-11,1.0]	⑥ [0.1,0.2]	[-0.00,0.00]	[0.51,0.55]	0.00	[0.00,-1.00]
Fig. A.3(e)	[0,1e-11,1.0]	② ④ ⑥	[-0.00,-0.00]	[1.50,1.64]	0.00	[0.00,1.00]
Fig. A.4(a)	[π/6,1e-11,1.0]	② [0.0,0.0]	[-0.00,0.00]	[0.65,0.70]	0.00	[0.00,-1.00]
Fig. A.4(b)	[π/6,1e-11,1.0]	④ [0.1,0.0]	[-0.00,0.00]	[0.53,0.57]	0.00	[0.00,-1.00]
Fig. A.4(c)	[π/6,1e-11,1.0]	⑤ [0.1,0.1]	[-0.00,0.00]	[0.38,0.41]	0.00	[0.00,-1.00]
Fig. A.4(d)	[π/6,1e-11,1.0]	⑥ [0.1,0.2]	[-0.00,0.00]	[0.26,0.27]	0.00	[0.00,1.00]
Fig. A.4(e)	[π/6,1e-11,1.0]	② ④ ⑥	[-0.00,0.00]	[1.16,1.25]	0.00	[0.00,-1.00]
Fig. A.5(a)	[0,1e-11,2.0]	② [0.0,0.0]	[0.02,0.02]	[0.90,0.94]	0.01	[0.12,-0.99]
Fig. A.5(b)	[0,1e-11,2.0]	④ [0.1,0.0]	[0.12,0.14]	[0.53,0.55]	0.05	[-0.13,0.99]
Fig. A.5(c)	[0,1e-11,2.0]	⑤ [0.1,0.1]	[0.01,0.01]	[0.53,0.55]	0.01	[0.12,-0.99]
Fig. A.5(d)	[0,1e-11,2.0]	⑥ [0.1,0.2]	[0.14,0.12]	[0.53,0.55]	0.05	[-0.13,-0.99]
Fig. A.5(e)	[0,1e-11,2.0]	② ④ ⑥	[0.19,0.19]	[1.57,1.63]	0.19	[0.00,1.00]
Fig. A.6(a)	[π/6,1e-11,2.0]	② [0.0,0.0]	[0.23,0.21]	[0.65,0.67]	0.02	[-0.21,-0.98]
Fig. A.6(b)	[π/6,1e-11,2.0]	④ [0.1,0.0]	[0.08,0.06]	[0.49,0.51]	0.03	[0.19,0.98]
Fig. A.6(c)	[π/6,1e-11,2.0]	⑤ [0.1,0.1]	[0.13,0.12]	[0.40,0.41]	0.01	[-0.21,-0.98]
Fig. A.6(d)	[π/6,1e-11,2.0]	⑥ [0.1,0.2]	[0.20,0.20]	[0.32,0.32]	0.06	[-0.33,-0.94]
Fig. A.6(e)	[π/6,1e-11,2.0]	② ④ ⑥	[0.42,0.38]	[1.16,1.20]	0.14	[-0.21,-0.98]

Table A.2: Robustness and accuracy in various cases of (quasi)isotropic materials($R_k' = K_1'/K_2' = 1$ and 2).

Fig. No.	$[\alpha', K_1', R_k']$ ([-,m^2,-])	Locations ([m,m])	Robustness		Accuracy	
			$\partial\varepsilon/\partial\alpha^{[+,-]}$	$\partial\varepsilon/\partial R_k^{[+,-]}$	$\partial\varepsilon/\partial s$	$\boldsymbol{e}_s'$
Fig. A.7(a)	[0,1e-11,5.0]	② [0.0,0.0]	[0.04,0.05]	[0.86,0.94]	0.01	[0.21,-0.98]
Fig. A.7(b)	[0,1e-11,5.0]	④ [0.1,0.0]	[0.29,0.36]	[0.51,0.55]	0.10	[-0.33,0.95]
Fig. A.7(c)	[0,1e-11,5.0]	⑤ [0.1,0.1]	[0.02,0.02]	[0.51,0.55]	0.02	[0.00,1.00]
Fig. A.7(d)	[0,1e-11,5.0]	⑥ [0.1,0.2]	[0.36,0.29]	[0.51,0.55]	0.10	[-0.33,-0.95]
Fig. A.7(e)	[0,1e-11,5.0]	② ④ ⑥	[0.45,0.45]	[1.50,1.64]	0.45	[0.21,-0.98]
Fig. A.8(a)	[π/6,1e-11,5.0]	② [0.0,0.0]	[0.58,0.49]	[0.69,0.74]	0.03	[0.65,0.76]
Fig. A.8(b)	[π/6,1e-11,5.0]	④ [0.1,0.0]	[0.15,0.10]	[0.45,0.50]	0.05	[0.46,0.89]
Fig. A.8(c)	[π/6,1e-11,5.0]	⑤ [0.1,0.1]	[0.30,0.25]	[0.43,0.45]	0.03	[-0.33,-0.95]
Fig. A.8(d)	[π/6,1e-11,5.0]	⑥ [0.1,0.2]	[0.56,0.52]	[0.46,0.47]	0.09	[0.82,0.57]
Fig. A.8(e)	[π/6,1e-11,5.0]	② ④ ⑥	[1.04,0.90]	[1.24,1.33]	0.26	[0.75,0.66]
Fig. A.9(a)	[0,1e-11,10.]	② [0.0,0.0]	[0.05,0.08]	[0.86,0.94]	0.02	[0.33,-0.95]
Fig. A.9(b)	[0,1e-11,10.]	④ [0.1,0.0]	[0.46,0.57]	[0.51,0.55]	0.11	[-0.46,0.89]
Fig. A.9(c)	[0,1e-11,10.]	⑤ [0.1,0.1]	[0.03,0.03]	[0.51,0.55]	0.03	[0.00,-1.00]
Fig. A.9(d)	[0,1e-11,10.]	⑥ [0.1,0.2]	[0.57,0.46]	[0.51,0.55]	0.11	[-0.46,-0.89]
Fig. A.9(e)	[0,1e-11,10.]	② ④ ⑥	[0.73,0.73]	[1.50,1.64]	0.63	[0.46,-0.89]
Fig. A.10(a)	[π/6,1e-11,10.]	② [0.0,0.0]	[0.77,0.64]	[0.67,0.72]	0.04	[-0.54,-0.84]
Fig. A.10(b)	[π/6,1e-11,10.]	④ [0.1,0.0]	[0.17,0.11]	[0.39,0.44]	0.04	[0.57,0.82]
Fig. A.10(c)	[π/6,1e-11,10.]	⑤ [0.1,0.1]	[0.39,0.31]	[0.41,0.45]	0.06	[-0.46,-0.89]
Fig. A.10(d)	[π/6,1e-11,10.]	⑥ [0.1,0.2]	[0.82,0.73]	[0.58,0.59]	0.08	[0.86,0.50]
Fig. A.10(e)	[π/6,1e-11,10.]	② ④ ⑥	[1.43,1.20]	[1.25,1.34]	0.25	[0.82,0.57]

Table A.3: Robustness and accuracy in various cases of anisotropic materials ($R_k' = K_1'/K_2' = 5$ and 10).

A.1.2 Figures

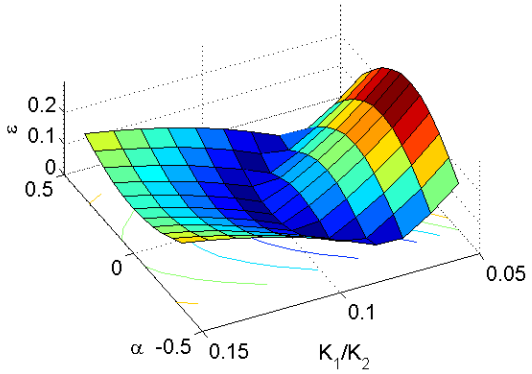

(a) point ②

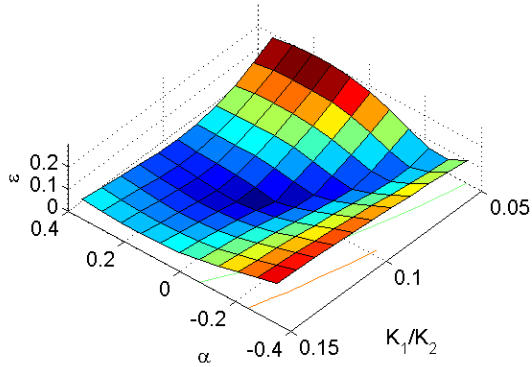

(b) point ④

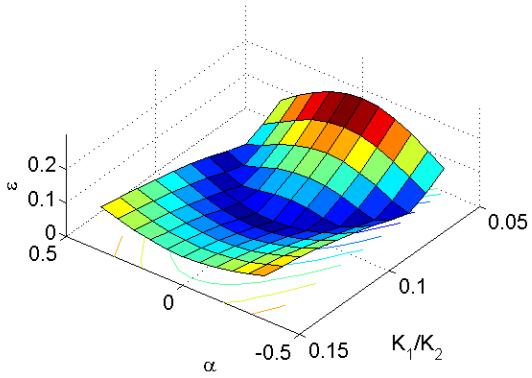

(c) point ⑤

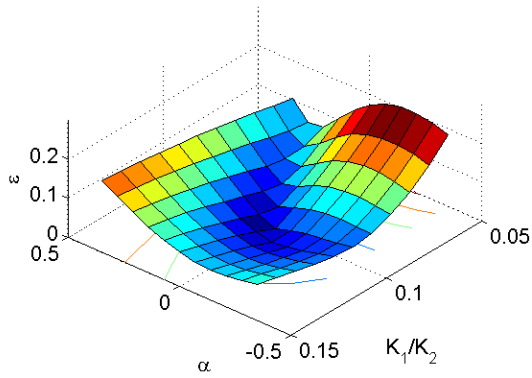

(d) point ⑥

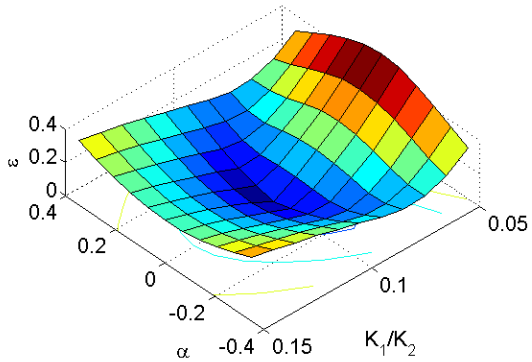

(e) points ② ④ ⑥

Fig. A.1: Objective function ε at different tested locations (input parameters: $R'_k = 0.1$ - $K'_1 = 1 \times 10^{-12}$ m^2, $K'_2 = 1 \times 10^{-11}$ m^2 and $\alpha' = 0$).

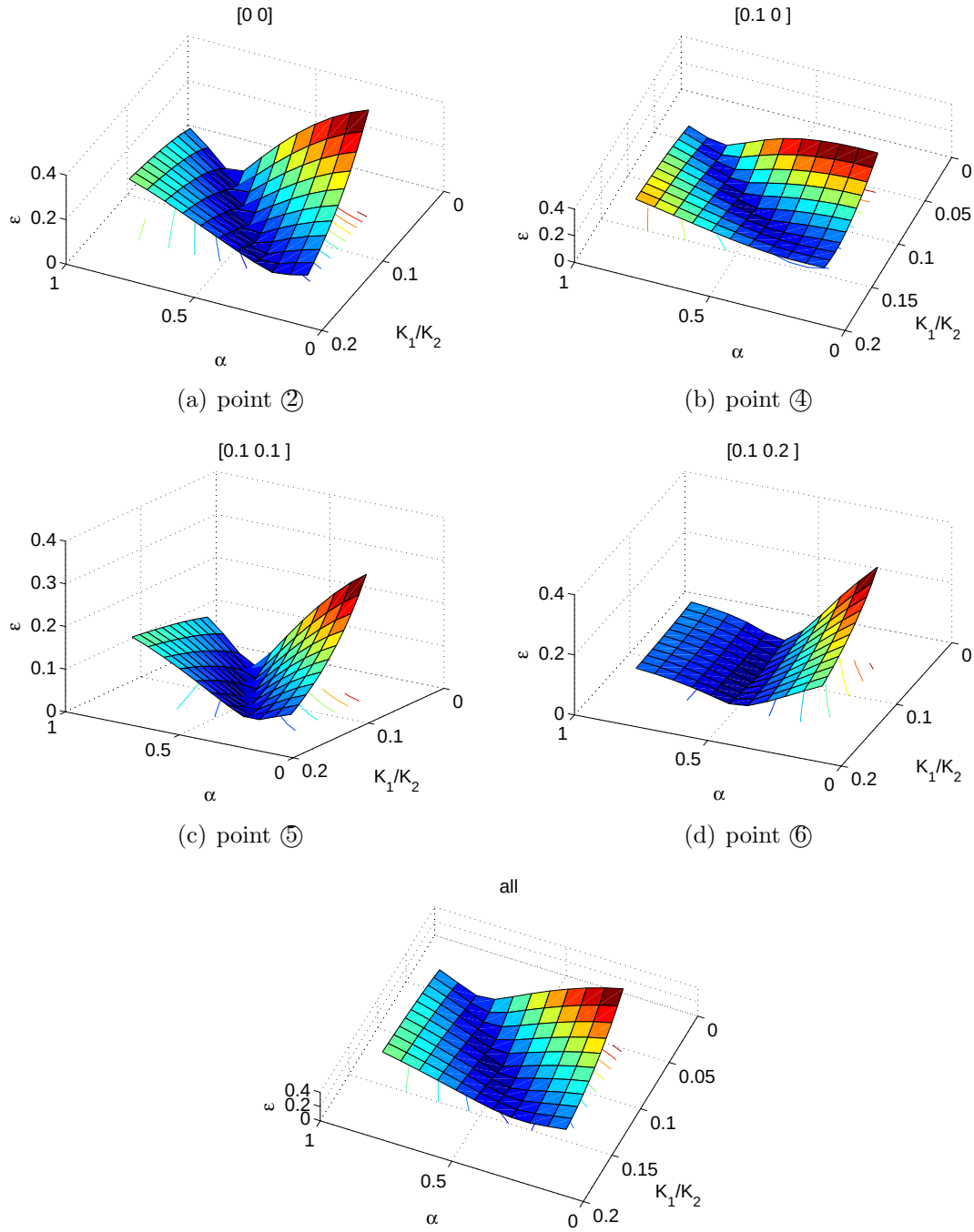

(a) point ②

(b) point ④

(c) point ⑤

(d) point ⑥

(e) points ② ④ ⑥

Fig. A.2: Objective function ε at different tested locations (input parameters: $R'_k = 0.1$ - $K'_1 = 1 \times 10^{-12}$ m^2, $K'_2 = 1 \times 10^{-11}$ m^2 and $\alpha' = \pi/6$).

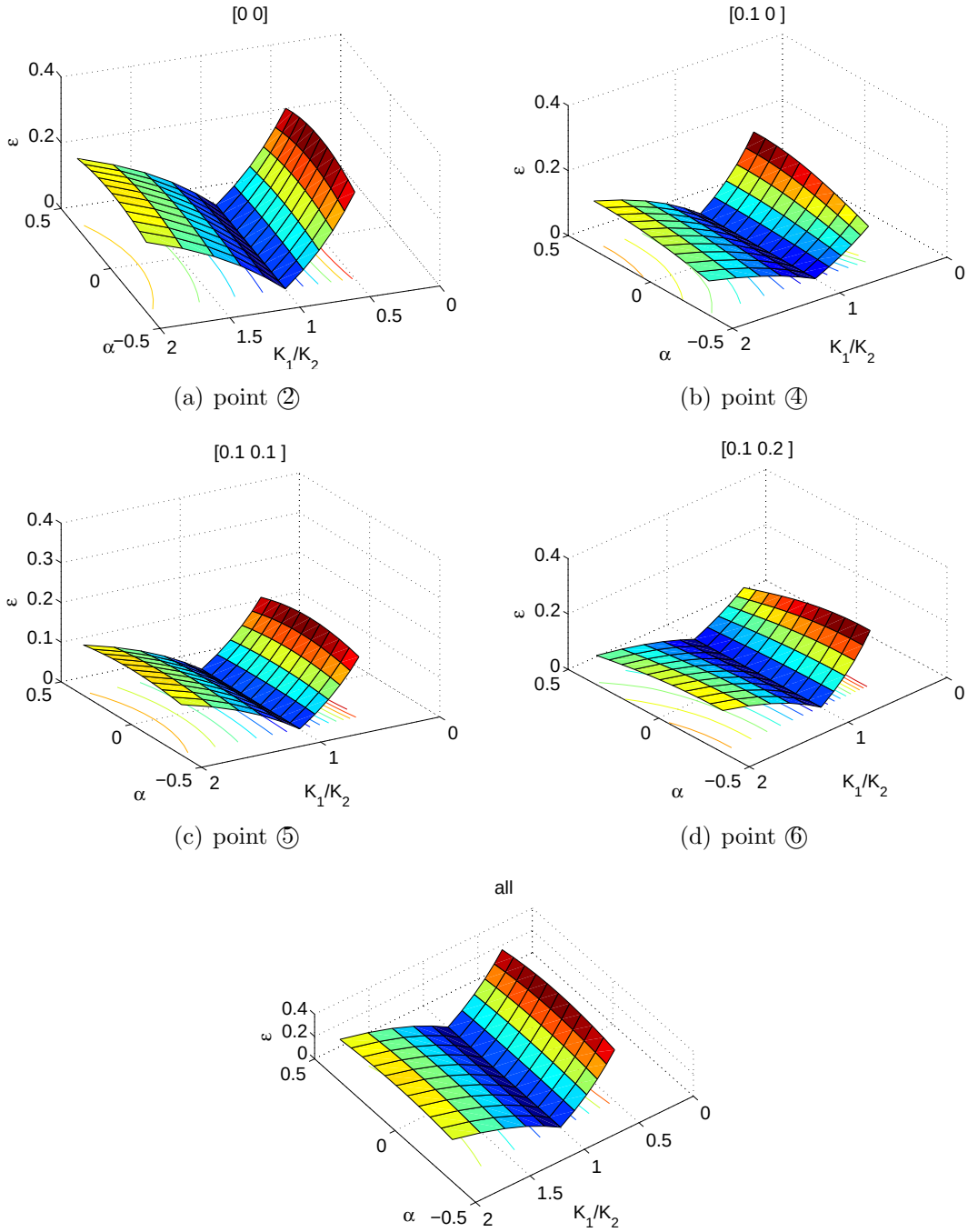

(a) point ②

(b) point ④

(c) point ⑤

(d) point ⑥

(e) points ② ④ ⑥

Fig. A.3: Objective function ε at different tested locations (input parameters: $R'_k = 1$ - $K'_1 = 1 \times 10^{-11}$, $K'_= 1 \times 10^{-11}$, and $\alpha' = 0$).

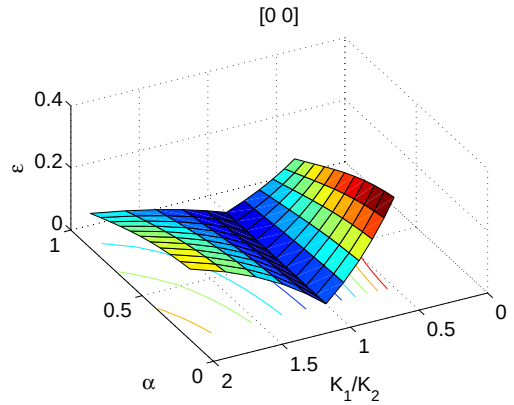

(a) point ②

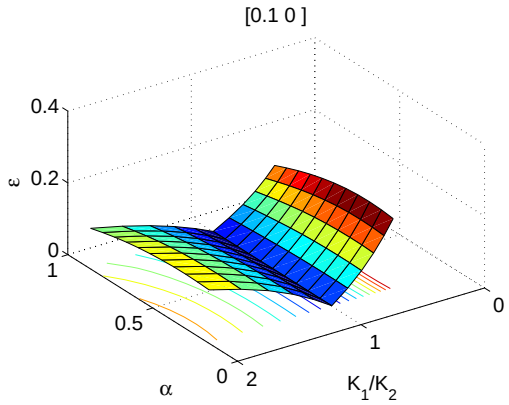

(b) point ④

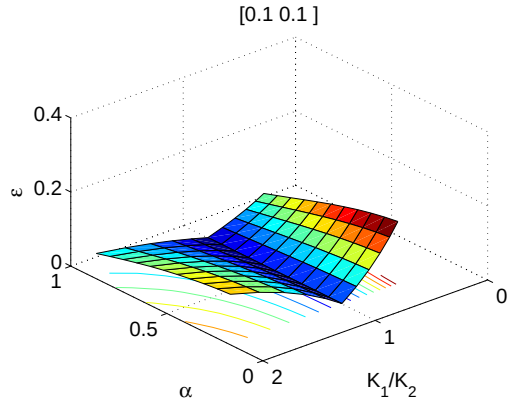

(c) point ⑤

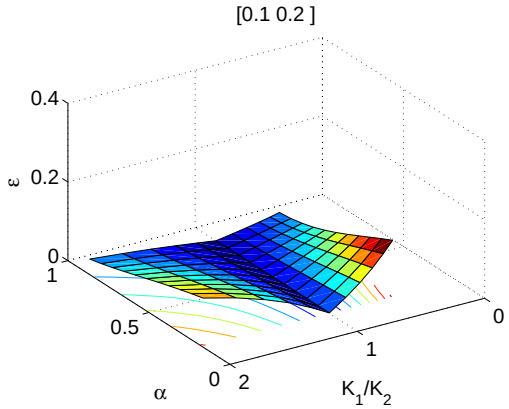

(d) point ⑥

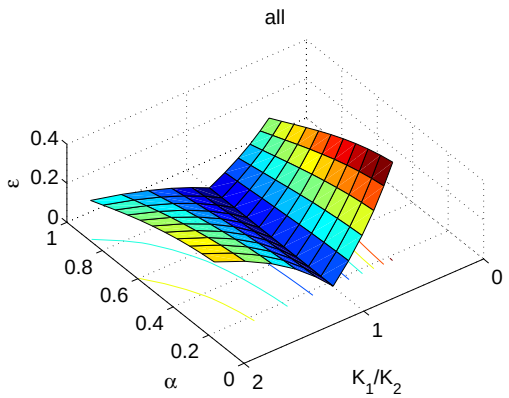

(e) point ② ④ ⑥

Fig. A.4: Objective function ε at different tested locations (input parameters: $R'_k = 1$- $K'_1 = 1 \times 10^{-11}$, $K'_2 = 1 \times 10^{-11}$, and $\alpha' = \pi/6$).

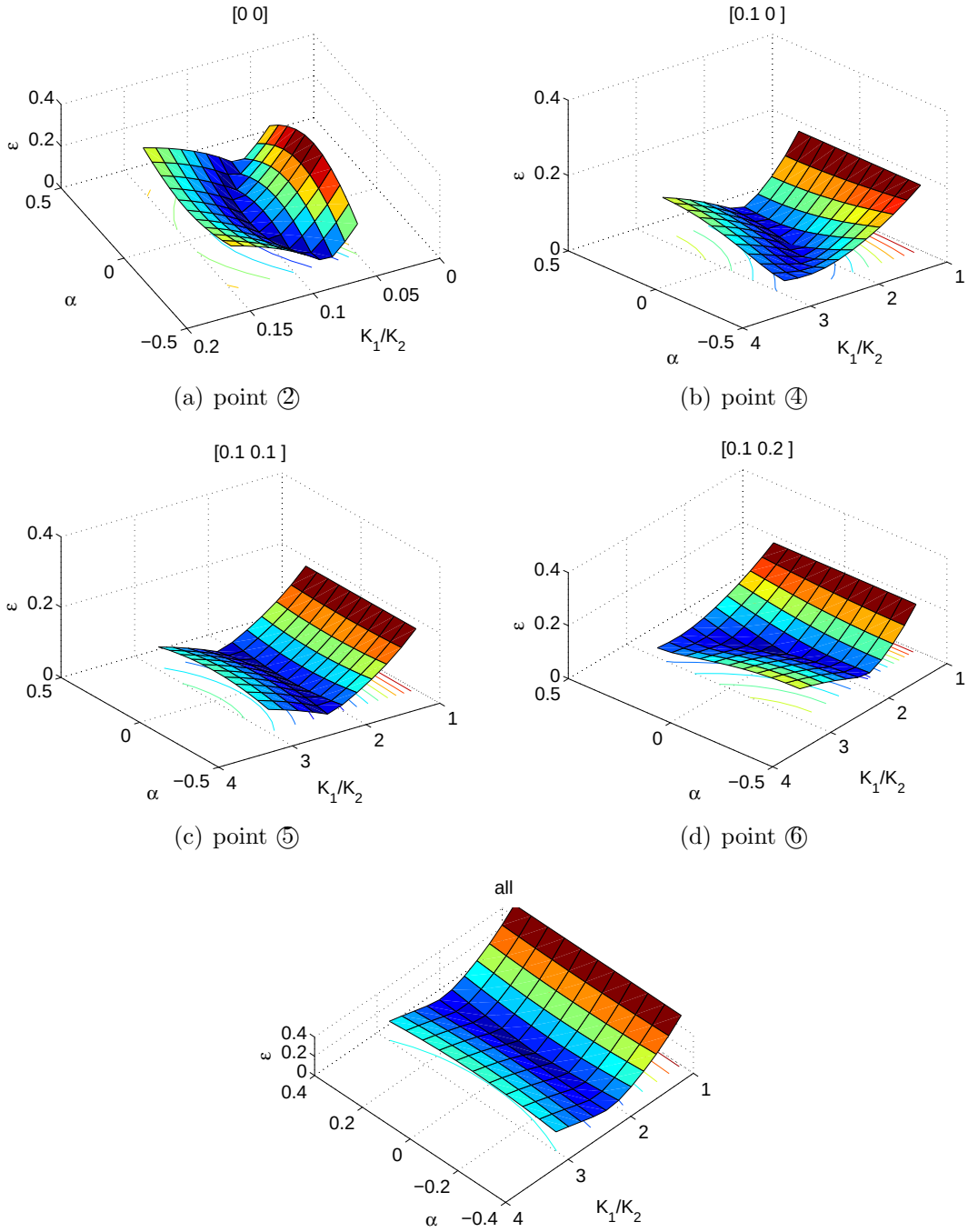

(a) point ②

(b) point ④

(c) point ⑤

(d) point ⑥

(e) points ② ④ ⑥

Fig. A.5: Objective function ε at different tested locations (input parameters: $R'_k = 2$ - $K'_1 = 1 \times 10^{-11}$, $K'_2 = 0.5 \times 10^{-11}$, and $\alpha' = 0$).

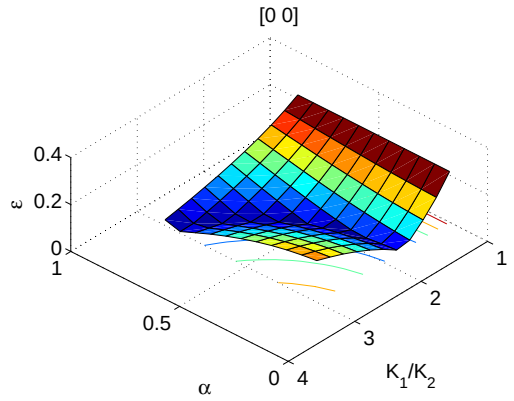

(a) $\alpha' = \pi/6$, point ②

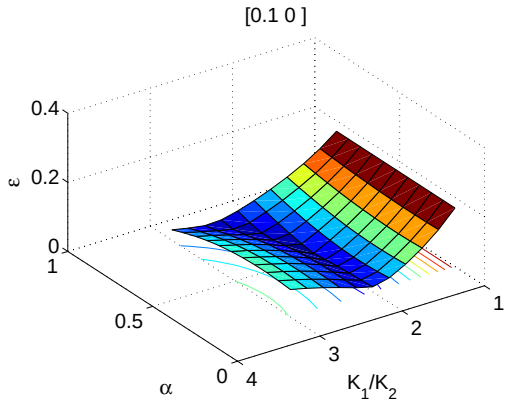

(b) $\alpha' = \pi/6$, point ④

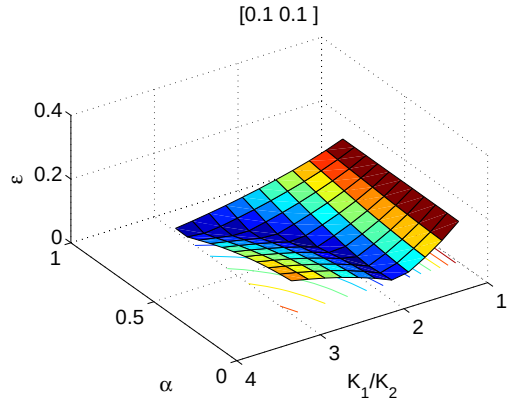

(c) $\alpha' = \pi/6$, point ⑤

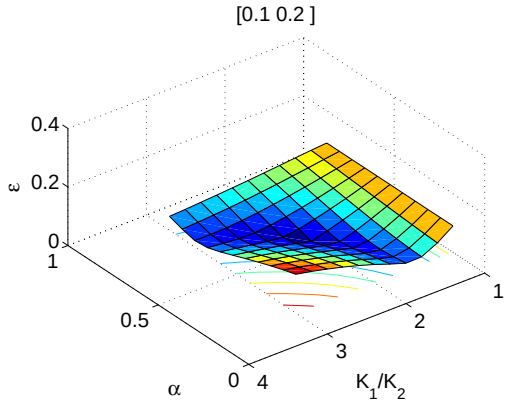

(d) $\alpha' = \pi/6$, point ⑥

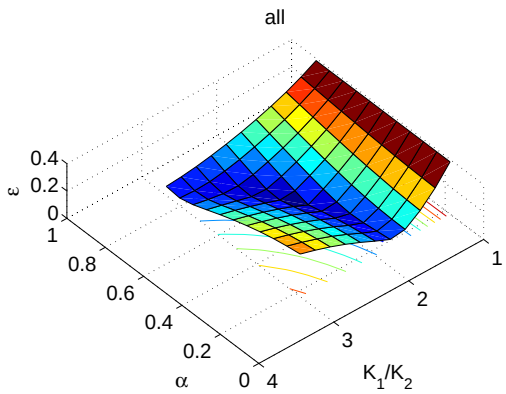

(e) $\alpha' = \pi/6$, point ② ④ ⑥

Fig. A.6: Objective function ε at different tested locations (input parameters: $R'_k = 2$ - $K'_1 = 1 \times 10^{-11}$, $K'_2 = 0.5 \times 10^{-11}$, and $\alpha = \pi/6$).

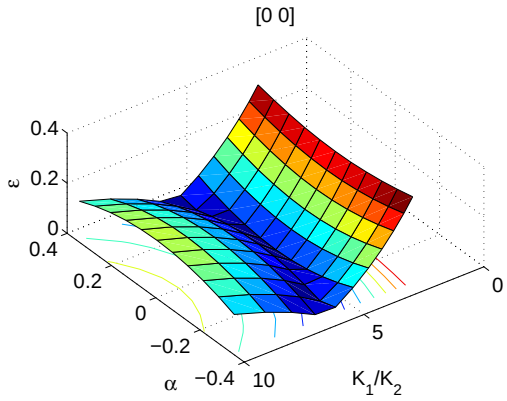

(a) $\alpha' = 0$, point ②

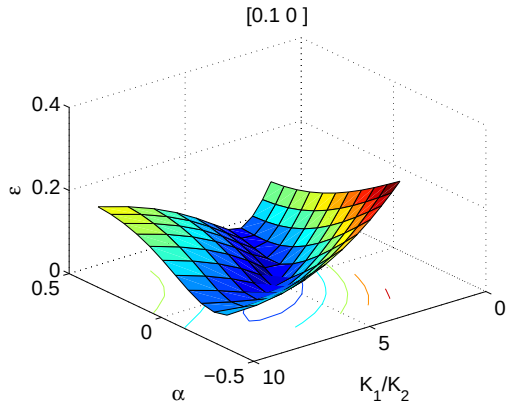

(b) $\alpha' = 0$, point ④

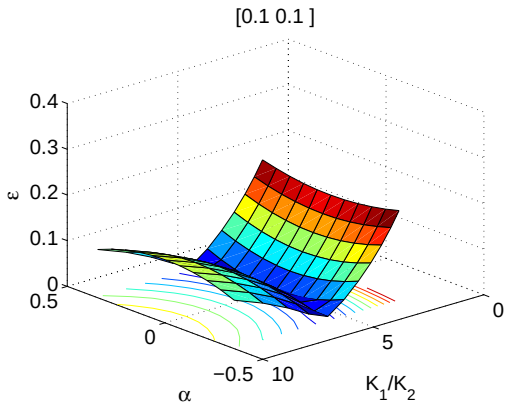

(c) $\alpha' = 0$, point ⑤

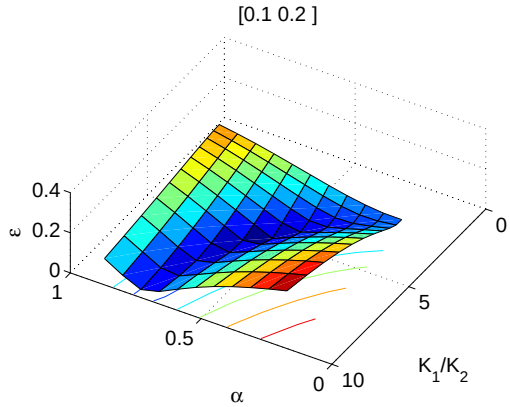

(d) $\alpha' = 0$, point ⑥

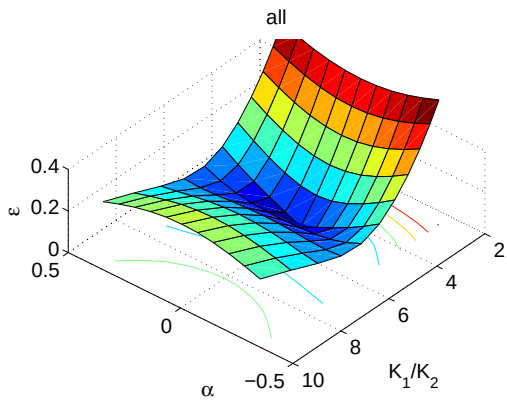

(e) $\alpha' = 0$, point ② ④ ⑥

Fig. A.7: Objective function ε at different tested locations (input parameters: $R'_k = 5$ - $K'_1 = 1 \times 10^{-11}$, $K'_2 = 0.2 \times 10^{-11}$, and $\alpha = 0$).

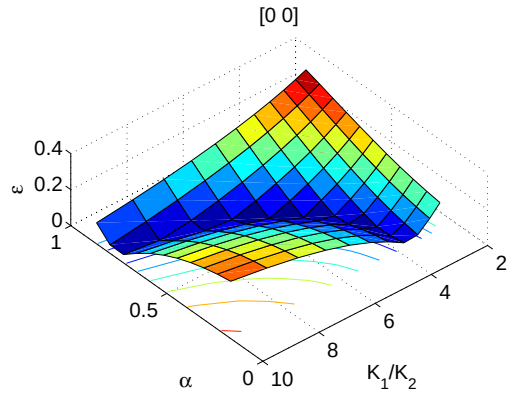

(a) point ②

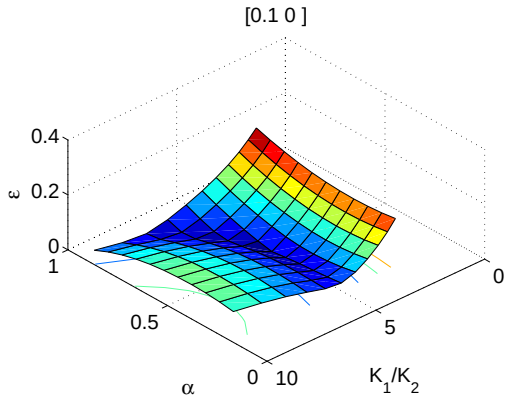

(b) point ④

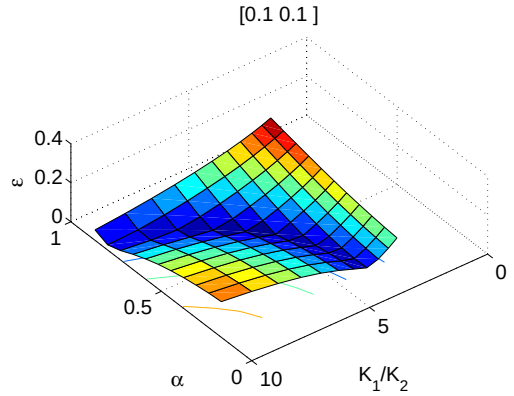

(c) point ⑤

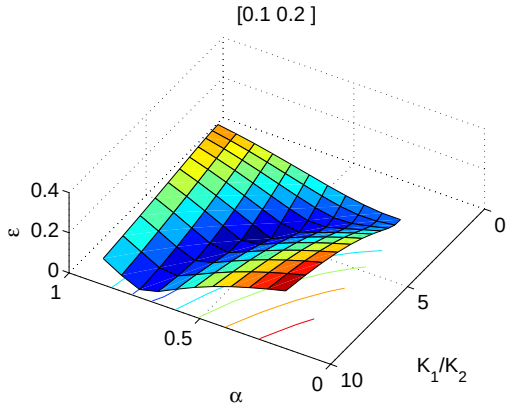

(d) point ⑥

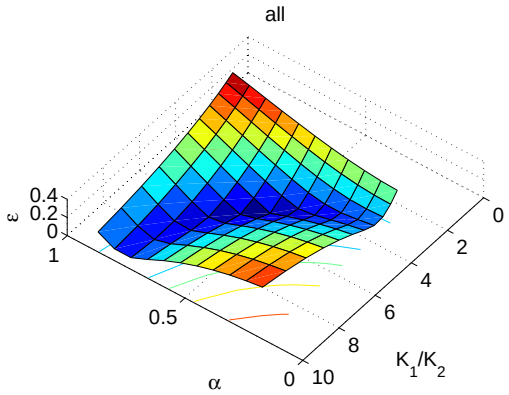

(e) points ② ④ ⑥

Fig. A.8: Objective function ε at different tested locations (input parameters: $R'_k = 5$ - $K'_1 = 1 \times 10^{-11}$, $K'_2 = 0.2 \times 10^{-11}$, and $\alpha = \pi/6$).

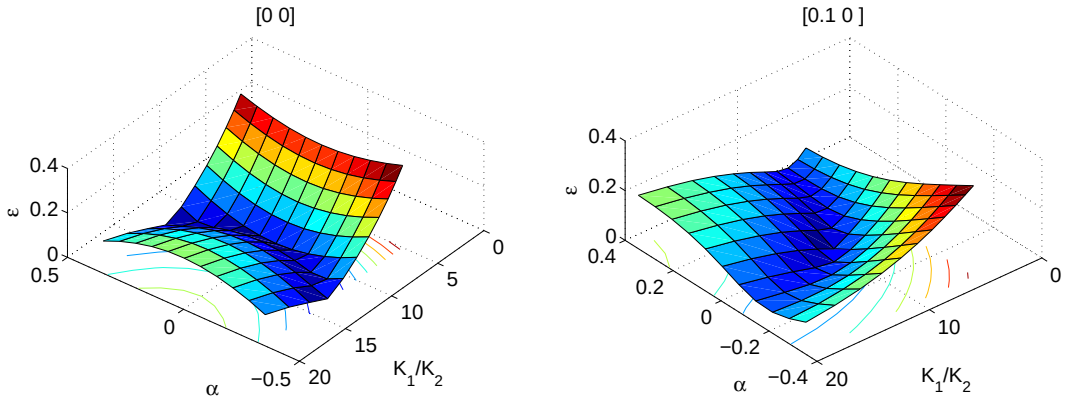

(a) point ②

(b) point ④

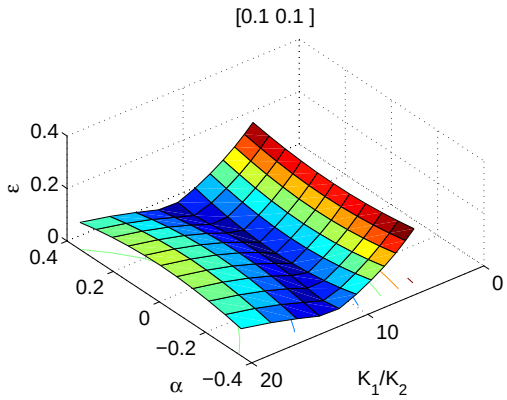

(c) point ⑤

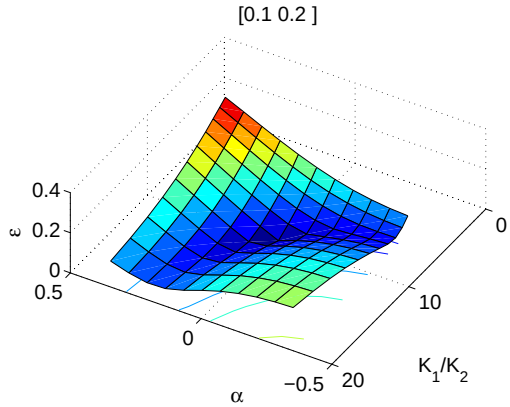

(d) point ⑥

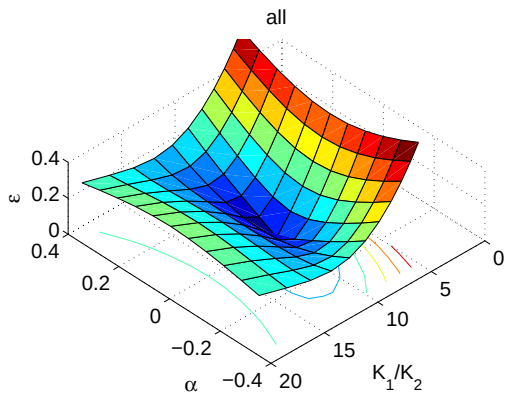

(e) point ② ④ ⑥

Fig. A.9: Objective function ε at different tested locations (input parameters: $R'_k = 10$ - $K'_1 = 1 \times 10^{-11}$, $K'_2 = 0.1 \times 10^{-11}$, and $\alpha' = 0$).

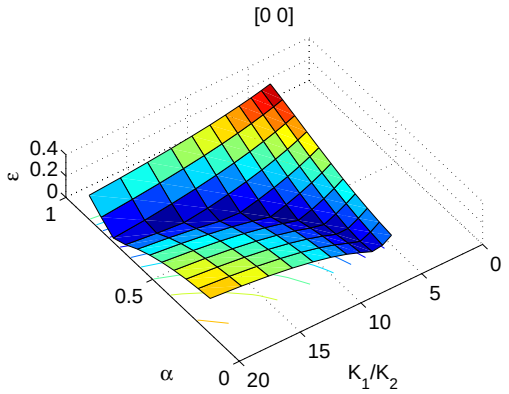

(a) point ②

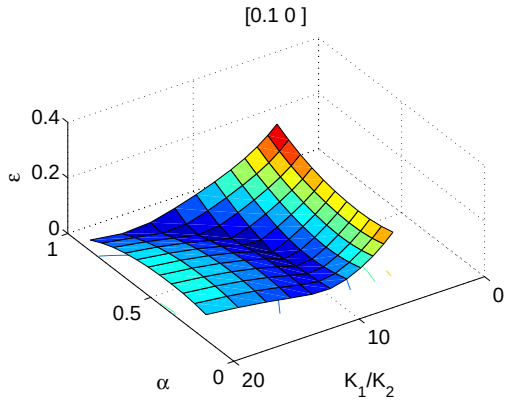

(b) point ④

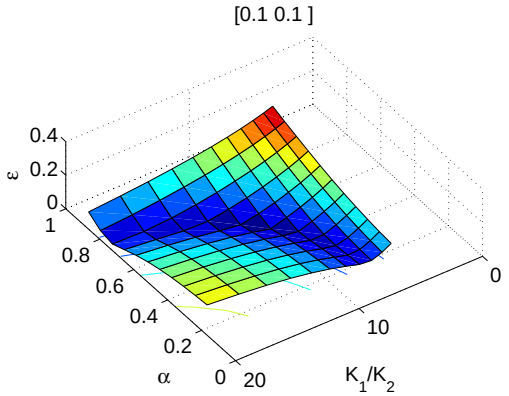

(c) point ⑤

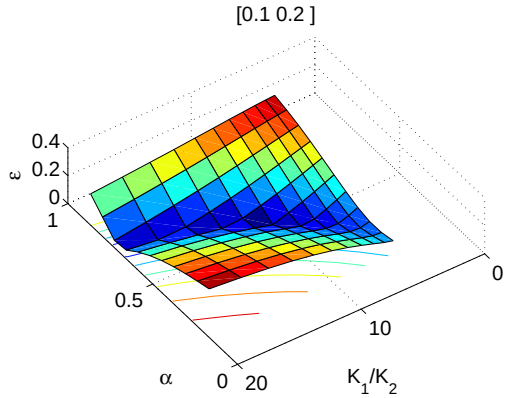

(d) point ⑥

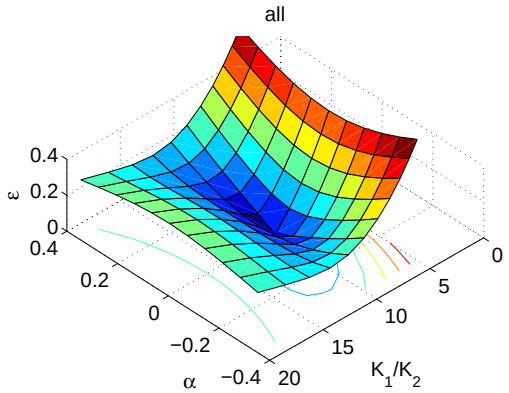

(e) points ② ④ ⑥

Fig. A.10: Objective function ε at different tested locations (input parameters: $R'_k = 10$ - $K'_1 = 1 \times 10^{-11}$, $K'_2 = 0.1 \times 10^{-11}$, and $\alpha' = \pi/6$).

A.2 2D set-up design

A.2.1 Tables

Sensor location	$[K_1', K_2']$ ([m^2, m^2])	Back-calculated $[K_1, K_2]$ ([m^2, m^2])
a	[2e-012, 1e-011]	[1.43e-012 8.92e-011]
b	[2e-012, 1e-011]	[5.30e-011 1.48e-012]
c	[2e-012, 1e-011]	[2.01e-012 1.00e-011]
d	[2e-012, 1e-011]	[1.03e-011 1.97e-012]
a, b	[2e-012, 1e-011]	[1.49e-012 5.06e-011]
a, c	[2e-012, 1e-011]	[2.01e-012 1.00e-011]
a, d	[2e-012, 1e-011]	[2.01e-012 9.83e-012]
a	[5e-012, 1e-011]	[3.64e-012 2.44e-011]
b	[5e-012, 1e-011]	[1.72e-011 3.75e-012]
c	[5e-012, 1e-011]	[4.13e-011 3.75e-012]
d	[5e-012, 1e-011]	[1.94e-011 3.30e-012]
a, b	[5e-012, 1e-011]	[4.89e-012 1.05e-011]
a, c	[5e-012, 1e-011]	[5.02e-012 9.94e-012]
a, d	[5e-012, 1e-011]	[4.96e-012 1.02e-011]
a	[1e-011, 1e-011]	[7.02e-012 2.46e-011]
b	[1e-011, 1e-011]	[2.56e-011 5.68e-012]
c	[1e-011, 1e-011]	[2.46e-011 7.03e-012]
d	[1e-011, 1e-011]	[1.21e-011 8.33e-012]
a, b	[1e-011, 1e-011]	[1.02e-011 9.90e-012]
a, c	[1e-011, 1e-011]	[1.02e-011 9.90e-012]
a, d	[1e-011, 1e-011]	[9.98e-012 9.96e-012]
a	[2e-011, 1e-011]	[1.99e-011 1.02e-011]
b	[2e-011, 1e-011]	[2.93e-011 8.25e-012]
c	[2e-011, 1e-011]	[2.03e-011 9.94e-012]
d	[2e-011, 1e-011]	[2.66e-011 8.08e-012]

Table A.4: Back-calculated K based on simulated curves at various sets of points for DPM (optimization parameters: termination tolerance on the function value is 100; termination tolerance on variables $\hat{K_x}$ and $\hat{K_y}$ are 0.1).

A.2.2 Figures

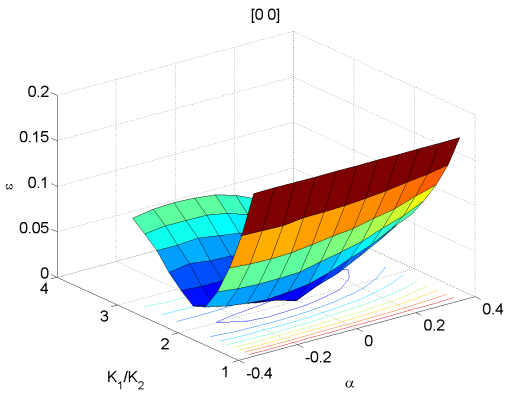

(a) point a (0,0)

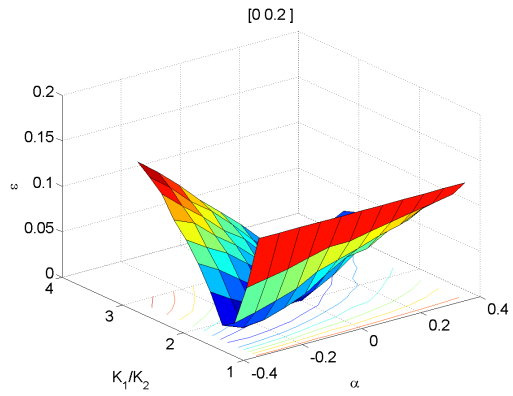

(b) point b (0,0.2)

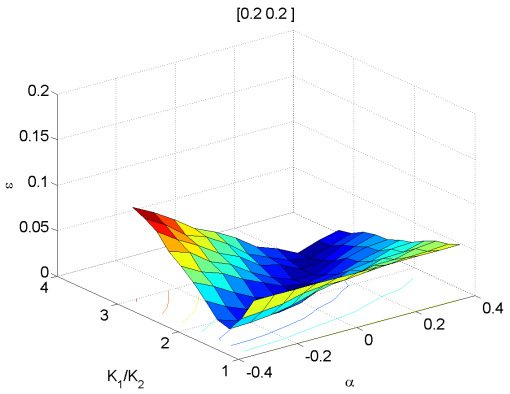

(c) point c (0.2,0.2)

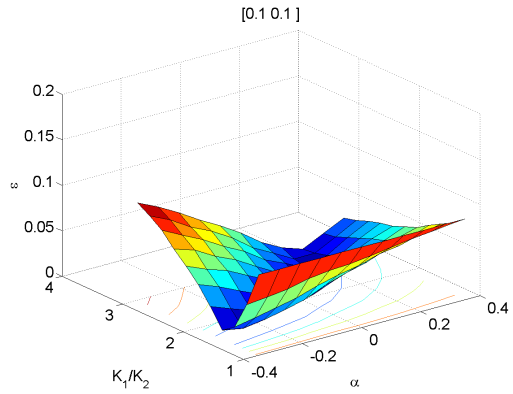

(d) point d (0.1,0.1)

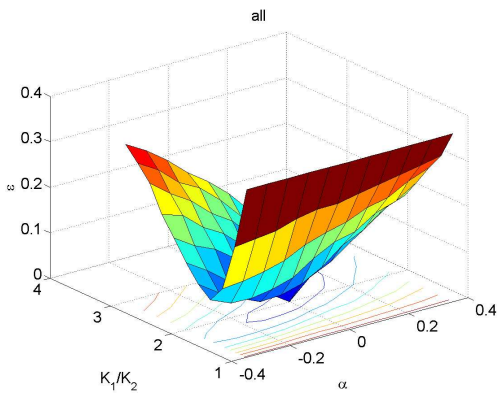

(e) points $a + b + c$

Fig. A.11: Objective function ε at different tested locations a, b, c, d, and $a + b + c$; ($R'_k = 2$, $K'_1 = 2 \times 10^{-12}\mathrm{m}^2$) and $\alpha' = \pi/6$). RPM loading.

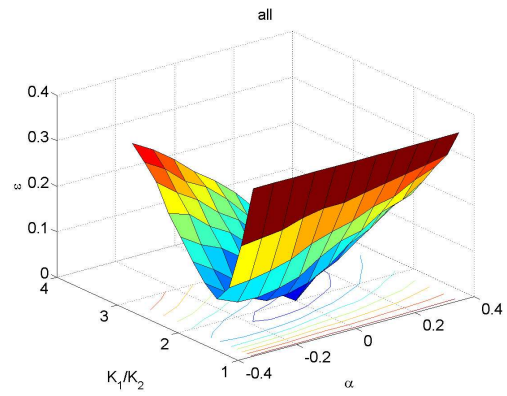

(a) $\alpha' = 0$

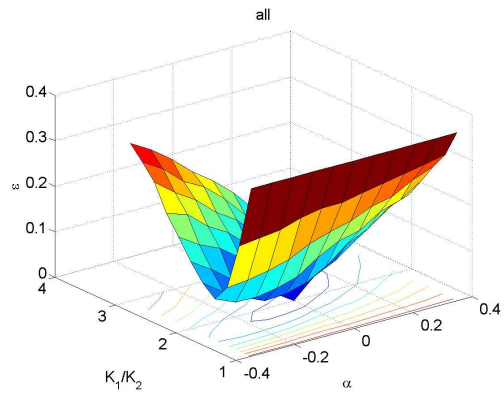

(b) $\alpha' = \pi/6$

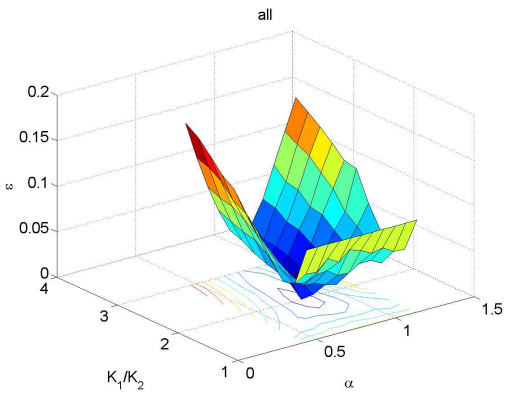

(c) $\alpha' = \pi/4$

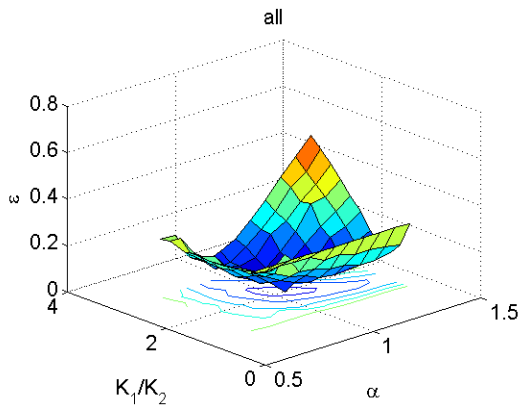

(d) $\alpha' = \pi/3$

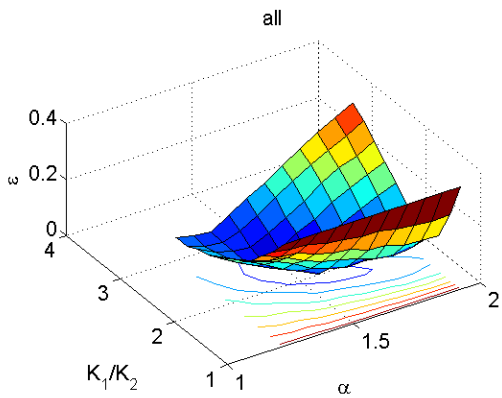

(e) $\alpha' = \pi/2$

Fig. A.12: Objective function ε for pressure responses at locations $a + b + c$; ($R'_k = 2$, $K'_1 = 2 \times 10^{-12}\mathrm{m}^2$) and $\alpha' \in [0; \pi/6; \pi/4; \pi/3; \pi/2]$. RPM loading.

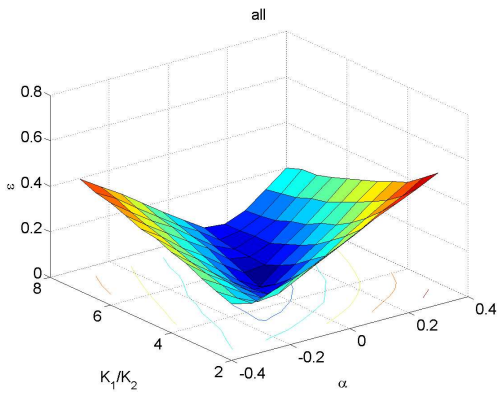

(a) $\alpha' = 0$

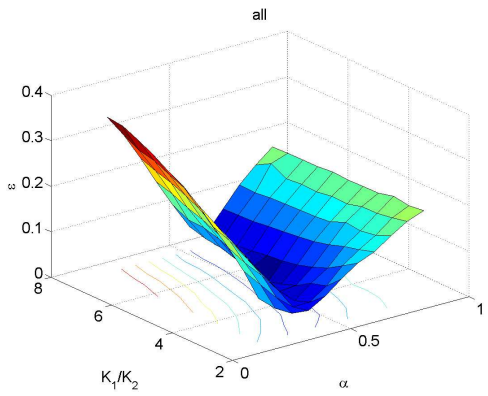

(b) $\alpha' = \pi/6$

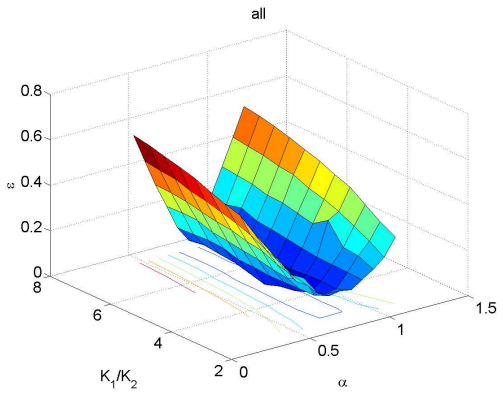

(c) $\alpha' = \pi/4$

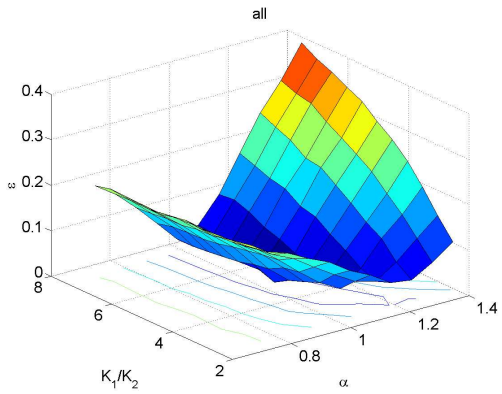

(d) $\alpha' = \pi/3$

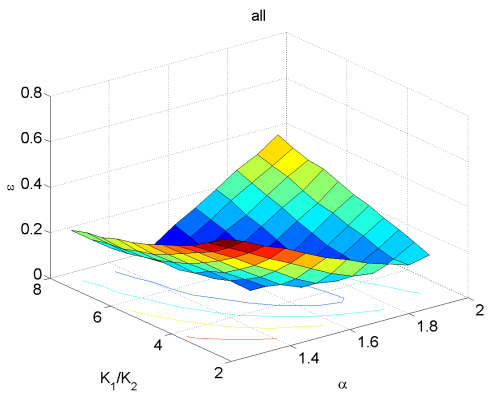

(e) $\alpha' = \pi/2$

Fig. A.13: Objective function ε for pressure responses at locations $a + b + c$; $R'_k = 5$ ($K'_1 = 2 \times 10^{-12}\mathrm{m}^2$) and $\alpha' \in [0; \pi/6; \pi/4; \pi/3; \pi/2]$. RPM loading.

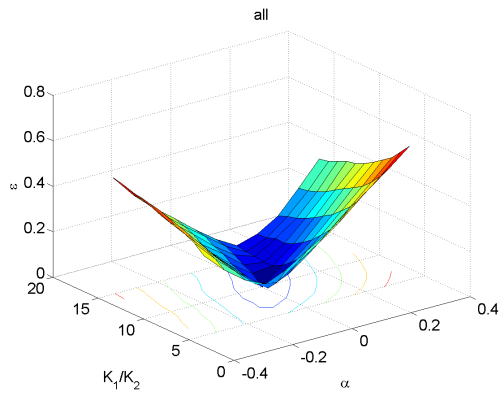

(a) $\alpha' = 0$

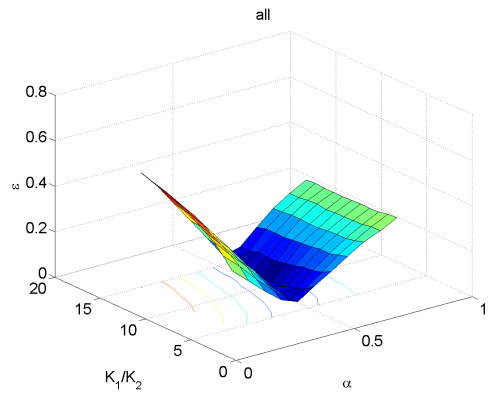

(b) $\alpha' = \pi/6$

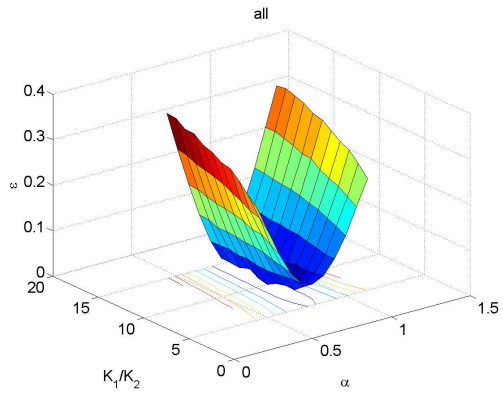

(c) $\alpha' = \pi/4$

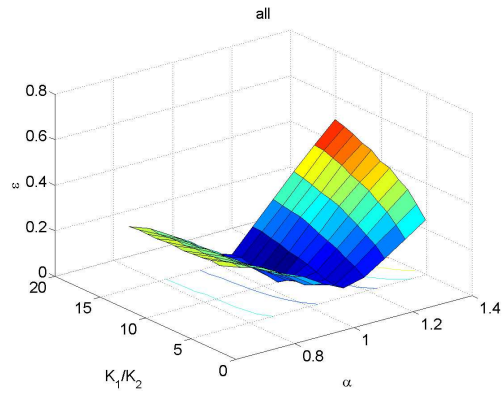

(d) $\alpha' = \pi/3$

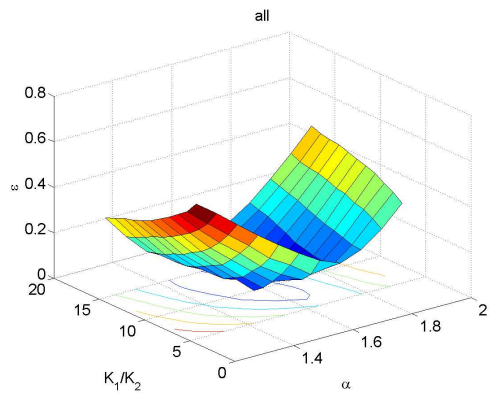

(e) $\alpha' = \pi/2$

Fig. A.14: Objective function ε for pressure responses at locations $a + b + c$; ($R'_k = 10$, $K'_1 = 2 \times 10^{-12}\mathrm{m}^2$) and $\alpha' \in [0; \pi/6; \pi/4; \pi/3; \pi/2]$.

École Nationale Supérieure des Mines
de Saint-Étienne

NNT : 2012 EMSE 0667

Yi HOU

EXPERIMENTAL CHARACTERIZATION AND MODELING OF THE PERMEABILITY OF FIBROUS PREFORMS USING GAS FOR DIRECT PROCESSES APPLICATION

Speciality : Mechanics and Engineering

Keywords : Fabric/Textile, in-plane permeability, transient gas flow, Darcy, Knudsen, Klinkenberg effect

Abstract :

A methodology to measure in-plane permeability of fibrous media using a transient one dimensional air flow is developed. The method, based on the measurement of gas pressure at the boundaries throughout the transient flow, is convenient, clean and fast, avoids usage of a gas flow meter and offers a way to study the gas transport within fibrous media.

The gas transport through fibrous porous media is described by several models to comply with different flow regimes. The permeability, only depending on the fibrous structure, is determined by inverse method, fitting the simulation results to the experimental data obtained using rising or dropping pressure methods. The results of viscous permeability K_v of Glass/Carbon Twill Woven fabrics (viscous permeability K_v ranging from 10^{-11} to 10^{-10} m^2) measured using gas match well the permeability measured with liquid compression and injection techniques from previous works. The deviation from Darcy's law caused by gas sliding effect on low permeability Carbon Uni-Directional fabrics (K_v from 10^{-14} to 10^{-12} m^2) is analyzed and a related parameter of fabric material shows a dependence in permeability, with a similar trend as the Klinkenberg sliding parameter in soils and rocks.

The experimental errors due to dimensions, thermal effect, pressure variation, sample handling, and trapped gas at boundaries are analyzed. It comes out that the sensitivities of pressure sensors and trapped gas volumes at the boundaries have the most important effects.

A design for 2D measurement using gas to obtain 2D permeability tensor in one single test is proposed to avoid the issues of trapped gas at boundaries. Simulated experiments show that the measurements based on pressure measured at three proposed locations could provide robust and accurate results for fabrics of anisotropic permeability ratios (K_1/K_2) ranging from 0.1 to 10, with various principal permeability direction orientations.

École Nationale Supérieure des Mines
de Saint-Étienne

NNT : 2012 EMSE 0667

Yi HOU

CARACTERISATION ET MODELISATION EXPERIMENTALE DE LA PERMEABILITE AU GAZ DE PREFORMES FIBREUSES POUR LES PROCEDES D'ELABORATION DIRECTE

Spécialité: Mécanique et Ingénierie

Mots clefs : Tissus/Textile, perméabilité dans le plan, l'écoulement de gaz transitoire, Darcy, Knudsen, Klinkenberg effet

Résumé :

Une méthodologie pour mesurer la perméabilité plane d'un milieu fibreux par un flux d'air transitoire est développée. Le procédé, basé sur la mesure de pression d'un gaz aux bornes du système, au cours d'un écoulement transitoire, est pratique, propre et rapide, et permet d'éviter l'utilisation d'un débitmètre de gaz et offre la possibilité d'étudier le transport d'un gaz à l'intérieur du milieu fibreux.

Le transport du gaz dans un milieu poreux fibreux est décrit par plusieurs modèles suivant les différents régimes d'écoulement. La perméabilité, dépendant uniquement de l'architecture fibreuse, est déterminée par une méthode inverse, en ajustant les résultats de la simulation aux données expérimentales obtenues par une hausse ou une chute de la pression. Les résultats pour la perméabilité visqueuse K_v des tissus sergés des verre/carbone (K_v allant de 10^{-11} à 10^{-10} m^2) mesurée à l'aide d'un gaz corrèlent bien à la perméabilité mesurée avec des techniques d'injection ou compression utilisant un liquide. L'écart avec la loi de Darcy causé par le glissement du gaz sur les tissus à faible perméabilité (tissus unidirectionnels de carbone: K_v de 10^{-14} à 10^{-12} m^2) est analysé et un paramètre lié au tissu montre une dépendance avec la perméabilité, avec une tendance similaire au paramètre de Klinkenberg utilisé pour les sols et les roches.

Les erreurs expérimentales dues à des dimensions, à l'effet thermique, à la variation de pression, à la manipulation des échantillons, et à du gaz emprisonné sur les bords sont analysés. Il en ressort que la sensibilité des capteurs de pression et des volumes de gaz piégés sur les bords sont les facteurs les plus importants.

La mise en place d'une méthode permettant une mesure directe de la perméabilité à l'aide d'un gaz du tenseur 2D de perméabilité est proposée pour les problèmes de gaz piégés sur les bords. Les expériences simulées montrent que les mesures basées sur la pression mesurée à trois positions pourraient fournir des résultats fiables et précis pour des tissus avec des rapports d'anisotropie perméabilité (K_1/K_2) allant de 0,1 à 10, et avec des orientations principales quelconques.